

Structural mechanics of a plate with multiple dimples



Daniel T Eatough

Supervisor: Dr K. A. Seffen

Department of Engineering
University of Cambridge

This dissertation is submitted for the degree of
Doctor of Philosophy

For Rachel ...

Acknowledgements

I first wish to thank my supervisor Dr Keith Seffen, for encouraging my interests in academia and in structures for many years. I'm especially grateful for stimulating discussions and supervisions as well as for guiding me through this new adventure and encouraging me to press on when progress seemed slow.

I would also like to acknowledge Dr Overend, for kindly allowing me use of his oven to heat treat my specimens, as well as the technicians in the labs for pandering to my requests and manufacturing many perforated sheets with the most peculiar and irregular patterns. A special mention must be made to Mr Christmas for saving all our ears by suggesting I use the fly press rather than a mallet to form the dimples of my many dimpled sheets.

I'm forever indebted to my excellent friend Luke Bounds, for walking alongside me through many years of engineering and life. For your persistent encouragement, open ears, insightful comments and stimulating discussions as well as reminding me there is more fun in life than just a PhD. You'll probably never realise quite how much I've valued your support through this process.

To my Mum, Dad and sister, you are all wonderful and supportive. Thanks for taking an interest in me and in my work, even when we are both hard to understand at times.

Finally, thank you Rachel, you've been the best girlfriend, fiancée and wife that any PhD student could wish for. Thank you for cheering me on, picking me up and most of all for pointing me to the author of all creation from whom no secrets are hid. All glory and knowledge belong to God, and I am blessed and humbled that he has revealed through me this work.

Declaration

This thesis is the result of my own work and includes nothing which is the outcome of work done in collaboration except as declared in the Preface and specified in the text. It is not substantially the same as any that I have submitted, or, is being concurrently submitted for a degree or diploma or other qualification at the University of Cambridge or any other University or similar institution except as declared in the Preface and specified in the text. I further state that no substantial part of my thesis has already been submitted, or, is being concurrently submitted for any such degree, diploma or other qualification at the University of Cambridge or any other University or similar institution except as declared in the Preface and specified in the text. It does not exceed the prescribed word limit for the relevant Degree Committee.

Daniel T Eatough
January 2020

Structural mechanics of a plate with multiple dimples

Daniel T Eatough

Thin plates, sheets and shells are an important category of structural components, and while commonly used, they are often only utilised in simplistic geometries. An increased understanding of the geometric and structural behaviour of more sophisticated geometries allows for the optimisation of performance. This thesis considers a thin plate which has (or has been given) out-of-plane depth or texture: a dimpled sheet. By developing new methods of analysis for these types of modified plate geometries, increases in performance can be sought and quantified. Compared to flat plates, corrugated sheets have an increased bending stiffness in one direction, whilst dimpled sheets have an increase in bending stiffness in both orthogonal directions. Comparing dimpled to corrugated sheets, a “second moment of area” approach might be used; however, this thesis will show that such an analysis is unsuitable. Instead a wholly new approach is developed to describe and quantify the structural behaviour of a dimpled sheet, with the key observation being the treatment of each dimple as an elastic inclusion. Theoretical analysis is carried out which confirms the applicability of representing a single dimple as an elastic inclusion, and which quantifies the relationship between dimple geometry and the effective stiffness of the inclusion. The applicability of this representation is also confirmed through use of relevant finite element analysis. Analysis of the overall performance of a plate with a pattern of inclusions is subsequently carried out. A theoretical formula is derived that accurately predicts the smeared overall elastic modulus of an inclusion patterned plate, and the suitability of this formula is backed-up by extensive finite element analysis. This formula also compares favourably to existing “rule-of-mixtures” approaches, although it is superior to existing rules due to its incorporation of Poisson’s ratio terms. Practical experiments on perforated strips explore the behaviour of plates which have inclusions of zero stiffness, with favourable agreement to the derived theory. By combining the analyses of the previous sections, the overall performance of a dimpled sheet is investigated. Making suitable adjustments to the effective inclusion representing each dimple, due to the proximity of adjacent dimples, a complete theoretical prediction of the structural performance of a dimpled sheet is derived. Finite element analysis is used to validate that the theoretical model is suitable for predicting and accurately capturing both the increase in bending stiffness of a dimpled sheet, as well as the reduction in stretching stiffness. Furthermore, practical experiments on physical dimpled sheet specimens confirm the increased bending stiffness which is obtained from dimpled sheets, as compared to identical specimens without dimpling.

Table of contents

List of figures	xv
List of tables	xxi
1 Introduction	1
1.1 Research aims and objectives	3
1.2 Scope and approach	4
2 Introduction to dimpled sheets	7
2.1 Summary	7
2.2 Introduction	7
2.3 Background	10
2.3.1 Dimples and dimpled sheets	10
2.3.2 Plates and shells	11
2.4 Expected structural performance in bending	12
2.5 Initial experimentation on dimpled sheets	20
2.5.1 Experimental method	20
2.5.2 Experimental results	26
2.6 Conclusions	27
3 Analysis of a single dimple	31
3.1 Summary	31
3.2 Introduction	32
3.3 Background	32
3.3.1 Axisymmetric analysis of a shell of revolution	33
3.4 Analytical model of a single dimple	39
3.4.1 Normalised stiffness of a dimple	39
3.4.2 Equivalent cone of a general dimple	42
3.4.3 Equivalence of an inclusion and a dimple in an infinite plate	45

3.5	Finite Element Analysis of a single dimple	49
3.5.1	FEA of a spherical cap vs Geckler theory	50
3.5.2	FEA verification of the equivalent cone technique	52
3.5.3	FEA verification of the equivalence of a dimple and an inclusion	55
3.6	Conclusions	61
4	Patterns of inclusions	67
4.1	Summary	67
4.2	Introduction	67
4.3	Background	68
4.4	Homogenisation of patterns of inclusions	69
4.5	Theoretical analysis of patterns of inclusions	71
4.5.1	Analysis of a single inclusion	71
4.5.2	Patterns of inclusions	79
4.6	FEA methodology	89
4.7	Biaxial loading	91
4.7.1	Regular patterns	91
4.7.2	Extreme material constants	96
4.7.3	Irregular patterns	98
4.7.4	Inclusion shape	101
4.8	Uniaxial and antisymmetric loading	103
4.8.1	Bending vs stretching	105
4.8.2	Regular patterns	106
4.8.3	Irregular patterns	109
4.9	Isotropy and homogeneity	113
4.9.1	Isotropy	114
4.9.2	Homogeneity	116
4.10	Experimental validation	121
4.10.1	Experimental method	122
4.10.2	Experimental results	123
4.11	Rule-of-mixtures comparison	127
4.11.1	Comparison of voids and empty inclusions	129
4.11.2	Comparison of stiff inclusions	131
4.12	Conclusions	133

5	Patterned dimpled sheets	135
5.1	Summary	135
5.2	Introduction	136
5.3	Initial findings	137
5.4	FEA methodology	140
5.5	Analytical model of dimpled sheets	143
5.5.1	Over-prediction of k_{bend}	144
5.5.2	k -degradation	144
5.5.3	Up–down dimples	148
5.5.4	Stress concentration factors	150
5.6	Biaxial behaviour of dimpled sheets	152
5.6.1	FEA results: Biaxial bending	152
5.6.2	FEA results: Biaxial stretching	159
5.6.3	Homogeneous smeared properties	159
5.7	Experimental validation	161
5.7.1	Experimental methodology	161
5.7.2	Experimental results	165
5.8	Uniaxial behaviour of dimpled sheets	170
5.9	Antisymmetric behaviour of dimpled sheets	172
5.10	Discussion	175
5.11	Conclusions	178
6	Conclusions	181
	References	185
	Appendix A Cross-sections of dimpled sheets	191
A.1	Calculating the second moment of area of a single dimple cross-section	191
A.1.1	Hemispherical and semi-ellipsoidal dimples	191
A.1.2	Spherical cap dimple	192
A.2	Calculating the second moment of area of an arbitrary cross-section	194
	Appendix B Inclusion stresses	199
B.1	Scaled superposition of stresses around adjacent inclusions	199
	Appendix C Aperiodic patterns	203
C.1	Penrose tilings	203
C.2	Penrose rhombus patterns	208

C.3	Penrose kite and dart patterns	211
Appendix D	Stiffnesses of circular plates	215
D.1	Stiffness of a finite plate with a central hole with internal loading	215
D.2	Stiffness of a circular plate with stiff central section and an overhang under a transverse ring loading	216
Appendix E	FEA normalised stiffness data	221
E.1	Normalised stiffness of inclusion patterned plates	221
E.2	Normalised stiffness of dimpled sheets	235
Appendix F	Perforated strips experimental data	243
F.1	Uniaxial stretching stiffness of perforated strips	243
F.2	Uniaxial bending stiffness of perforated strips	245
Appendix G	Patterns for experimental testing of dimpled sheets	247
G.1	Figures of patterns used for experimental testing	247
G.2	Tables of coordinates for patterns used for experimental testing	250

List of figures

1.1	Pantheon cross-section	2
1.2	A first millennium dimpled pot and a medieval thimble	3
1.3	Bending comparison between a plain and a dimpled sheet	4
2.1	Dimpled sheets	11
2.2	Corrugated sheet profile and dimpled sheet profile	13
2.3	Second moment of area of various cross-sections	14
2.4	Cross-section of a dimple	14
2.5	The cross-section of a dimpled sheet is not constant along its length	15
2.6	Hexagonal and phyllotaxis pattern	16
2.7	Second moment of area distributions of two dimpled sheets	17
2.8	Two dimples in the same direction and and two dimples in opposite directions	19
2.9	Hexagonal and phyllotaxis patterns split into two equal sets	20
2.10	Second moment of area distributions of two dimpled sheets with dimples in two directions	21
2.11	Diagram of indentation process	22
2.12	A thin sheet is held between two thick forming plates	23
2.13	Four square dimpled sheet samples	24
2.14	Three-point bend test set-up	25
2.15	Force-displacement characteristic of samples in the three-point bending test	27
3.1	General shell of revolution	34
3.2	Cross-section of a shell of revolution with a circular arc profile: a spherical cap	35
3.3	The equivalence of a spherical cap and a cone	38
3.4	Comparison of a dimple to a disc and an apex cone	40
3.5	The “equivalent cone” of an arbitrary dimple profile	43
3.6	FEA comparison of a quartic profile dimple and its equivalent cone	45
3.7	Axisymmetric superposition of a dimple and an inclusion into an infinite plate	46

3.8	FEA vs Geckler approximation for a spherical cap under applied edge moment	51
3.9	Comparison of theoretical and FEA normalised stiffnesses of a spherical cap dimple	53
3.10	FEA indentation simulation	55
3.11	Contour maps of α_4 for quartic dimples; FEA, apex cone theory and equivalent cone theory	56
3.12	Inclusion in infinite plate in generalised bending	57
3.13	FEA model of an inclusion or dimple in the centre of a large plate	58
3.14	Graphs comparing FEA results for moments, rotations and curvatures of a plate with a central inclusion or dimple	59
3.15	Graphs comparing FEA results for moments, rotations and curvatures of a plate with a dimple or an inclusion with k_{bend}	61
3.16	FEA model of an inclusion or dimple in the centre of a large plate in antisymmetric bending	62
3.17	Graphs of FEA results for moments, rotations and curvatures of a plate with a dimple compared with an inclusion in antisymmetric bending	63
3.18	Graphs of FEA results for moments, rotations and curvatures of a plate with a dimple compared with a higher stiffness inclusion in antisymmetric bending	64
4.1	Dithering block colours to perceive a homogeneous shade	70
4.2	Generalised loading of a thin infinite plate with a central circular inclusion.	72
4.3	Stress contours of an elastic inclusion and the surrounding plate under general loading	75
4.4	A circular elastic inclusion in a circular plate of a finite size under biaxial tension.	77
4.5	A regular hexagonal pattern of inclusions	80
4.6	Radial stress distributions for a hexagonal patterning of inclusions under biaxial loading	81
4.7	Radial and circumferential stress distributions for a hexagonal patterning of inclusions under biaxial loading	84
4.8	Superposed radial and circumferential stress distributions for a hexagonal patterning of inclusions under biaxial loading	87
4.9	A square plate with a hexagonal pattern of inclusions, modelled in FEA . .	90
4.10	Edge effects in an FEA model of an inclusion patterned plate	91
4.11	Biaxial normalised stiffness of regular hexagonal patterns of inclusions . . .	93
4.12	SCFs of hexagonally patterned inclusions in biaxial tension	94

4.13	Biaxial normalised stiffness of regular hexagonal and square patterns of inclusions	95
4.14	Biaxial normalised stiffness for hexagonal patterns with large or small k	97
4.15	Biaxial normalised stiffness for hexagonal patterns with large or small ν	98
4.16	Phyllotaxis pattern in a sunflower	99
4.17	Penrose tiling schemes for inclusion patterns	100
4.18	Biaxial normalised stiffness for irregular patterns of inclusions	101
4.19	Inclusion SCF for irregular patterns	102
4.20	Biaxial normalised stiffness for a square pattern of square inclusions	103
4.21	A concave C-shaped inclusion	104
4.22	A concave 4-pointed star inclusion	104
4.23	Normalised biaxial stiffness of concave inclusions	105
4.24	Biaxial bending of inclusion patterned plates	107
4.25	Uniaxial bending of inclusion patterned plates	107
4.26	Normalised uniaxial bending stiffness of inclusion patterned plates	108
4.27	Biaxial, uniaxial and antisymmetric normalised stiffness for hexagonally patterned plates	110
4.28	Biaxial, uniaxial and antisymmetric normalised stiffness for square patterned plates	111
4.29	Biaxial, uniaxial and antisymmetric normalised stiffness for square patterned plates at 45°	112
4.30	Antisymmetric normalised stiffness for irregular patterns of inclusions	113
4.31	Normalised antisymmetric bending stiffness of different pattern orientations	114
4.32	Normalised antisymmetric bending stiffness of different pattern orientations	115
4.33	Normalised antisymmetric bending stiffness of different pattern orientations	116
4.34	FEA of an inclusion patterned plate in biaxial bending	117
4.35	Rotation and out-of-plane deflections of an inclusion patterned plate are compared to the smeared homogeneous approximation	118
4.36	Experimental set-up of uniaxial stretching of a perforated strip	124
4.37	Experimental set-up of uniaxial bending of a perforated strip	125
4.38	Normalised bending and stretching stiffness of perforated strips	126
4.39	Experimental results of normalised stiffness compared with various theoretical predictions	130
4.40	FEA results of normalised stiffness compared with various theoretical predictions	132
5.1	Normalised biaxial stiffness of a dimpled sheet	138

5.2	<i>k</i> -degradation for biaxial bending of a dimpled sheet	139
5.3	A square plate with a hexagonal pattern of dimples, modelled in FEA	142
5.4	Comparison of shell and solid element meshes for a dimpled sheet	143
5.5	Biaxial stiffness and <i>k</i> -degradation of a dimpled sheet	145
5.6	Superposition states of a dimple in a finite plate	146
5.7	Two alternative up-down dimple patterns for the hexagonal patterning	149
5.8	Normalised biaxial stiffness of dimpled sheets with different patterns of dimples	153
5.9	Normalised biaxial stiffness of dimpled sheets with stiffer dimples	155
5.10	Normalised biaxial stiffness of dimpled sheets with quartic geometry dimples	157
5.11	SCFs of dimpled sheets with quartic geometry dimples	158
5.12	Normalised biaxial stretching stiffness of dimpled sheets with different patterns of dimples	160
5.13	Biaxial bending test rig	162
5.14	FEA of the biaxial bending test rig	164
5.15	Biaxial bending experimental test rig	165
5.16	Circular dimpled sheets	166
5.17	Circular dimpled sheet before and after heat treatment	166
5.18	Experimental force-displacement characteristic for biaxial bending of dim- pled sheets	168
5.19	Biaxial vs uniaxial bending characteristics	169
5.20	Normalised uniaxial bending stiffness of dimpled sheets	171
5.21	Normalised uniaxial bending stiffness of dimpled sheets	173
5.22	Normalised antisymmetric bending stiffness of dimpled sheets	174
5.23	Normalised bending stiffnesses of dimpled sheets	177
A.1	Semicircular dimple profile	191
A.2	Circular arc dimple profile	193
A.3	General cross-section of a dimpled sheet	194
C.1	Thin and thick rhombus prototiles	208
C.2	Three surrounding tile neighborhoods of a ‘S5’ vertex	211
C.3	Kite and dart prototiles	211
D.1	Biaxial bending test rig	217
G.1	Hexagonal, phyllotaxis, Penrose Rhombus and Penrose Kite and Dart patterns	248

G.2 Hexagonal, phyllotaxis, Penrose Rhombus and Penrose Kite and Dart Up/- Down patterns	249
---	-----

List of tables

2.1	Normalised stiffnesses of dimpled sheet samples in three-point bending . . .	28
5.1	Comparison of stiffness parameters of a dimple modelled with shell and solid elements; $a/t = 6$, $d/a = 1/6$, $\nu = 0.3$	144
C.1	The eight vertex neighbourhoods that occur in the Penrose rhombus tiling . .	203
C.2	The nine vertex neighbourhoods that occur in the Penrose kite and dart tiling	205
E.1	Normalised biaxial stiffnesses and SCF of inclusion patterned sheets, regular hexagonal pattern, $k = 3$ and $\nu = 0.3$	222
E.2	Normalised biaxial stiffnesses and SCF of inclusion patterned sheets, regular hexagonal pattern, $k = 0.2$ and $\nu = 0.3$	222
E.3	Normalised biaxial stiffnesses and SCF of inclusion patterned sheets, regular square pattern, $k = 3$ and $\nu = 0.3$	223
E.4	Normalised biaxial stiffnesses and SCF of inclusion patterned sheets, Penrose Rhombus pattern, $k = 3$ and $\nu = 0.3$	223
E.5	Normalised biaxial stiffnesses and SCF of inclusion patterned sheets, Penrose Kite and Dart pattern, $k = 3$ and $\nu = 0.3$	224
E.6	Normalised biaxial stiffnesses and SCF of inclusion patterned sheets, phyllotaxis pattern, $k = 3$ and $\nu = 0.3$	224
E.7	Normalised biaxial stiffnesses of inclusion patterned sheets, regular hexagonal pattern, $k = 10$ and $\nu = 0.3$	225
E.8	Normalised biaxial stiffnesses of inclusion patterned sheets, regular hexagonal pattern, $k = 0$ and $\nu = 0.3$	225
E.9	Normalised biaxial stiffnesses of inclusion patterned sheets, regular hexagonal pattern, $k = 3$ and $\nu = 0.1$	226
E.10	Normalised biaxial stiffnesses of inclusion patterned sheets, regular hexagonal pattern, $k = 3$ and $\nu = 0.5$	226

E.11	Normalised biaxial stiffnesses of inclusion patterned sheets, regular square pattern of square inclusions, $k = 3$ and $\nu = 0.3$	227
E.12	Normalised biaxial stiffnesses of inclusion patterned sheets, regular square pattern of concave star inclusions, $k = 3$ and $\nu = 0.3$	227
E.13	Normalised uniaxial bending stiffnesses of inclusion patterned sheets, regular hexagonal pattern, $k = 3$ and $\nu = 0.3$	228
E.14	Normalised uniaxial and antisymmetric stiffnesses of inclusion patterned sheets, regular hexagonal pattern, $k = 3$ and $\nu = 0.3$	228
E.15	Normalised uniaxial and antisymmetric stiffnesses of inclusion patterned sheets, regular hexagonal pattern, $k = 0.2$ and $\nu = 0.3$	229
E.16	Normalised uniaxial and antisymmetric stiffnesses of inclusion patterned sheets, regular square pattern, $k = 3$ and $\nu = 0.3$	229
E.17	Normalised uniaxial and antisymmetric stiffnesses of inclusion patterned sheets, regular square pattern, $k = 0.2$ and $\nu = 0.3$	230
E.18	Normalised uniaxial and antisymmetric stiffnesses of inclusion patterned sheets, regular square pattern aligned at 45° to the direction of primary loading, $k = 3$ and $\nu = 0.3$	230
E.19	Normalised antisymmetric stiffnesses of inclusion patterned sheets loaded in perpendicular directions, regular hexagonal pattern, $k = 3$ and $\nu = 0.3$. . .	231
E.20	Normalised antisymmetric stiffnesses of inclusion patterned sheets loaded in perpendicular directions, Penrose Rhombus pattern, $k = 3$ and $\nu = 0.3$. . .	231
E.21	Normalised antisymmetric stiffnesses of inclusion patterned sheets loaded in perpendicular directions, Penrose Kite and Dart pattern, $k = 3$ and $\nu = 0.3$.	232
E.22	Normalised antisymmetric stiffnesses of inclusion patterned sheets loaded in perpendicular directions, phyllotaxis pattern, $k = 3$ and $\nu = 0.3$	232
E.23	Normalised antisymmetric stiffnesses of a regular hexagonal pattern of inclusions as the pattern is oriented at different angles to the direction of primary loading, $k = 3$ and $\nu = 0.3$	233
E.24	Normalised antisymmetric stiffnesses of a regular square pattern of inclusions as the pattern is oriented at different angles to the direction of primary loading, $k = 3$ and $\nu = 0.3$	234
E.25	Normalised biaxial bending stiffnesses and SCF of dimpled sheets, regular hexagonal pattern, quartic dimple profile, $d/a = 1/3$, $a/t = 30$, $\nu = 0.3$ and $L/a = 100/3$	235

E.26 Normalised biaxial bending stiffnesses and SCF of dimpled sheets, regular square pattern, quartic dimple profile, $d/a = 1/3$, $a/t = 30$, $\nu = 0.3$ and $L/a = 100/3$	236
E.27 Normalised biaxial bending stiffnesses and SCF of dimpled sheets, Penrose Rhombus pattern, quartic dimple profile, $d/a = 1/3$, $a/t = 30$, $\nu = 0.3$ and $L/a = 100/3$	236
E.28 Normalised biaxial bending stiffnesses of dimpled sheets, regular hexagonal pattern, spherical cap dimple profile, $d/a = 1/6$, $a/t = 6$, $\nu = 0.3$ and $L/a = 100/3$	237
E.29 Normalised biaxial bending stiffnesses of dimpled sheets, regular square pattern, spherical cap dimple profile, $d/a = 1/6$, $a/t = 6$, $\nu = 0.3$ and $L/a = 100/3$	237
E.30 Normalised biaxial bending stiffnesses of dimpled sheets, Penrose Rhombus pattern, spherical cap dimple profile, $d/a = 1/6$, $a/t = 6$, $\nu = 0.3$ and $L/a = 100/3$	238
E.31 Normalised biaxial bending stiffnesses of dimpled sheets, regular hexagonal pattern, spherical cap dimple profile, $d/a = 1/6$, $a/t = 30$, $\nu = 0.3$ and $L/a = 100/3$	238
E.32 Normalised biaxial bending stiffnesses of dimpled sheets, regular square pattern, spherical cap dimple profile, $d/a = 1/6$, $a/t = 30$, $\nu = 0.3$ and $L/a = 100/3$	239
E.33 Normalised biaxial stretching stiffnesses of dimpled sheets, regular hexagonal pattern, spherical cap dimple profile, $d/a = 1/6$, $a/t = 6$, $\nu = 0.3$ and $L/a = 100/3$	239
E.34 Normalised biaxial stretching stiffnesses of dimpled sheets, regular square pattern, spherical cap dimple profile, $d/a = 1/6$, $a/t = 6$, $\nu = 0.3$ and $L/a = 100/3$	240
E.35 Normalised uniaxial bending stiffnesses of dimpled sheets, regular hexagonal pattern, quadratic dimple profile, $d/a = 1/3$, $a/t = 30$, $\nu = 0.3$ and $L/a = 100/3$	240
E.36 Normalised uniaxial bending stiffnesses of dimpled sheets, regular hexagonal pattern, spherical cap dimple profile, $d/a = 1/6$, $a/t = 30$, $\nu = 0.3$ and $L/a = 100/3$	241
E.37 Normalised uniaxial bending stiffnesses of dimpled sheets, regular square pattern, spherical cap dimple profile, $d/a = 1/6$, $a/t = 30$, $\nu = 0.3$ and $L/a = 100/3$	241

E.38	Normalised antisymmetric bending stiffnesses of dimpled sheets, regular hexagonal pattern, quadratic dimple profile, $d/a = 1/3$, $a/t = 30$, $\nu = 0.3$ and $L/a = 100/3$	242
E.39	Normalised antisymmetric bending stiffnesses of dimpled sheets, regular hexagonal pattern, spherical cap dimple profile, $d/a = 1/6$, $a/t = 30$, $\nu = 0.3$ and $L/a = 100/3$	242
F.1	Uniaxial stretching stiffnesses of perforated strips	244
F.2	Uniaxial bending stiffnesses of perforated strips	245
G.1	The x and y coordinates of the hexagonal pattern given in Fig. G.2a	250
G.2	The x and y coordinates of the phyllotaxis pattern given in Fig. G.2b	253
G.3	The x and y coordinates of the Penrose Rhombus pattern given in Fig. G.2c	257
G.4	The x and y coordinates of the Penrose Kite and Dart pattern given in Fig. G.2d	261

Nomenclature

Roman Symbols

a	Radius of a dimple or inclusion
B	Bulk modulus
D	Flexural rigidity of a shell, $D = \frac{Eh^3}{12(1-\nu^2)}$
d	Depth of a dimple
E	Young's modulus
F	Generalised loading parameter
G	Shear modulus
H	Horizontal force (per unit length)
I_0	Nominal second moment of area for a flat sheet, $I_0 = Lt^3/12$
I_{xx}	Second moment of area
K	Inclusion stress factor
k	Ratio of Young's moduli: $k = E_2/E_1$
L	Length
M	Moment (per unit length)
N	In-plane force (per unit length)
n	Number of points in a pattern
P	Point load

p	Area (or volume) packing fraction
Q	Shear force (per unit length)
r	The radial direction or coordinate
R	Radius of curvature or radius of a finite plate
s	Scalar distance
h	Thickness measured in the through-thickness direction
t	Thickness measured in the vertical direction

A,B,C ... Superposition states

Greek Symbols

α_i	Normalised stiffness coefficients for dimple bending and stretching
δ	Displacement or deflection
ε	Strain
κ	Curvature
Λ	Normalised radius of a finite plate: $\Lambda = R/a$
λ	Dimensionless characteristic shell length, $\lambda^4 = 3(1 - \nu^2)(R/h)^2$
ν	Poisson's ratio
ω	$\omega = \phi_0 - \phi$
Φ	Airy's stress function
ϕ	Meridional angle
ϕ_0	Subtended half-angle of a dimple; the angle of opening
Ψ	Normalised stiffness: $\Psi = \psi/\psi_0$
ψ	Stiffness
ρ	Normalised radius: $\rho = r/a$
σ	Stress

σ_Y Yield stress

τ The golden ratio: $\tau = (1 + \sqrt{5})/2$

Θ Rotation

Subscripts

0 Nominal or reference quantity

r The radial direction or coordinate

θ The circumferential direction or coordinate

x The x direction or coordinate

y The y direction or coordinate

Acronyms / Abbreviations

CoC Centre of Curvature

c.t.c Centre to centre

FEA Finite Element Analysis

FPT Finite Plate Theory

GSC Generalised Self-Consistent

LHS Left Hand Side

SCF Stress Concentration Factor. The stress, or stress component, at a location divided by the nominal stress, $\frac{\sigma}{\sigma_0}$

ss Superposition and scaling

Chapter 1

Introduction

Thin plates, sheets and shells are an important category of structural components with a wide range of applications, including in automotive and aircraft engineering [1], and in building construction, for example in roof structures, however they are often utilised in only simplistic geometries [2]. An increased understanding of the functional and physical behaviour of more sophisticated geometries would allow enhanced optimisation of their structural properties.

A thin plate or shell is a structural element possessing one dimension much smaller than its others. In the limiting case, the thin through-thickness dimension may be negligible, such that the local geometry of the plate or shell-wall can be represented analytically as a two-dimensional surface. In this work the term ‘plate’ is used to describe a flat planar surface, whereas a ‘shell’ has curvature in at least one direction. The through-thickness of a shell is assumed to be much smaller than the principle radii of curvature. Just as a beam can be considered a one-dimensional structural component, with overall properties dependent on its local geometry and cross-section, so too a sufficiently thin plate can be considered as a two-dimensional structural element, with known overall structural properties.

Plates and shells with thin, but finite, through-thickness are useful in lightweight structures because of their high tensile stiffness and strength per unit weight. However, thin plates and shells have very poor bending resistance. The bending stiffness (D) of a plate depends on its thickness (t) cubed:

$$D = \frac{Et^3}{12(1 - \nu^2)} \quad (1.1)$$

For this reason, some analyses of thin plates and shells may neglect the bending stiffness altogether (the membrane hypothesis). However, when thicker plates or shell-thicknesses are considered, bending stiffness must be taken into account, increasing the analysis complexity.

In many practical applications plates will possess significant through-thickness, and be required to have a finite bending stiffness. For example, the grid plates of a nuclear reactor must hold the weight of a heavy nuclear core, which will induce a bending moment in the plate [3].

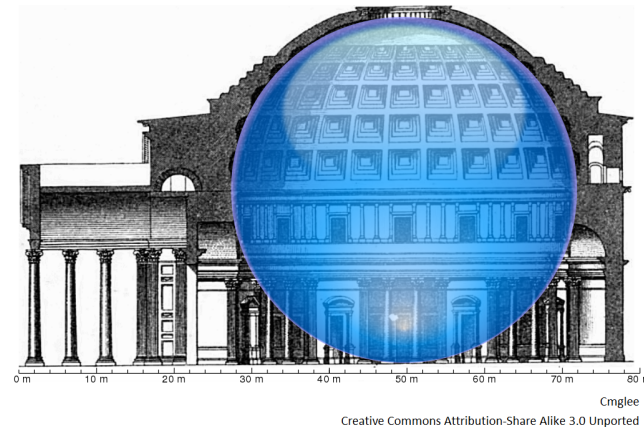


Fig. 1.1 A cross-section of the Pantheon in Rome, which demonstrates the hemispherical nature of its dome.

Plates which are initially flat may be deflected to form shells; and for some plates the resultant large displacements may allow the applied forces to be carried with ‘in-plane’ stresses rather than with bending stresses. This can also be the case for shell structures which have an initially curved geometry. So, for example a simply supported beam may carry a central point load with bending stresses, whereas arches or domes by virtue of their geometry can carry the same loading via in-plane stresses.

The structural benefits afforded by a hemispherical dome, especially for roof construction, have been appreciated for millennia. The Roman author Vitruvius, writing around the first century AD, says of domed roofs: “The proportions of the roof . . . should be such that the height of the rotunda, excluding the finial, is equivalent to one half of the diameter of the whole work.” [4]. The Pantheon in Rome, which dates from the time of the Emperor Hadrian, demonstrates well the principle of using hemispherical domes in roof construction, Fig. 1.1, and remains the largest unreinforced concrete dome in the world [5].

Of predominant interest in this present thesis however is not the behaviour of large individual domes, but rather the structural behaviour of dimpled sheets, which can be envisaged as containing an array of dome-like structures. Just as a single dome is geometrically a more structurally efficient shape than a flat plate, so a single dimple will be locally stiffer than the surrounding material. However it is the global structural performance of a sheet containing many dimples which will be of predominant interest here.

Dimpling of plate or shell surfaces is likewise a technique already used in ancient times, as illustrated by the Romano-British pot shown in Fig. 1.2a of a type manufactured in the Cambridge area early in the first millennium AD; and the medieval thimble shown in Fig. 1.2b, wherein the smooth surface of the shell is distorted out-of-plane to produce

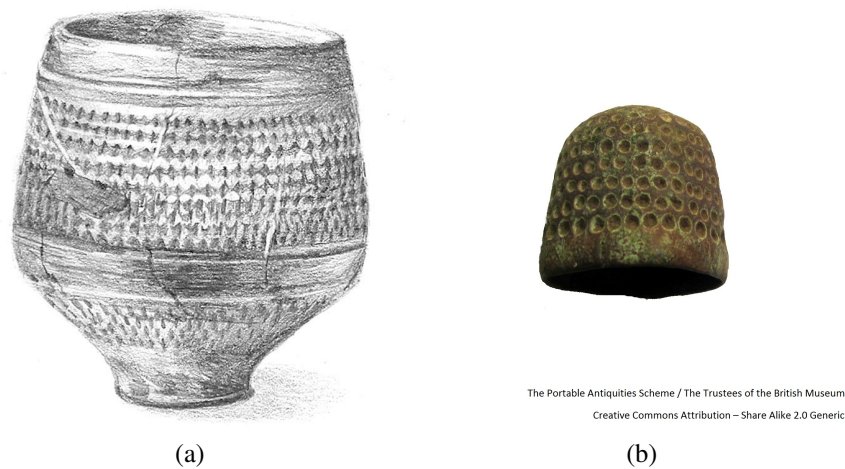


Fig. 1.2 (a) A first millennium Romano-British pot showing decorative dimpling. (b) A medieval thimble.

localised indentations or dimples. Adding this change in local geometry to the structure need not affect the global geometry, and thus dimpling can be seen as texturing of the shell. Dimpling in the historical examples shown, was most plausibly implemented for decorative or functional, rather than structural, reasons. However it is known from modern analyses that dimpling of a thin plate can affect the global structural properties in unusual ways beyond the basic considerations introduced above. States of self-stress induced by dimpling can cause global bi-stability of the plate [6]. Low, or even negative Poisson's ratios have been observed [7], and there may also be an increase in the overall bending stiffness of the plate [8]. It is the last of these properties to which the following chapters are primarily devoted.

1.1 Research aims and objectives

Motivated by the possibility of increasing the bending stiffness of a plate without adding additional material, see Fig. 1.3, the main research objective of this thesis is to analyse, characterise and allow optimisation of the structural behaviour of a dimpled sheet. In particular, this research aims to derive analytical equations to calculate the initial linear stiffness of a dimpled sheet under bending and under tension.

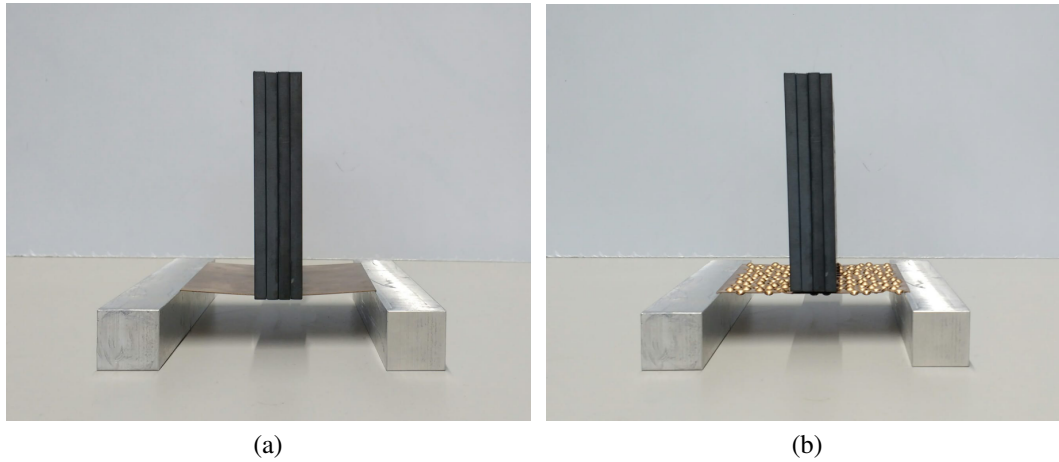


Fig. 1.3 (a) A plain flat sheet deflects under an imposed bending load (b) A dimpled sheet, of the same material and thickness, deflects less under the same bending load.

1.2 Scope and approach

The scope of this thesis is summarised below with a breakdown by chapter. A literature review summarising relevant material is given in specific background sections at the start of each chapter. After considering and subsequently dismissing a “second moment of area” method for analysing a dimpled sheet, the overall approach is to first understand the behaviour of a single dimple, both by itself and when included within an infinite plate, then establish an equivalence between an dimple and an elastic inclusion, derive an equation for calculating the overall stiffness of an inclusion patterned plate and finally combine the previous two stages to arrive at an analytical equation for the overall behaviour of a dimpled sheet.

In Chapter 2, the influence of dimples on the bending stiffness of a plate is analysed by comparison with corrugated sheets, which likewise utilise out-of-plane geometry to increase the bending stiffness of thin sheet material. In a corrugated sheet, material is moved away from the neutral axis, which increases the second moment of area. In a similar way, dimpling moves material away from the mid-surface of the plate, and so initially, dimpled plates are here analysed by considering the second moments of area. In this chapter, through comparison with practical testing of dimpled sheets, it will be shown that this initial analysis is flawed. Given the inadequacy of the second moment of area method the subsequent chapters of this thesis are therefore devoted to developing a new method of considering and analysing dimpled sheets.

As a first step towards understanding the effects of a pattern of dimples on a plate, Chapter 3 will examine the structural behaviour of a single dimple. Though dimples can be manufactured in a variety of shapes, axisymmetric dimples are a useful class for analytical

exploration. Such dimples have axisymmetric symmetry with a radial profile swept around 360° to form the three dimensional geometry, *i.e.* a shell of revolution. The plan outline of an axisymmetric dimple is thus circular. For the purposes of this thesis, attention will be focused exclusively on axisymmetric dimples.

Compared to a flat disc, the geometry of a dimple allows the same volume of material to have a higher bending stiffness. A key idea within this thesis is the proposal that the dimple can be treated as a circular disc of material which is stiffer in bending than the surrounding plate, *i.e.* the dimple can be treated like a stiff elastic inclusion. Modelling an elastic inclusion is easier than modelling the three dimensional geometry of a dimple – both analytically, and also when modelling using finite element analysis (FEA). An analytical approach to modelling a single dimple is examined and developed and the equivalence of a dimple and an inclusion is analytically justified. This provides a method of calculating the stiffness of the equivalent inclusion based on the dimple geometry.

Where sheets are patterned with numerous dimples, the concept of treating each dimple as an elastic inclusion provides further analytical benefits. The three dimensional problem of a dimpled sheet can be reduced to the two dimensional problem of a plate with many inclusions. Chapter 4 therefore considers the problem of analysing the structural performance of plates which contain patterns of multiple inclusions. By appealing to a macroscopic view of an inclusion-patterned plate, an overall homogenised stiffness is sought. While traditionally homogenisation approaches are normally used in the fields of materials and composites [9], some previous research has considered homogenisation on a structural level [10], treating corrugated sheets as orthotropic plates. In this work, starting from the elastic analysis of a single inclusion in a plate, a new method is devised for calculating a “rule-of-mixture” which captures the overall stiffness of an inclusion-patterned plate. This theoretical analysis is subsequently verified by FEA, and an excellent agreement is seen over a wide range of Young’s moduli ratios and Poisson’s ratios. Remarkably an independence of homogenised stiffness with the type of pattern is observed. The new rule-of-mixture derived here is also applicable to other homogenisation problems, and in Chapter 4, it is shown to compare favourably to other existing rules-of-mixtures. Due to the elastic stress analysis derivation, the new rule-of-mixtures can account for differing Poisson’s ratios, whereas many previous homogenisation techniques cannot.

Having demonstrated that dimples can be satisfactorily represented as elastic inclusions, and having developed a homogenisation technique to capture the structural performance of inclusion patterned plates, Chapter 5 combines these analyses in order to present a theoretical method for calculating the overall structural performance of a dimpled sheet. This theoretical understanding allows the optimisation of both the dimpling pattern and the dimple geometry.

Comparisons to FEA of dimpled sheets in Chapter 5 show the effectiveness and validity of the new method.

Chapter 2

Introduction to dimpled sheets

2.1 Summary

A dimpled sheet is similar in some respects to a corrugating a sheet; in that material is moved further away from the datum plane and the bending stiffness increases while the stretching stiffness decreases. The increase in bending stiffness of a corrugated sheet can be modelled satisfactorily through a second moment of area analysis, and so here a dimpled sheet is analysed in a similar manner. Taking multiple cross-sections through a dimpled sheet allows a second moment of area distribution along the length of the sheet to be calculated, and by averaging appropriately an estimate of the overall bending stiffness of the sheet can be made. The influence of different patterns of dimpling, different shapes of dimples and having dimples in both upward and downward directions is considered.

Experimental testing of a number of dimpled sheets with various patterns of dimples, dimple shapes and sheets with upward and downward dimples is undertaken. The experimental method, as well as the method of manufacturing dimpled sheet specimens is described. The experimental results show that while the bending stiffness of a dimpled sheet is increased compared to a flat plate, the proportional increase is an order of magnitude lower than predicted by the second moment of area analysis. The experimental results also provide evidence against some of the other trends predicted by the second moment of area analysis. This chapter concludes that analysing a dimpled sheet via a second moment of area analysis is inadequate and therefore indicates the need for a new theoretical analysis to understand the behaviour of dimpled sheets.

2.2 Introduction

A thin plate or shell is a structural element characterised by having one dimension much smaller than its others. This thin, through-thickness, dimension is typically so small that the geometry of the shell can be considered to be a two-dimensional surface. In much the same

way that a beam can be considered a one-dimensional structural component, with its overall structural properties dependent on its local geometry and cross-section, so too can a shell be considered as a two-dimensional structural element, with known overall structural properties.

Thin plates and shells have a wide variety of applications: they are often used in lightweight structures because of their good tensile strength and stiffness, particularly when considering tensile strength and stiffness per unit weight. However, plates and shells often have very low bending stiffness, due to their thinness. The bending stiffness of a shell, D , depends on the thickness cubed, and is given by:

$$D = \frac{Et^3}{12(1-\nu^2)} \quad (2.1)$$

Given this relationship the analysis of very thin shells often neglects the bending stiffness all together (the membrane hypothesis [11]). However, when thick shells are considered, the bending stiffness must be taken into account, and this increases the complexity of analysis.

Shells which are initially flat are referred to as plates. While shells are often assumed to have zero bending stiffness, thin plates are usually required to have some bending stiffness. For example, the grid plates of a nuclear reactor must hold the weight of the nuclear core, which induces a bending moment in the plate. The curvature of a thin shell often allows an applied load to be carried with in-plane stresses rather than in bending. Consider that a beam uses its bending stiffness to carry a central point load, whereas an arch or a dome uses its geometry to carry the same loading via in-plane stresses. Therefore, because of the globally flat geometry of a plate, the bending stiffness of a plate is of greater importance than for a globally curved shell.

Dimpling shells or plates is a process in which the smooth surface of the shell is distorted out-of-plane in localised indentations or dimples. Early examples of dimpling date from many centuries ago, see Fig. 1.2, however the analysis of dimpled sheets has only been considered relatively recently [8, 12, 13]. Adding this change in local geometry does not need to affect the global geometry, and thus dimpling can be seen as effectively texturing the shell. Dimpling a thin plate is known to affect the global performance of plate in some unusual ways. States of self-stress can cause global bi-stability of the plate [14, 6]. Low, or even negative Poisson's ratios, have been observed [12, 7], and there is an increase in the bending stiffness of the plate [12]. It is the last of these properties to which the following chapters give predominant attention.

In this chapter, the influence of dimples on the bending stiffness of a plate is analysed by comparison to corrugated sheets, which also use geometry to increase the bending stiffness of thin sheet material. In a corrugated sheet, material is moved away from the neutral axis of

the plate, and this increases the second moment of area. In a similar way, dimpling moves material away from the mid-surface of the plate, and so this chapter first analyses dimpled plates by considering the second moments of area. With comparison to practical testing of dimpled sheets, this initial analysis is shown to be flawed.

The subsequent chapters are therefore devoted to developing a new way of considering dimpled sheets. Chapter 3 focuses on the behaviour of a single dimple, and how a single dimple behaves when it is surrounded by a flat plate. Chapter 4 considers the behaviour of a plate which is patterned with elastic inclusions. Chapter 5 then combines the analysis of the two preceding chapters, developing the theory and comparing against FEA results of dimpled sheets. Although the primary motivation for this research is the increase in bending stiffness of a dimpled sheet, this new analysis also captures the associated reduction in stretching stiffness which also occurs.

2.3 Background

2.3.1 Dimples and dimpled sheets

A dimple is an out-of-plane geometric feature which can be introduced within a thin plate or shell. Often formed by an indentation process in which an initially flat sheet is plastically deformed, the resulting self-stresses generated can allow dimples to be independent bi-stable features [6, 15, 14]. Each dimple may be “popped through” and therefore exist in two stable equilibrium states, popped up or popped down. Patterning many dimples onto a larger sheet or plate creates dimpled sheets (Fig. 2.1), which are known to exhibit several interesting properties. The self-stress due to the indentation formation process of each dimple can give the overall dimpled sheet a significant curvature and plastically rolling the sheet in orthogonal directions can even facilitate bi-stability of the sheet as a whole [12]. Furthermore, due to work hardening effects during dimple formation the yield strength in uniaxial tension of a dimpled sheet is seen to be increased compared to an equivalent flat sheet [16] as well as the yield strength in bending [13]. However, disregarding the effects of self-stress, many interesting and unusual properties of dimpled sheets are the result of their geometry alone. Previous studies have noted that compared to a flat sheet, an increase in bending stiffness [12], a reduction in stretching stiffness [16], and a decrease in (and sometimes even negative) Poisson’s ratio in both bending and stretching [12, 7] can be achieved for dimpled sheets. An increase in heat transfer [17], improved impact response and reduced vibration compared to a flat sheet have also been noted [8].

The large number of interesting and unusual properties makes dimpled sheets an attractive choice for a wide range of practical applications. The increased surface area and potential to pass coolant between two adjacent layers make dimpled sheets attractive for use as heat exchangers and also for thermal insulation when multiple layers of these panels are bonded together, multi-wall dimpled panels are of interest in applications such as space shuttles [18] for example. On account of the superior heat transfer properties of dimpled sheets, pressure vessels can be made with dimpled jackets [19], which can be added as additional facade welded to the pressure vessel. Such dimpled jackets increase heat transfer due to turbulence created as the air passes over the dimpled surface, which is of particular use for reactions which produce heat, such as fermentation. The design of dimpled jackets for pressure vessels is codified by ASME regulations [20]. On account of their visual appeal, dimpled sheets also find practical application in architectural cladding, facades and sculpture, as well as in decorative functions around the domestic home in kitchens and bathrooms particularly [21]. Additionally dimpled sheets are used widely in construction of various industrial flooring, catwalks and platforms, where the surface texture can provide practical

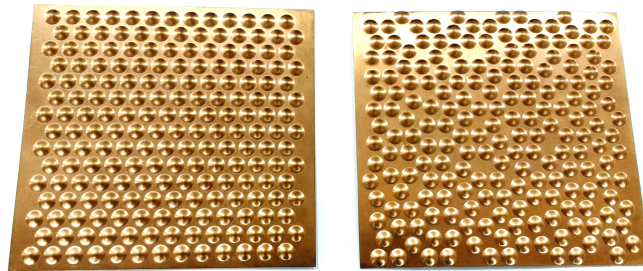


Fig. 2.1 Two dimpled sheets manufactured from copper beryllium: each has a different pattern of dimples.

benefits underfoot by providing enhanced grip [22]. While current applications of dimpled sheets are predominately used for their additional properties, in many cases an increased understanding of the structural properties would allow for more efficient use of dimpled sheets. For example, when dimpled sheets are used as thermal protection on space shuttles these panels are added as an additional facade layer to the outside of the craft. An improved theoretical understanding of the behaviour of a dimple plate might allow the dimpled sheet to function not only in its role as a thermal insulator, but also form part of the structural skin of the space shuttle, or pressure vessel. The same can be applied when used architecturally, allowing the dimpled sheet to be used structurally as well as aesthetically. Given the load-bearing nature of a platform or catwalk, the structural properties of a dimpled sheet, its stiffness and its strength, are of safety critical importance. While bespoke FEA calculations can be made, or potentially redundant additional supports added beneath such platforms, an analytical understanding of the behaviour of dimpled sheets has the potential to allow for safe and efficient use of dimpled sheets in such applications.

Previous studies of dimpled sheet behaviour have experimentally demonstrated such novel properties of dimpled sheets and confirmed these with numerical computational simulations using FEA. There do not appear to have been attempts to analytically predict the effect of dimpling on the overall elastic performance of a sheet under tension or bending. Of particular merit is the increase in bending stiffness of a dimpled sheet, and this is suggested to be worthy of detailed consideration.

2.3.2 Plates and shells

Although it is their defining feature, the thin depth of plates and shells can make them undesirable in some structural applications, especially those where bending moments are

required to be carried. From first principles it can be seen that the second moment of area of a beam is dependent on the thickness cubed: thus plates and shells, with their characteristic thin depth, have very low bending stiffness. It is possible to build up larger sections from thin plates: large bridge deck sections can be made as such, and box sections and girders are often of this form, utilising the efficiency and economy of thin plates, and the moment-bearing capacity of deep cross-sections [23]. Even in this capacity, the very thin depth of the plates can cause problems due to out-of-plane local buckling [24]. Again this is fundamentally caused by the small values of second moment of area that plates and shells exhibit in the directions perpendicular to the thickness. It would therefore be beneficial in many load-bearing situations if the second moment of area of a thin plate could be increased. This would be desirable not only in situations where the plate forms part of a larger section, but also where a single plate is required to be load-bearing. The classic example of the latter would be corrugated sheets (Fig. 2.2a), which are often used in roofing. Here a thin plate is bent out of plane, to increase its structural depth. By adding this undulating profile in one direction, material is moved further away from the neutral axis and thus the second moment of area, and hence the stiffness and strength of the sheet are dramatically increased in this direction. While the bending stiffness in this direction has greatly increased, the stretching stiffness in the perpendicular direction has greatly decreased. Stretching in this direction no longer directly strains the sheet, but rather simply unbends the corrugations. The trade-off between stretching and bending stiffness will become a recurrent theme.

The structural properties of corrugated sheets have been researched previously. Linear elastic analysis has been used to treat a corrugated sheet as a thin equivalent orthotropic shell of uniform thickness and analytical expressions have been developed for the equivalent stiffnesses in both bending and stretching [10, 25]. Such homogenisation based techniques have been compared favourably with FEA [26, 27], and recent improvements to the analytic expressions for stiffness properties are more accurate still [28]. One limitation of simple corrugations is that they only increase the bending stiffness substantially in a single direction; whereas the bending stiffness in the perpendicular direction is practically unchanged, leading to a distinctive strong and weak direction. In the context of roofing, this means that the corrugations can only effectively span across in one direction, and must be supported along their entire length in the perpendicular direction.

2.4 Expected structural performance in bending

Figure 2.2 compares the cross-sectional profiles of a corrugated sheet and a dimpled sheet. In both cases the cross-section is similar, material has been moved away from the flat datum



Fig. 2.2 (a) The undulating cross-sectional profile of a corrugated sheet greatly increases the bending stiffness in one direction by increasing the effective structural depth. (b) The cross-sectional profile of a dimpled sheet is also undulating, but unlike a corrugated sheet it undulates in the perpendicular direction also.

plane to form an undulating profile. However, a major difference is that in the dimpled sheet the profile undulates in the perpendicular direction as well, whereas in the perpendicular direction the profile is flat. This suggests that unlike for corrugations, the increase in stiffness of a dimpled sheet will be equal in both directions. Assuming that dimpled sheets benefit from an increase in structural depth due to their undulating profile, in a similar fashion to a corrugated sheet, the expected bending performance of dimpled sheets is analysed. However, as is seen by comparison to experimental testing in Section 2.5, this theory is inadequate.

The increase of structural depth in a corrugated sheet increases bending performance by moving material away from the neutral axis. Euler-Bernoulli beam theory tells us that the bending moment is carried by induced in-plane axial stresses. For a sagging moment this leads to axial compressive stresses at the top and tensile stresses on the bottom. By increasing the structural depth, the lever arm between the compressive and tensile stresses increases, and thus the bending stiffness increases. We measure the capacity of a section to withstand bending using the second moment of area, I_{xx} . We first calculate the location of the neutral axis of the section, which is at the same depth as the centroid of area of the cross-section. The second moment of area is then the integral of area with the square of the distance from the neutral axis.

$$I_{xx} = \int_{Area} z^2 dA \quad (2.2)$$

As an indentation dimpling process preserves volume, assuming that dimpling preserves vertical thickness we can ascribe a dimple cross-section by giving just the profile of the mid-surface. This assumption implies that shear deformation dominates during indentation

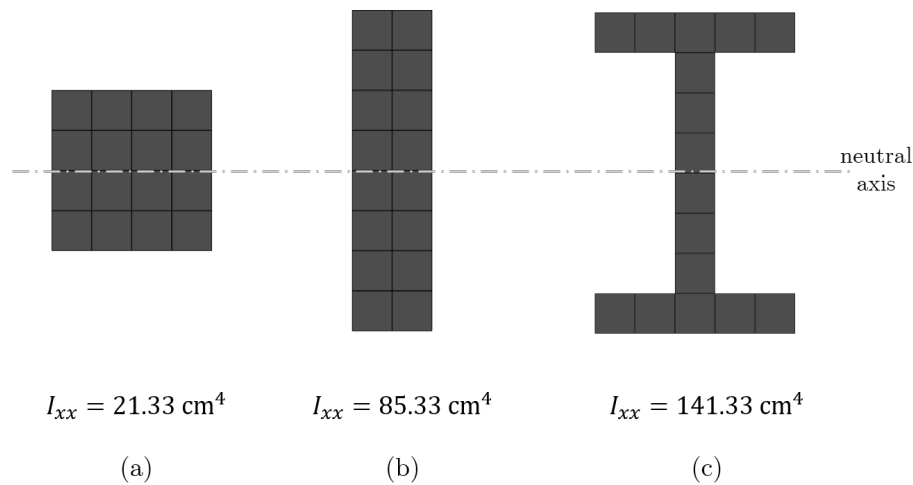


Fig. 2.3 Three cross-sections: each has the same area, 16cm^2 , but each has a different second moment of area. (a) A square, (b) A thin rectangle, (c) An I beam cross-section.

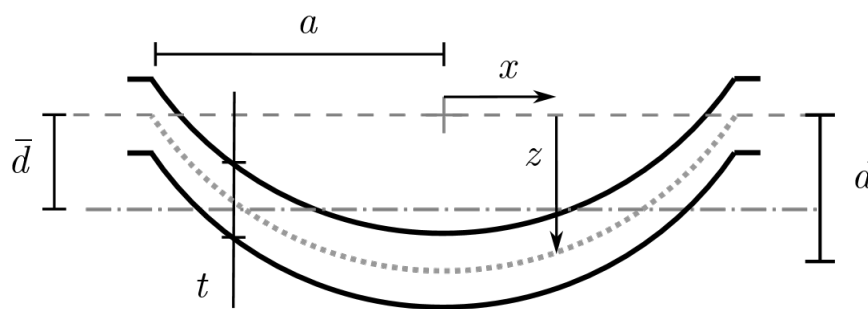


Fig. 2.4 Assuming a constant vertical thickness, t , the dimple cross-section is defined by the profile of the mid-surface, shown as a short dashed line, and described as a function of x . The radius of the dimple is a , the maximum depth of the mid-surface is d , and the centroid of area of the dimple is located \bar{d} below the datum.

as each vertical slice of material displaces purely perpendicularly to the plane. Figure 2.4 shows a dimple cross-section, and if the profile of the mid-surface is defined then the second moment of area for the dimpled cross-section can be calculated. For example, assuming a circular arc as the mid-surface profile leads to a revolved dimple geometry which is a spherical cap. The second moment of area of a dimple with a circular arc profile with constant vertical thickness is calculated in Appendix A.1.

If we know the dimple layout of a dimpled sheet and we know, or assume, a dimple profile, then we can take cuts at locations along the sheet and calculate the second moment of area of each cross-section. Figure 2.5 shows a dimpled sheet with a sparse hexagonal pattern of dimples, with three horizontal lines indicating the locations of three different

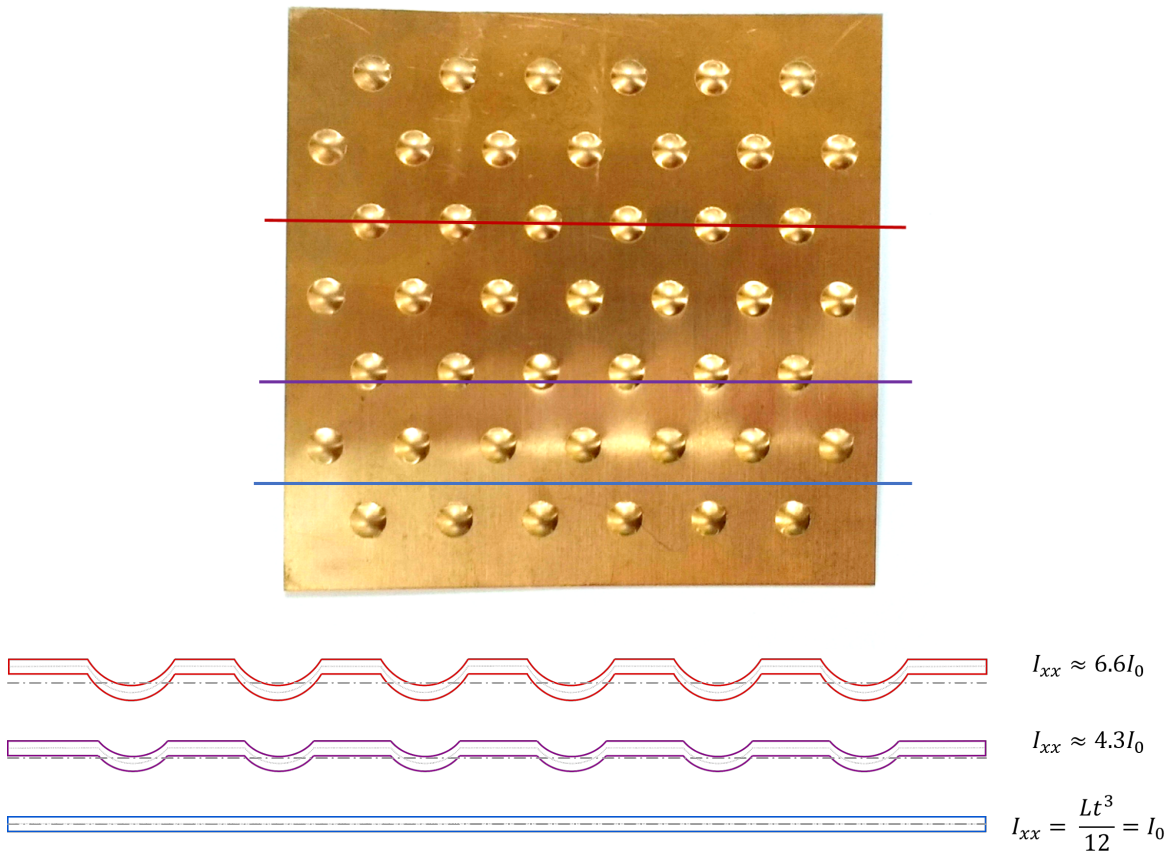


Fig. 2.5 A sparse hexagonal pattern of dimples on a square sheet. The cross-sectional profile differs at each of the three locations depicted by the horizontal lines, and the corresponding cross-sections are shown below the dimpled sheet. The sheet has width L , and the dimples have a radius $a = 3L/100$, depth $d = 1.8L/100$ and vertical thickness $t = L/100$. The mid-surface profile is shown as a faint short dashed line and the neutral axis is shown as a dot-dashed line.

cross-sections. The second moments of area are calculated for each cross-section, and are seen to vary significantly in value from each other. In particular, when the cross-section intersects no dimples the second moment of area is very low. What is more, for this hexagonal pattern note that there are many horizontal cuts which intersect no dimples, whereas in the perpendicular direction practically every cross-section intersects some dimples. This gives rise to the ideas of “lines-of-weakness”: lines where there are no dimples at all at a given cross-section, and thus a very low value of second moment of area. Such ideas are used to propose that there should be weak directions and stiff directions [12] for such textured sheets.

The methodology for calculating the second moment of area for any cross-section which intersects an arbitrary number of dimples is presented in Appendix A.2. This process can be

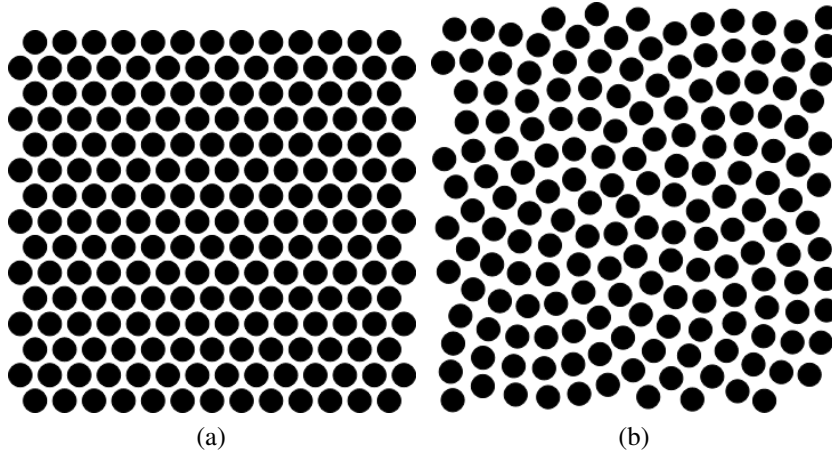


Fig. 2.6 (a) A regular hexagonal packing of circles (b) A phyllotaxis spiral pattern. Both of these patterns are used as dimpling locations for a square dimpled sheet. The second moments of area for cross-sections through these sheets are shown in Fig. 2.7.

automated using a MATLAB script [29], allowing for the calculation of the second moment of area for every cross-section of a sheet with an arbitrary dimple pattern. Figure 2.6 shows two different patterns of dimples. For each pattern, the second moments of area at each cross-section are calculated, in both orthogonal directions, using the MATLAB script. The results of these calculations are presented graphically in Fig. 2.7. The sheets are square with side length L and thickness $t = L/200$, the dimples have radius $a = 3L/100$ and depth $d = 1.8L/100$. The second moments of area are normalised by the second moment of area for a flat sheet:

$$I_{\text{amplification factor}} = \frac{I_{xx}}{Lt^3/12} = \frac{I_{xx}}{I_0} \quad (2.3)$$

The second moment of area variations indicate some observations about dimpled sheets. As a semi-ellipsoid dimple pushes more material to a deeper depth than a spherical cap dimple of the same depth, one would expect a higher second moment of area when assuming a semi-ellipsoidal dimple. Indeed Fig. 2.7b indicates this clearly. Additionally, as expected from the regular hexagonal pattern, we see a periodic fluctuation in the second moment of area. Notice particularly that for the cross-sections which cut through the pattern in Fig. 2.6a horizontally, the amplification factor drops to unity between each row of dimples. These lines-of-weakness are expected from the pattern, as along these lines the cross-section does not intersect any dimples at all. In contrast, the irregular phyllotaxis pattern has no periodic fluctuation and much less variation in second moment of area overall. This was only a reasonably small patch of phyllotaxis pattern and it would be anticipated that a larger number

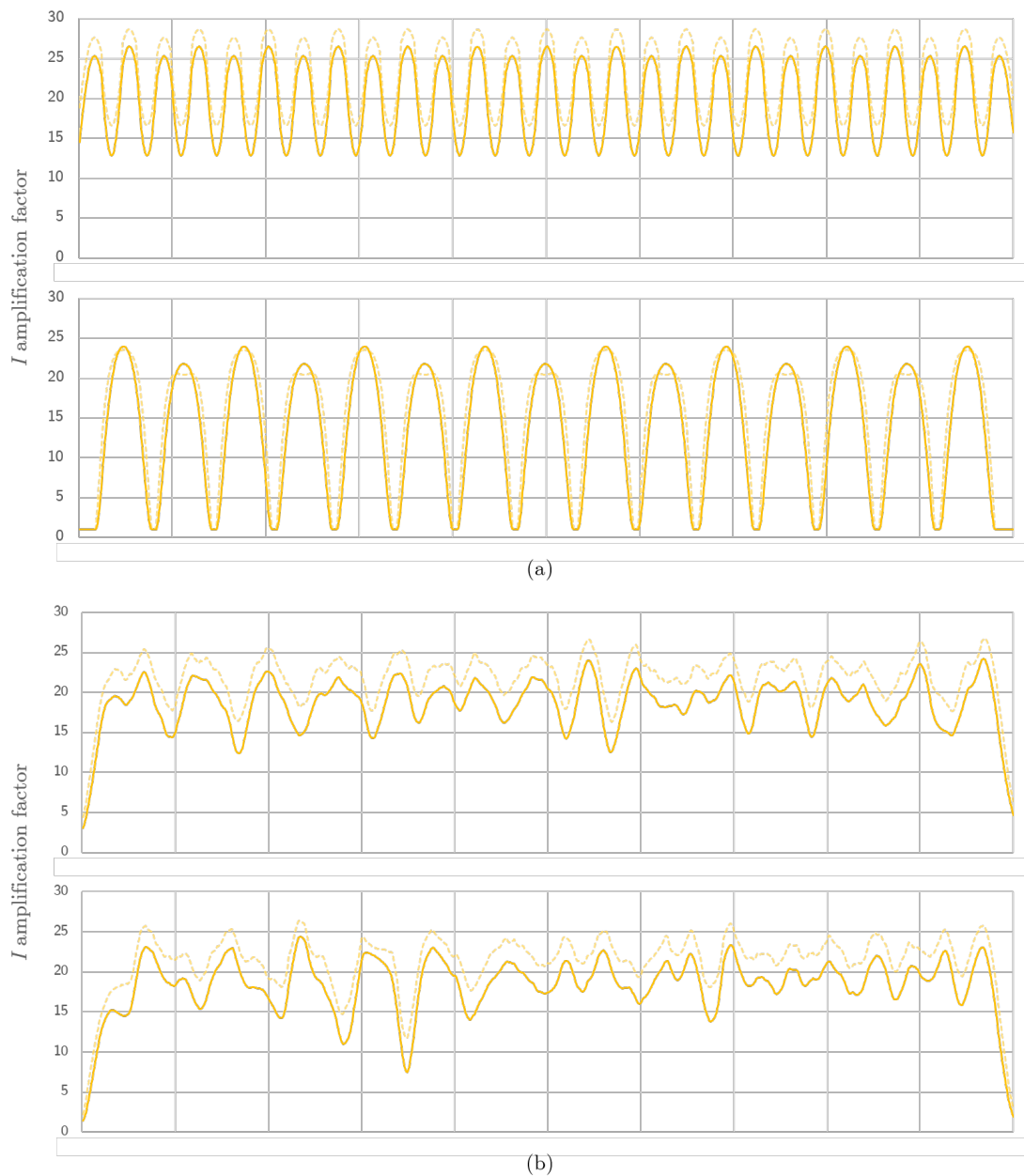


Fig. 2.7 The variation in normalised second moment of area is plotted as successive cross-sections are taken across the dimpled sheet. The top graph in each pair shows cross-sections that cut across the pattern vertically and the bottom graph in each pair shows cross-sections that cut across the pattern horizontally. Solid lines indicate that a spherical cap dimple has been assumed while the dashed line indicates a semi-ellipsoidal dimple. The sheets are square with side length L and thickness $t = L/200$ and the dimples have radius $a = 3L/100$ and depth $d = 1.8L/100$. (a) Hexagonal pattern. (b) Phyllotaxis pattern.

of dimples in such a pattern would reduce the fluctuations in second moment of area even more.

To estimate an overall homogeneous approximation for the stiffness of a beam which has a variable second moment of area along its length, it is natural to take an average value of I_{xx} . Provided that the changes in cross-section are not too abrupt, it is reasonable to consider the varying second moment of area of a beam with a changing cross-section [30]. A beam in 4-point bending is under a constant moment between the two inner supports and therefore the curvatures are inversely proportional to the stiffness at each section. Integrating curvatures along the length of the beam to find the end rotations, we can calculate an overall stiffness by dividing the applied moment by the end rotation. This analysis shows that an appropriate global stiffness of such a beam will be found by taking an average of the reciprocals of the section stiffness and then inverting the answer. Or in other words, taking an equally weighted harmonic average of the second moment of area distribution, as:

$$I_{\text{harmonic}} = \frac{L}{\int_0^L (1/I_{xx})} \quad (2.4)$$

The harmonic average adds some further explanation to the concept of lines-of-weakness. The harmonic average is lowered significantly more by a few low values than the arithmetic average is. Thus having a few cross-sections where the stiffness is very low, *i.e.* lines-of-weakness, will significantly lower the overall stiffness.

The change in cross-section is relatively smooth for dimpled sheets, and thus taking a harmonic average of the stiffness distributions shown in Fig. 2.7 would seem appropriate. Calculating the harmonic averages for the hexagonal pattern with spherical cap dimples gives $I_{\text{harmonic}} = 18.72I_0$ for the first direction and $I_{\text{harmonic}} = 4.24I_0$ in the orthogonal direction. In comparison the phyllotaxis pattern has harmonic averages of $I_{\text{harmonic}} = 16.37I_0$ and $I_{\text{harmonic}} = 17.70I_0$ for the two orthogonal directions. This would suggest that a dimpled sheet with a hexagonal patterning should exhibit strongly orthotropic behaviour, with the stiffness in perpendicular directions being significantly different from each other. For the orientations in which the rows of dimples align perpendicular to the loading direction, this analysis would suggest that the lines-of-weakness make these orientations significantly less stiff. By contrast, for an irregular patterning, like the phyllotaxis pattern, the quasi-random arrangement of the dimples was such that there were no cross-sections that intersected very few, or no dimples at all. By removing such potential lines-of-weakness, the harmonic average of second moment of area was greatly increased.

Rather than have all the dimples in a dimpled sheet going in the same direction, an obvious extension to the concept of dimpled sheets is to have dimples going in both directions. It

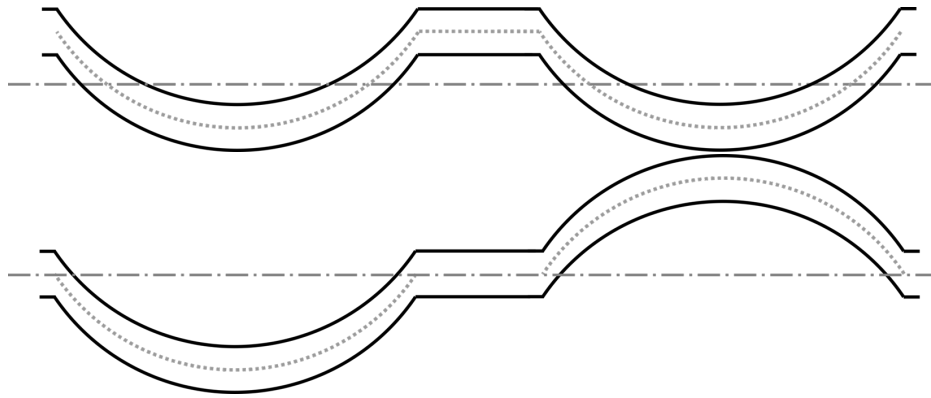


Fig. 2.8 Each cross-section has two identical dimples with radius $a = 3L/15$, depth $d = L/15$ and vertical thickness $t = L/30$. The top cross-section has both dimples in the same direction, whereas the other has one dimple pointing up and the other pointing down. The neutral axis of each cross-section is shown as a dot-dashed line.

seems intuitive that having dimples pushed through in both the upwards and downwards direction should increase the bending performance of the sheet more than dimples in a single direction. The natural expectation would be that this improvement is maximised when exactly half of the dimples point one way and half the other.

Having dimples in both directions will increase the structural depth of the sheet even more than single direction dimples, and thus the corresponding second moments of area will be significantly higher. Figure 2.8 compares two cross-sections which have two identical dimples. In one case both dimples are in the same direction and in the other the two dimples point in opposite directions. In this example when the dimples are in the same direction, $I_{xx} = 7.86I_0$, whereas for dimples in opposite directions, $I_{xx} = 22.12I_0$.

Using dimples which go in both directions has the potential to significantly increase the second moment of area of a cross-section: for the example shown in Fig. 2.8 the up-down dimple combination was almost three times as stiff. However, one practical consideration that limits the effectiveness of this is that it is harder to find a pattern which effectively spreads out the two directions of dimples in such a way to maintain a roughly constant second moment of area across all cross-sections. Nevertheless, a noticeable improvement can be made.

Figure 2.9 shows a possible split of the hexagonal and phyllotaxis pattern into two equal sets. The second moments of area for dimpled sheets which used these patterns to designate dimples in both directions are shown graphically in Fig. 2.10. Calculating the harmonic averages for the hexagonal pattern with the spherical cap dimples in both directions gives $I_{\text{harmonic}} = 21.82I_0$ for the first direction and $I_{\text{harmonic}} = 5.01I_0$ in the orthogonal direction. In comparison the phyllotaxis pattern has harmonic averages of $I_{\text{harmonic}} = 26.40I_0$ and $I_{\text{harmonic}} = 24.72I_0$ for the two orthogonal directions. For the phyllotaxis pattern the harmonic

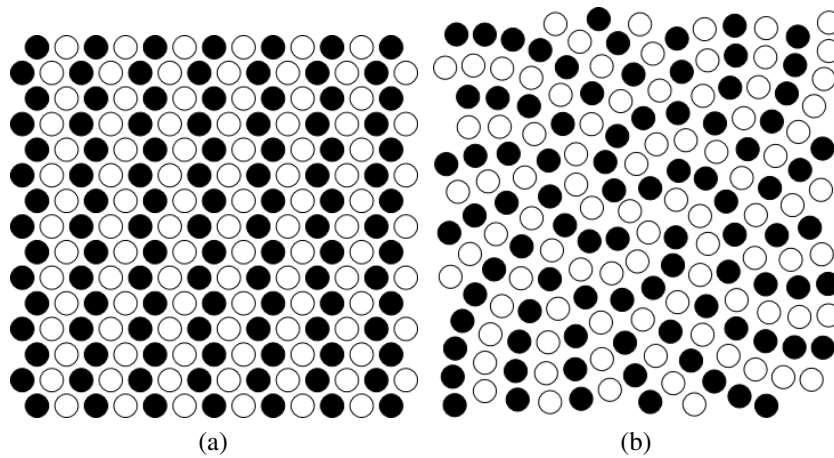


Fig. 2.9 (a) A regular hexagonal packing of circles. (b) A phyllotaxis spiral pattern. Both of these patterns have been split into two equal sets, black and white. These can be used to assign two different directions to dimples.

average of the stiffness distribution was seen to increase by 50% using dimples in both directions compared to single direction dimples. For the hexagonal pattern despite up-down dimpling increasing the peak bending stiffness of the weak direction by over a factor of three, the overall average stiffness in this direction increased by less than 20%. Thus again, a very large difference in stiffness in orthogonal directions was seen in the hexagonal pattern, while the phyllotaxis pattern appears more isotropic in its behaviour.

2.5 Initial experimentation on dimpled sheets

2.5.1 Experimental method

Thin sheet materials are popular in practical applications, at least in part due to their ease of manufacture and thus relatively low cost. The ease of manufacturing metal ingots into a simple flat geometry using a rolling process, for example, enables sheet metal to be economically viable in many situations. Therefore, though the more complex geometry of a dimpled sheet could be manufactured directly through a process such as casting, in reality forming dimpled sheets through the deformation of an initially flat sheet is likely to be most common.

In order to run practical experiments on dimpled sheets, manufacturing some samples is necessary. A suitable candidate material must be reasonably malleable, such that dimples can be formed through local plastic deformation. To this end, samples were manufactured

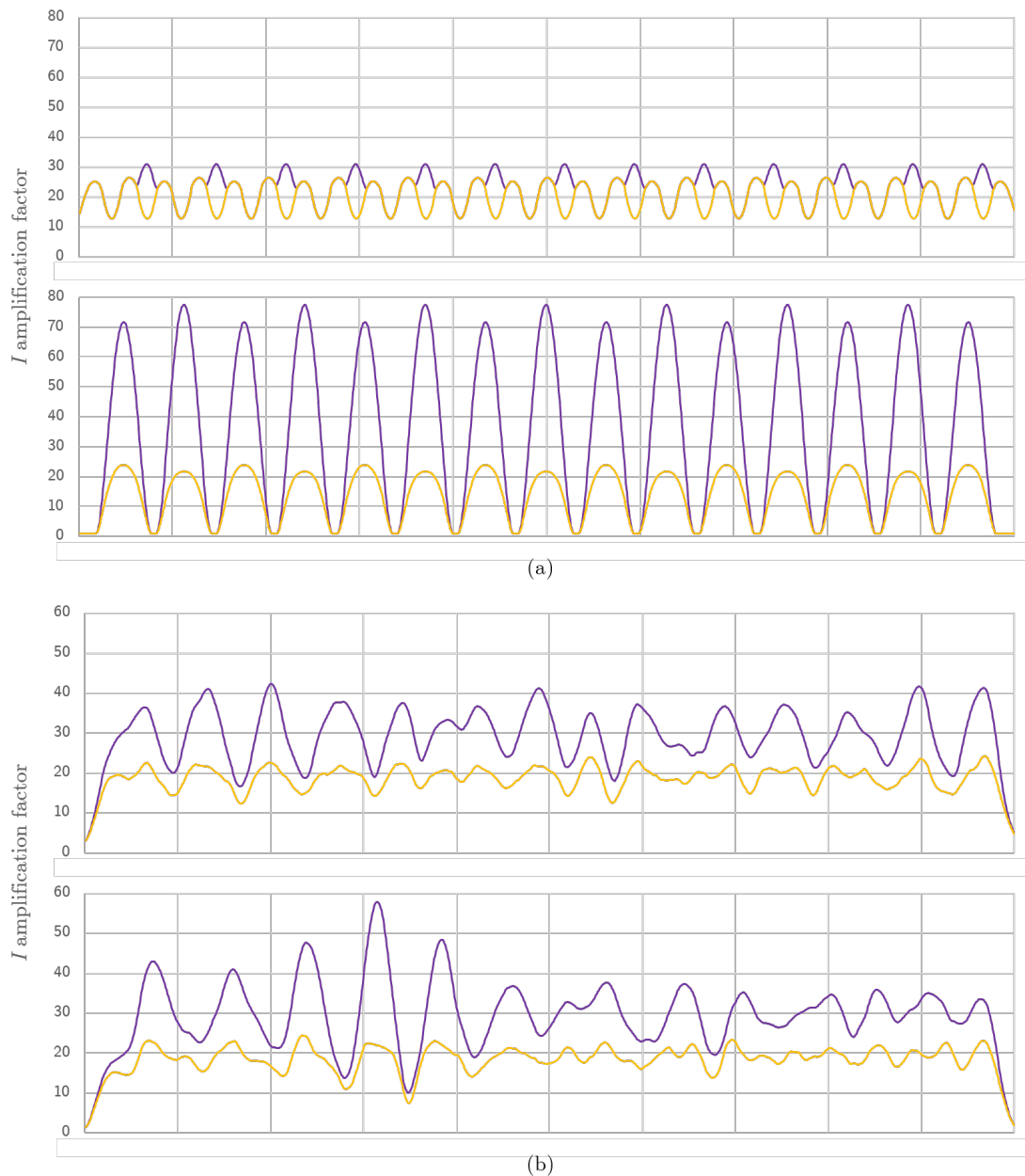


Fig. 2.10 For sheets which are dimpled in both directions the variation in normalised second moment of area is plotted as successive cross-sections are taken across the sheet. The top graph in each pair shows cross-sections that cut across the pattern vertically and the bottom graph in each pair shows cross-sections that cut across the pattern horizontally. Purple lines indicate sheets which have dimples in both directions and yellow lines are given for comparison with single direction dimples. The sheets are square with side length L and thickness $t = L/200$, and the dimples have radius $a = 3L/100$ and depth $d = 1.8L/100$ and have a spherical cap profile. (a) Hexagonal pattern. (b) Phyllotaxis pattern.

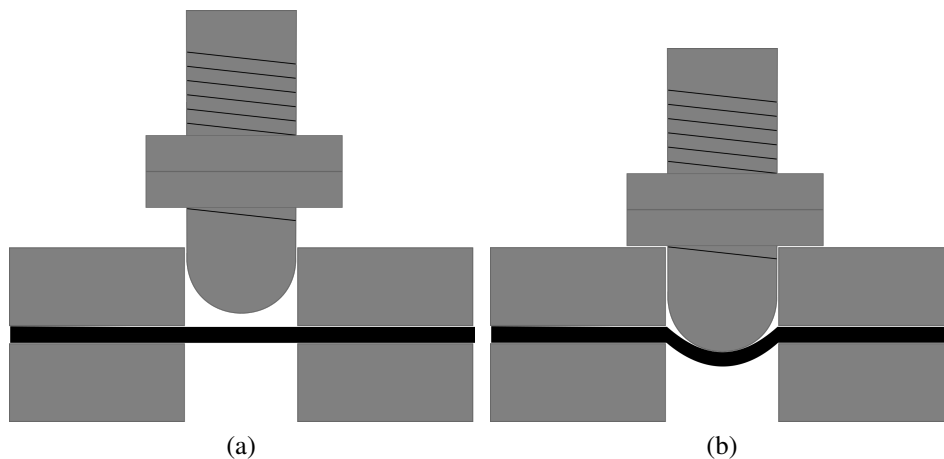


Fig. 2.11 (a) A diagrammatic cross-section showing the dimple indentation process. The thin copper beryllium sheet, shown in black, is held between two thick steel forming plates, shown in grey. Holes in the forming plates allow a rounded indenter to be located at the required dimple location. (b) Two nuts are locked together on the threaded shaft of the indenter to form a collar which limits the depth that the indenter can be inserted and thus controls the dimple depth.

using copper beryllium, which in addition to being malleable in its annealed state can also be subsequently heat treated to increase its yield strength.

The dimpling process employed was an indentation process. The thin copper beryllium sheet was held between two thick steel “forming plates”. Each forming plate comes with a matching pair and each has as a pattern of holes to locate the dimples. The holes in the forming plates are equal to the nominal radius of the dimples. Using a fly press, a hardened steel rounded indenter is pushed through the hole in the forming plate in order to create a dimple at the required location in the copper beryllium sheet, Fig. 2.11. The indenter has a threaded shaft, which allows a collar of two locking nuts to be attached. The collar can be adjusted to allow for different depths of dimple to be formed, but when set and locked into position it ensures that the dimple depth is consistent for every dimple.

As well as locating the indenter, the thick forming plates confine the deformation of the copper beryllium sheet to within the defined nominal radius of the dimple. Each pattern of dimples requires a different pair of forming plates, and to ensure consistency and to maximise versatility, each dimple was stamped individually using a single indenter. The forming plates were CNC milled so that the locations of the dimples were accurate, even for complex and irregular patterns. The nominal dimple radius chosen was 3mm, and the forming plates have a thickness of 6mm. By comparison, the thickest copper beryllium sheet used has a thickness of 0.514mm. Accounting also for the higher Young’s modulus of steel (210GPa) than copper beryllium (125GPa), we note that the each forming plate should have approximately 2500

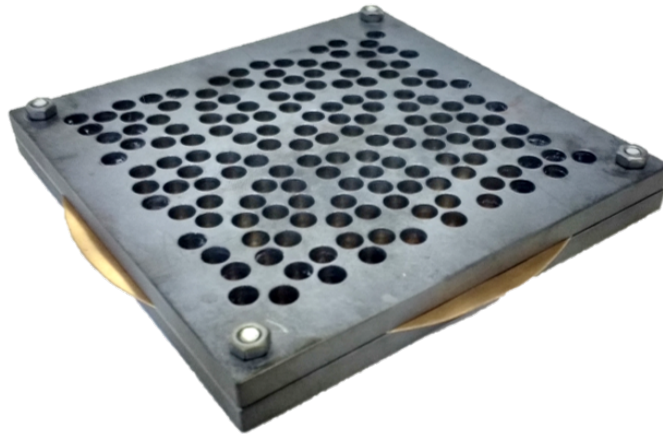


Fig. 2.12 A pair of thick steel forming plates are bolted together at their corners to clamp a thin copper beryllium sheet in place so that it can be dimpled using an indenter.

times the bending stiffness of the thin copper beryllium sheet. The forming plates are 120mm squares and were bolted together at each corner to clamp the thin copper beryllium sheet in place and prevent it from slipping during the indentation process, Fig. 2.12. The patterns of holes cover the central 100mm square.

Four sets of forming plates were manufactured, each with a unique pattern. Square copper beryllium sheets with a thickness of 0.514mm and a side length of 100mm were dimpled using these forming plates. For each pattern, two different depths of dimpling were chosen, and a variation of each pattern with upwards and downwards dimples was chosen. Thus 16 different dimpled sheet samples were produced. The patterns were chosen to have the same minimum distance (1mm) between the edges of the dimples. Four samples representing the four chosen dimple patterns are shown in Fig. 2.13. After some experimental trials, nominal dimple depths of 1.15mm and 1.8mm were chosen, as these were seen to be within practical forming limits. Attempting to indent a dimple too far could exceed the plastic limit of the sheet and cause fracture, leading to partial or total separation of the dimple from the sheet. After being dimpled, due to the presence of some self-stress arising from the dimpling process, some of the sheets were found to develop a small amount of global curvature in one direction.

The dimpled sheet samples were tested under three-point bending. A three-point bending test (or flexural test) is a well established test of bending stiffness and is routinely used to test beam-like specimens [31]. While in some respects a four-point bending test is superior, as it brings the entire central section into a uniform moment, the analysis of three-point bending is also well known, and has advantages in the ease of set-up and of specimen preparation. Figure 2.14a shows the idealised three-point bending set-up: the sample is simply supported

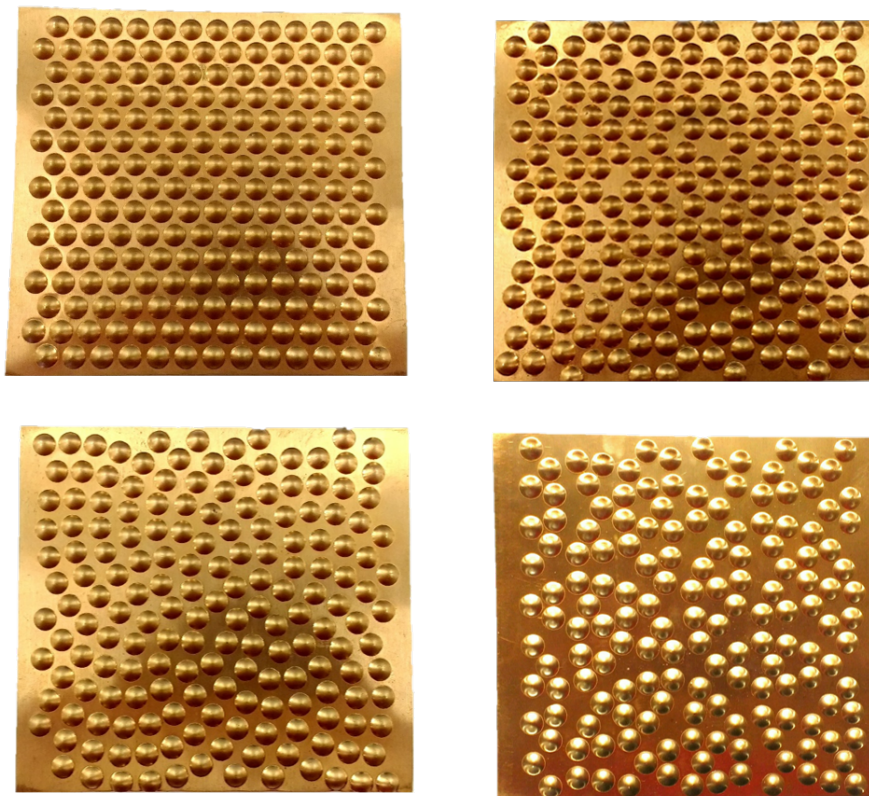


Fig. 2.13 Four square dimpled sheet samples, each with a different dimpling pattern. In each case the sheet has a 100mm side length and thickness of 0.514mm. The dimples are 6mm in diameter and have a minimum of 1mm spacing.

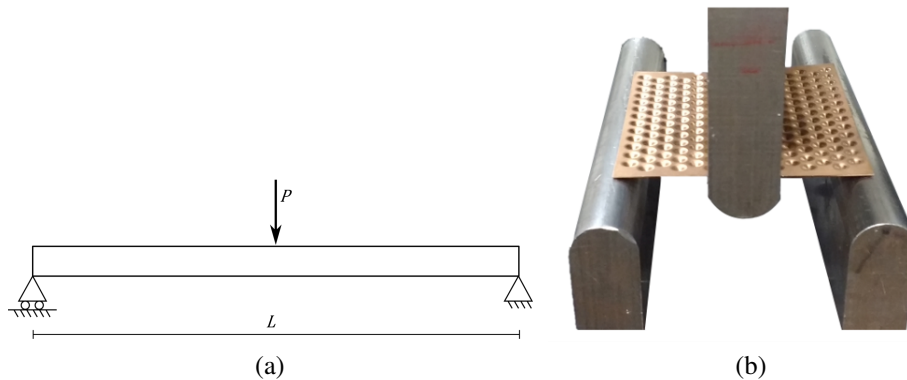


Fig. 2.14 (a) Diagrammatic set-up of a three-point bending test. The sample is simply supported at each end and has a concentrated load applied at the midspan. (b) A photograph of the experimental INSTRON test set-up. The sheet is simply supported along two edges and a line load is applied at midspan. Friction between the sample and supports is low and as the supports provide no explicit horizontal restraint, the test set-up is consistent with the idealised 3-point bending test.

at each end and has a concentrated load applied at the midspan, which brings the sample into uniaxial loading. For a specimen of length L , Young's modulus E and second moment of area I , a central force P causes a deflection at the midspan of:

$$\delta = \frac{PL^3}{48EI} \quad (2.5)$$

Figure 2.14b shows a photograph of the actual experimental INSTRON test set-up. The dimpled sheet is simply supported along two edges and a line load is applied at the midspan. Though the three-point bending test doesn't develop a constant moment region, this set-up does easily allow the two orthogonal directions to be tested. Additionally as the test is statically determinate, any minor defects in shape such as a very slight initial curvature will not significantly affect the results. As the dimpled sheet is square and simple line supports are used at each end and a line load applied in the middle, the sheet will not quite be in pure uniaxial bending as any anticlastic curvature will not be able to form properly. However, as a deft way of managing this situation and simultaneously reducing uncertainty arising from dimension and material property measurements, an identical flat copper beryllium sheet can be tested in this experimental set-up. The results of the dimpled sheet specimens can then be normalised against the flat sheet.

2.5.2 Experimental results

Using the experimental set-up shown in Fig. 2.14b, the dimpled sheet specimens which had been manufactured were tested. In addition two flat square samples of the same thickness and of the same material as the dimpled sheets were also tested.

The displacement of the midspan and the force applied are given as outputs from the INSTRON universal testing machine. After a little uptake, there is a clear linear region in the force-displacement characteristic as expected, Fig. 2.15. The gradient of this curve is the stiffness of the sample, which is directly proportional to the effective second moment of area of the sample, see Eq. 2.5. Orthogonal directions are tested with stiffnesses being denoted ψ_{xx} and ψ_{yy} respectively. As well as being rotated to test the stiffness of orthogonal directions, for each direction the dimpled sheet was flipped upside down and tested again, and hence two readings were taken for each direction. Initial stiffness should not be affected by reversing the direction of loading, and so the average of the two readings was taken. As expected the flat copper beryllium plates behave isotropically and only a slight variance in stiffness is observed. An average of the stiffnesses of the flat plates was taken to calculate the value of ψ_0 , which was then used to normalise the stiffness results of the dimpled sheets. The manufactured dimple depths were estimated by using a caliper to measure the depth of a sample of 6 dimples per sheet. The results compared favourably with the nominal dimple depths of 1.15mm and 1.8mm. The normalised stiffness, Ψ , is calculated by dividing the stiffness of the dimpled sample, ψ , by the stiffness of the flat sheets, ψ_0 , for the x and y directions respectively:

$$\Psi_{xx} = \frac{\psi_{xx}}{\psi_0}, \quad \Psi_{yy} = \frac{\psi_{yy}}{\psi_0} \quad (2.6)$$

The experimental results, Table 2.1, show that an increase in bending performance is indeed seen for dimpled sheets. As no extra material was added during the indentation dimpling process, and it is known that self-stress does not alter initial elastic stiffness, the increase in bending performance must be due to the dimpled geometry alone. However, notice that the normalised stiffnesses, Ψ , are much lower than expected from the second moment of area analysis. The phyllotaxis pattern in Fig. 2.6b was predicted to be 17 times stiffer than a flat sheet. Whereas the corresponding sheet with the same dimple pattern, sheet thickness, dimple radius and dimple depth was found experimentally to have a normalised stiffness of between $\Psi_{xx} = 1.64$ and $\Psi_{yy} = 1.59$. Another surprising result was that the deeper dimples did not increase the normalised stiffness as much as expected. As second moment of area is proportional to depth squared the deep dimpled sheets were expected to be at least twice as stiff as the sheets with shallower dimples, however in test the deep dimpled

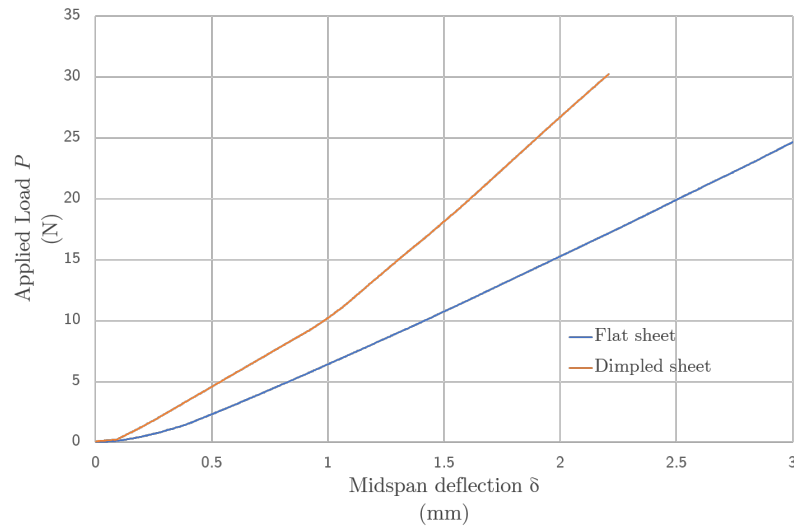


Fig. 2.15 Two representative force-displacement characteristics produced during the three-point bending testing of thin square copper beryllium sheets. After an initial uptake region behaviour is seen to be linear. This particular curve is from a sheet dimpled with a Kite and Dart pattern using dimples with a nominal depth of 1.8mm each pointing in the same direction.

sheets were on average only 27.5% stiffer. Similarly, having dimples in both directions was predicted to significantly increase the bending stiffness. Comparison of Fig. 2.7 and Fig. 2.10 suggests an improvement of 50%, however the experimental results show only a 22% increase in normalised stiffness. Perhaps most surprising of all however, the expected orthotropic nature of the hexagonal patterning when all the dimples are in the same direction was not observed experimentally. For both the deep and the shallow dimples, the orthogonal directions had an equal stiffness to within a couple of percent. Compared to the prediction that lines-of-weakness should cause a difference in stiffness of more than a factor of four, this result is remarkable. The stark differences between the experimental results and the theoretical predictions suggest that a dimpled sheet cannot be treated like a Euler-Bernoulli beam, and thus the second moment of area analysis is not valid. Considering the geometry of a dimpled sheet, it can be seen that the tips of the dimples cannot carry load directly between them, successive cross-sections therefore don't develop linearly varying in-plane stress distributions, and thus the sheets are seen not to behave like Euler-Bernoulli beams.

2.6 Conclusions

Analysing a dimpled sheet using a second moment of area analysis, in a similar way to a corrugated sheet, has been shown to predict significant increases in bending stiffness.

Table 2.1 Normalised stiffnesses of dimpled sheet samples in three-point bending

Sample pattern	Dimple direction	Dimple depth (mm)	Ψ_{xx}	Ψ_{yy}
Flat	-	-	1.03	1.00
	-	-	0.99	0.98
Hexagonal	One way	1.18	1.58	1.62
		1.79	1.74	1.73
	Both ways	1.15	2.17	1.65
		1.62	2.78	1.87
Kite and Dart	One way	1.14	1.70	1.62
		1.80	1.55	1.61
	Both ways	1.16	1.73	1.73
		1.76	1.99	2.20
Rhombus	One way	1.17	1.35	1.48
		1.80	1.72	1.61
	Both ways	1.15	1.73	1.82
		1.72	1.98	2.06
Phyllotaxis	One way	1.17	1.61	1.47
		1.77	1.64	1.59
	Both ways	1.13	1.82	2.00
		1.72	1.88	1.94

Although the second moment of area of successive cross-sections varies, the variation is reasonably smooth, and the variation is smaller for closely packed but random patterns of dimples. Such an analysis also predicts a strong correlation between depth of dimples and bending stiffness, as well as indicating that regular patterns such as square and hexagonal will have greatly reduced bending stiffness compared to irregularly patterned dimples due to “lines-of-weakness”. A significant increase in bending stiffness is predicted by this analysis when dimples are in both up and down directions compared to all the dimples being in a single direction.

Although some of the trends predicted by the second moment of area analysis were seen experimentally, such as increased stiffness with deeper dimples, and dimples in both directions, overall it was seen that using a second moment of area analysis to model the bending performance of dimpled sheets is wholly inadequate. Not only does such a theory overpredict the stiffness of such sheets by an order of magnitude, but predictions of significant orthotropic behaviour caused by “lines-of-weakness” were also shown by experimental results to be invalid. The second moment of area based calculations are not valid because the dimpled

sheet does not behave as an Euler-Bernoulli beam. The tips of the dimples cannot carry load directly between them, successive cross-sections therefore don't develop linearly varying in-plane stress distributions.

A new theory of dimpled sheet stiffness is therefore needed to understand and capture the behaviour of such sheets. Initial experiments have confirmed the potential of dimpling to increase the bending performance of thin sheets, and in the subsequent chapters of this thesis, this improvement is quantified by developing a new method for analysing dimpled sheets.

Chapter 3

Analysis of a single dimple

3.1 Summary

The analysis of a shell of revolution under asymmetric edge loading is a problem which has received the attention of various authors over a number of decades. Here, starting with the derivation of the governing equations of the problem, the subsequent approximate solutions for the edge displacement and rotation of a spherical cap and cone under an applied axisymmetric moment or horizontal force are quoted. The validity of these approximate solutions is tested against FEA and seen to be very good. Taking these analytical solutions for rotations and displacements and normalising appropriately, the normalised rotational and stretching stiffness of a spherical cap or cone can be written in terms of the radius, thickness and depth of the cap or cone, allowing general observations to be made about the form of these stiffnesses which are also expected to hold for dimples of a general shape.

A method for approximating the rotational stiffnesses under bending for a dimple of arbitrary shape is proposed. The proposal is an equivalent cone method which matches the radius and thickness of a dimple to a cone whose depth is chosen such that the equivalent cone matches the shape of the dimple over a suitable edge region. The edge region is defined to extend to such a distance that the stresses due to the applied edge moment have decayed away to a sufficiently small value. FEA analysis shows that the equivalent cone method provides a good approximation over a wide range of dimple geometries.

Next, analysis of a dimple in an infinite plate in biaxial loading will show that a dimple is equivalent to an elastic inclusion of the correct stiffness. A superposition analysis not only confirms such an equivalence, but also provides an analytical solution for the stiffness of such an inclusion. The effective stiffness of a dimple which is included within an infinite plate is greater than the stiffness of the dimple by itself. The superposition analysis will show that this is due to the bending-stretching interaction of the dimple and the horizontal restraint provided by the infinite plate. FEA analysis of a dimple or inclusion in a large quasi-infinite plate confirms the equivalence of a dimple to an elastic inclusion of the effective stiffness

calculated by the analytical theory. While this equivalence proves exact for biaxial bending and biaxial stretching, under different loading conditions the behaviour of a dimple is not quite captured by an elastic inclusion, even allowing a slight change in the effective stiffness of the inclusion.

3.2 Introduction

In order to understand the effects of a pattern of dimples on a plate, it is first necessary to look more closely at the structural behaviour of a single dimple. Compared to a flat disc, the geometry of a dimple allows that same volume of material to have a higher bending stiffness. The key idea developed here is to realise that the dimple can be treated as a small patch of material which is stiffer in bending than the surrounding plate, *i.e.* the dimple can be treated like a stiff elastic inclusion. In this section an analytical approach to modelling a single dimple will be examined and developed and then the equivalence of a dimple and an inclusion will be analytically justified. This will provide a method of calculating the stiffness of the equivalent inclusion based on the dimple geometry.

Though dimples could be manufactured into a whole variety of shapes, the most common class is axisymmetric. Such dimples have circular (axisymmetric) symmetry: they have a radial profile which is swept around 360° to form the three dimensional geometry, a shell of revolution. While the profile can be arbitrary and vary as a function of radius, the profile is constant as it is revolved, the plan outline of an axisymmetric dimple is a circle. For the purposes of this thesis, attention will be focused on axisymmetric dimples only.

3.3 Background

The analysis of a single shell of revolution under axisymmetric edge loading is a problem which has received the attention of various authors over a number of decades. The first to set up the governing differential equations to this problem were Reissner [32] and Meissner [33], see Eqns 3.1 - 3.2. The exact solution to these equations is generally not possible in closed form. Further work has thus focused on the special geometric case of a spherical cap, where the constant and equal principle radii of curvature allow for considerable analytical simplification. Even for the simple spherical cap geometry, the solution is found to be an infinite hypergeometric series, which unfortunately does not allow for amenable calculations in practice. Therefore, most subsequent authors considered approximate solutions for the case of a spherical cap loaded asymmetrically, notably the approximations of Geckler [34] and Hetényi [35]. A good summary and overview of the axisymmetric loading of shells

of revolution is given by Zingoni [36]. Section 3.3.1 sets out the problem and provides an overview of the existing work in this area, re-deriving previous results in the consistent notation used in this work. Sections 3.4.1 - 3.4.3 are original work which, building upon the analyses of Section 3.3.1, analyse the behaviour of a dimple.

3.3.1 Axisymmetric analysis of a shell of revolution

Given the inherent axisymmetry in a shell of revolution dimple, a great simplification in the analysis is possible by considering a loading which is also axisymmetric. By utilising this symmetry the three dimensional geometry is reduced down to a problem which is a function of radius only. There are four key properties which will be useful in this discussion, which will later be parameterised by α_1 , α_2 , α_3 and α_4 . These capture the bending and stretching stiffness of a dimple under an applied edge moment or radial horizontal force. As well as generically having a smaller edge rotation under an applied moment than a flat disc (a higher rotational stiffness), a dimple is also seen to deflect horizontally more than a flat disc when under a radial tension (a lower stretching stiffness). Additionally, unlike a flat disc, there is a coupling between the bending and stretching behaviour; a horizontal radially applied force produces an edge rotation and an applied moment produces a radial edge displacement.

A generic shell of revolution is shown in Fig. 3.1a with a infinitesimal element showing the moments M , in-plane forces N , and shear forces Q , which act upon it. The rotation of the shell, Θ , is the change in slope of the meridional circle due to bending and D is the flexural rigidity of the shell. Setting up the coordinate system as per Fig. 3.1b and defining the instantaneous principle radii of curvature to be R_ϕ and R_θ , the equilibrium and compatibility of such an element lead to the following general equations for a shell of revolution under axisymmetric loading [36]:

$$\begin{aligned} \left[D \frac{R_\theta}{R_\phi} \sin \phi \right] \frac{d^2 \Theta}{d\phi^2} + \left[D \frac{R_\theta}{R_\phi} \cos \phi + \sin \phi \frac{d}{d\phi} \left(D \frac{R_\theta}{R_\phi} \right) \right] \frac{d\Theta}{d\phi} \\ + \left[v \left(\cos \phi \frac{dD}{d\phi} - D \sin \phi \right) - D \frac{R_\phi \cos^2 \phi}{R_\theta \sin \phi} \right] \Theta = R_\phi R_\theta \sin \phi Q \quad (3.1) \end{aligned}$$

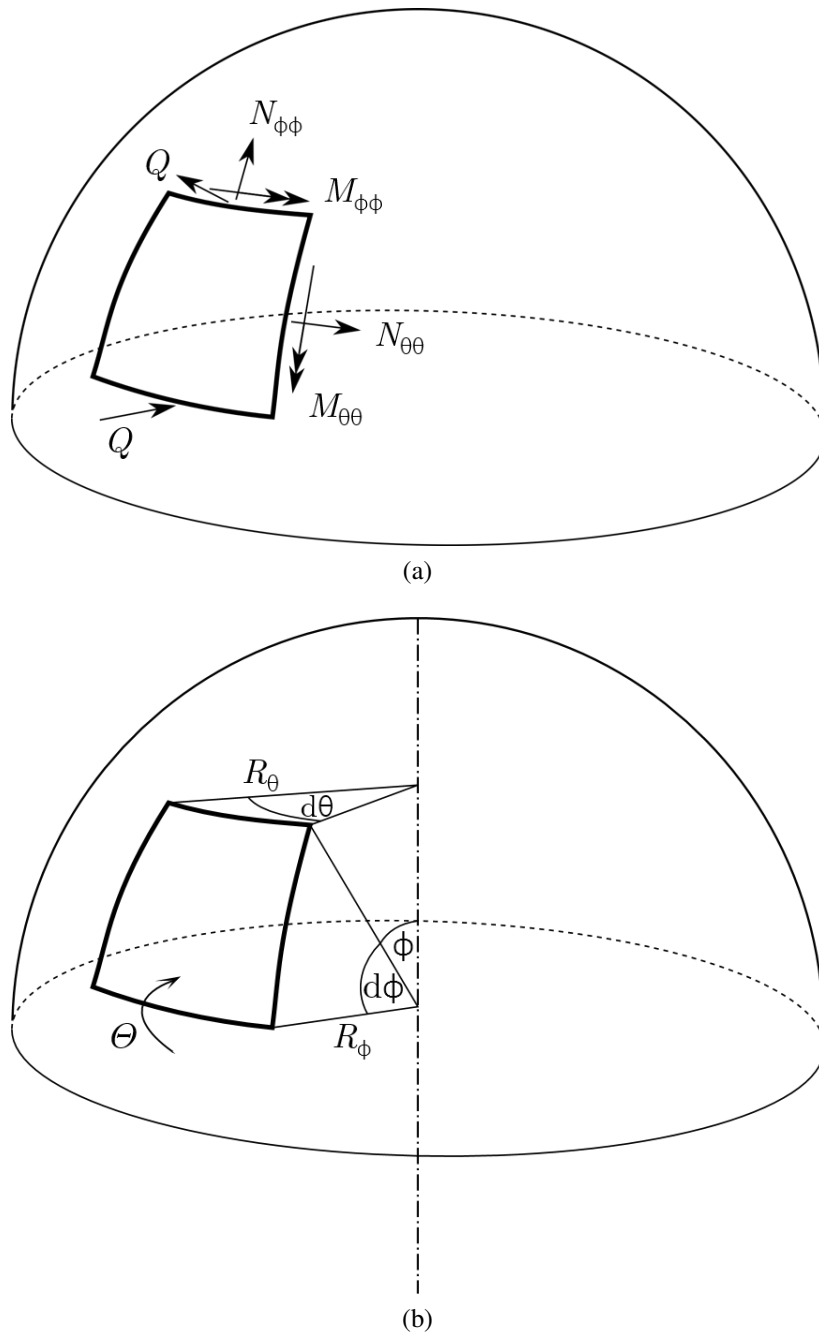


Fig. 3.1 Diagrammatic set-up for the analysis of a general shell of revolution. (a) The moments M , in-plane forces N , and shear forces Q , which act are shown on an infinitesimal element of the shell. (b) Coordinates ϕ , θ , principle radii of curvature R_ϕ and R_θ and shell rotation Θ are shown on an infinitesimal element.

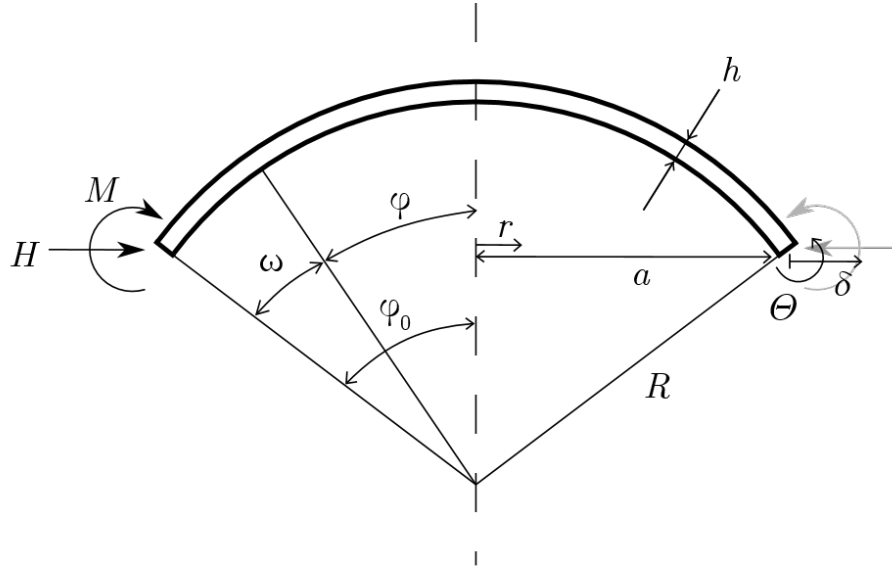


Fig. 3.2 Diagrammatic set-up for a spherical cap. The axis of revolution is shown as a dashed line. The shell has a constant radius of curvature R and constant through-thickness h . The subtended half-angle of the shell is ϕ_0 , and ϕ and ω parameterise the meridional angle from the centre and edge of the shell respectively. An axisymmetric moment per unit length M and a horizontal force per unit length H are applied to the edge of the shell. The edge rotation Θ and horizontal radial displacement δ are shown as well as the horizontal radial coordinate r .

$$\begin{aligned} \frac{R_\theta^2}{hR_\phi} \frac{d^2Q}{d\phi^2} + \left[\frac{R_\theta^2}{hR_\phi} \cot\phi + \frac{R_\theta}{hR_\phi} \frac{dR_\theta}{d\phi} + \frac{d}{d\phi} \left(\frac{R_\theta^2}{hR_\phi} \right) \right] \frac{dQ}{d\phi} + \left[\frac{R_\theta}{hR_\phi} \frac{d^2R_\theta}{d\phi^2} \right. \\ \left. + \left\{ \frac{d}{d\phi} \left(\frac{R_\theta}{hR_\phi} \right) \right\} \frac{dR_\theta}{d\phi} + \left\{ \left(\frac{R_\theta + \nu R_\phi}{R_\phi} \right) \frac{dR_\theta}{d\phi} - (R_\phi + \nu R_\theta) \cot\phi \right\} \frac{\cot\phi}{h} \right. \\ \left. - \nu \left\{ \cot\phi \frac{d}{d\phi} \left(\frac{R_\theta}{h} \right) - \frac{R_\theta}{h \sin^2\phi} \right\} \right] Q = -R_\phi E \Theta \quad (3.2) \end{aligned}$$

These equations show that there is a fundamental coupling between bending and stretching in a shell of revolution: a stretching-bending interaction. Finding a general solution to these equations would be “extremely difficult” [36], due to the complexity of the coefficients of the differential terms. However, when considering special geometric cases, such as a cone or a spherical cap, some helpful simplification can be made due to constant or zero values for principle curvatures. When considering a spherical cap shell, Eqns 3.1 and 3.2 can be simplified greatly to give the following simultaneous equations:

$$\frac{d^2\Theta}{d\phi^2} + \frac{d\Theta}{d\phi} \cot\phi - \Theta (\cot^2\phi + \nu) = \frac{R^2}{D} Q \quad (3.3)$$

$$\frac{d^2Q}{d\phi^2} + \frac{dQ}{d\phi} \cot\phi - Q (\cot^2\phi - \nu) = -Eh\Theta \quad (3.4)$$

Nevertheless, even here the hypergeometric series solution which can be obtained [32, 33] is too cumbersome to be of much practical value [35]. Therefore, in practice, approximate analytical solutions to these equations are sought. Perhaps the best known and simplest solution is the Geckler approximation [34], which keeps only the second order derivative terms from the LHS (Left Hand Side) of Eqns 3.3 and 3.4. The rapid decay of moment and rotation near the edge of the shell in these problems makes the second derivative terms large in comparison to Q , $\frac{dQ}{d\phi}$, Θ and $\frac{d\Theta}{d\phi}$, allowing the lower order terms to be neglected. For a spherical cap of constant through-thickness, the Geckler approximation gives relatively compact expressions for the rotational and stretching response under axisymmetric bending and tension. Where ω is the meridional angle from the edge of the shell, the rotation of the shell is Θ and the horizontal radial displacement is δ , for an applied moment per unit length M , the Geckler solution gives:

$$Q = M \frac{2\lambda}{R} e^{-\lambda\omega} \sin(\lambda\omega) \quad (3.5)$$

$$N_{\phi\phi} = -M \frac{2\lambda}{R} \cot(\phi_0 - \omega) e^{-\lambda\omega} \sin(\lambda\omega) \quad (3.6)$$

$$N_{\theta\theta} = -M \frac{2\sqrt{2}\lambda^2}{R} e^{-\lambda\omega} \sin\left(\lambda\omega - \frac{\pi}{4}\right) \quad (3.7)$$

$$M_{\phi\phi} = M\sqrt{2}e^{-\lambda\omega} \sin\left(\lambda\omega + \frac{\pi}{4}\right) \quad (3.8)$$

$$M_{\theta\theta} = M \left(\frac{1}{\lambda} e^{-\lambda\omega} \cot\phi_0 \cos(\lambda\omega) \right) + \nu M_{\phi\phi} \quad (3.9)$$

$$\Theta = M \frac{1}{\lambda} e^{-\lambda\omega} \cos(\lambda\omega) \quad (3.10)$$

$$\delta = -\frac{R \sin(\phi_0 - \omega)}{Eh} \lambda \sqrt{2} C e^{-\lambda\omega} \sin\left(\lambda\omega - \frac{\pi}{4}\right) \quad (3.11)$$

where $\lambda = \sqrt[4]{3(1-\nu^2)(R/h)^2}$

These equations show that the resulting moment and in-plane force distributions, and thus stresses, decay away quickly as they move towards the centre of the dimple, as seen from

the exponential decay term $e^{-\lambda\omega}$. λ is a non-dimensional parameter which describes the characteristic attenuation distance. Similarly, equations can be obtained for an applied radial force per unit length on the edge of the shell. The most useful result from these solutions is the overall edge response, rotation and horizontal radial displacement, to a unit moment or force per unit length. These can be given in the surprisingly elegant form [35]:

$$\Theta_m = \frac{4\lambda^3}{ERh} \quad (3.12)$$

$$\delta_m = \Theta_{hrz} = \frac{2\lambda^2 \sin \phi_0}{Eh} \quad (3.13)$$

$$\delta_{hrz} = \frac{2\lambda R \sin^2 \phi_0}{Eh} \quad (3.14)$$

The rotation at the edge of a shell due to a unit moment, Θ_m , has no dependence on the subtended angle of the dimple, ϕ_0 . The horizontal radial displacement at the edge of a shell due to a unit moment δ_m , and the rotation due to a unit horizontal force Θ_{hrz} , transpire to have the same value. The horizontal radial displacement at the edge of a shell due to a unit horizontal force is denoted δ_{hrz} .

The solution for a spherical cap can be seen to be approximately equal to a cone which has the same thickness and the same angle of opening [35]. Figure 3.3 shows such a pair of equivalent shells, note that each has the same gradient at its edge. The depth of the cone which corresponds to a spherical cap is given by:

$$d_{\text{cone}} = \frac{2d_{\text{sph}}}{1 - \left(\frac{d_{\text{sph}}}{a}\right)^2} \quad (3.15)$$

Therefore if we have a dimple profile which is conical or a spherical cap then we can use the Geckler approximation (Eqns 3.12-3.14), to calculate the stiffness properties of the dimple. These solutions assume a constant thickness in the through-thickness direction, whereas here the assumption, based on preservation of material during an indentation process, was of a constant *vertical* thickness. However, because of the nature of shells of revolution problems with an externally applied axisymmetric load, the stresses decay away rapidly on approaching the middle of the shell. Therefore it is sufficient to match the exact thickness at the edge of the dimple only, *i.e.*

$$t = \frac{h}{\cos \phi_0} \quad (3.16)$$

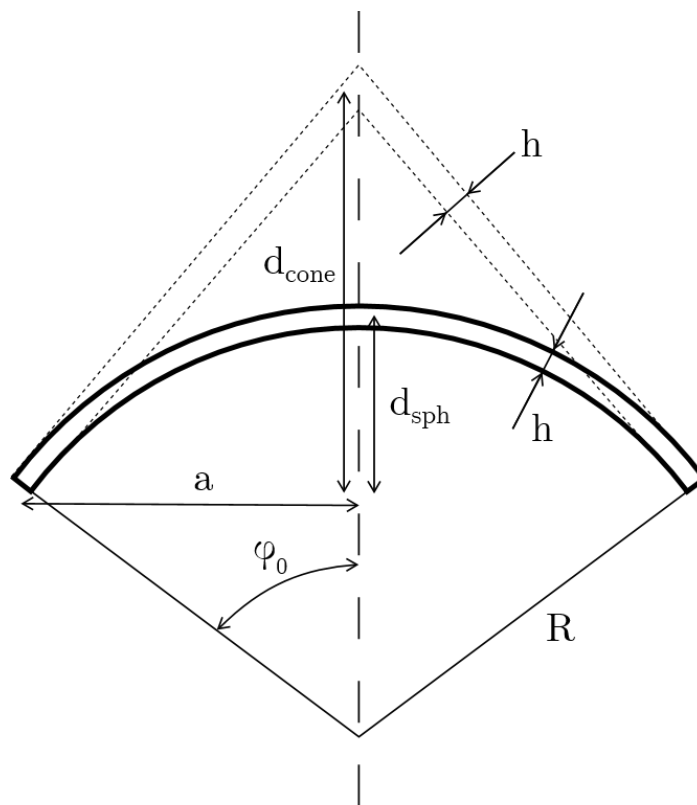


Fig. 3.3 A spherical cap can be seen to be approximately equivalent to a cone which has the same thickness and the same angle of opening. The radius of the dimple a , is related to the radius of curvature by $a = R \sin \phi_0$.

3.4 Analytical model of a single dimple

3.4.1 Normalised stiffness of a dimple

For a shell of revolution dimple with an arbitrary profile we parameterise the geometry as having a radius a , maximum depth d and vertical thickness t . In general we expect that the maximum depth occurs at the centre of the dimple. However, we can actually define the dimple geometry using just two non-dimensional parameters. Here we will choose to use d/a and a/t , the depth to radius ratio and the radius to thickness ratio.

It is useful to seek a suitable normalisation for the structural response characteristics given in Eqns. 3.12-3.14. This will be particularly helpful when comparing different dimple shapes against one another. The most natural comparison would be to compare a dimple with a flat disc of the same radius and same thickness, and thus an equal volume of material. A flat disc of radius a , thickness t , Young's modulus E and Poisson's ratio ν has a radial displacement $\delta_{\text{hrz-disc}}$ under a unit radial force per unit length. The rotation of the edge of a flat disc under a unit moment per unit length, is $\Theta_{\text{m-disc}}$. However, as a flat disc does not have any coupled bending-stretching response, an applied moment does not lead to any radial displacement, and an applied radial force does not lead to any rotation. Therefore an ‘‘apex’’ cone is chosen which has the same maximum depth of the dimple d , the same radius a , and a constant through-thickness equal to the vertical thickness of the dimple t . Such a cone has a rotation due to an applied radial force of $\Theta_{\text{hrz-apex}}$ and radial displacement due to an applied moment of $\delta_{\text{m-apex}}$. These displacements and rotations are illustrated in Fig. 3.4 and given in Eqns 3.17-3.20. $\delta_{\text{m-apex}}$ and $\Theta_{\text{hrz-apex}}$ are derived from Eqn 3.13, substituting in for the apex cone parameters: $R = a/\sin \phi_0$, $h = t \cos \phi_0$.

$$\delta_{\text{hrz-disc}} = \frac{a(1-\nu)}{Et} \quad (3.17)$$

$$\Theta_{\text{hrz-apex}} = \frac{a \, 2\sqrt{3(1-\nu^2)}}{Et^2} \quad (3.18)$$

$$\delta_{\text{m-apex}} = \frac{a \, 2\sqrt{3(1-\nu^2)}}{Et^2} \quad (3.19)$$

$$\Theta_{\text{m-disc}} = \frac{a(1-\nu)}{Et^3/12} \quad (3.20)$$

For a general dimple, the structural response characteristics are thus normalised using the flat disc and apex cone appropriately. α_1 is the stretching stiffness of the dimple normalised against a flat disc in stretching. α_2 is the rotational stiffness of the dimple under radial tension normalised by the apex cone. α_3 is the stretching stiffness of a dimple under bending

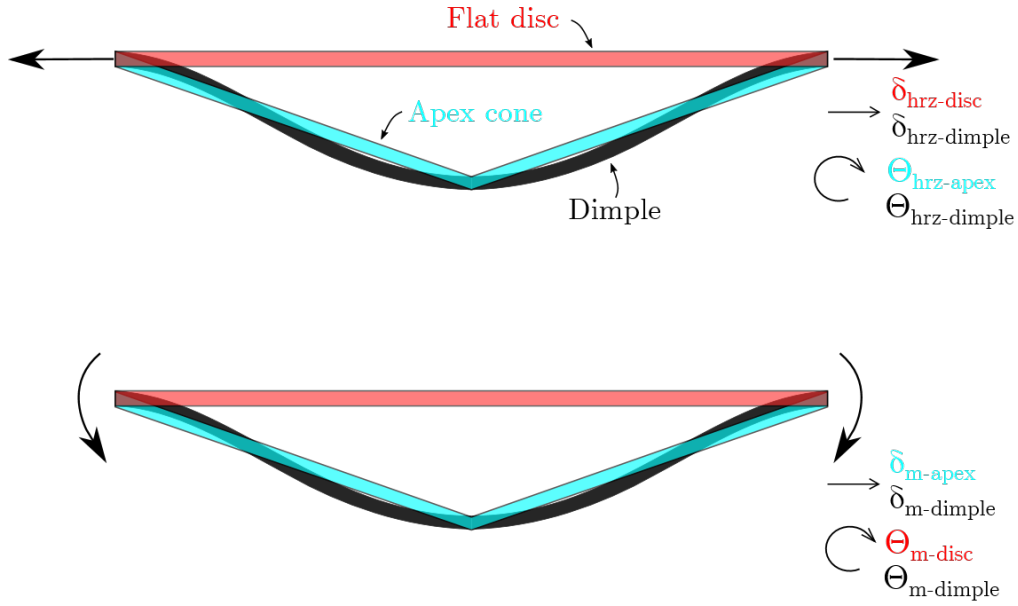


Fig. 3.4 A general dimple profile and its corresponding flat disc and apex cone. The edge rotations and horizontal radial edge displacements presented in Eqns 3.17-3.24 are indicated.

normalised by the apex cone. α_4 is the bending stiffness of the dimple normalised against a flat disc in bending. Note that as α_2 and α_3 are expected to be equal in value, consequently Θ_{hrz} and δ_m are of equal value.

$$\delta_{hrz-dimple} = \frac{a(1-\nu)}{Et} \frac{1}{\alpha_1} \quad (3.21)$$

$$\Theta_{hrz-dimple} = \frac{a}{Et^2} \frac{2\sqrt{3(1-\nu^2)}}{\alpha_2} \quad (3.22)$$

$$\delta_{m-dimple} = \frac{a}{Et^2} \frac{2\sqrt{3(1-\nu^2)}}{\alpha_3} \quad (3.23)$$

$$\Theta_{m-dimple} = \frac{a(1-\nu)}{Et^3/12} \frac{1}{\alpha_4} \quad (3.24)$$

Spherical cap and cone dimple

As the structural response of a spherical cap and a cone can be analytically calculated using the Geckler approximation, it is then possible to derive the values of α_1 , α_2 , α_3 and α_4 in terms of the non-dimensionalised geometric dimple parameters. For a cone, such as shown in Fig. 3.3, noting that $R = a/\sin \phi_0$, $d = a \tan \phi_0$, $h = t \cos \phi_0$ and $\lambda = \sqrt[4]{3(1-\nu^2)(R/h)^2}$, the

rotational stiffness under bending can be written in terms of the three geometric parameters a , d and t :

$$\frac{1}{\Theta_m} = \frac{REh}{4\lambda^3} = \frac{a^2Et}{4d \left[3(1-\nu^2) \left(\frac{a^2+d^2}{at} \right) \right]^{3/4}} = \frac{Et^3}{12a(1-\nu)} \alpha_4 \quad (3.25)$$

Thus the normalised rotational stiffness under bending, α_4 , can be written in terms of the two dimensionless geometric parameters d/a and a/t :

$$\alpha_4 = \frac{[3(1-\nu)]^{1/4}}{(1+\nu)^{3/4}} \cdot \frac{\sqrt{a/t} \sqrt{d/a}}{(1+(d/a)^2)^{3/2}} \quad (3.26)$$

The values of α_1 , α_2 and α_3 can be calculated similarly and expressed in terms of the dimensionless geometric parameters:

$$\alpha_1 = \frac{(1-\nu)^{3/4}}{2[3(1+\nu)]^{1/4}} \cdot \frac{1}{\sqrt{d/a} \sqrt{a/t} \sqrt{1+(d/a)^2}} \quad (3.27)$$

$$\alpha_2 = \frac{1}{1+(d/a)^2} \quad (3.28)$$

$$\alpha_3 = \frac{1}{1+(d/a)^2} \quad (3.29)$$

Note that α_1 and α_4 can both be split into two terms: a purely geometric term solely in d/a and a/t , and a material parameter term as a function of ν . Furthermore, each has a simple dependence on the dimple radius to thickness ratio, a/t . The rotational stiffness in bending, α_4 , increases with the square root of a/t . Thus for a sheet of a given thickness, the rotational stiffness of a conic dimple in bending will increase with the square root of the dimple radius. In contrast the stretching stiffness of a conic dimple will, for a given sheet thickness, become less stiff with the square root of the dimple radius. Additionally, the formulae tell us that while α_1 , α_2 and α_3 all decrease for an increasing value of d/a , for α_4 there is actually an optimum dimple depth to dimple radius ratio. It also suggests that this optimum depth of dimple is solely a function of dimple radius and not influenced by the Poisson's ratio or the thickness. The rotational stiffness under bending of a conic dimple is maximised when $d/a = \sqrt{1/5} \approx 0.4472$.

As seen in Fig. 3.3, a cone and a spherical cap with the same edge gradient, thickness and radius are equivalent to each other. Therefore, the above formulae are equally applicable to spherical cap dimple too, provided the value of depth is adjusted accordingly using Eqn 3.15. Thus the maximum value of α_4 for a spherical cap dimple is equal to that of a conic dimple

and occurs when the spherical cap has $d/a = \sqrt{6} - \sqrt{5} \approx 0.2134$. This indicates, in contrast to the second moment of area theory from Chapter 2, that a deeper dimple is not always better at increasing the bending stiffness. It also indicates that the optimum dimple depth is surprisingly shallow, around just 20% of the dimple radius for a spherical cap dimple.

General profile dimple

For a general dimple profile calculating the stiffness parameters α_1 , α_2 , α_3 and α_4 is much less amenable to analytical calculations. Perhaps the best way to calculate these normalised stiffness parameters is to run an axisymmetric FEA simulation on the chosen dimple profile. As rotational symmetry is present the analysis needs to only consider a single segment, and thus only a two dimensional mesh is needed, modelling the dimple profile. Compared to a three dimensional model, a far smaller number of elements need to be modelled, which allows such simulations to have very quick run times. Additionally such an FEA model can also capture through-thickness effects when the dimple is comparatively thick and also deal with changes in thickness.

3.4.2 Equivalent cone of a general dimple

Analytically calculating the normalised stiffness parameters of an arbitrary dimple profile is not generally feasible. Therefore FEA simulations or other numerical methods will generally be required to calculate the stiffness parameters, see Section 3.5. However, because there is some conceptual insight to which can be gained by exploring analytically the stiffness of a dimple, this section investigates techniques for approximate calculations. The accuracy of these analytical calculations is compared against FEA in Section 3.5.2. For dimples with a constant vertical thickness, but arbitrary profile which increases up to a maximum depth which occurs at the dimple centre, an “equivalent cone” model can be used to analytically approximate α_4 . Taking a cone which has the same radius and vertical thickness of such a dimple, an estimate of the depth of the equivalent cone is found, and the rotational stiffness of the equivalent cone is then taken as an approximation for the rotational stiffness of the dimple. This section focuses on the parameter α_4 , as the rotational bending stiffness to an applied moment is of most interest when considering dimples because it is this parameter where improved performance is observed compared to a flat disc.

For a general dimple profile which is formed by an indentation process we expect the depth to increase up to a maximum central value. Such a profile is therefore, in a macroscopic sense at least, like a conic dimple, and as a first approximation therefore a cone which is equal in radius, vertical thickness and depth may be suggested. An apex cone as such

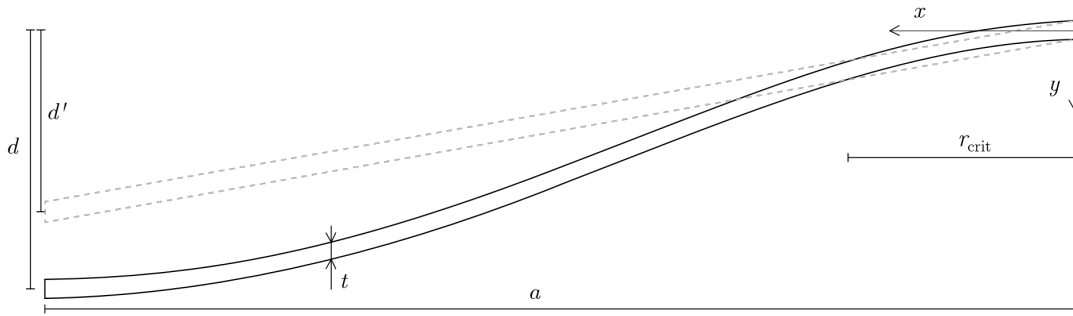


Fig. 3.5 A dimple of an arbitrary profile with radius a , vertical thickness t and depth d . The dashed line shows the equivalent cone geometry for this dimple; it also has radius a and vertical thickness t , but the depth of the equivalent cone is d' .

provides a reasonable approximation in some cases, but a significant improvement can be made by allowing the depth of the equivalent cone which we pick to be different to the actual depth of the dimple d . We will seek to choose an equivalent depth d' , which gives a good representation of the true dimple geometry, despite the conic shape being locally different in places.

Noting the equivalence of a spherical cap dimple and a conic dimple, Fig. 3.3, matching the edge gradient and thickness gives good equivalence despite significant difference in geometry near the centre. We justify this approach by utilising the fact that for thin shell of revolution problems like these, the bending stresses and in-plane stresses only permeate a small distance in from the edge of the shell, as was seen as the $e^{-\lambda\omega}$ term in Eqns 3.5-3.11. This means that we are required only to seek an equivalent conic shape which matches the true dimple geometry over a small region near the edge of the dimple. For the spherical cap and cone example, this region was declared to be sufficiently small that matching just the edge gradient would suffice. However, many practical dimple profiles formed using an indentation process may have a smooth transition from the sheet and thus, like the quartic profile shown in Fig. 3.6, $y = d \left(\frac{x}{a} - 2 \right)^2 \left(\frac{x}{a} \right)^2$, have an edge gradient which is zero. For such a dimple the effective depth would be zero if matching edge gradients, and therefore this would suggest that the dimple still acted like a flat disc. The best approximation of the equivalent depth comes from matching the equivalent cone geometry to the true dimple geometry over a small but non-infinitesimal region around the edge of the shell as defined by the non-dimensional length λ .

The $M_{\phi\phi}$ term is the major contributor to stresses in a dimple under axisymmetric bending. As shown in Eqn 3.8, it has a maximum value equal to the applied moment at the edge of the shell, and decays away with $e^{-\lambda\omega}$ as well as having a sinusoidal variation. We shall define a good equivalent cone to be one which intersects the true dimple geometry when $M_{\phi\phi}$

becomes less than 1/4 of its maximum value. The function $\sqrt{2}e^{-\lambda\omega} \sin(\lambda\omega + \pi/4)$ reduces to less than 1/4 when $\lambda\omega = 1.47415$. Thus the critical location, where the equivalent cone and true dimple geometry intersect is given when:

$$\omega_{\text{crit}} = \frac{1.47415}{\lambda} \quad (3.30)$$

$$r_{\text{crit}} = a \left(1 - \frac{\tan(\phi_0 - \omega_{\text{crit}})}{\tan \phi_0} \right) \quad (3.31)$$

Given the profile of the arbitrary dimple, we can now formulate an expression for the intersection and then calculate the depth of the equivalent cone. As an example, this calculation is performed for a quartic dimple profile. The profile of the equivalent cone is $y = d'(\frac{x}{a})$ and the quartic profile, shown in Fig. 3.6, is $y = d(\frac{x}{a} - 2)^2(\frac{x}{a})^2$. Thus, as we define the profiles to intersect at $x = r_{\text{crit}}$, we can calculate the depth of the equivalent cone d' :

$$d' \frac{r_{\text{crit}}}{a} = d \left(\frac{r_{\text{crit}}}{a} - 2 \right)^2 \left(\frac{r_{\text{crit}}}{a} \right)^2 \quad (3.32)$$

$$d' = d \left(1 + \frac{\tan(\phi_0 - \omega_{\text{crit}})}{\tan \phi_0} \right)^2 \left(1 - \frac{\tan(\phi_0 - \omega_{\text{crit}})}{\tan \phi_0} \right) \quad (3.33)$$

Expressed in terms of the two non-dimensional geometric parameters, $\phi_0 = \tan^{-1}(d/a)$ and $\lambda = \sqrt[4]{3(1-\nu^2)} \sqrt{\frac{a}{t}(\frac{a}{d} + \frac{d}{a})}$. Hence the depth of the equivalent cone can be calculated directly from the geometric parameters of a dimple. For the quartic dimple shown in Fig. 3.6, $d/a = 0.25$ and $a/t = 60$. Thus it can be calculated that $\omega_{\text{crit}} = 0.07182$ and therefore $d'/d = 0.8677$. Once the depth of the equivalent cone is known, the value of α_4 can be calculated using Eqn 3.26, substituting in the equivalent cone depth d' in place of the true dimple depth d . In this case, the equivalent cone has $\alpha_4 = 3.329$, a 5% reduction compared to the apex cone approximation which assumed a depth d and thus calculated $\alpha_4 = 3.497$. The equivalent cone model is compared against FEA in Section 3.5.2.

What is more, this method allows us to spot the regimes where the equivalent cone approximation will not be valid. When the value of ω_{crit} calculated is greater than the opening angle of the dimple ϕ_0 , then we know that the stresses are no longer confined to the edge of the dimple, but actually permeate right across the centre and will start interacting with each other. This normally occurs for thick, shallow dimples, as the increasing thickness decreases the value of λ (hence increasing ω_{crit}) and the shallowness reduces ϕ_0 . While, even for this case, Eqn 3.33 finds a solution for d' , the intersection found actually occurs on the far side of the centre, and is thus not a physically viable solution. What is more, in such

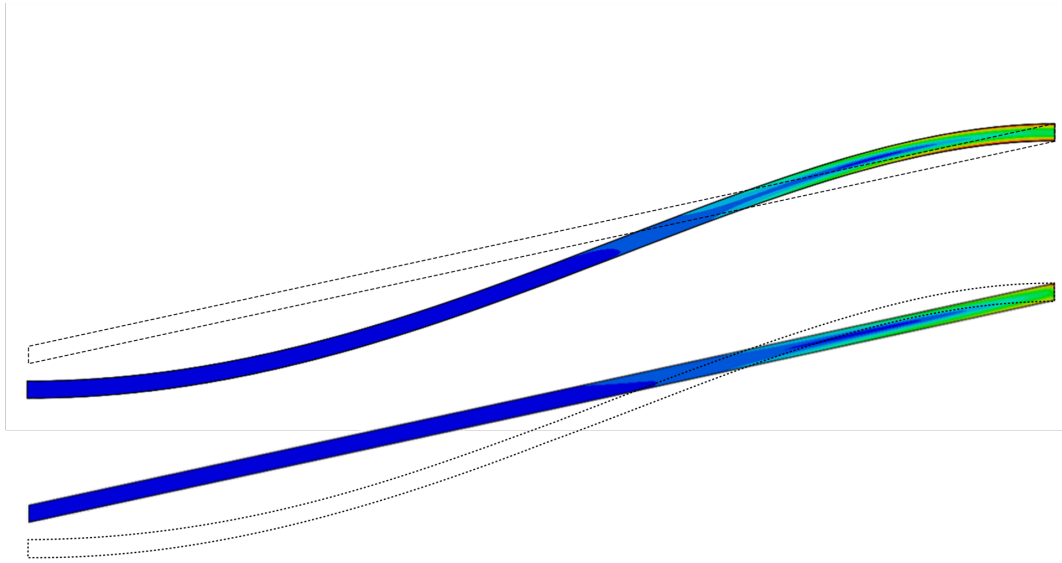


Fig. 3.6 Axisymmetric FEA is used to find the von Mises stress distributions due to an applied moment for a quartic dimple with $d/a = 0.25$ and $a/t = 60$, colour contours range from [Dark blue, 0 MPa] to [Red, 4.5 MPa]. The equivalent cone for this geometry is calculated to have $d'/d = 0.8677$, and this is shown as a dashed line. The FEA of the equivalent cone is also shown and the quartic profile is superposed onto it as a dashed line to allow for ease of comparison.

situations the value of α_4 predicted is often less than 1, however as a thick shallow dimple is approximately a flat disc, we know that in reality α_4 should be approximately equal to 1.

3.4.3 Equivalence of an inclusion and a dimple in an infinite plate

Having analysed the behaviour of a shell of revolution dimple acting on its own, we now seek to understand how such a dimple behaves when it is part of a larger flat sheet or plate. We will compare the effect of a single dimple at the centre of an infinite plate to a circular elastic inclusion. The plate is studied in biaxial bending and biaxial tension because such loading is equivalent to axisymmetric loading. We shall find that in such circumstances a dimple can be represented exactly by an elastic inclusion which is of the same thickness as the infinite plate and the same radius of the dimple. The effective stiffness of the inclusion in stretching E_{stretch} , and the effective stiffness in bending E_{bend} , can be determined by the dimple geometry.

The principle of superposition can be used to analyse the effect of an inclusion or a dimple which is included into the middle of an infinite plate which is under biaxial (axisymmetric) loading. For each of the eight states shown in Fig. 3.7, the rotation and/or radial deflection at a radius of a is shown for a unit loading. The radial displacements and rotations of an

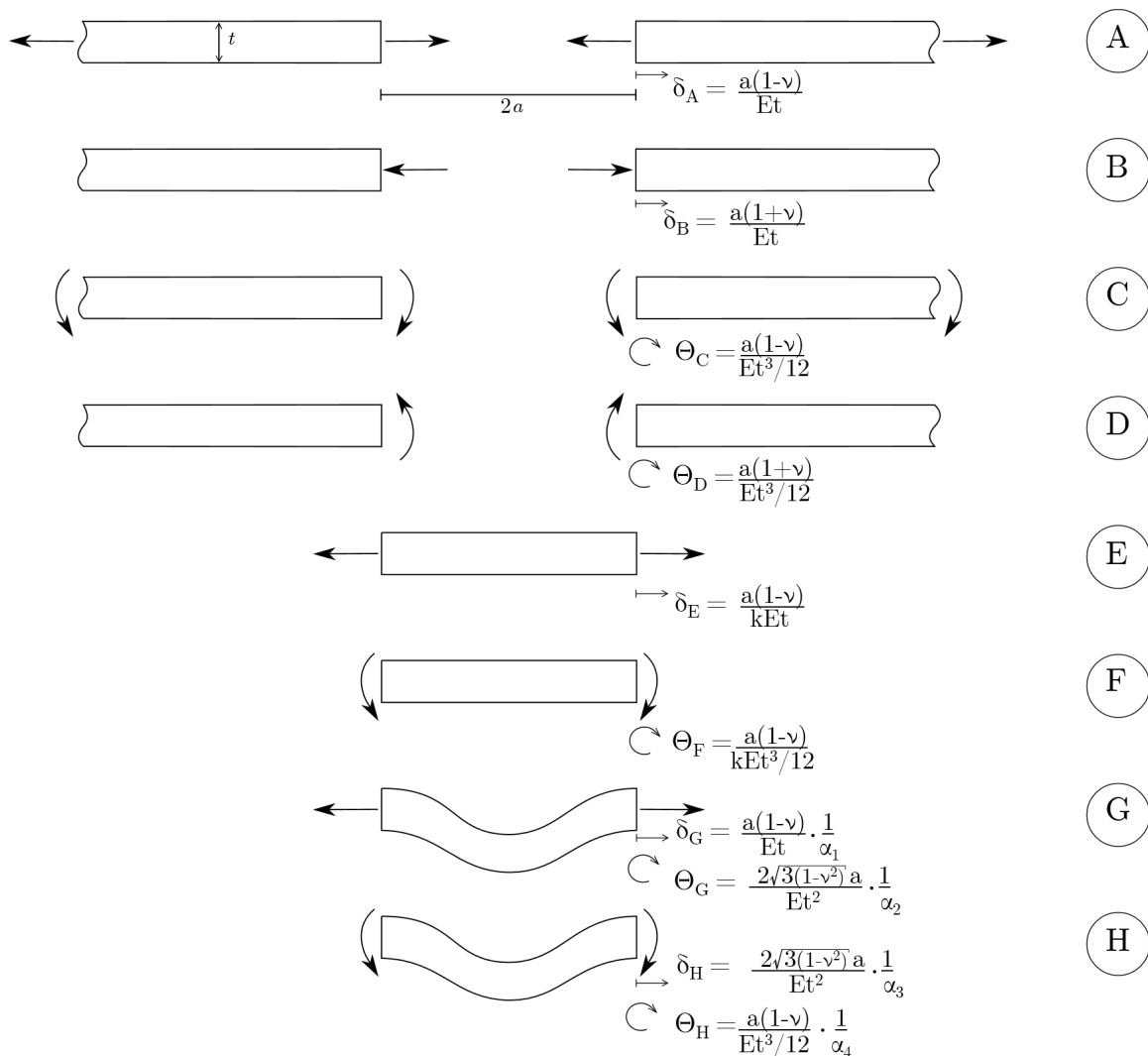


Fig. 3.7 The principle of superposition can be used to analyse the effect of an inclusion or a dimple which are included into the middle of an infinite plate which is under biaxial (axisymmetric) loading. In each of the eight states the rotation and/or radial deflection at a radius of a is shown for a unit loading. States A and C show an infinite plate with a central annulus under a uniform biaxial tension and uniform biaxial bending respectively. States B and D show an infinite plate with an applied loading on the edge of the central annulus. States E and F show an elastic inclusion with stiffness kE , under an applied biaxial tension or biaxial bending respectively. States G and H show an arbitrary dimple under an applied biaxial tension or biaxial bending respectively. A combination of these states can be superposed together to provide an equilibrium of forces and moments and a compatibility of displacements and rotations at the interfaces.

arbitrary dimple under an applied moment or radial tension are calculated in terms of α_1 , α_2 , α_3 and α_4 . Superposing states A, B and E allows for the analysis of an elastic inclusion within an infinite plate under biaxial tension to be analysed. Considering equilibrium and compatibility at a radius of a :

$$A \cdot \delta_A + B \cdot \delta_B = E \cdot \delta_E \quad (\text{Compatibility}) \quad (3.34)$$

$$A - B = E \quad (\text{Equilibrium}) \quad (3.35)$$

Where A, B and E are used to indicate the proportions of each state which must be superposed to give the total solution. Setting $A = 1$ to equate to a unit tension at the boundary and hence solving the simultaneous equations, the displacement at the edge of the inclusion can be expressed as:

$$E \cdot \delta_E = \frac{\delta_A + \delta_B}{\delta_B + \delta_E} \delta_E = \frac{2k}{(1+\nu)k + (1-\nu)} \delta_E = \frac{2a(1-\nu)}{Et[(1+\nu)k + (1-\nu)]} \quad (3.36)$$

Superposing states A, B, D, G and H allows for the analysis of a dimple within an infinite plate which is under a far-field uniform biaxial tension. Considering compatibility of rotation and radial displacement and equilibrium of moment and radial force:

$$A \cdot \delta_A + B \cdot \delta_B = G \cdot \delta_G + H \cdot \delta_H \quad (\text{Compatibility of displacement}) \quad (3.37)$$

$$D \cdot \Theta_D = G\Theta_G + H \cdot \Theta_H \quad (\text{Compatibility of rotation}) \quad (3.38)$$

$$A - B = G \quad (\text{Force equilibrium}) \quad (3.39)$$

$$D = -H \quad (\text{Moment equilibrium}) \quad (3.40)$$

Once more setting $A = 1$, these four simultaneous equations can be solved, which allows the radial displacement at the edge of the dimple to be expressed as:

$$G \cdot \delta_G + H \cdot \delta_H = \frac{\delta_A + \delta_B}{\delta_B + \delta_G - \frac{\Theta_G \delta_H}{\Theta_D + \Theta_H}} \cdot \delta_G + \frac{-\Theta_G}{\Theta_D + \Theta_H} \frac{\delta_A + \delta_B}{\delta_B + \delta_G - \frac{\Theta_G \delta_H}{\Theta_D + \Theta_H}} \cdot \delta_H \quad (3.41)$$

This can be rewritten:

$$\frac{\delta_A + \delta_B}{\delta_B + \delta_G - \frac{\Theta_G \delta_H}{\Theta_D + \Theta_H}} \cdot \left(\delta_G - \frac{\Theta_G}{\Theta_D + \Theta_H} \delta_H \right) = \frac{\delta_A + \delta_B}{\delta_B + \delta_G(1 - \zeta)} \cdot \delta_G(1 - \zeta) \quad (3.42)$$

where:

$$\zeta = \frac{\Theta_G \delta_H}{\delta_G(\Theta_D + \Theta_H)} = \frac{(1 + \nu)\alpha_1}{\left(1 + \nu + \frac{1-\nu}{\alpha_4}\right)\alpha_2\alpha_3} \quad (3.43)$$

Comparing the displacement of an inclusion to that of a dimple within an infinite plate in far field tension, Eqns 3.36 and Eqn 3.42, we note that the expressions are equivalent when $\delta_E = \delta_G(1 - \zeta)$. This then provides the way to calculate the effective elastic inclusion in stretching which matches the dimple. Comparing the values of δ_E and δ_G , Fig. 3.7, we can deduce that:

$$k_{\text{stretch}} = \frac{\alpha_1}{1 - \zeta} \quad (3.44)$$

A very similar superposition analysis can be undertaken for an elastic inclusion and a dimple which are included in an infinite plate under uniform far-field bending. In a similar manner, comparing the rotations of the inclusion to a dimple thus reveals the effective stiffness of inclusion which matches the bending behaviour of a dimple:

$$k_{\text{bend}} = \frac{\alpha_4}{1 - \gamma} \quad (3.45)$$

where:

$$\gamma = \frac{\Theta_G \delta_H}{\Theta_H(\delta_B + \delta_G)} = \frac{(1 + \nu)\alpha_4}{\left(1 + \nu + \frac{1-\nu}{\alpha_1}\right)\alpha_2\alpha_3} \quad (3.46)$$

Notice that both ζ and γ are simply functions of the normalised stiffness parameters of the dimple, α_1 , α_2 , α_3 , α_4 and the Poisson's ratio ν . Therefore the effective inclusion stiffness can be calculated given these normalised stiffness parameters.

Contrasting Θ_F to Θ_H directly could lead to the conclusion that the effective value of stiffness, $E k_{\text{bend}}$, would be equal to $E \alpha_4$. However, this analysis shows that when considered as part of a larger sheet, a dimple is slightly stiffer than one might naïvely assume. This is because of the bending-stretching interaction in a dimple: applying a pure axisymmetric moment to the edge of a dimple, as in Fig. 3.7 H, leads to an outward radial expansion of the dimple, however this expansion is partially restrained when it is included in a plate. The resulting inward radial reaction force from the plate then – once again from the bending-stretching interaction, but this time in reverse – leads to a small upward rotation, therefore

reducing the overall rotation and increasing the bending stiffness. This effect is captured by the dimensionless parameter γ , the larger the value of γ the larger the increase in stiffness is. Smaller values of α_2 and α_3 indicate a greater interaction between bending and stretching for a dimple, and consequently γ , which is inversely proportional to α_2 and α_3 , is commensurate to the bending-stretching interaction. The value of γ can often be large enough to have a significant affect on the value of k_{bend} , however the value of ζ is normally significantly smaller and so the effective stiffness in stretching is not much affected. This is due to γ being proportional to α_4 whereas ζ is proportional to α_1 , and dimples by design have values of α_4 which are greater than 1, but values of α_1 tend to be significantly less than 1.

Because in a globally flat plate in the initial linear elastic regime there is no interaction of stretching and bending this superposition analysis shows that bending performance of a dimple and the stretching performance of a dimple can be exactly captured by elastic inclusions of the same radius and with the appropriate values of k_{bend} and k_{stretch} . While an elastic inclusion and a dimple achieve their greater stiffness in bending by different mechanisms, they have the same effect on the surrounding plate. A slight caveat is that while a dimple in a plate in biaxial tension results in exactly the same distribution of in-plane stresses and radial displacements as an elastic inclusion with k_{stretch} , the dimple also will result in some small rotations and out-of-plane deflections near the dimple, however these do not make any contribution to the radial displacements and are only localised around the dimple and decay away such that they have no effect at the edge of the plate. Additionally it must be noted that this analysis has been conducted for biaxial loadings and is not necessarily applicable to uniaxial loading or other general loadings.

3.5 Finite Element Analysis of a single dimple

Analytical calculations of the stiffness parameters of a dimple, α_1 , α_2 , α_3 and α_4 , are only amenable to very limited to special geometries such as a spherical cap or cone. Other dimple profiles can only be approximated using techniques such as the equivalent cone method, Section 3.4.2. Using FEA, the stiffness parameters of dimples of arbitrary profile can be calculated numerically to a high degree of accuracy. This section assesses the accuracy of the analytical predictions for spherical caps and cones from Section 3.4.1, as well as the accuracy of the equivalent cone method from Section 3.4.2. Furthermore FEA analyses of a dimple included within a larger plate and analyses of an inclusion within a larger plate, Section 3.5.3, verify the theoretical equivalence of an dimple and inclusion of the appropriate stiffness established in Section 3.4.3.

FEA simulations are run using the commercial software package ABAQUS 6.14 [37]. Axisymmetric modelling using CAX8R quadratic reduced integration elements is performed, a high mesh density is chosen and loading is applied via a reference point which is coupled to the edge of the dimple geometry with a continuum coupling. Typically analyses use approximately 5000 CAX8R elements and correspondingly have approximately 30000 degrees of freedom. Edge rotations and edge displacements are applied and the resulting edge reaction forces and reaction moments can be extracted from the reference point located at the mid-thickness on the outer edge of the dimple. These forces, displacements and rotations allow for the calculation of α_1 , α_2 , α_3 and α_4 for each dimple. Within the dimple, the in-plane forces can be calculated by averaging the stress at each cross-section and the moments can be calculated by considering the difference in stress at the top and bottom surface. Where dimple geometries had a non-zero gradient at the outer edge, small spikes in stress were observed at the very edge of the dimple: this was due to the edge of the dimple not being perpendicular to the mid-surface as a result of the constant vertical thickness of the profile. Making a very small adjustment to the geometry to make the edge of the dimple perpendicular to the mid-surface removed these stress anomalies without any significant change to the stress distribution in the rest of the dimple.

3.5.1 FEA of a spherical cap vs Geckler theory

As the Geckler approximation for the solution of applied axisymmetric edge loading is based on a shell of constant thickness in the through-thickness direction, rather than the constant vertical thickness that we assume the dimples possess, it is useful to verify the applicability of the theory by comparing to FEA results. Additionally, as we know that the Geckler solution is only an approximation to the true solution, since it neglects the lower order derivative terms, it is especially important to check the accuracy via FEA comparison.

Figure 3.8 shows the moments and in-plane forces per unit length for an axisymmetric FEA model of a spherical cap under an applied edge moment in comparison with the Geckler approximation, Eqns 3.6-3.9. The applied moment per unit length is $M = 1\text{Nmm/mm}$, the dimple has constant vertical thickness $t = 0.2\text{mm}$, radius $a = 12\text{mm}$ and depth $d = 3\text{mm}$, thus $R = 25.5\text{mm}$ and $\phi_0 = 0.48996$. The moments and in-plane forces are plotted against the meridional angle as measured from the edge of the dimple, ω , see Fig. 3.2. An excellent agreement between the FEA and the theory is seen, for both moment and in-plane force distribution an excellent fit of both shape and magnitude is observed. As predicted the stresses decay away quite rapidly from the edge of the dimple; even for this relatively thick dimple $a/t = 24$, the stresses are negligible near the dimple centre.

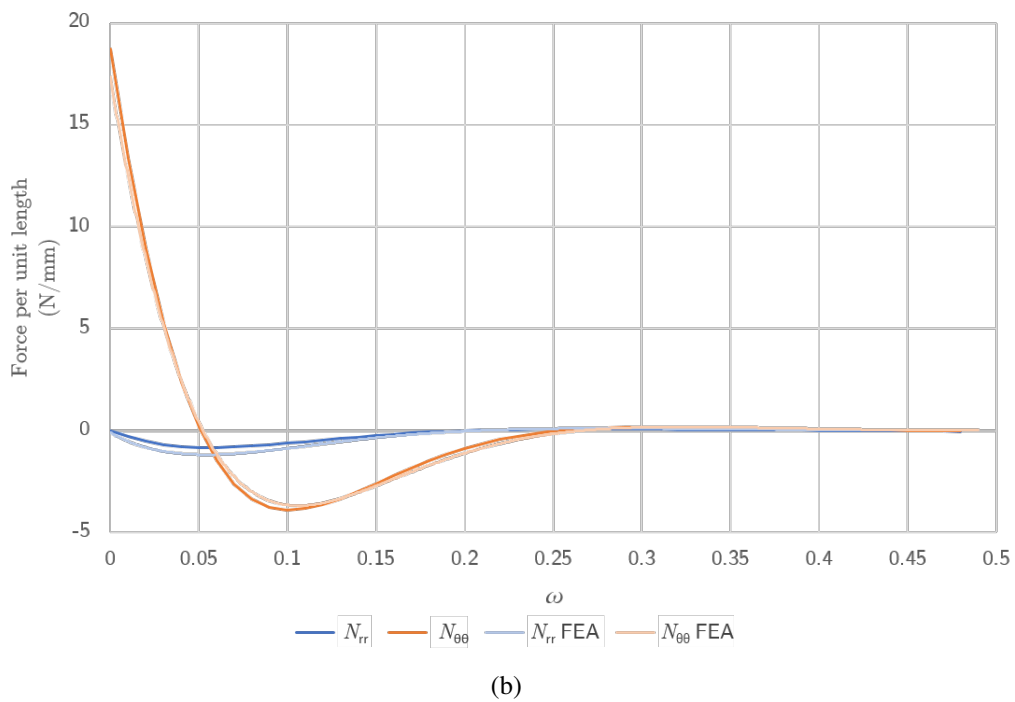
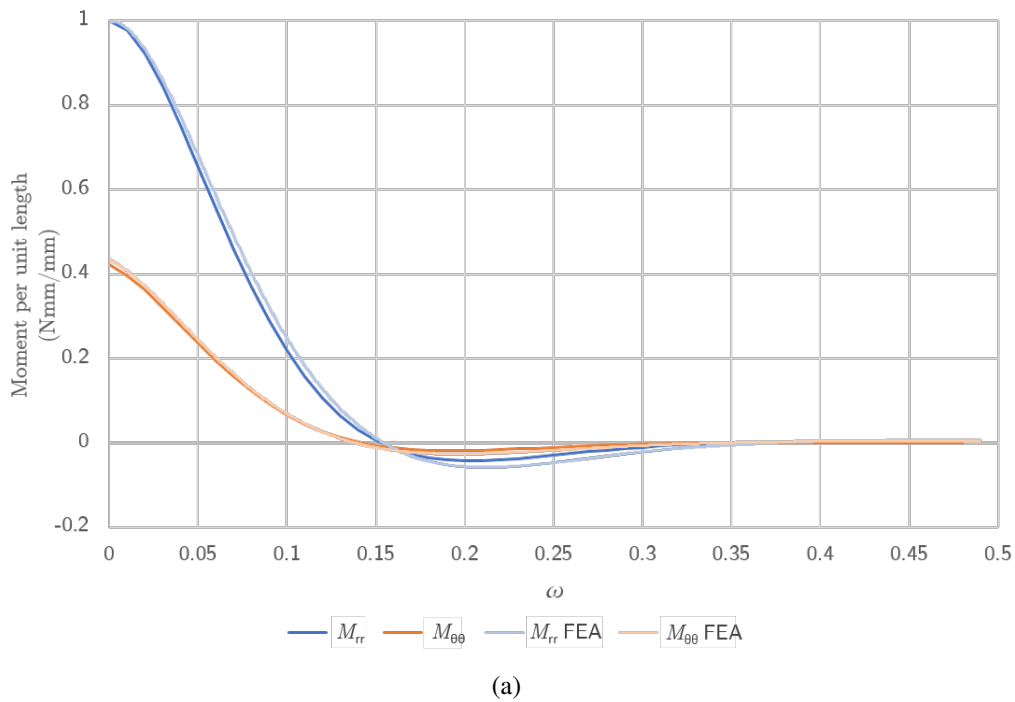


Fig. 3.8 An axisymmetric FEA model of a spherical cap dimple with a constant vertical thickness subjected to an applied edge moment has been modelled using ABAQUS [37]. The applied moment per unit length is $M = 1\text{Nmm/mm}$, and the dimple geometry is $a = 12\text{mm}$, $d = 3\text{mm}$ and $t = 0.2\text{mm}$. (a) The radial and circumferential moments from FEA are compared to the Geckler solution, Eqns 3.8-3.9 (b) The radial and circumferential in-plane forces from FEA are compared to the Geckler solution, Eqns 3.6-3.7.

Additionally, it is seen that the values of normalised bending and stretching stiffness are very accurately predicted. Calculating the corresponding cone depth for a spherical cap using Eqn 3.15, $d_{\text{cone}} = 6.4\text{mm}$, then using the Geckler approximation, Eqns 3.26-3.29, we find $\alpha_1 = 0.0672$, $\alpha_2 = 0.7785$, $\alpha_3 = 0.7785$ and $\alpha_4 = 2.4301$. The FEA results for the same geometry give $\alpha_1 = 0.0765$, $\alpha_2 = 0.8118$, $\alpha_3 = 0.8118$ and $\alpha_4 = 2.4245$. The value of α_4 , the normalised stiffness in bending due to an applied moment, is correctly predicted to within 0.25%. The other values are also accurately predicted and moreover, these values are seen to increase in accuracy for thinner shells. Figure 3.9 shows a series of coloured heatmap tables which compare the normalised stiffness values of a spherical cap dimple as calculated using the Geckler approximation and as found from FEA.

As noted earlier, for a given depth to radius ratio, the value of α_4 increases with $\sqrt{a/t}$, and FEA confirms this trend. Additionally FEA confirms that there is an optimum depth to radius ratio, d/a , which is independent of a/t , and that it occurs near the theoretically predicted value of $d/a = \sqrt{6} - \sqrt{5} \approx 0.2134$. While α_4 is predicted very accurately over the entire range of geometries considered, for α_1 , α_2 and α_3 , the prediction is less good for the thicker shells, although very good agreement is seen for dimples with a high a/t ratio, *i.e.* thin shells. Furthermore, FEA results confirm that the values of α_2 and α_3 are equal to each other, as the theory suggests. However, unlike the theory, the FEA does suggest a slight dependence on a/t , particularly for thicker dimples. Dimples with a lower a/t ratio have a higher value of α_2 and α_3 than predicted, and this is especially notable for shallow dimples. This should not be completely unexpected; a thick shallow dimple is close to a flat disc, and as a flat disc has no bending-stretching interaction, it would have $\alpha_2 = \alpha_3 = \infty$.

As the value of γ is roughly constant and changes only slowly with varying d/a and a/t , k_{bend} is also, like α_4 , approximately proportional to $\sqrt{a/t}$ and also has an optimum value which occurs for a similar depth to radius ratio. The calculated values for k_{bend} from FEA are very similar to those calculated from the theory, within a couple of percent, the accuracy is particularly good for the stiffer dimples, which are of most practical interest. The theoretical approximations for k_{stretch} are slightly less accurate, though still within 10% for most geometries. Pleasingly the predictions are most accurate for the dimples of most practical interest, *i.e.* those with a high value of α_4 . Additionally for these thin spherical caps, the stretching stiffness is close to zero, and thus assuming that they have no stretching stiffness is an easy, conservative, and yet not too inaccurate assumption.

3.5.2 FEA verification of the equivalent cone technique

Since in reality the geometry of a dimple may be more arbitrary than the simple spherical caps and cones which the Geckler approximation can calculate, it is of interest to see how

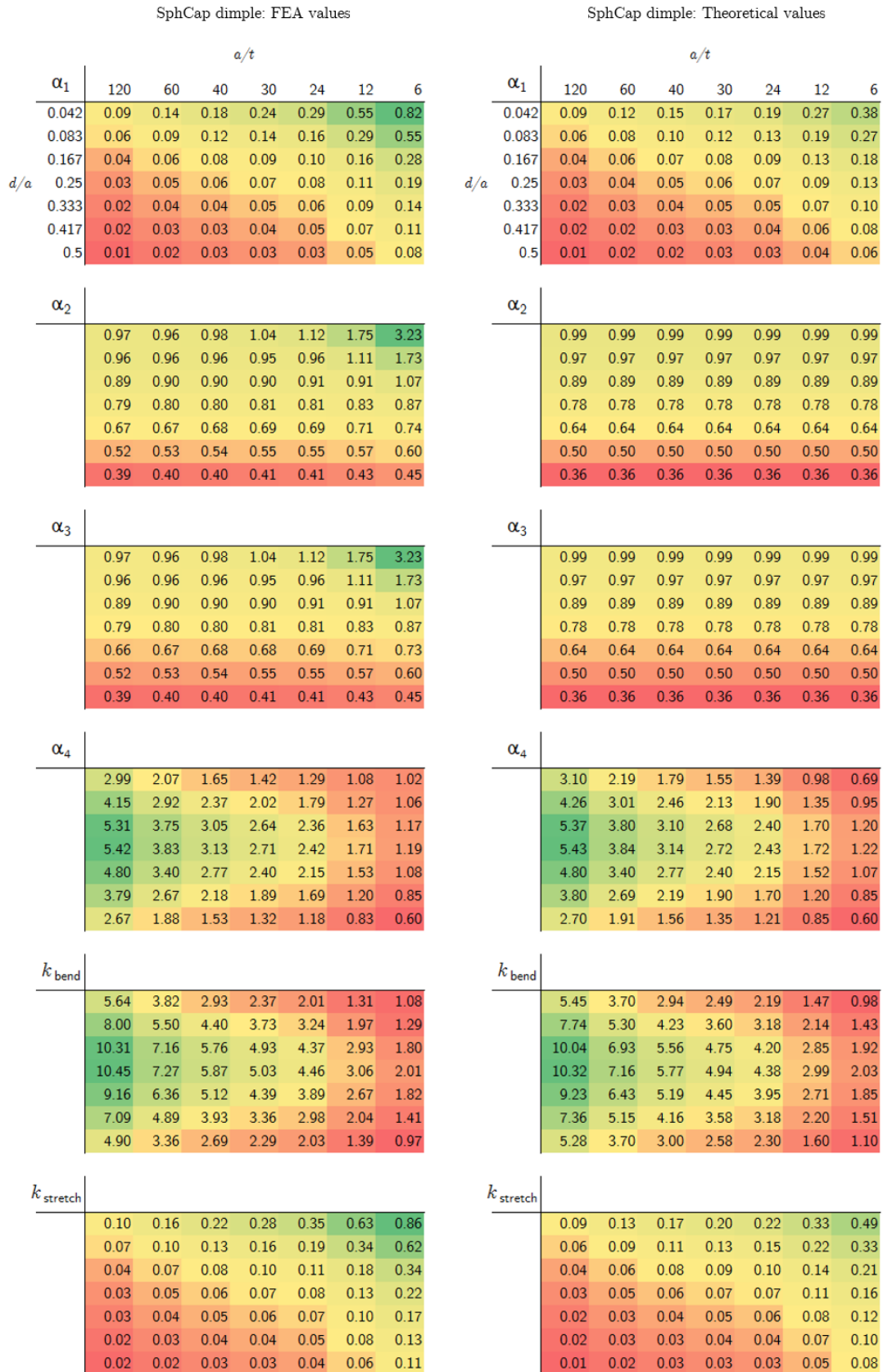


Fig. 3.9 A series of heatmap tables show the normalised stiffnesses of a spherical cap dimple, comparing the FEA values to the theoretical Geckler approximation. Values are calculated for a range of dimple depth to radius, d/a , and radius to thickness, a/t , ratios, representing the expected range of practical dimple geometries. Values of k_{bend} and $k_{stretch}$ are also calculated, using Eqns 3.45 and 3.44.

accurately the modified equivalent cone technique can predict values of α_4 . A quartic curve is a well known profile which can be used to model shells of revolution where a smooth profile with gradients of zero at the edge and the centre is desired. This particular curve is often used as its particularly simple analytical expression can make calculations more amenable [38]. A quartic curve has the formula $y = d \left(\frac{x}{a} - 2\right)^2 \left(\frac{x}{a}\right)^2$; the unequal rate of change of meridional curvature as the profile dips and then flattens out again is typical of a dimple formed by indentation.

Performing an FEA axisymmetric indentation test using ABAQUS [37], an idea of what realistic dimple profiles could look like could be gained. Setting up the FEA axisymmetric model as before, but starting with a flat profile, surface contact was modelled between a rigid hemi-spherical indenter and the initial flat disc. The indenter has a radius equal to the radius of the initial disc. Additionally, non-linear geometry is used as deformations are, by definition, large. The plate was given material properties of $E = 125,000\text{N/mm}^2$, $\nu = 0.3$ and $\sigma_0 = 300\text{N/mm}^2$. Pinned roller boundary conditions were applied to the top and bottom surface of the plate outside the indentation region. This allowed the plate material to slide horizontally, but prevented any vertical deformation in the flat section of the plate, mimicking the restraint imposed by the thick steel forming plates. Figure 3.10 shows the resulting shape of dimple which is formed when $a/t = 15$ and the indenter moves downward by $d/a = 1/3$ and is then lifted up again. Elastic rebound causes the final dimple shape to have $d/a = 0.3052$. The dashed white line shows the quartic profile, superposed onto the FEA figure which shows the resulting shape of the dimple as well as the resulting self-stresses. This figure confirms that the assumption of constant vertical thickness is reasonably valid and also that the quartic curve is indeed a good approximation to a dimple profile formed by indentation.

Axisymmetric FEA simulations of quartic dimples with a range of geometries are performed in an equivalent way to the spherical cap dimples as described in Section 3.5.1. The rotations and edge displacements are extracted for both an applied edge moment and applied radial force and thus the normalised stiffness coefficients can be calculated. Of particular interest is the normalised bending stiffness due to an applied moment, α_4 . Three dimensional contour plots of α_4 are shown in Fig. 3.11; theoretical values calculated using an apex cone and the equivalent cone, are compared to the FEA values. The apex cone assumes a cone depth equal to the true dimple depth, whereas the depth of the equivalent cone is calculated based on the distance the stresses propagate in from the edge, see Section 3.4.2. Additionally, where the equivalent cone model calculates that the stresses propagate further than the centre of the dimple, $\omega_{\text{crit}} > \phi_0$, the value of α_4 is set to 1, as in this case the dimple is acting like a flat disc. It is seen that the equivalent cone is much better at predicting performance of

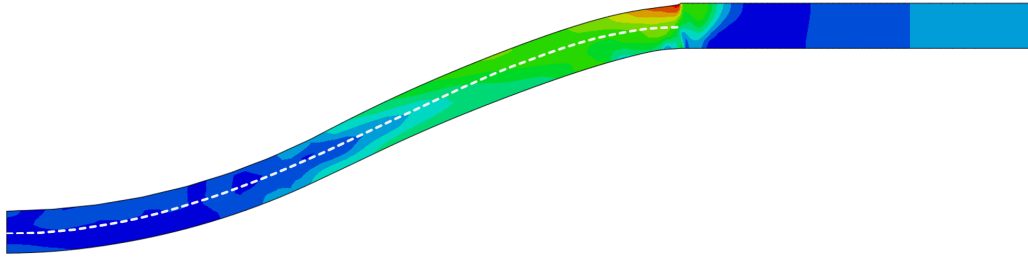


Fig. 3.10 FEA simulation of the plastic deformation occurring during the indentation process, the final geometry and von Mises stresses are shown. The indenter is depressed by a distance $d/a = 1/3$ and then raised again, allowing a small elastic rebound. The indenter is a rigid hemisphere of radius a ; the dimple has $a/t = 15$. Colour contours range from [Dark blue, 0 MPa] to [Red, 400 MPa]. A quartic profile, shown as a dashed white line, is superposed onto the FEA geometry.

the quartic dimple than the apex cone is. For thick and deep dimples, where the bending stiffness is less than a flat disc, behaviour is captured reasonably accurately by both apex and equivalent cone; however, the equivalent cone correctly identifies the thick shallow dimples that have a value of $\alpha_4 \approx 1$, whereas the apex cone does not and instead predicts a value of α_4 less than 1. For thinner dimples with higher values of a/t , the equivalent cone model is better at both predicting the overall trend and also the values of α_4 than the apex cone. The FEA and equivalent cone model both show that the optimum value of d/a is higher than for the spherical cap, occurring around $d/a = 0.5$. It also shows that there is a less sharp dependence on optimum d/a for a quartic profile: this allows for a broader range of dimple depth to radius ratios to achieve an α_4 value which is close to the optimum. The quartic cone FEA and equivalent cone theory confirm that the $\alpha_4 \propto \sqrt{a/t}$ relationship that was seen for the spherical cap dimple holds for other dimple geometries too; this information is useful from a design perspective. Additionally the spherical cap theory which showed that the optimum dimple depth to radius ratio is independent of a/t , is proved to approximately hold true for the quartic dimple too, though a slight increase in optimum depth is seen for thinner dimples.

3.5.3 FEA verification of the equivalence of a dimple and an inclusion

The superposition analysis of Section 3.4.3 suggested that a dimple could be considered to be an elastic inclusion, and gave a formula for calculating the effective Young's modulus for a dimple under tension and under bending. FEA simulations are carried out to compare the effects of an inclusion in a thin plate to the effects of a dimple on the surrounding plate,

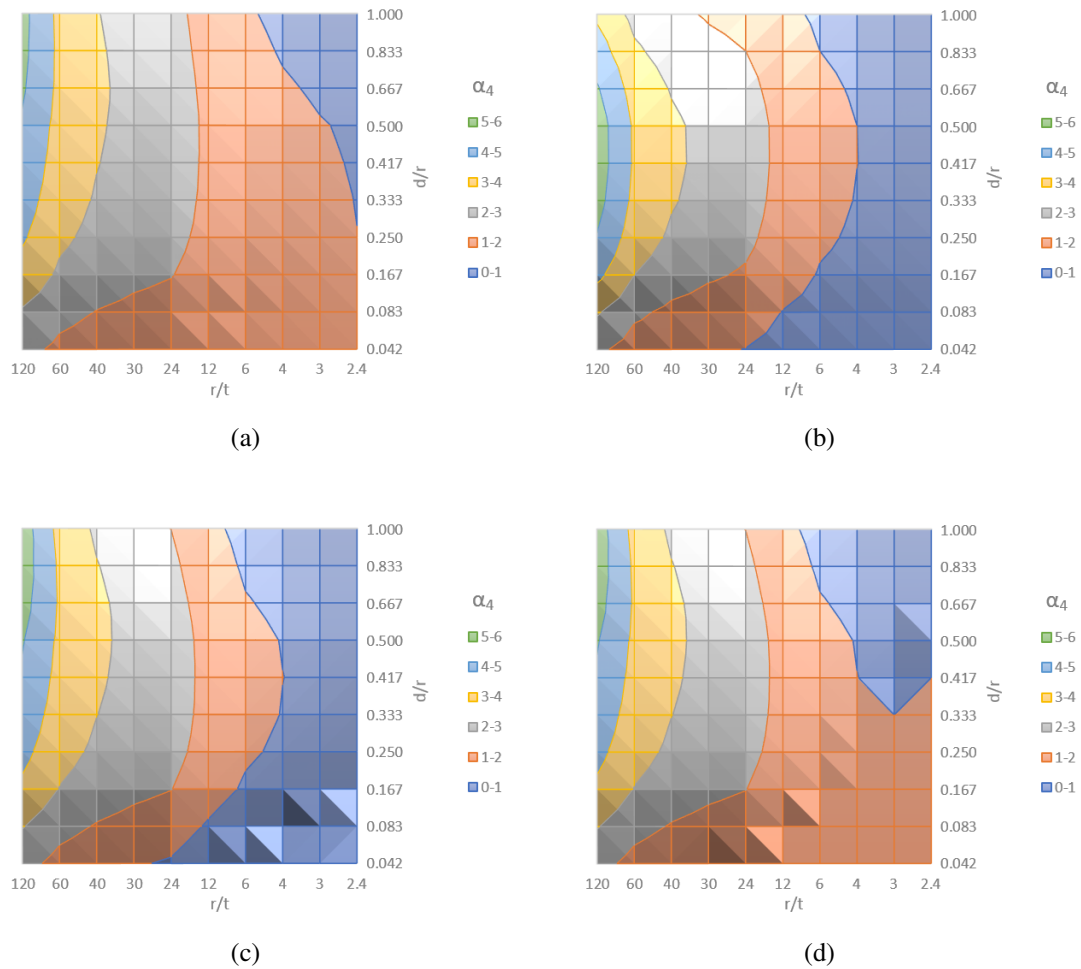


Fig. 3.11 Contour maps of α_4 : (a) FEA results for quartic profile dimples; (b) Apex cone theory; (c) Equivalent cone theory; (d) Equivalent cone theory with values set to unity where $\omega_{\text{crit}} > \phi_0$.

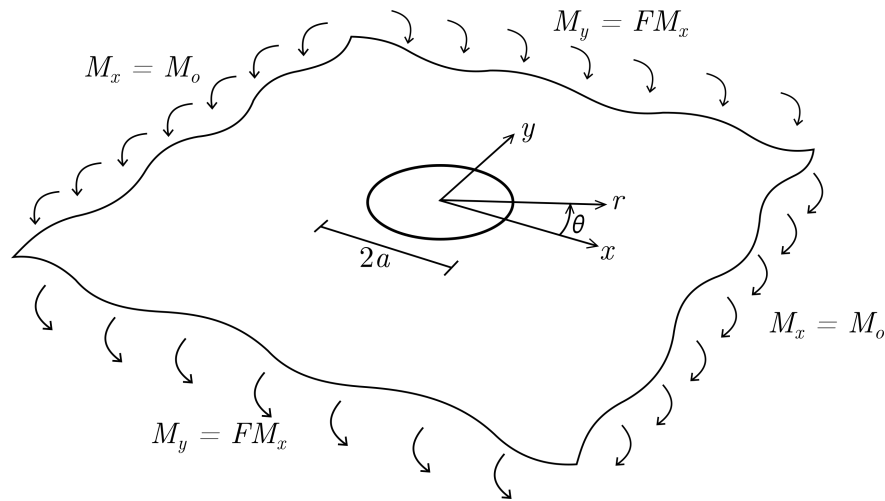


Fig. 3.12 An infinite plate with a single central circular dimple or inclusion, is subjected to a general bending loading. The loading is parametrised with the parameter F , where $F = 1$ corresponds to biaxial bending.

Fig. 3.12 shows a diagrammatic layout of such a generalised bending set-up. A square plate which is sufficiently large to be considered infinite is modelled: the half-width of the plate to radius ratio is $L/a = 16$. A quarter model is used to exploit the inherent symmetry and three layers of C3D20R 3D stress elements in a fine mesh ensure an accurate and smooth stress distribution can be extracted.

Figure 3.13 shows the stress distributions seen from the FEA modelling of a dimple and of an inclusion when subjected to an externally applied equi-biaxial bending loading. Stresses are axisymmetric in both cases as expected and while the stresses inside an inclusion are higher than the nominal stress, in a dimple the stresses are significantly less than in the rest of the plate. However, the stresses seen in the rest of the plate, $r > a$, seem to have the same distribution in both cases. Extracting the stresses on the top and bottom surfaces along a radial line allows for a calculation of moment; circumferential and radial stresses respectively allow for radial and circumferential moments to be calculated as a function of radius. The curvature and rotation along a radial line can also be extracted from the FEA and Fig. 3.14 shows these for an inclusion and a dimple, along with the radial and circumferential moments.

The behaviour for $\rho = r/a < 1$ is very different for a dimple and an inclusion. The inclusion has a high approximately uniform stress across it, but the curvature is lower than that of a flat homogeneous sheet, $\kappa < \kappa_0$, due to the higher material stiffness of the inclusion. (Note that the curvature of a homogeneous sheet is $\kappa_0 = M_0(1 - F\nu)/(Et^3/12)$). For a dimple, geometry makes the stresses decay away to zero at the centre, in fact the stresses

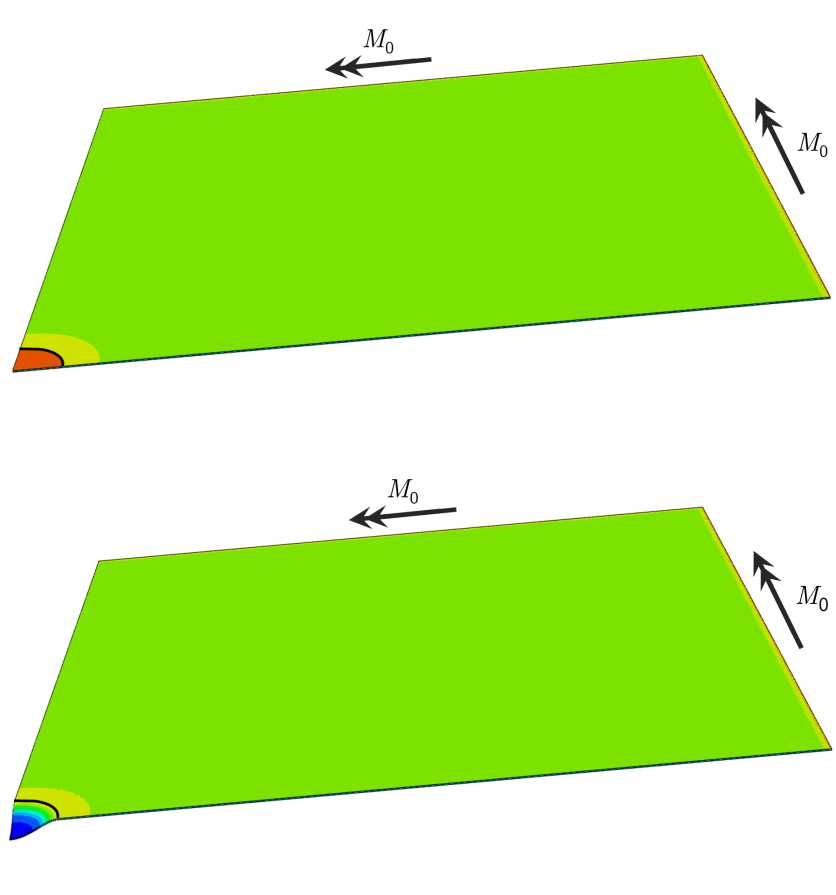


Fig. 3.13 An inclusion and a dimple of the same radius are modelled as part of a large flat plate under biaxial moment using FEA. The inclusion has $k = 2.607$ and the dimple has $d/a = 1/3$ and $a/t = 30$. The plate has a half-width which is 16 times larger than the radius of the dimple or inclusion, $L/a = 16$. Colour contours show von Mises stresses from low stress [Dark blue] to high stress [Red].the outline of the dimple and inclusion are shown by a bold black line.

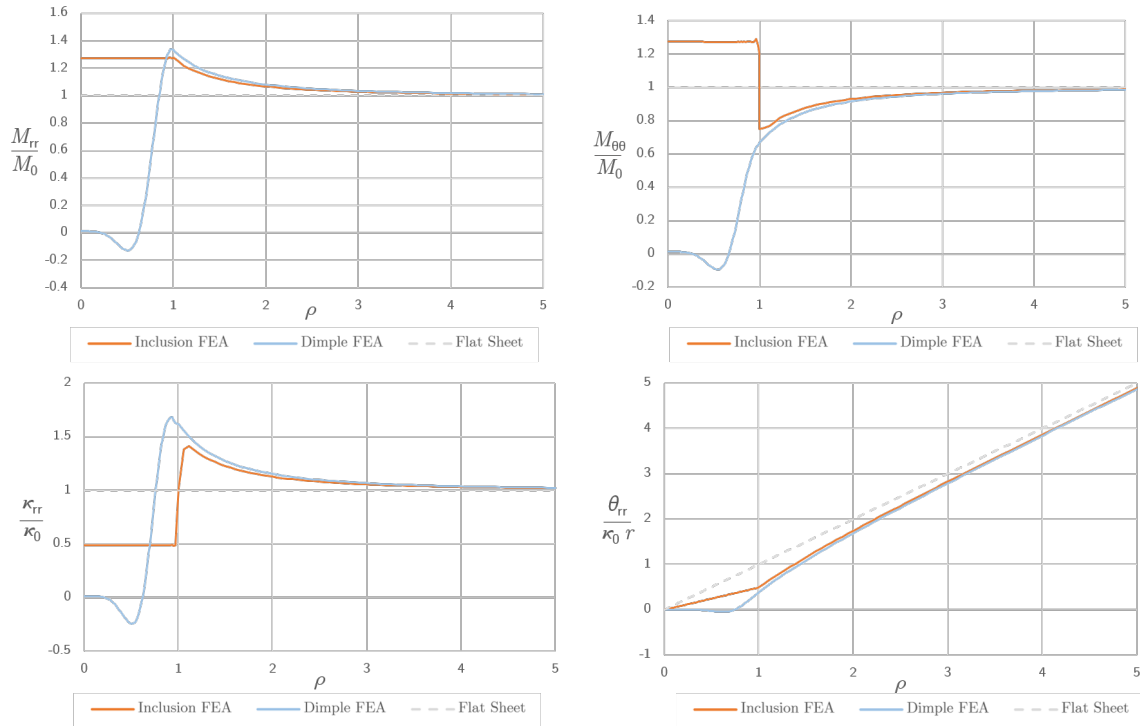


Fig. 3.14 The radial and circumferential moments of a dimple in a plate and of an inclusion in a plate are shown, normalised by the applied moment per unit length M_0 and as a function of normalised radius $\rho = r/a$. Rotation and curvature along a radial line are given for both the dimple and inclusion case; curvature is normalised against the curvature of a flat sheet under a biaxial bending κ_0 . Rotation is plotted against and compared to the rotation of a flat homogeneous plate. The dimple has a quartic profile with $d/a = 1/3$ and $a/t = 30$, the inclusion has $k = 2.607$. The plate modelled is sufficiently large to be effectively infinite, $L/a = 16$ and is subjected to biaxial bending, see Fig. 3.13.

even reverse, M_{rr} becomes negative. Thus the curvatures decay to zero near the centre of the dimple and even becomes negative around $\rho = 0.5$, however near the edge of the dimple the curvature is higher than κ_0 . Overall however, the curvature in the dimple is less than a flat homogeneous sheet, and this is seen by noting the lower rotation at the edge of the dimple than that of a flat sheet at $\rho = 1$. In contrast the behaviour of the outer plate, $\rho > 1$, is similar for both an inclusion and a dimple. The moments, curvatures and rotations, both radially and circumferentially, take exactly the same form, irrespective of whether a dimple or inclusion is present in the middle of the plate. In this case the inclusion stiffness is chosen to be equal to the α_4 value of the dimple, $k = 2.607$. This can be seen to be an underestimation however, as the rotation of the inclusion plate is slightly higher than that of the dimple plate. As shown in Section 3.4.3, the effective k of an inclusion in bending which corresponds to a dimple is not simply α_4 , but because of bending-stretching interaction and the radial restraint of the surrounding plate, it is slightly stiffer. Equation 3.45 gives the effective stiffness as $\alpha_4/(1 - \gamma)$. For the dimple presented in Fig. 3.14, $d/a = 1/3$ and $a/t = 30$; $\alpha_1 = 0.147$, $\alpha_2 = 1.467$, $\alpha_3 = 1.465$ and $\alpha_4 = 2.607$, thus $\gamma = 0.255$ and the effective value of k_{bend} is 3.501. Figure 3.15 shows that the behaviour of an inclusion with $k = k_{\text{bend}} = 3.501$, the FEA results verify that the behaviour in the plate, $\rho > 1$, matches perfectly; both radial and circumferential moments are identical for the dimple and the inclusion case, when $k = k_{\text{bend}}$. While the stresses and curvatures are different while $\rho < 1$, the rotation at $\rho = 1$ is the same for both cases, thus confirming that the analysis of Section 3.4.3 is valid and that under biaxial loading a dimple can be modelled very effectively as an inclusion of the relevant stiffness, k_{bend} . This means that a dimple and an inclusion of the relevant stiffness can be considered interchangeable as far as the rest of the sheet goes. This will be examined further in Chapter 5.

Although the theory has focused analytically on biaxial/axisymmetric behaviour, it is valuable to compare how dimples and inclusions behave under different types of loading, *i.e.* uniaxial or antisymmetric. Here the term antisymmetric loading is used to describe a loading which is equal and opposite in perpendicular directions. Using superposition of the biaxial and antisymmetric loading conditions, any arbitrary state of loading can be achieved. Thus considering the antisymmetric case in addition to the biaxial case is sufficient for complete generality. If an equivalence between an inclusion in a plate and a dimple in a plate is seen, then this equivalence will be valid for any load state.

Figure 3.16 shows the von Mises stresses developed around a dimple and an inclusion when a large flat plate is subjected to an antisymmetric bending load. Graphs of circumferential and radial moments as well as curvatures and rotations are shown in Fig. 3.17. While the moment distributions are different, even for $\rho > 1$, the curvature and rotations seem at least

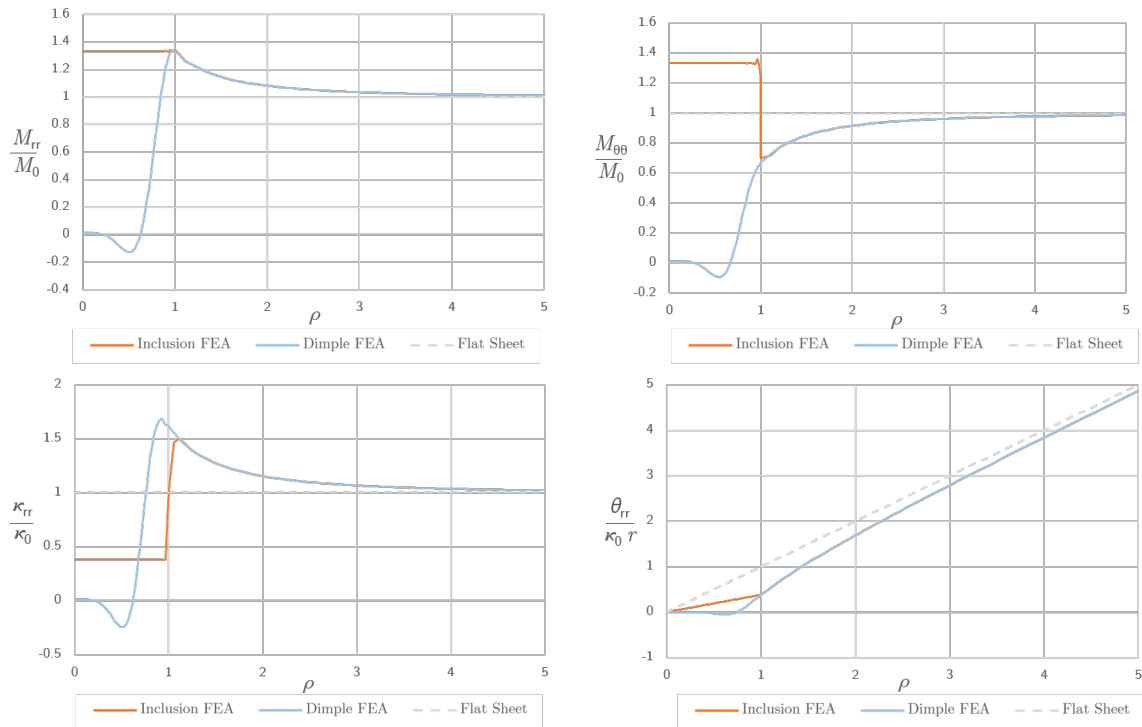


Fig. 3.15 The radial and circumferential moments of a dimple in a plate and of an inclusion in a plate are shown, as per Fig. 3.14. However the inclusion in this case has $k = k_{\text{bend}} = 3.501$.

to have a very similar form, even if the magnitudes are slightly different. Considering the rotations, it would seem that a slightly higher value of k would allow for a more representative inclusion, see Fig. 3.18

To achieve the best agreement of curvatures and rotations between the dimple and inclusion when under antisymmetric bending, the stiffness of the inclusion must be larger by about 15%, such that $k \approx 4$. While the radial and circumferential moments take a significantly different form between the two cases, the radial curvatures and rotations do correlate very well for this slightly stiffer inclusion. This suggests that while a dimple and an inclusion do not have an exact equivalence as was proven for biaxial bending, for antisymmetric bending an inclusion still captures the behaviour of a dimple reasonably well.

3.6 Conclusions

The analysis of general cones of revolution under axisymmetric loading is amenable to closed form solutions only for special geometries, such as a spherical cap or cone, where simplification can be made on account of constant radii of curvature. Approximate solutions such as the Geckler approximation allow for the stretching and rotational stiffness of a dimple

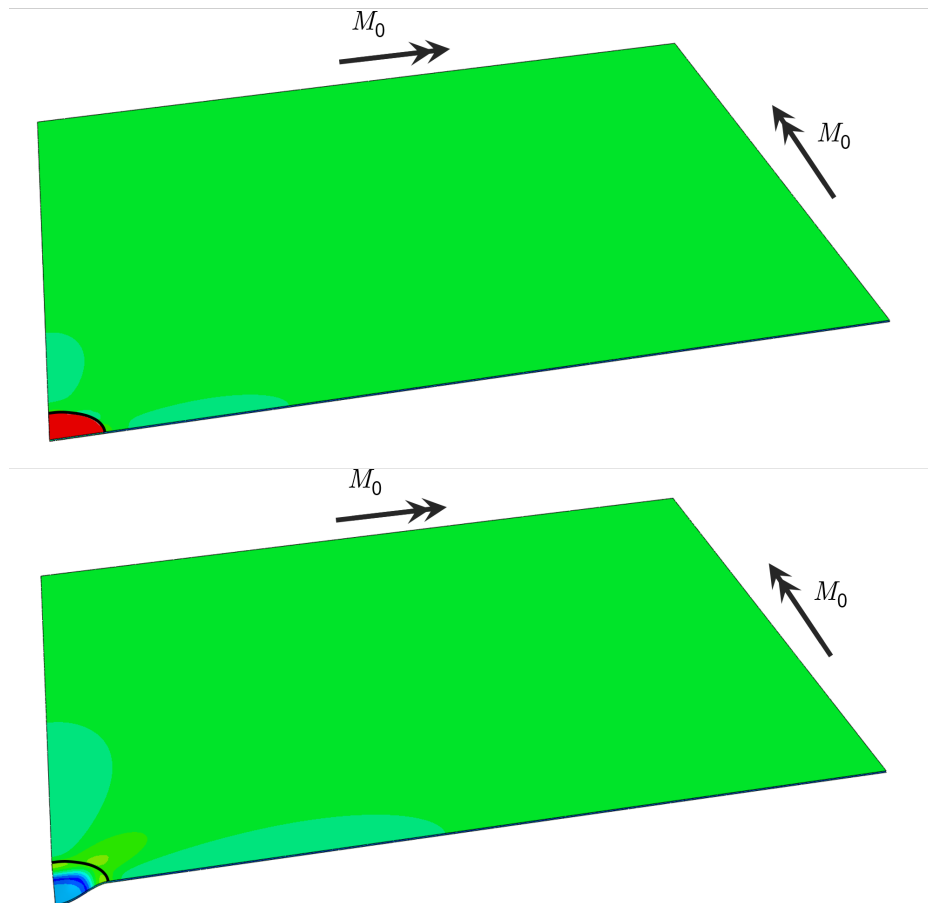


Fig. 3.16 An inclusion and a dimple of the same radius are modelled as part of a large flat plate under antisymmetric moment using FEA. The inclusion has $k = 3.501$ and the dimple has $d/a = 1/3$ and $a/t = 30$. The plate has a half-width which is 16 times larger than the radius of the dimple or inclusion, $L/a = 16$. Colour contours show von Mises stresses from low stress [Dark blue] to high stress [Red]. The outline of the dimple and inclusion are shown by a bold black line.

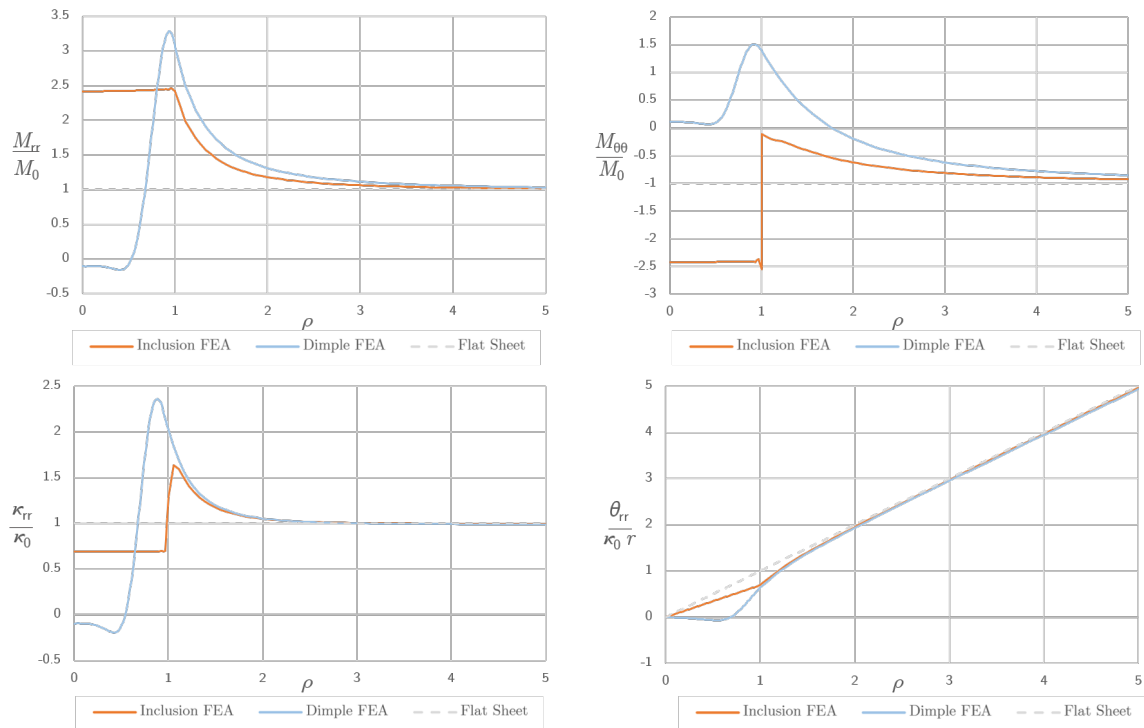


Fig. 3.17 The radial and circumferential moments, curvatures and rotations of a dimple in a plate and of an inclusion in a plate in antisymmetric bending. The dimple has a quartic profile with $d/a = 1/3$ and $a/t = 30$, the inclusion has $k = k_{\text{bend}} = 3.501$.

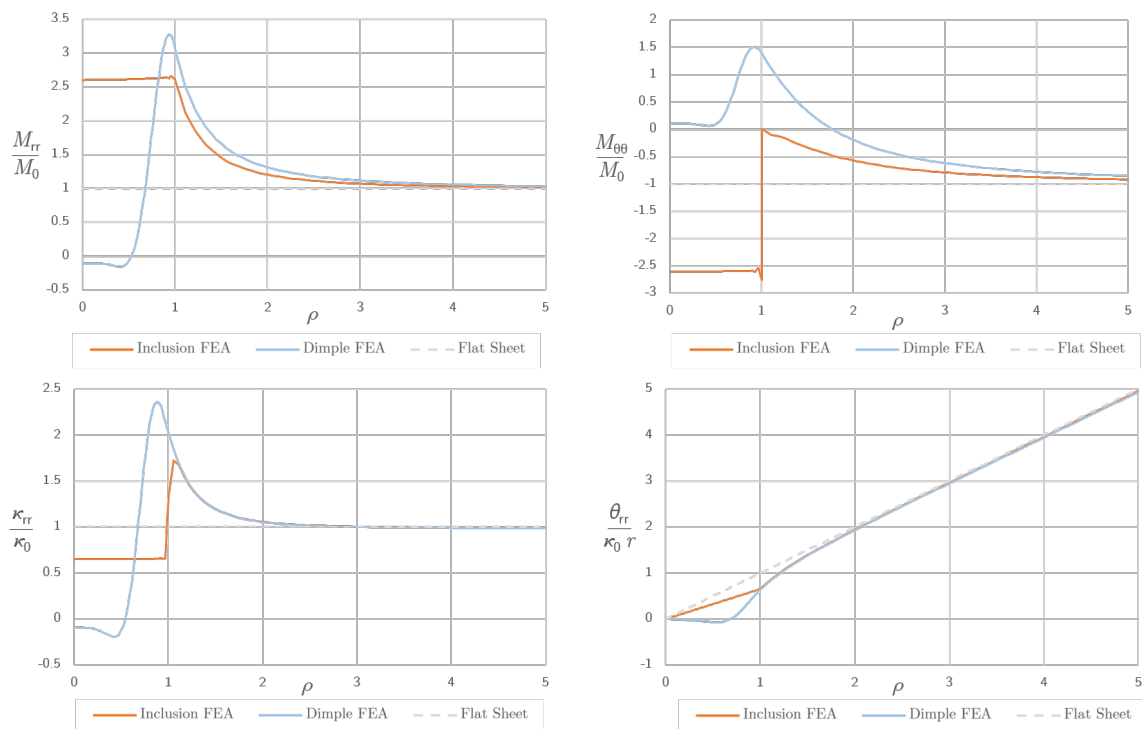


Fig. 3.18 The radial and circumferential moments, curvatures and rotations of a dimple in a plate and of an inclusion in a plate in antisymmetric bending. The dimple has a quartic profile with $d/a = 1/3$ and $a/t = 30$, the inclusion has $k = 4$.

to an applied axisymmetric moment or horizontal loading to be derived. Expressing the normalised stiffnesses, α_1 , α_2 , α_3 , α_4 , of a spherical cap or conical dimple in terms of d/a and a/t allows general observations to be drawn about the bending and stretching stiffness of a dimple. For example the rotational stiffness due to an applied moment, α_4 , is proportional to the square root of the radius to thickness ratio, $\sqrt{a/t}$, while the stretching stiffness due to an applied horizontal force, α_1 is inversely proportional to $\sqrt{a/t}$. There is an optimum depth to radius ratio for maximising α_4 , however α_2 , α_3 and α_4 all decrease with increasing d/a . While analytical solutions for dimples of arbitrary shape are not amenable to closed form solutions, the equivalent cone method shows that by analysing a cone of the same thickness and radius of the dimple and of a depth chosen to match the shape of the dimple over a suitable edge region, a good approximation can be made of the dimple's rotational stiffness. Axisymmetric modelling in FEA confirms the accuracy of the analytical solutions for cones and spherical caps, as well as the accuracy of the equivalent cone approximation. Provided that the thickness at the edge of the shell is matched appropriately, it is found that assuming a constant thickness in the through-thickness direction or assuming a constant vertical thickness makes a negligible difference for typical dimple geometries. Furthermore axisymmetric FEA is found to be an excellent method for determining numerically the rotational and stretching stiffnesses of a dimple of any shape.

This chapter has also shown that there is an equivalence between a dimple and an elastic inclusion in an infinite plate. When considering a linear elastic plate under biaxial tension or biaxial bending the equivalence is exact, which is proved by both analytical consideration as well as FEA. The analytical superposition of a dimple or an inclusion into a hole in the centre of an infinite plate allowed for the derivation of an equation to calculate the effective stiffness of an inclusion for a given dimple, in terms of the normalised rotational and stretching stiffness of the dimple to an axisymmetric moment or horizontal force (α_1 , α_2 , α_3 , α_4). The effective rotational stiffness of a dimple in bending, k_{bend} , is typically greater than unity, is maximum for an intermediate value of d/a and can be especially large for dimples with high a/t ratios. The effective stretching stiffness of a dimple, $k_{stretch}$, is lower than unity and decreased with increasing d/a and a/t . Due to the bending-stretching interaction of a dimple and the horizontal restraint provided by the surrounding plate, the effective stiffnesses of a dimple in an infinite plate, k_{bend} and $k_{stretch}$, are greater than the rotational and stretching stiffness of a dimple by itself, α_4 and α_1 .

For a dimple in an infinite plate under uniaxial or antisymmetric loading, the equivalence of a dimple and an inclusion is not exact. FEA shows that while stress distributions in the plate are different, the resulting curvatures and rotations are very similar. However, to get

the best correlation with a dimple, an inclusion of slightly higher stiffness must be used compared to the stiffness of inclusion calculated to be equivalent in the biaxial bending case.

Chapter 4

Patterns of inclusions

4.1 Summary

Homogenisation is a technique used in various disciplines and here will prove to be a useful approach to characterise the overall linear elastic stiffness of a plate patterned with inclusions. Analytical analysis of a single inclusion in a circular plate of finite size under axisymmetric loading will provide the basis for a derivation of a novel “rule-of-mixtures” which predicts the smeared stiffness of an inclusion patterned plate. The resulting Finite Plate Theory formula is able to predict the stiffness of a plate for inclusions of an arbitrary stiffness and Poisson’s ratio.

Comparing this Finite Plate Theory prediction against FEA of inclusion patterned plates shows an excellent agreement across a wide range of modular ratios, Poisson’s ratios, and pattern spacing. Even for very high packing ratios, when inclusions are close together and stress fields around neighbouring inclusions strongly interact, the prediction is excellent. Smeared stiffness is seen to be isotropic and pattern independent and the homogeneity proportional to the ratio of the inclusion radius to overall plate size. The overall stiffness is also seen to be independent of loading type, with biaxial, uniaxial and antisymmetric loading all having equal values of normalised stiffness. Compared to existing “rules-of-mixtures” the newly derived theory is shown to be superior, providing a better match for both FEA results as well as for experimental data from uniaxial tension and 4-point bending of perforated strips.

4.2 Introduction

In the previous chapter it was shown that a single dimple in an infinite plate could be well modelled by an elastic inclusion of an appropriate stiffness. This is helpful as it is much easier to model elastic inclusions than it is to model the complicated three dimensional geometry of a dimple – not just analytically easier, but also easier to model using FEA.

The three dimensional problem of a dimpled sheet has been reduced to a two dimensional problem by using inclusions. However, in the case of a dimpled sheet which is patterned with many dimples, the idea of treating each one as an elastic inclusion really comes into its own. Therefore in this chapter the analysis of plates which contain a pattern of multiple inclusions will be considered and subsequently verified by FEA.

4.3 Background

Understanding the overall structural and material properties of plates with microscopic or macroscopic inclusions is useful in many areas, from the design of perforated nuclear reactor grid plates [3, 39] to composite materials [40–42]. The effect of a single hole or an elastic inclusion within a larger plate is a classical problem [43], with much of the subsequent work in this field driven by analysis of composite structures where fibres running through a matrix are understood as stiff inclusions, or perforated plates where holes are inclusions of zero stiffness. For a single inclusion of arbitrary stiffness in an infinite thin plate, analytical solutions exist in both generalised bending and generalised stretching [44, 45]. However, the practical interest in such questions often concerns not one, but multiple inclusions. For regular patterns, previous authors used point-matching techniques to truncate infinite expressions [9, 46] satisfying boundary conditions of a unit cell at a finite number of points, but this is a mathematically lengthy method. While this is a useful technique by which (an arbitrarily close approximation of) the true stress distribution can be found, it needs to be recalculated for every new pattern, and is strictly limited to infinite plates of regular repeating patterns (because analysing a single unit cell with appropriate symmetry conditions on its edges is a key premise of this technique).

FEA can overcome this restriction, and can give an accurate numerical solution (to an arbitrarily close approximation) even for finitely sized plates and those with irregular patterns of inclusions. However, FEA is computationally expensive, with each new pattern requiring a new simulation. Often the key property of interest is the global bending or stretching stiffness of the overall plate. Calculating the exact stress distribution is therefore often simply a somewhat complicated and lengthy means to an end.

Homogenisation is a technique which can be used to give an overall view of the performance of a structure or material which is in reality not actually homogeneous when observed close up, but these inhomogeneities are small compared to the overall scale of the structure. Early motivations for homogenisation theory were for finding overall material properties, such as the elastic properties of metal alloys [47] or the magnetic permeability of a multiphase materials [48]. Subsequently it was seen that homogenisation was a useful

technique to use when considering composites [9, 49, 50]. More recently homogenisation approaches have been used to capture the overall structural behaviour of structural elements or materials where the size of the inhomogeneities is comparatively large, no longer on a microscopic scale. Examples range from finding the equivalent orthotropic properties of a corrugated sheet [10] to the effective elastic modulus of foamed concrete [51, 52].

As a result of academic interest in homogenisation emanating from various different fields, a number of different methods of estimating the smeared homogeneous properties have been developed and such methods are termed “rules-of-mixtures”. These are often developed from somewhat different perspectives, each bring a slightly different set of assumptions to the problem. A comparison of many different rules-of-mixtures is given in Section 4.11.

4.4 Homogenisation of patterns of inclusions

When considering a large sheet patterned with many inclusions, rather than attempt to analyse every detail of it, we seek an overall idea of how the sheet behaves. In other words we wish to calculate what the smeared properties of the sheet are. Taking a flat plate with a large number of inclusions patterned across it, the task is to calculate what the overall “material” properties the plate would have if it were instead a plate of the same dimensions but made of a single material throughout. Finding the new “material” properties which capture the global behaviour of the overall structure is a technique called homogenisation. Homogenisation is a valid method to employ when the size of the inclusions is small compared to the overall size of the plate. In the case of metal alloys for example: though each metal which makes up the alloy has different intrinsic material properties, the interspersion of atoms or grains is on such a small scale, that overall homogenised material properties can be given. Alternatively consider the way in which newspapers achieve grayscale images using just a single shade of black ink. By using small black dots, either of varying size on a constant grid, or varying clustering density with a single size of dot (or sometimes a combination of both), an image is formed which from a distance appears to have greyscale shading; this technique is called halftoning or dithering. An example of this process is displayed in Fig. 4.1; the black and white squares each comprise of exactly 50% of the total image in each case. However, increasing the number of squares in an image, and correspondingly decreasing the size of each little square, starts to make the overall image appear as a single homogeneous colour: grey. Stepping away from the page and viewing from a distance amplifies this effect. Figures 4.1d-4.1f show the same effect using blue and red squares; using 4, 64 and 4096 total squares successively, the overall image appears to become purple. Here it is apparent that the relative size of the squares, compared to the scale of the overall view being taken,

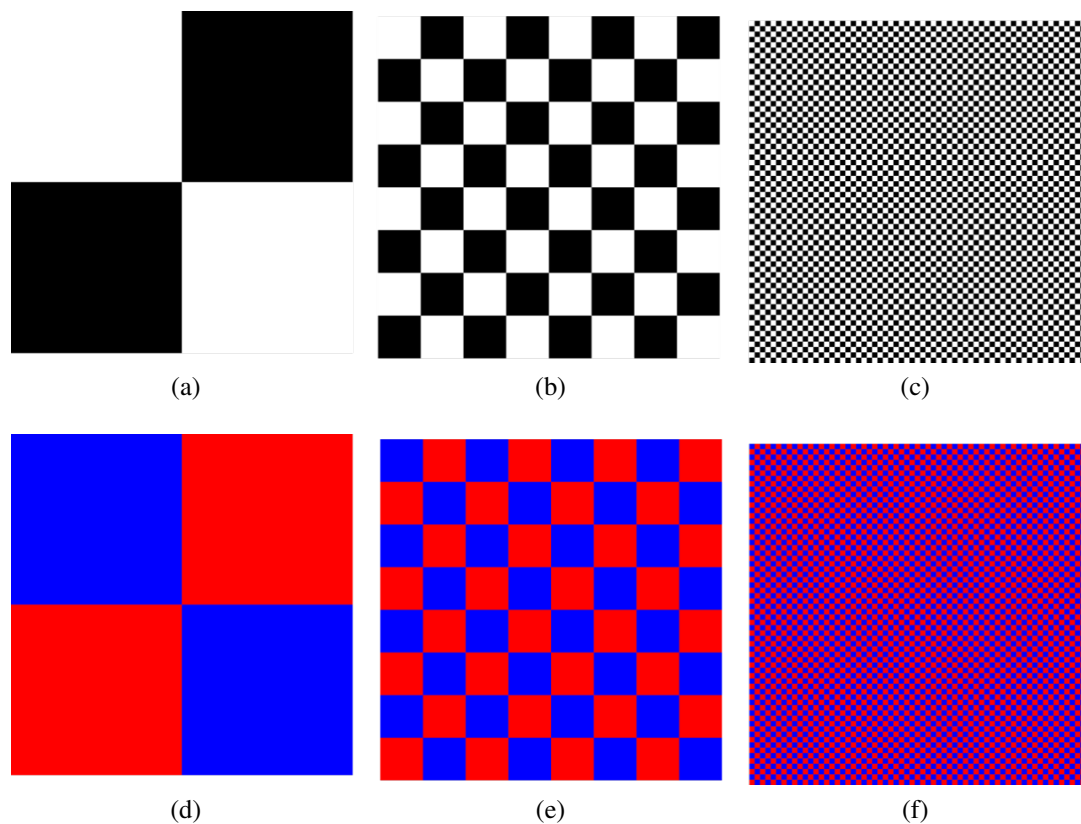


Fig. 4.1 Black and white squares are alternately tiled, with each making up exactly 50% of the total image in each case; however a different size and hence different number of small squares is used in each case: (a) 4 squares, (b) 64 squares, (c) 4096 squares. When red and blue squares are dithered in this manner, a homogeneous purple shade is perceived: (d) 4 squares, (e) 64 squares, (f) 4096 squares.

is important to the level of perceived homogeneity. Likewise for a pattern of inclusions in a plate, the relative size of the inclusions to that of the overall plate will be important to determine the validity of taking a homogenisation approach. Smaller inclusions will result in a higher level of homogeneity, however it is useful to investigate the level of homogeneity achieved with varying size of inclusions relative to the plate. In particular, it is important to determine how valid a homogenisation will be when the inclusions are relatively large, noting that for very large inclusions boundary conditions will become important.

Previous studies of composites have often sought to calculate homogenised values of elastic constants [9, 49]. When determining the homogenised behaviour of plates patterned with inclusions there are four factors which are likely to affect the value of the smeared elastic moduli calculated: inclusion stiffness, the distance between inclusions, the proportion of the plate which is made of inclusion material and the shape of the inclusions. In this chapter

the homogenised elastic moduli for an inclusion patterned plate are calculated analytically, primarily based upon the analysis of the behaviour of an inclusion under biaxial loading, Section 4.5. Formulas for predicting the elastic moduli are then verified using FEA modeling of a wide variety of inclusion patterned plates and the effects of patterning, inclusion shape and loading type are also investigated, Section 4.7.

4.5 Theoretical analysis of patterns of inclusions

4.5.1 Analysis of a single inclusion

Infinite plate behaviour

Unlike shells of revolution, circular inclusions have been analysed under generalised loadings, not just axisymmetric loadings [43, 45, 53]. Here the term generalised loading refers to load states with a unit loading in one direction while the loading in the perpendicular direction can take any value between positive unity to negative unity, as indicated by the generalised loading parameter F , for example see Fig. 4.2. While in general the effects of an inclusion within a plate in bending or in-plane tension are slightly different, for symmetrical loading (biaxial stretching or biaxial bending) the stress distributions formed around the inclusion within an infinite plate are identical for linear elastic behaviour. One can understand this straightforwardly: slicing the plate in biaxial bending into many thin layers in the through-thickness direction produces layers, each performing as a thin plate in biaxial stretching.

The solutions to the elastic stress field around an elastic inclusion in an infinite plate are given by Goodier [54]. Alternatively one can start with the well known solution for a hole in an infinite plate under uniaxial tension [43], and then use superposition (in the manner of Deryugin, Lasko and Schmauder [53]), to obtain the solution for an inclusion of arbitrary rigidity under generalised in-plane tension. At the plate-inclusion interface there must be an equilibrium of radial stress, and circumferential strains must be equal to satisfy compatibility. Using a polar coordinate system, Fig. 4.2, an Airy's stress function can specify the stress distribution around a linear elastic inclusion in an infinite linear elastic plate for a generalised in-plane loading, *e.g.* uniaxial tension, antisymmetric tension and biaxial tension, see Equations 4.1 which are consistent with those derived in [53]. In a similar manner, Bert [45] considers generalised bending of a linear elastic inclusion of arbitrary rigidity.

For an infinite plate with a central inclusion of arbitrary rigidity under a generalised in-plane tension loading, the stress distributions are given by [53]. Updating the notion to be consistent with Fig. 4.2a, denoting the plate with a "1" subscript, and the inclusion with "2",

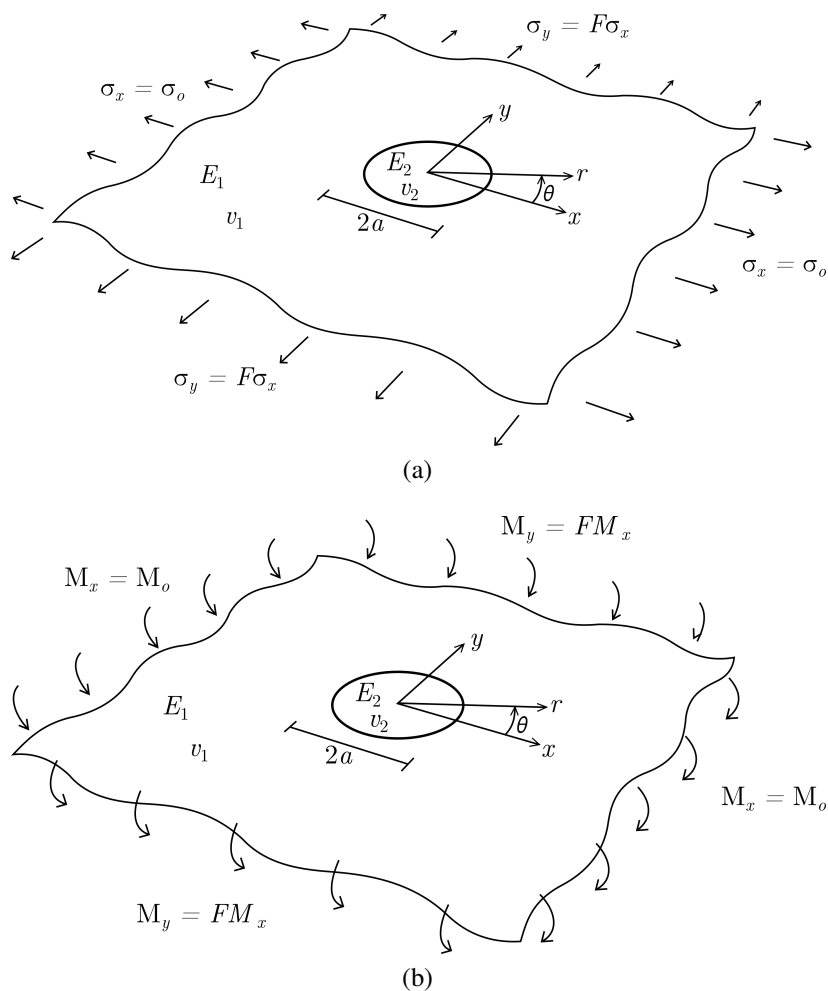


Fig. 4.2 A thin infinite plate with a central circular elastic inclusion under (a) generalised in-plane tension loading, (b) generalised bending moment loading: $F = 0$ is uniaxial loading and $F = 1$ is biaxial/symmetrical loading. The plate is thin and is defined to have unit thickness, σ_0 is an applied force per unit length and M_0 is an applied moment per unit length.

Poisson's ratio ν , Young's modulus ratio $k = E_2/E_1$, generalised loading parameter F and normalised radius $\rho = r/a$, the stress distributions are given by:

$$\left. \begin{aligned} \frac{\sigma_{1rr}}{\sigma_0} &= \frac{1+F}{2} + \frac{K_y + K_x - 1 - F}{2} \rho^{-2} + \frac{1-F + (1-F + K_y - K_x)(-4\rho^{-2} + 3\rho^{-4})}{2} \cos(2\theta) \\ \frac{\sigma_{1\theta\theta}}{\sigma_0} &= \frac{1+F}{2} - \frac{K_y + K_x - 1 - F}{2} \rho^{-2} + \frac{1-F + (1-F + K_y - K_x)(+3\rho^{-4})}{2} \cos(2\theta) \\ \frac{\sigma_{1r\theta}}{\sigma_0} &= \frac{(1-F + K_y - K_x)(2\rho^{-2} - 3\rho^{-4})}{2} \sin(2\theta) \end{aligned} \right\} \rho \geq 1 \quad (4.1)$$

$$\left. \begin{aligned} \frac{\sigma_{2rr}}{\sigma_0} &= \frac{K_x + K_y}{2} + \frac{K_x - K_y}{2} \cos(2\theta) \quad , \quad \frac{\sigma_{2xx}}{\sigma_0} = K_x \\ \frac{\sigma_{2\theta\theta}}{\sigma_0} &= \frac{K_x + K_y}{2} - \frac{K_x - K_y}{2} \cos(2\theta) \quad , \quad \frac{\sigma_{2yy}}{\sigma_0} = K_y \\ \frac{\sigma_{2r\theta}}{\sigma_0} &= -\frac{K_x - K_y}{2} \sin(2\theta) \quad , \quad \frac{\sigma_{2xy}}{\sigma_0} = 0 \end{aligned} \right\} 0 \leq \rho \leq 1 ; \quad (4.2)$$

where:

$$K_x = k \frac{(3\nu_2 - 1) + (1 - 3\nu_1)k + [(3 - \nu_2) + (5 + \nu_1)k]F}{(1 + 2k)^2 - [\nu_2 + (1 - \nu_1)k]^2} \quad (4.3)$$

$$K_y = k \frac{[(3\nu_2 - 1) + (1 - 3\nu_1)k]F + (3 - \nu_2) + (5 + \nu_1)k}{(1 + 2k)^2 - [\nu_2 + (1 - \nu_1)k]^2} \quad (4.4)$$

For generalised bending of a thin linear elastic plate with a circular linear elastic inclusion Bert [45] gives the stresses in and around the inclusion:

$$\left. \begin{aligned} \frac{M_{1rr}}{M_0} &= (1 + \nu_1)a_1 - \frac{(1 - \nu_1)A_1}{2} \rho^{-2} + [(1 - \nu_1)b_1 - 2B_1\nu_1\rho^{-2} + 3C_1(1 - \nu_1)\rho^{-4}] \cos(2\theta) \\ \frac{M_{1\theta\theta}}{M_0} &= (1 + \nu_1)a_1 + \frac{(1 - \nu_1)A_1}{2} \rho^{-2} + [-(1 - \nu_1)b_1 - 2B_1\nu_1\rho^{-2} - 3C_1(1 - \nu_1)\rho^{-4}] \cos(2\theta) \\ \frac{M_{1r\theta}}{M_0} &= (1 - \nu_1)(-b_1 + B_1\rho^{-2} + C_1\rho^{-4}) \sin(2\theta) \end{aligned} \right\} \rho \geq 1 \quad (4.5)$$

$$\left. \begin{aligned} \frac{M_{2rr}}{M_0} &= k[A_2(1 + \nu_2) + B_2(1 - \nu_2)\cos(2\theta)] & , & \quad \frac{M_{2xx}}{M_0} = k[A_2(1 + \nu_2) + B_2(1 - \nu_2)] \\ \frac{M_{2\theta\theta}}{M_0} &= k[A_2(1 + \nu_2) - B_2(1 - \nu_2)\cos(2\theta)] & , & \quad \frac{M_{2yy}}{M_0} = k[A_2(1 + \nu_2) - B_2(1 - \nu_2)] \\ \frac{M_{2r\theta}}{M_0} &= k[-B_2(1 - \nu_2)\sin(2\theta)] & , & \quad \frac{M_{2xy}}{M_0} = 0 \end{aligned} \right\} 0 \leq \rho \leq 1 ; \quad (4.6)$$

where:

$$a_1 = \frac{1 + F}{2(1 + \nu_1)} \quad (4.7)$$

$$b_1 = \frac{1 - F}{2(1 - \nu_1)} \quad (4.8)$$

$$A_1 = \frac{1 + F}{1 + \nu_1} \frac{1 + \nu_1 - (1 + \nu_2)k}{1 - \nu_1 + (1 + \nu_2)k} \quad (4.9)$$

$$A_2 = \frac{1 + F}{1 + \nu_1} \frac{1}{1 - \nu_1 + (1 + \nu_2)k} \quad (4.10)$$

$$B_1 = \frac{1 - F}{1 - \nu_1} \frac{1 - \nu_1 - (1 - \nu_2)k}{3 + \nu_1 + (1 - \nu_2)k} \quad (4.11)$$

$$B_2 = \frac{1 - F}{1 - \nu_1} \frac{2}{3 + \nu_1 + (1 - \nu_2)k} \quad (4.12)$$

$$C_1 = \frac{-B_1}{2} \quad (4.13)$$

The stress distributions described by Eqns 4.1 - 4.6 are presented graphically as stress contour plots in Fig. 4.3. Note that the plane stress assumption has been used in each case – the through-thickness stress component is assumed to be zero because the plate is thin. The polar equations of stress have been transformed to show the stresses in the x direction. The Stress Concentration Factor (SCF) indicates the stress relative to the nominal stress, σ_{xx}/σ_0 or M_{xx}/M_0 respectively. The stress distributions are for an infinite plate, though only a quadrant with side length $\rho = 5$ is shown. In every case the stress component σ_{xx} is constant within the inclusion, however the magnitude of this stress changes depending on the load type and loading condition. For in-plane stretching the inclusion SCF is almost unchanged across the different load cases, however its value becomes marginally closer to unity as F decreases. In contrast, for a plate in bending, more extreme values of SCF (*i.e.* further from unity) are seen in the inclusion for decreasing F . For biaxial loading, identical SCF distributions are seen in the plate for both bending and stretching. However, differences in shape and magnitude of the SCF distributions are seen between bending and stretching when $F \neq 1$. While Fig. 4.3 is shown for $k = 2$, these observations hold for all values of k .

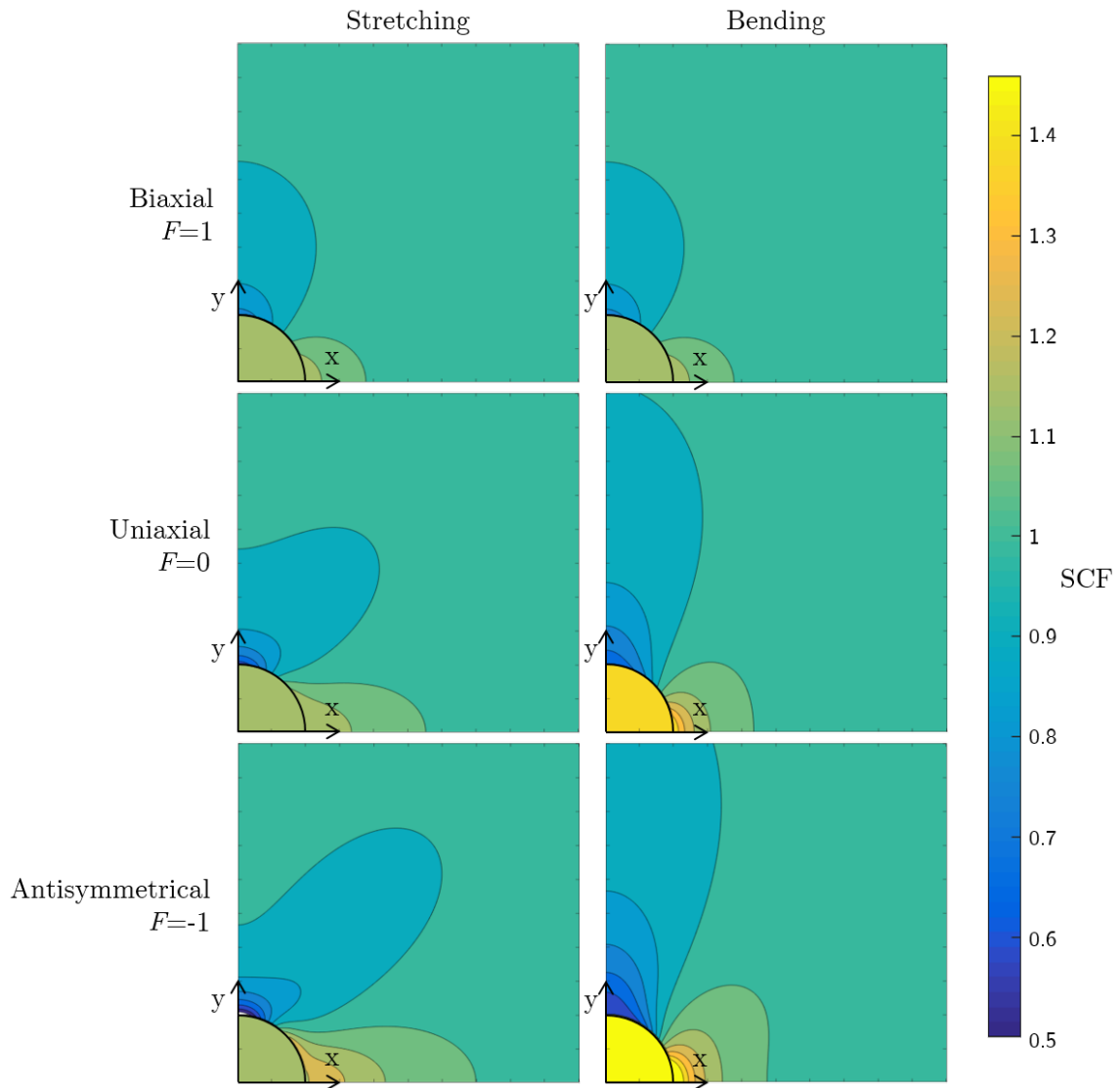


Fig. 4.3 The normalised stress distributions around an inclusion in a thin infinite plate in stretching or in bending are shown for three load conditions, biaxial, uniaxial and antisymmetrical. Transforming the polar expressions in Eqns 4.1 - 4.6, the normalised stresses in the x direction are plotted and shown for $k = 2$. The outline of the inclusion is indicated with a black line in each case.

In general these stress distributions are functions of both radius, r , and in-plane polar angle, θ ; however for the special case of symmetrical loading (biaxial tension or bending where $F = 1$ in Fig. 4.2), the stresses are simply a function of radius. Effectively, we have a one dimensional problem where the stresses, strains and deflections are now solely a function of radius.

Denoting the plate with a “1” subscript, and the inclusion with “2”, the generalised equations for the stress distributions can be simplified in the biaxial case to give:

$$\left. \begin{array}{l} \frac{\sigma_{1rr}}{\sigma_0} = 1 + (K-1)\rho^{-2} \\ \frac{\sigma_{1\theta\theta}}{\sigma_0} = 1 - (K-1)\rho^{-2} \end{array} \right\} \rho \geq 1 \quad \left. \begin{array}{l} \frac{\sigma_{2rr}}{\sigma_0} = K \\ \frac{\sigma_{2\theta\theta}}{\sigma_0} = K \end{array} \right\} 0 \leq \rho \leq 1 \quad (4.14)$$

where:

$$\rho = \frac{r}{a}, \quad k = \frac{E_2}{E_1}, \quad K = \frac{k(2 + 2\nu_2 + (6 - 2\nu_1)k)}{(1 + 2k)^2 - (\nu_2 + (1 - \nu_1)k)^2} \quad (4.15)$$

and σ_0 is the far-field stress amplitude.

This is a significant simplification of the general equations, and additionally, since both bending and in-plane tension offer equivalent stress distributions, we shall now proceed in terms of in-plane tension only: the results obtained are equally applicable to biaxial bending, replacing force per unit length for moment per unit length, strain for curvature and displacement for rotation.

From Eqns 4.14 the stresses in the plate outside of the inclusion tend towards σ_0 with the inverse square of the normalised radius. Using the stress distributions from Eqn. 4.14 and Hooke's Law, the corresponding strains in the plate and in the inclusion for linear elastic behaviour are:

$$\frac{\epsilon_{1rr}}{\epsilon_0} = 1 + \frac{(1 + \nu_1)}{(1 - \nu_1)}(K-1)\rho^{-2} = 1 + \epsilon^*\rho^{-2} \quad \frac{\epsilon_{2rr}}{\epsilon_0} = \frac{K(1 - \nu_2)}{k(1 - \nu_1)} = 1 - \epsilon^* \quad (4.16)$$

$$\frac{\epsilon_{1\theta\theta}}{\epsilon_0} = 1 - \frac{(1 + \nu_1)}{(1 - \nu_1)}(K-1)\rho^{-2} = 1 - \epsilon^*\rho^{-2} \quad \frac{\epsilon_{2\theta\theta}}{\epsilon_0} = \frac{K(1 - \nu_2)}{k(1 - \nu_1)} = 1 - \epsilon^* \quad (4.17)$$

where:

$$\epsilon_0 = \frac{\sigma_0(1 - \nu_1)}{Et} \quad \epsilon^* = \frac{(1 + \nu_1)}{(1 - \nu_1)}(K-1) \quad (4.18)$$

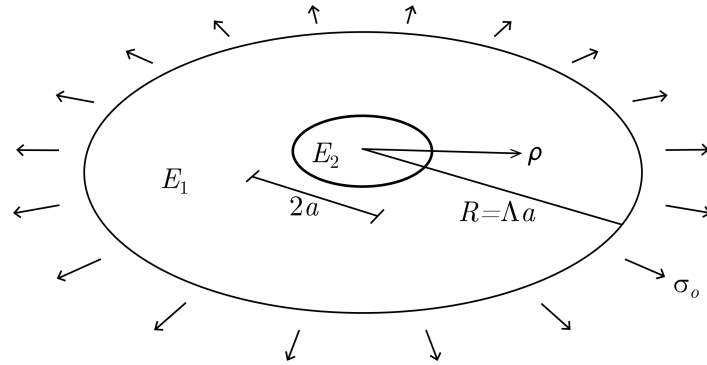


Fig. 4.4 A circular elastic inclusion in a circular plate of a finite size R under biaxial tension. The plate has a unit thickness.

Note that in the case where the Poisson's ratios of the inclusion and the plate are equal, $\nu_1 = \nu_2 = \nu$, the inclusion stress factor, K , and consequently ε^* , can be simplified to give:

$$K = \frac{2k}{(1-\nu) + (1+\nu)k} \quad \varepsilon^* = \frac{(1+\nu)(k-1)}{(1-\nu) + (1+\nu)k} \quad (4.19)$$

We can now either integrate the radial strains or use the identity $\delta_{rr} = r \varepsilon_{\theta\theta}$ to find the radial displacement in the plate, δ_{rr} , as a function of ρ :

$$\delta_{rr} = a\varepsilon_0 \left(\rho - \frac{\varepsilon^*}{\rho} \right) \quad (4.20)$$

The radial stiffness of a finite circular plate, Fig. 4.4, is defined to be the applied load divided by the radial extension at the edge of the plate. Given that the inclusion acts as a stress concentrator and the stresses decay towards unity with increasing distance away from the inclusion, if we assume that the boundary ($\rho = \Lambda$) of a finite plate is large enough so that stresses are not significantly changed from the infinite plate case, using the radial displacement function of the infinite plate (Eqn 4.20), we can calculate approximately the stiffness of the finite plate:

$$\psi_{\text{infinite}} = \frac{2\pi R\sigma_0}{a\varepsilon_0 (\Lambda - \varepsilon^*/\Lambda)} \quad (4.21)$$

The radial stiffness of a circular homogeneous plate, of the same material parameters and thickness, but without an inclusion is:

$$\psi_0 = \frac{2\pi R\sigma_0}{a\varepsilon_0 \Lambda} \quad (4.22)$$

Thus the normalised stiffness, Ψ , is found by dividing by the stiffness of the inclusion plate by the stiffness of the homogeneous plate:

$$\frac{\Psi_{\text{infinite}}}{\Psi_0} = \Psi_{\text{infinite}} = \frac{\Lambda^2}{\Lambda^2 - \varepsilon^*} = 1 + \frac{\varepsilon^*}{\Lambda^2 - \varepsilon^*} \quad (4.23)$$

Finite plate behaviour

If the actual stress distribution in a finite plate is known (rather than approximating it with the infinite plate stress distribution), the stiffness calculation can be further improved. An elegant approach is to take a free body cut around a plate of a finite radius ($\rho = \Lambda$) within the infinite plate case. From Eqn 4.14 we know that the stress at the free body edge is $\sigma_0(1 + (K - 1)\rho^{-2})$. We now scale down the entire stress field in order to arrive at a radial stress of σ_0 on the external boundary. Thus, the stresses in the finite plate case are exactly the stresses from the infinite plate case scaled down by the factor $1 + (K - 1)\Lambda^{-2}$. The overall stiffness now increases by this same factor *i.e.*

$$\Psi_{\text{finite}} = \left(\frac{\Lambda^2}{\Lambda^2 - \varepsilon^*} \right) \left(1 + \frac{K - 1}{\Lambda^2} \right) \quad (4.24)$$

Elastic smeared modulus

Alternatively, we can approximate the normalised stiffness by calculating a smeared Young's modulus using the relative area of each material. The two most natural ways are to take an arithmetic average or a harmonic average:

$$E_{\text{arithmetic}} = \frac{(\pi a^2)E_2 + \pi(R^2 - a^2)E_1}{\pi R^2} = E_1 \left(1 + \frac{k - 1}{\Lambda^2} \right) \quad (4.25)$$

$$E_{\text{harmonic}} = \frac{\pi R^2}{(\pi a^2)/E_2 + \pi(R^2 - a^2)/E_1} = E_1 \left(1 + \frac{1 - 1/k}{\Lambda^2 - 1 + 1/k} \right) \quad (4.26)$$

The arithmetic average is equivalent to finding the average stiffness of a set of structural elements; consider a set of springs in parallel. The harmonic average is equivalent to finding the average flexibility of a set of structural elements; consider a set of springs in series. The limiting behaviour of ε^* can be easily verified from Eqn 4.19 when the modular ratio, k , takes extreme values of 0 and ∞ . The normalised stiffnesses using the infinite plate stress

distributions, Ψ_{infinite} from Eqn 4.23, then become:

$$k \rightarrow 0, \quad \varepsilon^* \rightarrow \approx k - 1; \quad \Psi_{\text{infinite}} = 1 + \frac{\varepsilon^*}{\Lambda^2 - \varepsilon^*} \rightarrow 1 + \frac{k - 1}{\Lambda^2} \quad (4.27)$$

$$k \rightarrow \infty, \quad \varepsilon^* \rightarrow 1 - \frac{1}{k}; \quad \Psi_{\text{infinite}} = 1 + \frac{\varepsilon^*}{\Lambda^2 - \varepsilon^*} \rightarrow 1 + \frac{1 - 1/k}{\Lambda^2 - 1 + 1/k} \quad (4.28)$$

These indicate that the normalised stiffness calculated using infinite plate stress distributions is equivalent to the harmonic smeared Young's modulus when the inclusion is rigid; however, when the inclusion is much less stiff and “approaches” a hole, it is close to the arithmetic average. As the harmonic and arithmetic averages are known provide upper and lower bounds for smeared homogenised stiffness, it is helpful to verify that the infinite plate method estimates an intermediate value for stiffness for intermediate values of k , and tends towards these upper and lower bound for extreme values of k .

4.5.2 Patterns of inclusions

Inscribed tile stiffness

Consider a large plate with a pattern of inclusions. Around each inclusion we can draw the “tile” – the patch of plate associated with the inclusion. For a regular hexagonal pattern, the tile is a hexagon, as shown in Fig. 4.5; more generally, the tile, also known as a “Voronoi cell” [55], of a given inclusion is the region of plate which is closer to the centre of that inclusion than to any other. For a sparse pattern with large distances between each inclusion, it is reasonable to consider each tile as a finite plate with a single inclusion at the centre and the far field stress, σ_0 , at its edge. Approximating the tile with an appropriate finite circular plate allows us to use the results of Section 4.5.1 to estimate the overall stiffness of the patterned plate.

Taking the inscribed circle of the tile, we can use Eqn 4.24 to calculate the stiffness of a plate of this radius for an overall stiffness of the patterned plate. Taking the separation between the edges of two adjacent inclusions, see Fig. 4.5, and normalising by the inclusion radius, we find a non-dimensional measure of the separation of inclusions, which we denote as the “gap-ratio”. For the hexagonal pattern the inscribed circle of the tile has radius, Λ equal to: $1 + (\text{gap-ratio}/2)$.

$$\text{gap-ratio} = \frac{\text{Separation between edges of adjacent inclusions}}{\text{Radius of inclusions}} \quad (4.29)$$

The finite plate method also gives a prediction for the stress concentration factor inside the inclusions. Dividing the uniform stress inside the inclusion for an infinite plate from

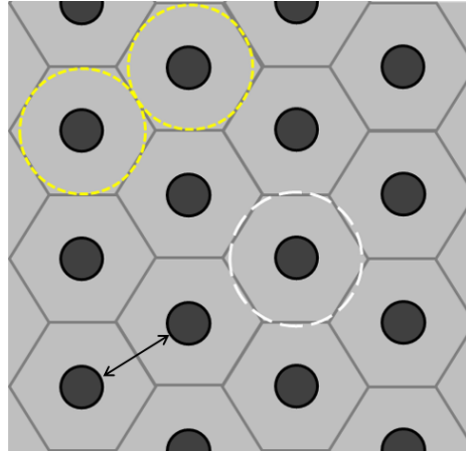


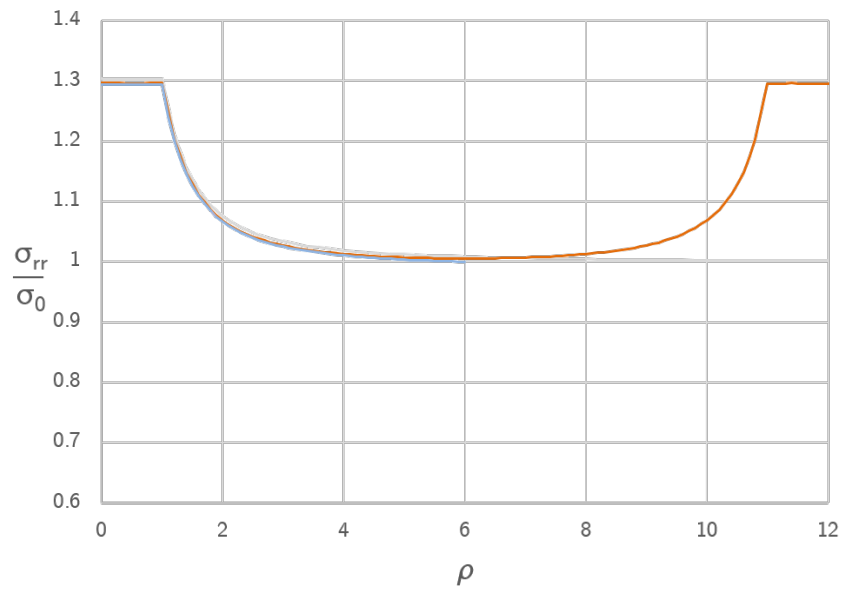
Fig. 4.5 A regular hexagonal pattern of inclusions. The outlines of the hexagonal “tiles” of each inclusion are shown in grey. Two adjacent finite circular plates inscribed by the tiles are shown (short-dashed line). An adjusted size of finite circular plate, of the same area as one hexagonal tile is shown using a long-dashed line. The separation between the edges of two adjacent inclusions is shown with the black arrow. The gap-ratio of the pattern is equal to the separation divided by the inclusion radius.

Eqn 4.14, by the finite plate factor from Section 4.5.1 and substituting for K from Eqn 4.19, we obtain Eqn 4.30:

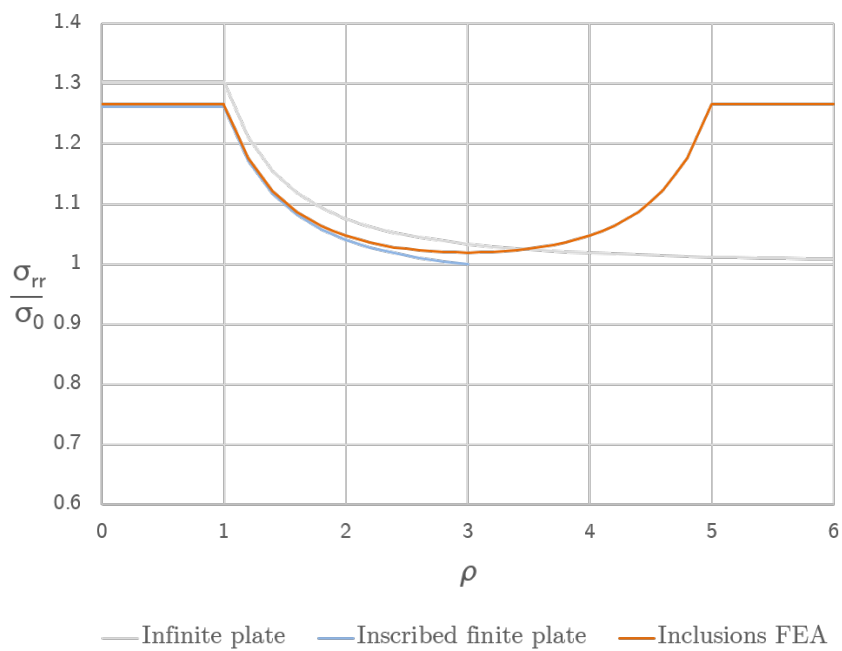
$$\text{SCF} = \frac{K}{1 + (K - 1)\Lambda^{-2}} = \frac{2k}{k(1 + \nu) + (1 - \nu) + (k - 1)(1 - \nu)\Lambda^{-2}} \quad (4.30)$$

When the gap-ratio is large and thus when there is a large spacing between inclusions, assuming each tile to behave like a finite plate with the radius of the inscribed circle should be a good assumption. However, when there is close spacing then the stress distributions around the inclusions will start to interact with each other, and the stresses will no longer decay away to unity at the midpoint between inclusions, *i.e.* at the edge of the assumed finite plate. Therefore we expect that while the Finite Plate Theory of Section 4.5.1, using the inscribed tile circle, should predict the stresses and thus stiffness of the patterned plate very well for large gap-ratios, it will be less accurate as gap-ratios become smaller.

Figure 4.6 compares the stress distribution around an inclusion in an infinite plate and that around an inclusion in a finite plate, Fig. 4.4, of radius equal to that of the inscribed tile radius, to the stresses found from FEA of a regular hexagonal pattern of inclusions under biaxial loading. The radial stresses are plotted along the line that joins the centers of two adjacent inclusions for two different gap-ratios. When the gap-ratio is large, Fig. 4.6a, the inscribed finite plate gives an excellent prediction, and as the finite plate factor is very small, the infinite plate stresses are also a good approximation. For a moderate gap-ratio, Fig. 4.6b,



(a)



(b)

Fig. 4.6 The normalised radial stress distributions for a biaxially loaded plate with a hexagonal pattern of inclusions, $k = 3$, along the line connecting two inclusion centers. Stresses calculated assuming a plate of infinite size, Eqn 4.14, and for an inscribed finite plate from Section 4.5.1, are compared to FEA. (a) gap-ratio = 10; (b) gap-ratio = 4.

the infinite plate stress, Eqn 4.14, no longer provides a good approximation. The inscribed finite plate theory predicts the stress inside the inclusion ($\rho < 1$) very well and provides a good approximation of the stresses in the rest of the plate. The main discrepancy seen is at the midpoint between inclusions, where though the inscribed finite plate predicts a radial stress of exactly σ_0 by definition, the FEA of the patterned inclusions suggests a stress slightly higher than unity.

Considering the symmetry of a regular hexagonal pattern of inclusions, we expect that there should be a point of zero gradient in the stress distribution at the midpoint between adjacent inclusions. Mirroring the inscribed finite plate radial stress distribution in Fig. 4.6b, would however create a discontinuity in stress gradient, and this clearly should not be the case as there is no geometric or material feature at this point in the plate to cause it. Both radial and circumferential stresses should have zero gradient at the midpoint between adjacent inclusions due to symmetry, Fig. 4.7, but not necessarily a value of radial stress equal to σ_0 . Thus instead of finding a stress distribution in a finite plate which has a radial stress of σ_0 at its edge, we could seek a solution which has zero stress gradient for both radial and circumferential stresses, *i.e.*

$$\left. \frac{d\sigma_{rr}}{dr} \right|_{r=R} = 0 \qquad \left. \frac{d\sigma_{\theta\theta}}{dr} \right|_{r=R} = 0 \qquad (4.31)$$

Still considering axisymmetric solutions around a circular inclusion in a finite plate we can use an Airy's stress function to derive a general solution for stresses. Then relaxing the boundary condition that the stress should be equal to σ_0 at $r = R$, but enforcing the two zero stress gradient boundary conditions, Eqns 4.31, find a particular solution. Solving the biharmonic equation requires a biharmonic function, and restricting ourselves to an axisymmetric function which is solely a function of r , the general Airy's stress function is:

$$\Phi = c_0 + c_1 r^2 + c_2 r^2 \ln r + c_3 \ln r \qquad (4.32)$$

and thus:

$$\sigma_{rr} = \frac{1}{r} \frac{\partial \Phi}{\partial r} + \frac{1}{r^2} \frac{\partial^2 \Phi}{\partial \theta^2} = 2c_1 + c_2(1 + 2 \ln r) + \frac{c_3}{r^2} \qquad (4.33)$$

$$\sigma_{\theta\theta} = \frac{\partial^2 \Phi}{\partial r^2} = 2c_1 + c_2(3 + 2 \ln r) - \frac{c_3}{r^2} \qquad (4.34)$$

where c_0, c_1, c_2 and c_3 are arbitrary constants. Calculating the stress gradients at $r = R$:

$$\left. \frac{d\sigma_{rr}}{dr} \right|_{r=R} = \frac{2c_2}{R} - \frac{2c_3}{R^3} = 0 \quad (4.35)$$

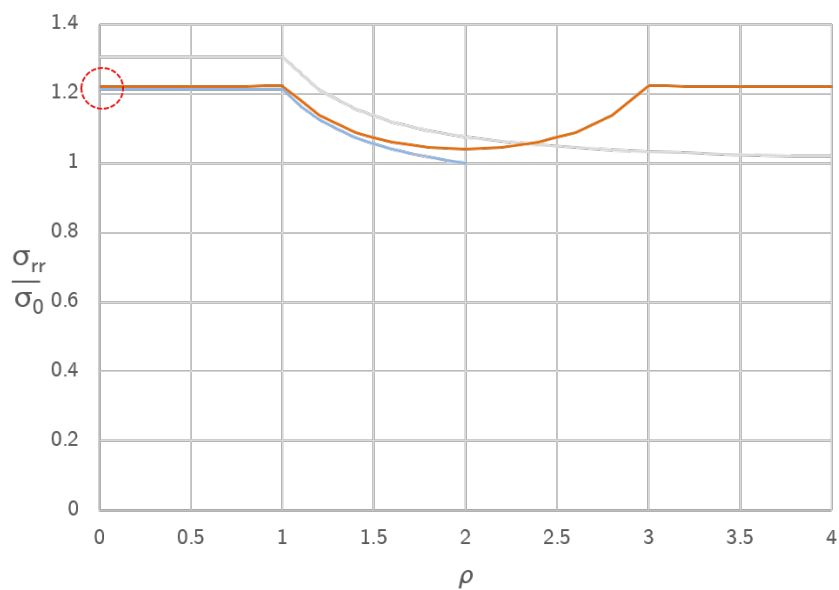
$$\left. \frac{d\sigma_{\theta\theta}}{dr} \right|_{r=R} = \frac{2c_2}{R} + \frac{2c_3}{R^3} = 0 \quad (4.36)$$

thus $c_2 = c_3 = 0$. Hence it is also impossible to enforce the zero stress gradient boundary conditions, except in the trivial case of a constant uniform stress everywhere. As the Airy's stress function was as general as it could be in axisymmetry, we conclude that there is no suitable axisymmetric stress function for a finite circular plate which will correctly display the zero stress gradient conditions which we know must exist in a regular pattern of inclusions due to symmetry.

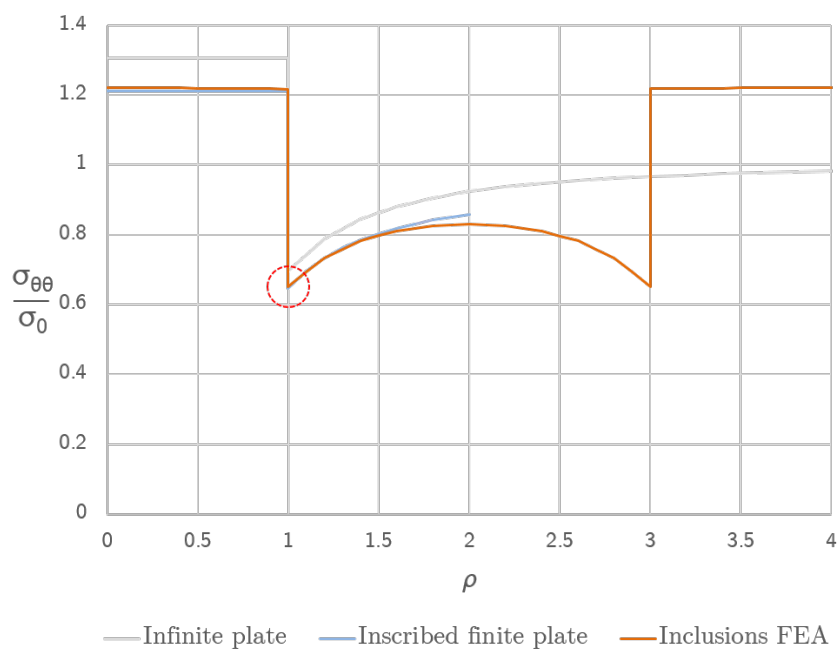
Superposition and scaling method

Comparing the inscribed finite plate stresses to the FEA hexagonally patterned inclusions stresses in Fig. 4.7, we notice that for such a small gap-ratio the stresses are approximated even less well. However, we notice that even for such a small gap-ratio there are two points which seem to be predicted very well: the radial stress at the centre of the inclusion and the circumferential stress just outside the inclusion, highlighted by red circles on Fig. 4.7a and Fig. 4.7b respectively. Note also that the stresses in the inclusions are no longer completely constant for such a small gap-ratio: the radial stress increases slightly towards the edge of the inclusion whereas the circumferential stress becomes fractionally lower. This observation can be explained by considering that when very close together, the decaying stress from one inclusion is not quite negligible when it reaches the adjacent inclusion, and thus the effect of this interaction is seen as a slight variation in the otherwise constant internal inclusion stress. Indeed, considering superposing two identical stress distributions, each emanating from the centre of adjacent inclusions, would also be guaranteed to give a zero stress gradient at the midpoint, as desired. Choosing a stress distribution which has radial stress which reaches σ_0 at the centre of the adjacent inclusion is one such option and allows relatively easy calculation analytically: such a finite plate thus has twice the radius of the inscribed finite plate.

Given that a homogeneous plate has a constant stress of σ_0 , and the inclusions cause deviations about this value, when considering superposing different stress distributions together it is the differences in stresses from σ_0 which need to be considered, see Eqn 4.37. In this way we can see that the stress distributions of other, more distant inclusions, will have a negligible effect, as these will have decayed away to almost exactly σ_0 , and so their contribution will be negligible. Where two stress states A and B are to be superposed:



(a)



(b)

Fig. 4.7 The normalised stress distributions for a biaxially loaded plate with a hexagonal pattern of inclusions, gap-ratio = 2, $k = 3$, along the line connecting two inclusion centers. Stresses calculated assuming a plate of infinite size, Eqn 4.14, and for an inscribed finite plate from Section 4.5.1, are compared to FEA. (a) Radial stresses; (b) Circumferential stresses.

$$\sigma_{\text{superposition}} = (\sigma_A - \sigma_0) + (\sigma_B - \sigma_0) + \sigma_0 \quad (4.37)$$

Figure 4.8 plots the finite plate stress distributions around two adjacent inclusions, where the assumed radius of each finite plate is equal to the centre to centre (c.t.c) distance between the inclusions. The resulting superposition of stresses is also plotted in Fig. 4.8. For both the radial and circumferential stresses, the shape of the resulting superposed distribution is similar to that found from the FEA of hexagonally patterned inclusions. However, particularly for the radial stresses, the magnitude of the stresses do not match that well to FEA. We know that the inscribed finite plate gave a very good approximation to the radial stress at the centre of an inclusion, so we can scale down the superposed stress by a constant factor everywhere such that the stress at the centre of the inclusion is as per the inscribed finite plate prediction, Fig. 4.8a. This superposed and scaled distribution of radial stresses is shown in Fig. 4.8a. For the circumferential stresses such a scaling will not be appropriate. Considering equilibrium, we know that the average circumferential stress must be equal to σ_0 . Consider a free body cut which passes through the centre of a row of inclusions, such as a vertical line through Fig. 4.5, as the far field stress perpendicular to this cut is σ_0 , so also the perpendicular stresses at this cut must have an average value equal to σ_0 to maintain equilibrium. Therefore any scaling which we apply to the circumferential stresses should not change the average stress from the value of σ_0 . Therefore we shall apply a scaling factor only to the difference from σ_0 , and therefore the average stress will remain unchanged. The scaling factor is chosen to match the superposition stress to the inscribed finite plate stress just outside the inclusion, as per Fig. 4.7b. The scaled superposition stress distributions are plotted in Fig. 4.8 and comparison to FEA is extremely good. While this method of scaling the superposed stresses is somewhat physically dubious and not entirely justifiable, *e.g.* the compatibility of strains no longer exactly holds, it does capture the stress distribution remarkably well, even for very small gap-ratios such as 0.5. Of course, being able to accurately predict the radial and circumferential stresses allows for the calculation of the resulting strains and therefore displacements. The radial strain is given by $\epsilon_{rr} = (\sigma_{rr} - \nu\sigma_{\theta\theta})/E$, and integrating the radial strain gives the radial displacement. From the displacement we can thus calculate an overall normalised stiffness. Even considering the simpler case of $\nu_1 = \nu_2 = \nu$, the analytical derivation is quite algebraically long (see Appendix B.1), but the final result is given here:

$$\Psi_{ss} = 1 \div \left[1 - \frac{2(k-1)}{kd} + \frac{2(k-1)}{c_a d^3 (d-1)} \left([d^3 - 4.5d^2 + 7.5d + 5] + \frac{1}{k} [d^3 - d^2 - 6d + 5] + \nu c_b [d^3 - d^2 - 3d + 2] \frac{k-1}{k} \right) \right] \quad (4.38)$$

where d is the centre to centre distance between adjacent inclusions, $c_a = k(1 + \nu) + (1 - \nu) + (k-1)(1 - \nu)(d/2)^{-2}$ and $c_b = \frac{1+(d/2)^{-2}}{1+(d-1)^{-2}+2d^{-2}}$.

As the stresses are predicted so accurately by this scaled superposition analysis, so too are the strains and displacements and thus the overall stiffness calculated will be a very good approximation for a plate of hexagonally patterned inclusions.

Finite Plate Theory

As an alternative to the accurate, though lengthy, predictions of stresses around patterns of inclusions using the superposition and scaling method, it is possible to extract another prediction of behaviour by using the analysis of a finite plate. While the inscribed tile theory worked well, using a radius $\Lambda = 1 + \text{gap-ratio}/2$, another choice is to choose a radius which gives the finite plate the same area as the tile of the inclusion. This adjusted size of finite circular plate is shown as a dashed white circle in Fig. 4.5. For a regular hexagonal pattern a circle with equal area to the tile has a radius $\Lambda = \sqrt{(2\sqrt{3}/\pi)}(1 + \text{gap-ratio}/2)$.

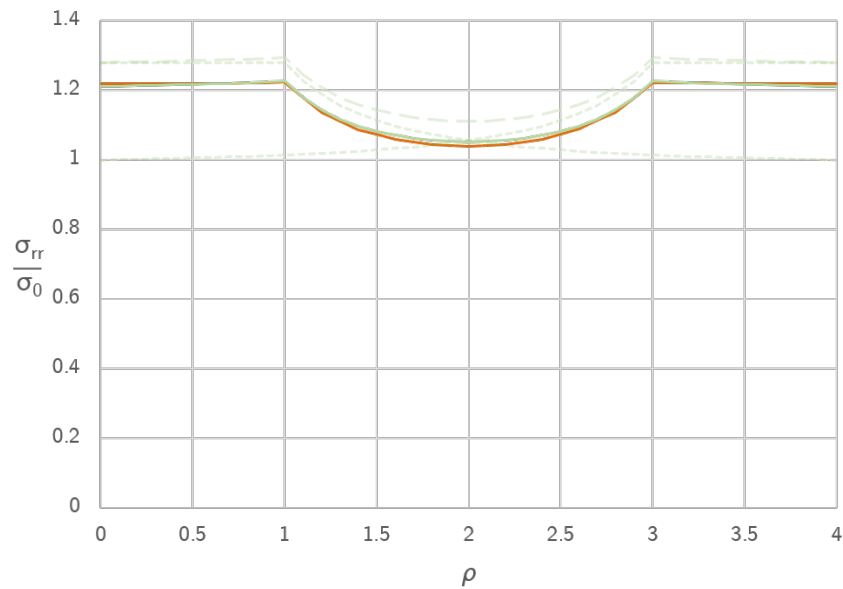
Calculating the radius of such a circle for the tile of any regular pattern, we find that the value can be neatly written as $\Lambda = \sqrt{1/p}$, where p is the proportion of the area of the total plate which is inclusions. This is helpful as it makes the resulting calculations of normalised stiffness and of inclusion SCFs independent of the gap-ratio between inclusions. Substituting $\Lambda = \sqrt{1/p}$ into Eqn 4.24:

$$\Psi_{\text{FPT}} = \left(\frac{1}{1 - p\varepsilon^*} \right) (1 + (K-1)p) \quad (4.39)$$

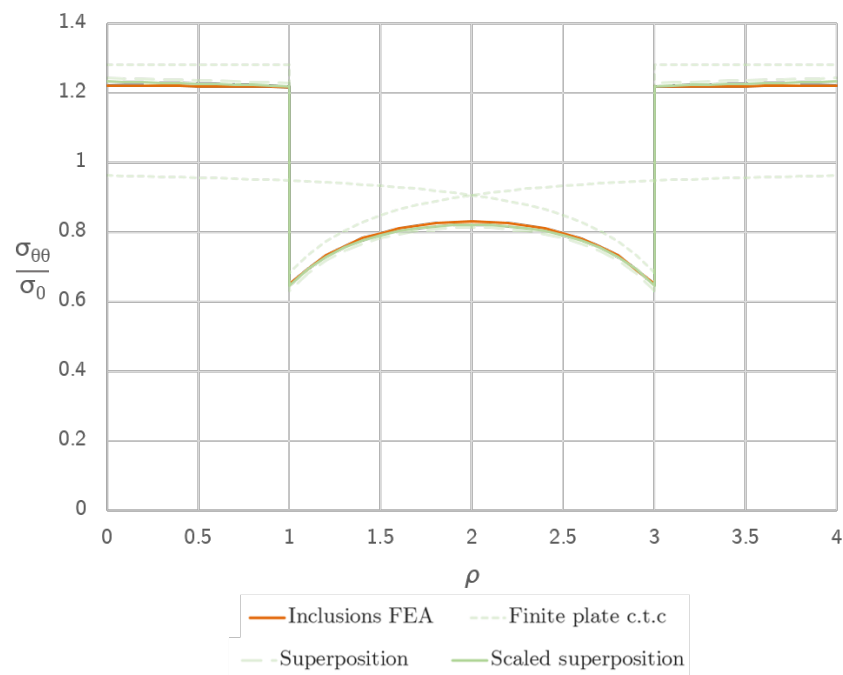
When the plate and inclusion have the same Poisson's ratio, $\nu_1 = \nu_2 = \nu$, substituting in K and ε^* from Eqn 4.19, yields a remarkably simple form:

$$\Psi_{\text{FPT}} = \frac{2k - (1-p)(k-1)(1-\nu)}{2 + (1-p)(k-1)(1+\nu)} \quad (4.40)$$

Similarly the SCF inside the inclusion, from Eqn 4.30, is given by:



(a)



(b)

Fig. 4.8 Stress distributions for a finite plate which has a diameter equal to the centre to centre (c.t.c) distance between inclusions. These stresses are superposed together and then the superpositioned stresses are scaled to correspond with the stresses at the two key locations identified in Fig. 4.7.

$$\text{SCF}_{\text{FPT}} = \frac{K}{1 + (K-1)p} = \frac{2k}{k(1+\nu) + (1-\nu) + (k-1)(1-\nu)p} \quad (4.41)$$

Using the normalised stiffness, an expression for the effective overall Young's modulus of an inclusion patterned plate.

$$E_{\text{FPT}} = E_1 \Psi_{\text{FPT}} = E_1 \left(\frac{1}{1 - p\varepsilon^*} \right) (1 + (K-1)p) \quad (4.42)$$

Similarly, by considering the stresses predicted by the Finite Plate Theory inside the inclusion and in the plate at the inclusion interface, a prediction can be made of when first yield will occur. In general the plate and the inclusion may have different material values of yield stress, σ_{Y1} and σ_{Y2} respectively. First yield could occur in either the inclusion or the plate, and thus both possibilities must be checked.

In the inclusion the radial and circumferential stress are equal to $(\sigma_0 K)/(1 + (K-1)p)$; the through-thickness stress, σ_{tt} , is equal to zero due to the plane stress assumption of a thin plate. Thus according to both Tresca and von Mises criterion, first yield will occur when $(\sigma_0 K)/(1 + (K-1)p)$ is equal to σ_{Y2} . Consequently the effective yield stress of the overall plate, when governed by inclusion yielding, is:

$$\sigma_{Y_{\text{FPT}}} = \sigma_{Y2} \frac{1 + (K-1)p}{K} \quad (4.43)$$

The maximum stresses in the plate are found at the inclusion/plate interface. Considering the stresses in the plate at the interface, $\rho = 1$, we find:

$$\frac{\sigma_{1rr}}{\sigma_0} = \frac{K}{1 + (K-1)p} \quad \frac{\sigma_{1\theta\theta}}{\sigma_0} = \frac{2-K}{1 + (K-1)p} \quad \frac{\sigma_{1tt}}{\sigma_0} = 0 \quad (4.44)$$

Using a Tresca criterion, first yield will occur when the maximum difference between any pair of principle stresses is equal to σ_{Y1} . For a stiff inclusion, $K > 1$, $\sigma_{1\theta\theta}$ is positive and thus $\sigma_{Y1} = \sigma_{1rr} - \sigma_{1tt}$. For a soft inclusion, $K < 1$, $\sigma_{1\theta\theta}$ is negative and thus $\sigma_{Y1} = \sigma_{1rr} - \sigma_{1\theta\theta}$.

$$\text{When } K > 1 \quad \sigma_{Y_{\text{FPT}}} = \sigma_{Y1} \frac{1 + (K-1)p}{K} \quad (4.45)$$

$$\text{When } K < 1 \quad \sigma_{Y_{\text{FPT}}} = \sigma_{Y1} \frac{1 + (K-1)p}{2-K} \quad (4.46)$$

Alternatively using von Mises criterion:

$\sigma_Y = \sqrt{0.5[(\sigma_{rr} - \sigma_{\theta\theta})^2 + (\sigma_{rr} - \sigma_{tt})^2 + (\sigma_{\theta\theta} - \sigma_{tt})^2]}$, the effective yield stress of the over-

all plate, when governed by plate yielding is:

$$\sigma_{Y_{\text{FPT}}} = \sigma_{Y1} \frac{1 + (K - 1)p}{\sqrt{3K^2 - 6K + 4}} \quad (4.47)$$

Note that when the Poisson's ratio of the inclusion and the plate are equal, $\nu_1 = \nu_2 = \nu$, then the appropriate Tresca regime is easily established as $K > 1$ when $k > 1$ and $K < 1$ when $k < 1$. Additionally, when the inclusion material is stiffer than the plate, $k > 1$, then using the Tresca criterion, the effective yield stress expressions are the same for inside the inclusion and in the plate itself, and can be simplified to give:

$$\sigma_{Y_{\text{FPT}}} = \sigma_Y \frac{(1 - \nu) + (1 + \nu)k + (k - 1)(1 - \nu)p}{2k} \quad (4.48)$$

where σ_Y is the minimum of σ_{Y1} and σ_{Y2} .

4.6 FEA methodology

In order to test the validity and accuracy of the theoretical predictions of the behaviour of an inclusion patterned plate, finite element simulations were conducted using ABAQUS [37]. Linear elastic models were tested in both bending and stretching for a variety of inclusion shapes, patterns and loading conditions. The FEA methodology is set out below.

A square plate has a centred pattern of inclusions and in-plane forces per unit length apply biaxial tension to the edges, see Fig 4.9. Partitioning is used to define the inclusion geometry and pattern and divide the plate into sections and then each section is given the relevant material properties. Using appropriate mirror symmetry conditions, only a quarter of the overall plate needs to be analysed, for computational efficiency. The mesh distribution itself is fine and non-uniform to mitigate mesh sensitivity effects. A sufficiently large number of inclusions are modelled so that edge effects are confined in very narrow bands, much smaller than the plate width: Fig 4.10 clearly shows the edge effects present in the FEA, but confirms that these are reasonably small in magnitude and decay away very quickly. The stresses around the outer row of inclusions in each case have a small but discernible deviation; however, the remainder of the inclusions behave identically to each other. Quadratic shell elements (S8R or STRI65), with 9 through-thickness integration points, are used as their formulation assumes a plane stress condition (zero stress in the through-thickness direction) which allows for a significantly more efficient run time. Selected geometries were modelled using quadratic full 3D stress elements (C3D20R), and these simulations confirmed the validity of using the shell elements. For these models three layers of elements through-

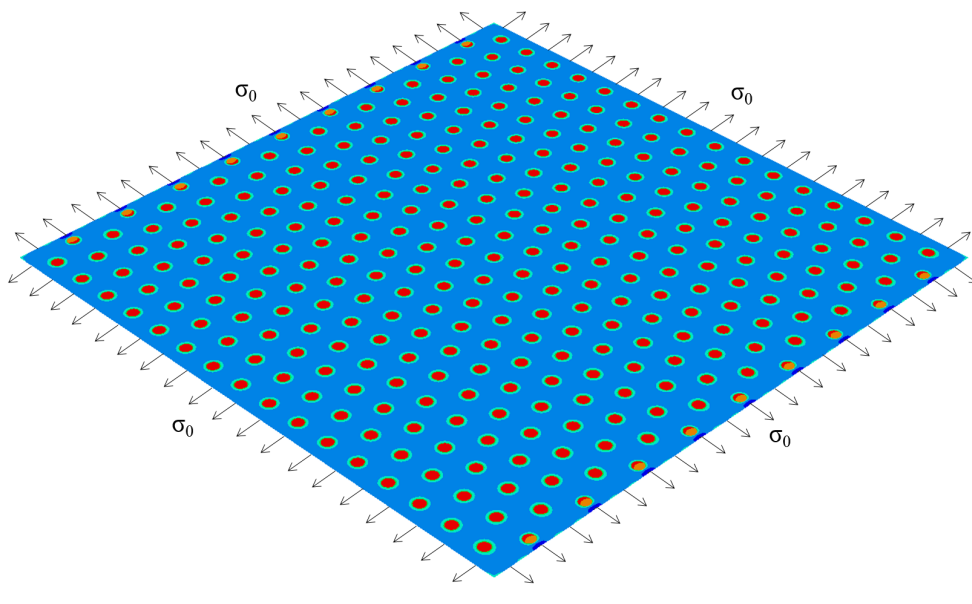


Fig. 4.9 A square plate with a hexagonal pattern of inclusions, modelled in ABAQUS [37]. An equal biaxial loading is applied equal in magnitude to σ_0 . Colour contours of SCF range from [Dark blue, 0.9] to [Red, 1.3]. Here: $k = 3$, $\nu = 0.3$, gap-ratio = 4; thus $p = 0.1008$.

thickness were used, giving a total of 7 through-thickness integration points; the plate thickness was chosen to be either $1/30^{\text{th}}$ or $1/60^{\text{th}}$ of the radius of the inclusions. The quarter plate model, mirrored along symmetry lines to show the full plate in Fig. 4.9, when modelled with quadratic shell elements contains 76574 elements, and correspondingly a total number of degrees of freedom of 1384338. This equates to an inclusion being modelled with approximately 200 elements. A corresponding analysis using solid elements, with the same plan view mesh density, contained 186053 elements and had 2807310 degrees of freedom in the model. The run time for solving the solid element FEA formulation was just over an order of magnitude higher than the shell element FEA model. Selected geometries were also run with finer mesh densities to confirm that convergence had been established.

For the hexagonal pattern the local stress variations in Fig. 4.10a are practically axisymmetric, which underpins this assumption in Section 4.5. In contrast, the stress distributions around inclusions in a square pattern exhibit a distinct four-fold symmetry. For both patterns the stresses inside each inclusion are practically uniform (*c.f.* Eqn 4.14) and SCFs are found by taking the von Mises stress at the middle of a central inclusion and dividing by σ_0 . The plate stiffness can be calculated by considering the displacement at the edge of the plate; alternatively, for a regular pattern we may consider the deformation of the central unit cell. The stress, strain and displacement distributions along a line which connects the centers of adjacent inclusions, Fig. 4.6, can be extracted by using the “path” functionality in

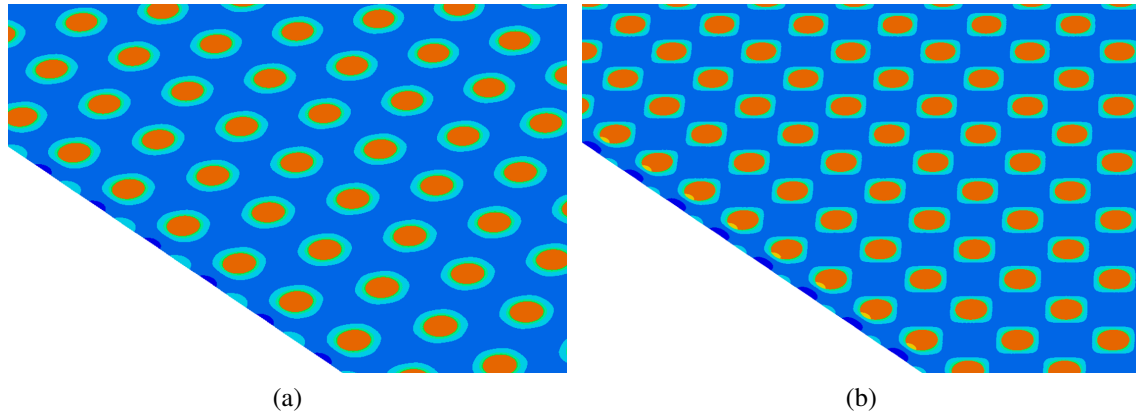


Fig. 4.10 Von Mises stress from FEA for (a) hexagonal pattern, (b) square pattern. The stress distributions in (b) are distinctly less axisymmetric compared to (a). Colour contours of SCF range from [Dark blue, 0.9] to [Red, 1.3].

ABAQUS. The mesh must be partitioned in such a way that the mesh elements are aligned to the intended path: in the case of a regular pattern centered on the plate the quarter model naturally provides such an edge. By modelling just a single inclusion in the centre of a large plate the performance in various states of bending and stretching can be compared against Eqns 4.1–4.6 and validate these theoretical expressions.

4.7 Biaxial loading

4.7.1 Regular patterns

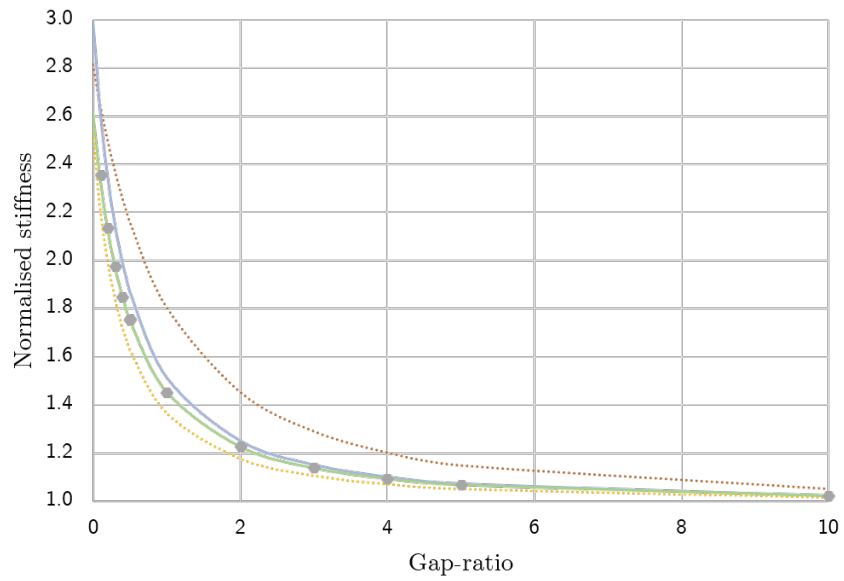
The normalised stiffnesses from Eqns 4.24, 4.25, 4.26, 4.38, 4.40 are compared together in Fig. 4.11 for two different values of inclusion stiffness, k , over a wide ratio of gap-ratios. These are additionally compared to the FEA results of thin plates patterned hexagonally with inclusions. There is close correlation between FEA and the inscribed finite plate stiffness when there is large separation between inclusions that, however, diminishes as the inclusions become closer together. The arithmetic and harmonic approximations provide upper and lower bounds on the overall stiffness, but do not provide such an accurate prediction as the other methods. As expected from the extremely good match between theoretical and FEA stresses in Fig. 4.8, the superposition and scaling method gives a very good prediction of the normalised stiffness of a hexagonally patterned plate when $k > 1$; better than the inscribed finite plate theory. However, when the inclusions are less stiff than the surrounding plate, $k < 1$, while still a very good prediction for large gap-ratios it is poor for small gap-ratios. Using Finite Plate Theory Eqn 4.40, even better agreement with FEA is observed when

the finite plate has an area equal to the hexagonal tile. The agreement is excellent over all gap-ratios and for inclusions which are both more stiff and less stiff than the surrounding plate, $k > 1$ and $k < 1$. Additionally, as well as having a superior prediction for closed spaced soft inclusions, the Finite Plate Theory, Eqn 4.40, has a shorter and less complex expression than the superposition and scaling method, Eqn 4.38.

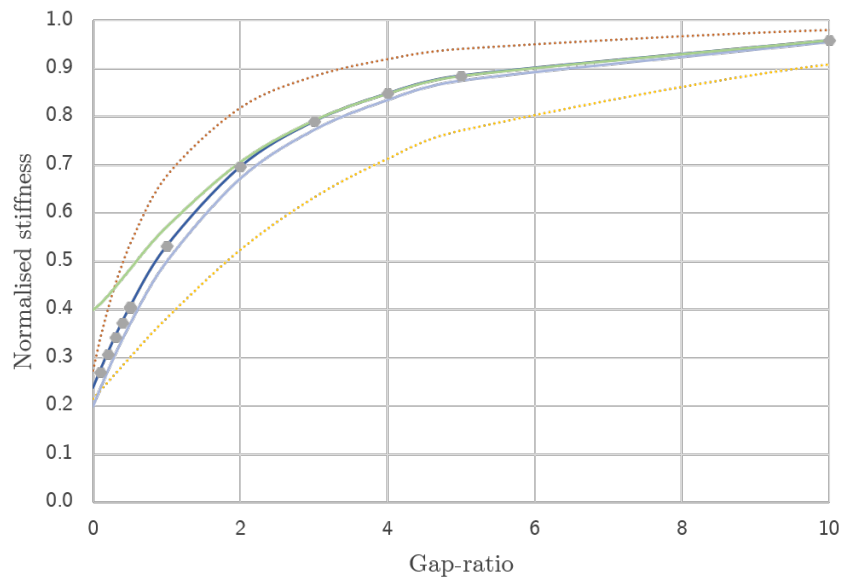
Additionally, the Finite Plate Theory gives a prediction of the SCF inside the inclusions Eqn 4.30. Choosing the inscribed tile radius and the equal tile area radius as values of Λ , predictions of SCF are compared to FEA in Fig. 4.12. The inscribed finite plate theory works well for larger values of gap-ratio, but the Finite Plate Theory (with $\Lambda = \sqrt{1/p}$) is remarkably accurate over the entire range, even for very small gap-ratios.

Noting that when the finite plate is chosen such that it has an equal area to the tile of the pattern, $\Lambda = \sqrt{1/p}$, the normalised stiffness becomes independent of gap-ratio and instead is a function of p , Fig. 4.13 plots the normalised stiffness expressions against p . Figure 4.13a plots the same data as Fig. 4.11a, but shows more clearly the superiority of the Finite Plate Theory compared to both the inscribed finite plate theory and superposition and scaling method. Note that, along with the arithmetic and harmonic smeared averages, the Finite Plate Theory tends to the value of k as p tends to unity – as expected, since the plate would be entirely inclusion material. Additionally we can observe that the inscribed finite plate theory takes a value of k when p is the maximum packing of the pattern *e.g.* when $p = \pi/(2\sqrt{3}) \approx 90.7\%$ for hexagonal packing. This is a consequence of the inscribed finite plate stiffness being equal to k when the gap-ratio is equal to zero. This observation explains why, for a square pattern of circular inclusions, the inscribed finite plate theory predicts a value of k when $p \approx 78.5\%$, Fig 4.13b, and hence why the inscribed finite plate theory does not predict the response of square patterning so well. The same gap-ratios are used in both patterns of FEA but as the square packing is less efficient than hexagonal packing, the values of p are slightly lower. The superposition and scaling method is also seen to be much less accurate when predicting the stiffness of a square pattern of inclusions, however the Finite Plate Theory prediction matches the FEA extremely well.

We conclude therefore that the Finite Plate Theory, Eqn 4.40, provides the best prediction of normalised stiffness of inclusion patterned plates, due to its accuracy over a wide range of gap-ratios, ability to capture behaviour for $k > 1$ and $k < 1$ equally well, and its applicability to both the square and hexagonal pattern. In the following sections FEA results are contrasted in detail against the Finite Plate Theory, and other curves will be omitted for clarity, apart from the smeared average curves which are provided as upper and lower bounds.



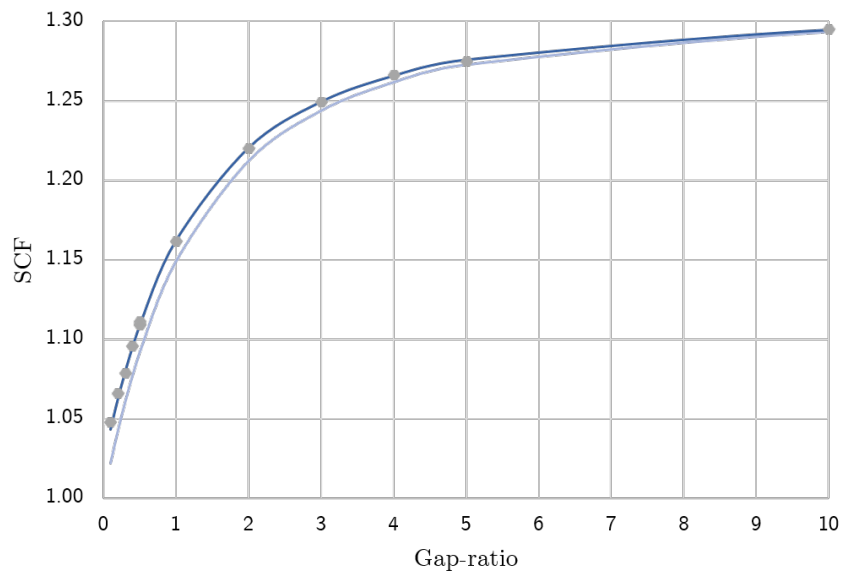
(a)



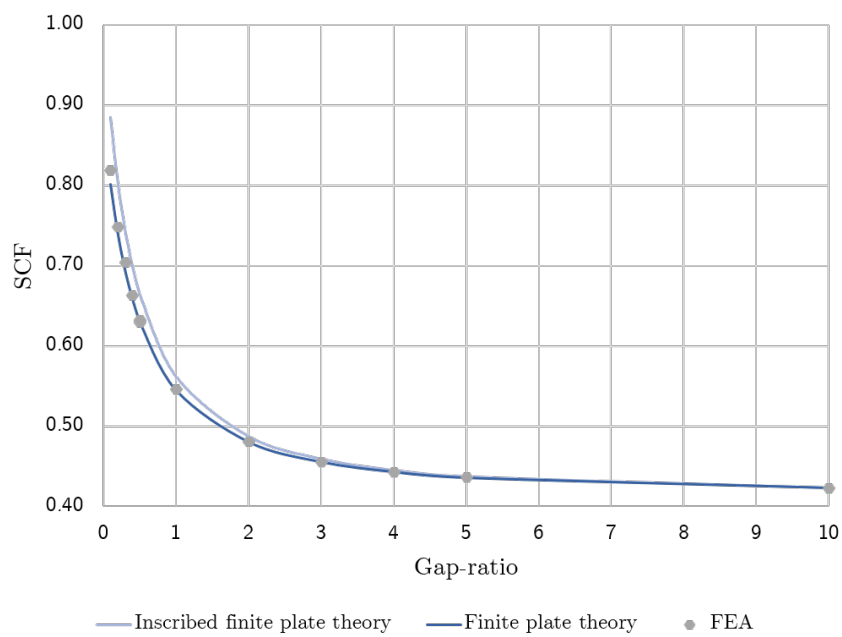
(b)

..... Harmonic smeared average Arithmetic smeared average
— Inscribed finite plate theory — Finite plate theory
— Superposition and scaling ● FEA

Fig. 4.11 Biaxial normalised stiffness for regular hexagonal patterns of inclusions: (a) $k = 3$, $\nu = 0.3$; (b) $k = 0.2$, $\nu = 0.3$.

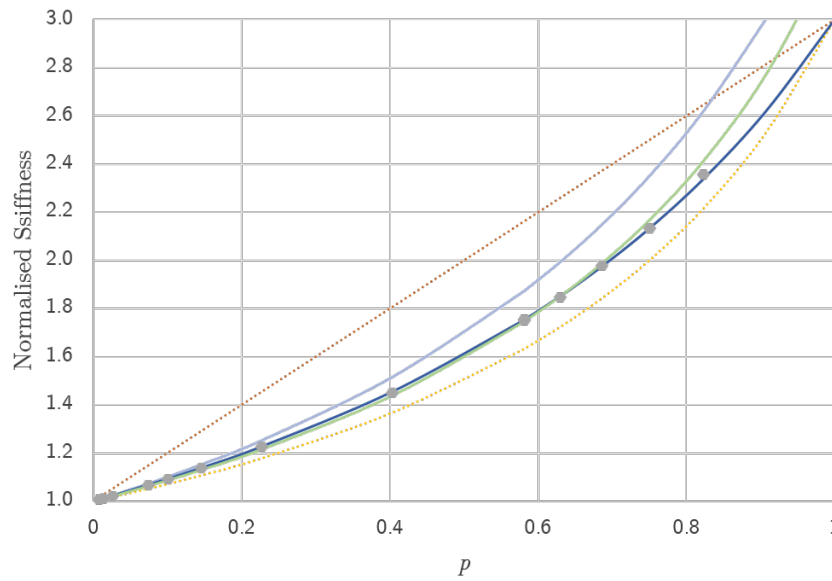


(a)

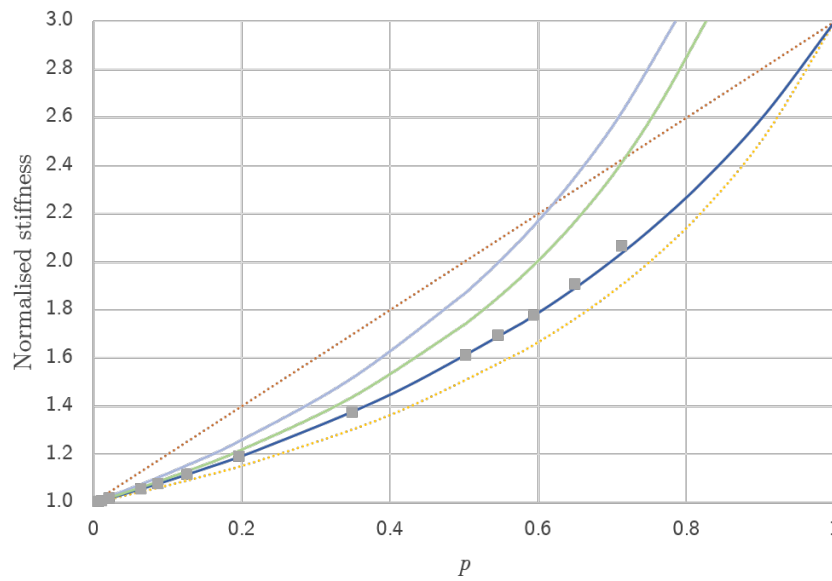


(b)

Fig. 4.12 SCFs of hexagonally patterned inclusions in biaxial tension: (a) $k = 3$, $\nu = 0.3$; (b) $k = 0.2$, $\nu = 0.3$.



(a)



(b)

..... Harmonic smeared average Arithmetic smeared average
 — Inscribed finite plate theory — Finite plate theory
 — Superposition and scaling ■ FEA

Fig. 4.13 Biaxial normalised stiffness for regular patterns of circular inclusions vs p ; $k = 3$ and $\nu = 0.3$: (a) Hexagonal pattern (b) Square pattern.

4.7.2 Extreme material constants

The effect of extreme values of modular ratio, k , is shown in Fig 4.14. When the inclusions are much stiffer than the plate, $k = 10$, the arithmetic smeared average becomes a very poor approximation, Fig. 4.14a. However, the Finite Plate Theory provides an excellent prediction. Figure 4.14b shows the case of $k = 0$, which is equivalent to a hole: thus the plate is effectively “perforated”. Analysis of perforated plates in general are of practical interest in applications such as tube plates of heat exchangers and the grid plates of nuclear reactors [3, 39]. Note that the most significant difference between FEA and theory is for the highest values of p , where the inclusions are extremely close together and separated by only 5% of the inclusion diameter. For low values of p and thence large gap-ratios, the stress distributions can decay to σ_0 between inclusions, whereas this cannot happen for very small gap-ratios.

While values of elastic modulus can take any positive value, allowing for extreme ranges of k from 0 to ∞ , the Poisson’s ratio of any material *must* be within the range $-1 < \nu < 0.5$, and practically all solid non-porous materials have a Poisson’s ratio between 0.1 and 0.5 [56]. Figure 4.15 shows that there is excellent agreement between the variation predicted by Eqn 4.40 with respect to Poisson’s ratio and FEA. While both tend towards limiting values of 1 and k as p goes to 0 and 1 respectively, the lower value of Poisson’s ratio, $\nu = 0.1$, is slightly more stiff for intermediate values of p than the higher Poisson’s ratio value, $\nu = 0.5$.

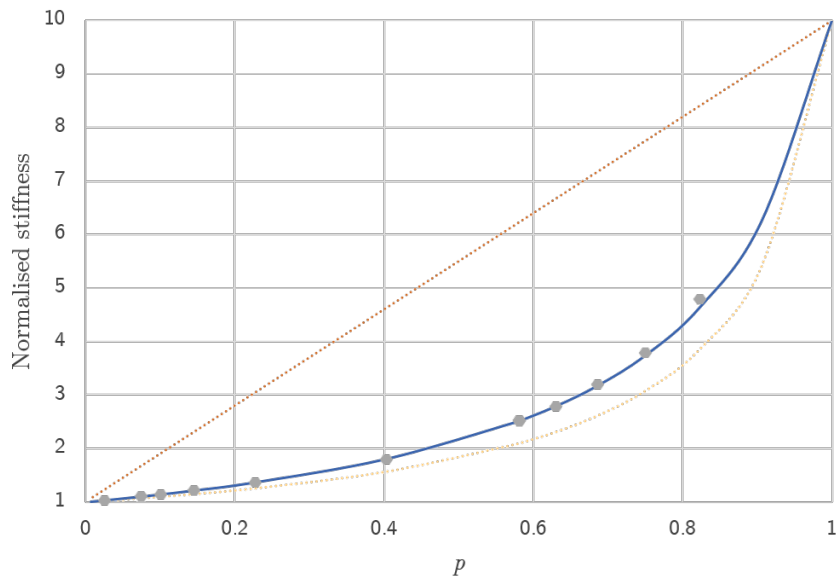
It is interesting to observe the behaviour of the Finite Plate Theory stiffness expression as ν takes the values 1 and -1. When a value of $\nu = -1$ is substituted into Eqn 4.40, the result simplifies to be exactly equal to the arithmetic average. Conversely, when the Poisson’s ratio is increased beyond the physically obtainable upper limit of 0.5, to $\nu = 1$, the Finite Plate Theory simplifies to give the harmonic average:

$$\nu \rightarrow -1; \quad \Psi_{\text{FPT}} \rightarrow (1 - p) + pk \quad (4.49)$$

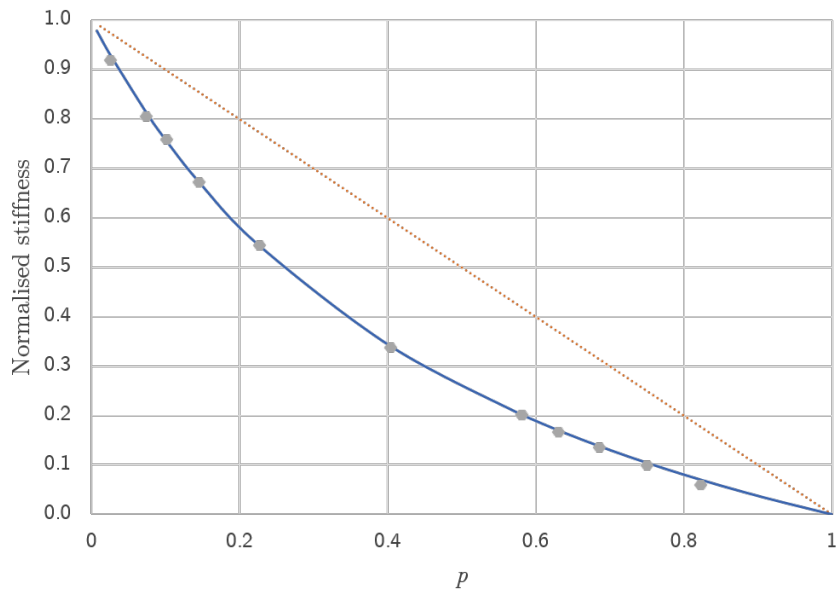
$$\nu \rightarrow +1; \quad \Psi_{\text{FPT}} \rightarrow \frac{1}{p/k + (1 - p)} \quad (4.50)$$

While these absolute extreme values are not physically realistic, this does highlight the affect of Poisson’s ratio, and the importance of considering it when calculating a normalised stiffness. The Finite Plate Theory captures the variation in stiffness with Poisson’s ratio very well, Fig. 4.15, and also shows that the arithmetic and harmonic averages are indeed good upper and lower bounds on overall stiffness.

Additionally, out of interest, it is noted that when $\nu_1 \neq \nu_2$, it is possible to obtain a value of $K = 1$ when $k \neq 1$. For example for when $k = 1.2$, $\nu_1 = 0.25$ and $\nu_2 = 0.1$, then



(a)



..... Harmonic smeared average Arithmetic smeared average
—— Finite plate theory ● FEA

(b)

Fig. 4.14 Biaxial normalised stiffness for regular hexagonal patterns: (a) $k = 10, \nu = 0.3$; (b) $k = 0, \nu = 0.3$.

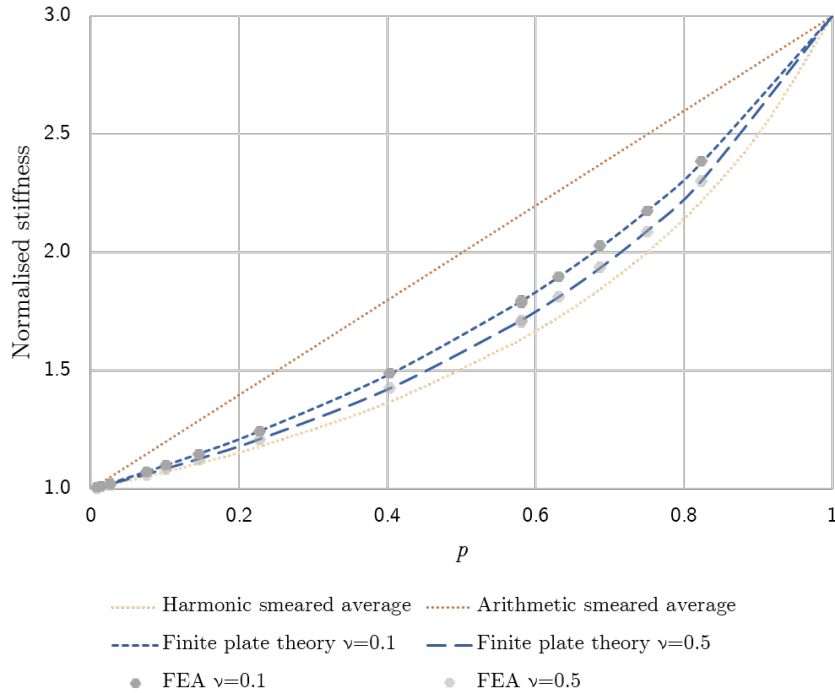


Fig. 4.15 Biaxial normalised stiffness for regular hexagonal patterns with Poisson's ratio $\nu = 0.1$ and $\nu = 0.5$; $k = 3$.

$K = 1$ and consequently the inclusion and plate both have a uniform constant stress of σ_0 . In biaxial loading such an inclusion effectively acts identically to a homogeneous plate with no inclusion. The condition for this to be the case is:

$$\frac{E_1}{1 - \nu_1} = \frac{E_2}{1 - \nu_2} \quad (4.51)$$

4.7.3 Irregular patterns

In Fig. 4.13b we saw that the normalised stiffness was predicted very accurately by the Finite Plate Theory, despite the stress distributions around each inclusion not conforming to the axisymmetric distribution which we assumed in Section 4.5.1, see Fig. 4.10b. Since the Finite Plate Theory does not explicitly use information about the exact type of inclusion patterning, but rather the proportion of inclusions, p , we have an analytical basis for assessing irregular patterns provided that the non-uniform pattern is well distributed in a global sense.

Rather than using completely random patterns, the use of pseudo-random patterns can achieve non-regular patterning with a high packing density. Phyllotaxis is a spiral-like pattern which is often found in close packing problems in nature: fundamentally connected with the “golden ratio”, it has a clear centre but no lines of symmetry or repeating unit cells [57].



Fig. 4.16 The seeds in the head of a sunflower naturally form the spiral like phyllotaxis pattern.

The seeds in the head of a sunflower are a classic example of phyllotaxis, Fig. 4.16. The phyllotaxis distribution can be characterised by giving the position of a point n with the polar coordinates [58]:

$$\rho = s\sqrt{n} \qquad \theta = \frac{2\pi n}{\tau} \qquad (4.52)$$

where s is a scalar characteristic distance and τ is the golden ratio.

Another aperiodic pattern is Penrose tiling, with the two best known variations, Rhombus tiling and Kite-and-Dart tiling [59], each using two different prototiles to tile an infinite plane without any translational symmetry. Each vertex in the tiling has one of a finite number of combinations of prototiles around it, and each will appear many times, but there is no overall repeating unit cell. The two most straight forward methods of utilising a Penrose tiling to find an inclusions patterning are to locate an inclusion at the centre of each prototile or to locate an inclusion at every vertex in the tiling. Unfortunately however, neither of these choices result in an efficient packing; for example if locating inclusions at the centers of the rhombus prototiles, when two thin rhombi are adjacent to each other, the narrow width of the thin rhombus prototile greatly limits packing density. By considering the vertex neighbourhoods [60, 61], the arrangement of tiles around a vertex, the locations of inclusions

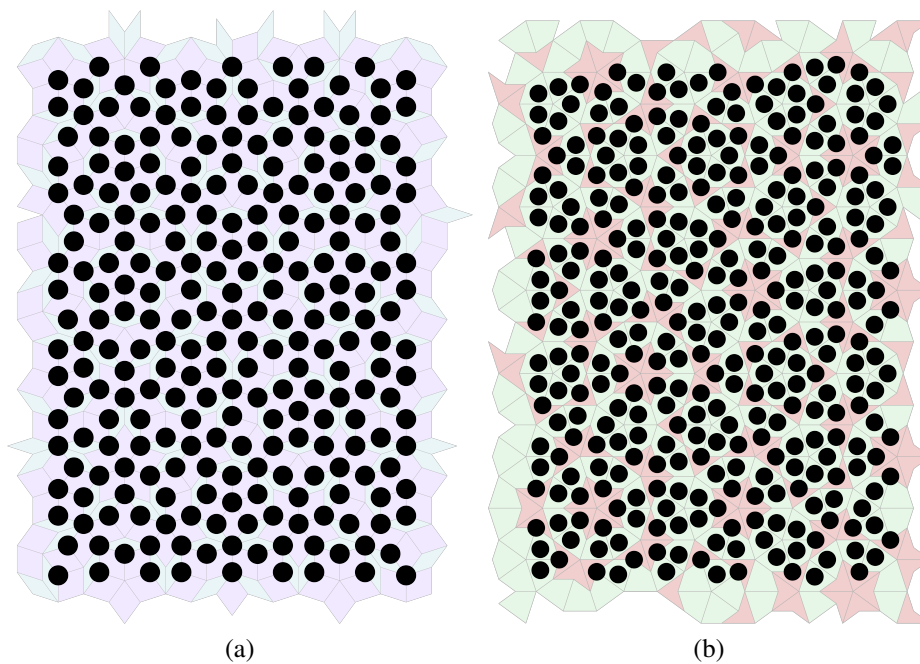


Fig. 4.17 Penrose tiling schemes for inclusion pattern: (a) Rhombus tiling; (b) Kite-and-Dart tiling. Further details of these patterns are given in Appendix C.

may be adjusted systematically in order to allow for a denser packing. The modifications to, and subsequent calculations of packing density for Penrose tiling based patterns are detailed in Appendix C and numerical coordinates for the Penrose pattern specimens of Section 2.5 are given in Appendix G. Figure 4.17 shows a small section of the two chosen patterns superposed onto their underlying tiling. Packing percentages of up to 76.3% and 64.7% can be achieved respectively from each pattern, compared to 70.2% for phyllotaxis.

Using FEA, as per Section 4.6, reasonably large but finite patches of these irregular patterns are modelled; Fig. 4.18 shows that the corresponding stiffness, remarkably, is very accurately predicted by the Finite Plate Theory. The exact nature of the pattern, it seems, is not particularly important for determining the overall stiffness. Some of the scatter in the data stems from taking the stiffness via the displacement at the edge of the plate which inevitably includes a small error due to edge effects.

As well as normalised stiffness, the Finite Plate Theory also predicts with good accuracy the SCF inside the inclusions (as well as the stresses in the plate at the inclusion interface). The peak stress in the plate will tell us how much loading can be applied before yielding begins. This will allow us to make a good estimate of the strength of the plate, and thus calculate a prediction of homogeneous overall yield stress for the inclusion plate. Figure 4.19 compares inclusion SCFs for a variety of regular and irregular patterns from FEA to the

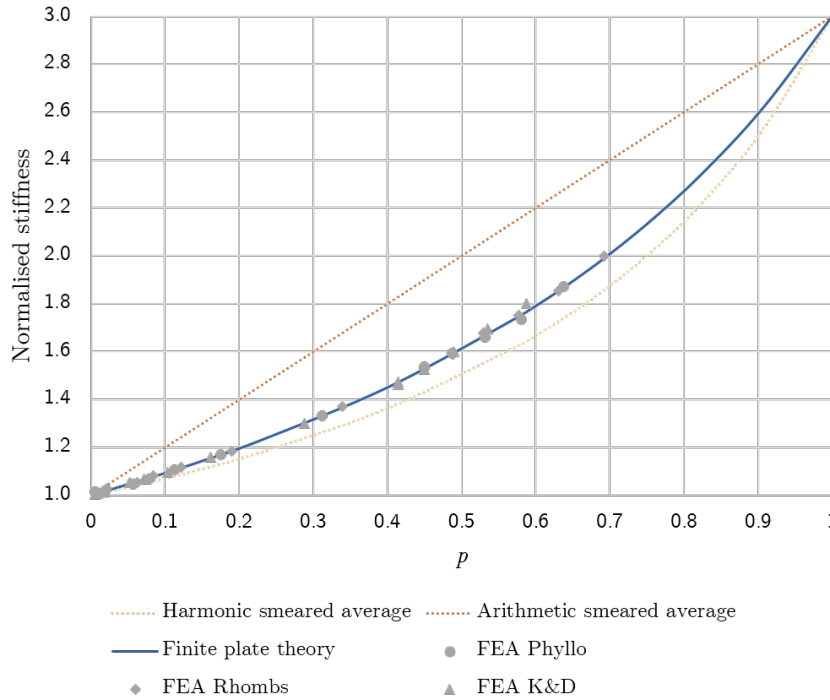


Fig. 4.18 Biaxial normalised stiffness for irregular patterns of inclusions; $k = 3$, $\nu = 0.3$.

theoretically predicted values from the infinite plate, Eqn 4.14, and a finite plate with radius $\Lambda = \sqrt{1/p}$, Eqn 4.41. We see that the Finite Plate Theory accurately predicts the inclusion SCF, which is most accurate for the regular hexagonal and square patterns. For irregular patterns, each inclusion has a different neighbourhood and proximity to adjacent inclusions which affects the SCF. Particularly for low p , the prediction of the Finite Plate Theory is still reasonably accurate but, for closer packing of irregular patterns, the SCF is slightly larger than theory.

4.7.4 Inclusion shape

While the plan form shape of inclusions is known to affect overall stiffness [50], especially aspect ratio [62], FEA shows that the Finite Plate Theory, Eqn 4.40, is equally as valid for plates with square inclusions, see Fig. 4.20, where p can approach unity due to perfect tessellation. Even for exceptionally high p values the Finite Plate Theory gives a very accurate prediction, it is especially surprising that the theory models these square inclusions so well as now both assumption of Section 4.5.1, *i.e.* a circular inclusion and stresses decaying to σ_0 between inclusions, are no longer upheld. Extra care must be taken when modeling inclusion shapes which have have sharp corners in FEA. Sharp corners lead to

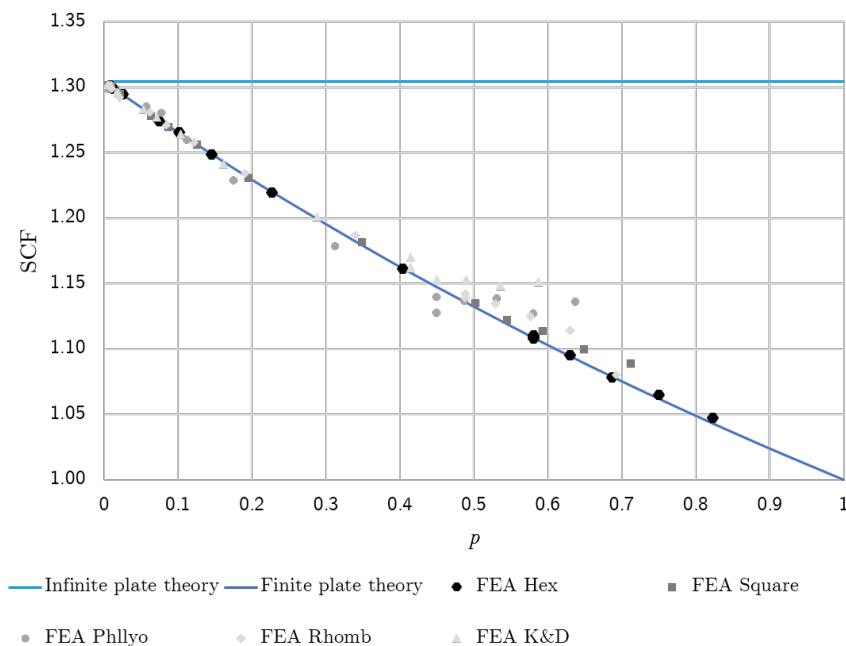


Fig. 4.19 Inclusion SCFs for a variety of regular and irregular patterns; $k = 3$, $\nu = 0.3$.

stress hot spots which FEA struggles to capture accurately, therefore extra fine mesh must be used at such locations.

However, unlike a square, inclusion shapes which still have an aspect ratio of unity, but have concave outlines give slightly higher stiffnesses than expected. This is because concave inclusions have a slightly larger effective area than their nominal area. Considering a ‘C’-shaped inclusion allows this phenomenon to be understood, Fig. 4.21. Supposing the C-shaped inclusion to have $k = 0$ and thus be equivalent to a hole, it is clear to see that the uvula shaped portion of the plate is just dangling in free space by a narrow strip of material and will be unable to carry any load, and thus can not contribute to the stiffness of the plate. This patch of material is essentially useless therefore, and as the behaviour of the plate would be unchanged if it were not there at all. The effective area of the inclusion will therefore be the total area enclosed by the dashed line. Conversely, if the inclusion is rigid, $k = \infty$, then the ‘C’ shape will not open up at all under load: therefore the material which is practically enclosed by the inclusion may as well be rigid too, and thus the inclusion will effectively be equivalent to a solid circular inclusion of the size indicated by the dashed line. Note that equally, if the rigid inclusion was a thin circular ring with a central hole, it would have an effective area equal to that of the entire circular area encompassed, not just the area of the thin ring.

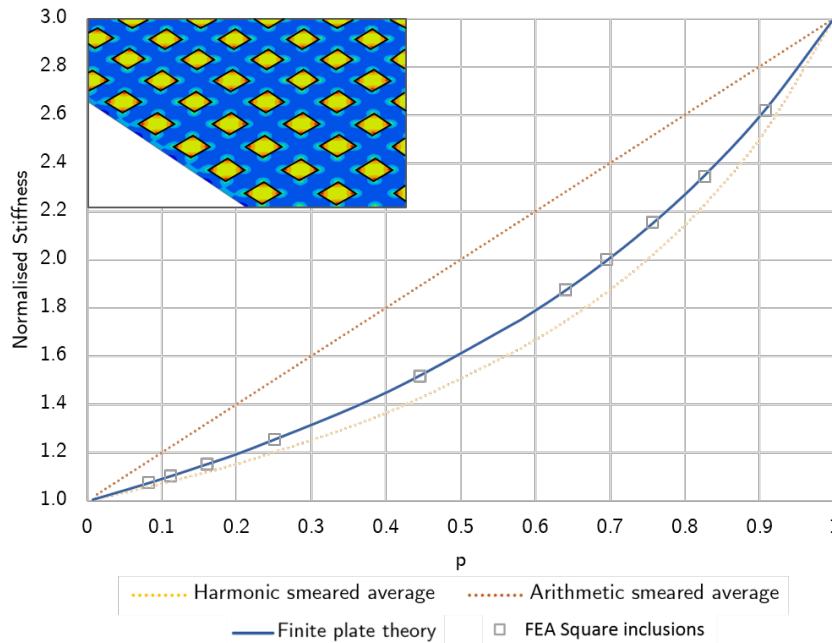


Fig. 4.20 Biaxial normalised stiffness for a square pattern of square inclusions; $k = 3$, $\nu = 0.3$. The insert figure shows an example of the square patterns of square inclusions, where the colour contours show SCFs of von Mises stress, with the outlines of the square inclusions shown by black lines. .

A concave shape which has four sharp corners or points which are connected by concave circular arc segments is shown in Fig. 4.22. The nominal area of this shape is $4a^2(1 + \sqrt{3} - 2\pi/3) \approx 2.55a^2$, however because of the concave nature of this shape we expect the effective area to be slightly larger. Figure 4.23 compares the FEA results of plates with these concave 4-pointed star inclusions against the Finite Plate Theory expectation. When plotted against the nominal inclusion area, the normalised stiffness is seen to be slightly higher than predicted. Increasing the nominal area by 3.5% gives an effective area which does align very closely with the Finite Plate Theory curve; an effective area which is 3.5% larger than the nominal area is shown as a dashed line on Fig. 4.22.

4.8 Uniaxial and antisymmetric loading

The theory developed in Section 4.5 assumed a state of biaxial loading, because this greatly simplified the analytical complexity and also allowed for identical treatment of bending and stretching. Figure 4.3 shows that for general loading the effects of an inclusion in stretching are slightly different to bending. However, we expect a similar behaviour overall to occur, both for different load cases of stretching and also between bending and stretching. Think

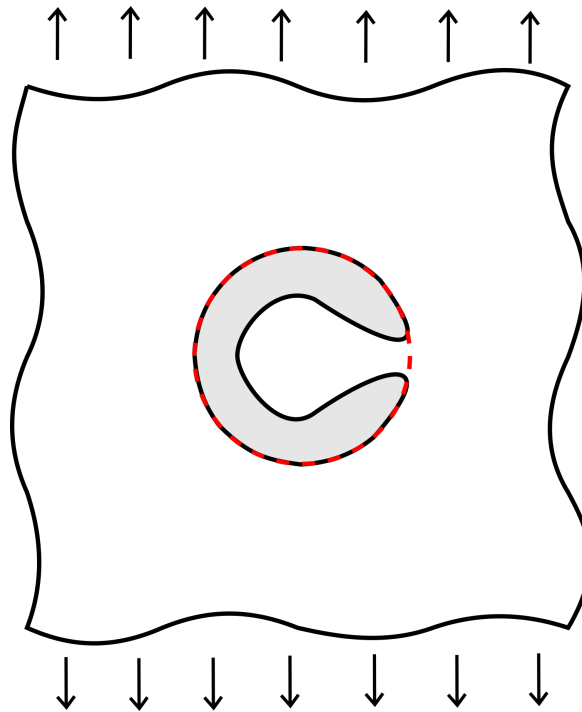


Fig. 4.21 A concave C-shaped inclusion in a plate in uniaxial tension. The nominal area of the inclusion is shaded in grey and the approximate effective area is outlined with a dashed line.

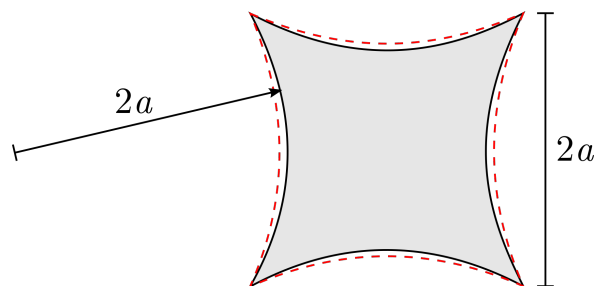


Fig. 4.22 A concave 4-pointed star inclusion. The four points make a square of width $2a$, and the connecting concave curves are circular arc segments of radius $2a$. The nominal area of the inclusion is shaded in grey, the approximate effective area is outlined with a dashed line.

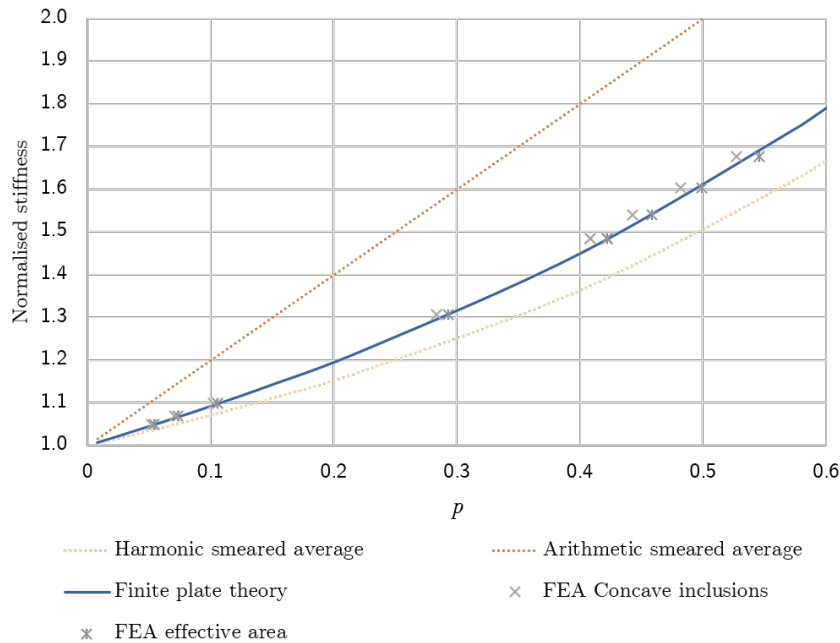


Fig. 4.23 The normalised biaxial stiffness of a plate with concave 4-pointed inclusions in a square patterning. The stiffnesses from FEA are plotted against both the nominal as well as the effective inclusion area. $k = 3$, $\nu = 0.3$.

for example of a metallic substitutional alloy; it has a microstructure which is effectively a matrix of the main alloying element with inclusions of the minor alloying element, however we expect it to have a single value of Young's modulus which is the same for both uniaxial and biaxial loading, for both stretching and bending. In order to assess the suitability of the Finite Plate Theory to inclusion patterned plates in more general load cases, FEA of plates in uniaxial and antisymmetric tension is undertaken in the following sections.

4.8.1 Bending vs stretching

We note first that alongside the FEA of inclusion patterned plates in biaxial tension, FEA in biaxial bending was also carried out on identical plates. Both biaxial bending and stretching gave practically identical results for normalised stiffness, as expected. These simulations also confirmed that, as theoretically predicted, the stress distributions around the inclusions were identical for biaxial stretching and bending. Additionally we note that, provided a reasonably large number of inclusions were modelled, the overall stiffness was unaffected by the exact number of inclusions, as expected. For example, Fig 4.24 shows two plates in biaxial bending, each has the same hexagonal patterning and gap-ratio, however the inclusions in Fig. 4.24a are four times larger than those in Fig. 4.24b; approximately 110

inclusions and 1880 inclusions respectively. Calculating the normalised stiffness of each of these plates, in the manner of Section 4.6, we find almost identical values, but the larger inclusions are just 0.4% less stiff.

However, modelling uniaxial and antisymmetric bending of inclusion patterned plates, FEA found that the normalised stiffness appeared to be dependent on the total number of inclusions modelled. FEA of plates where the inclusions were larger relative to the overall size of the plate were calculated to be stiffer. Figure 4.25 shows von Mises stresses from FEA for two plates under uniaxial bending; while both have the same pattern and gap-ratio, Fig. 4.25a has inclusions which are four times as large relative to the overall plate. From Saint-Venant's principle the central patch in such a plate should behave like a central patch from an infinite pattern provided that it is a sufficient distance away from the edge of the plate in order to allow edge effects to dissipate. Furthermore, while the absolute scale of a problem should not affect the stresses or stiffness, the plate in Fig. 4.25a is 2.2% more stiff. It is not an edge effect phenomenon: rather, the edge effects are seen to die away within a couple of inclusion radii from the edge and the stress distributions around the central inclusions in both cases match those around themselves but are slightly different between Fig. 4.25a and Fig. 4.25b. Neither is this a mesh effect, because modelling each plate with the same number of elements per inclusion still yields this same differing result.

Regardless of the exact cause of this phenomenon, it appears to be a problem with the FEA model, however it is possible to observe the behaviour as increased numbers of inclusions are modelled, Fig 4.26. As previously found, modelling a greater number of inclusions results in a slightly lower normalised stiffness; the results tend towards the Finite Plate Theory prediction of normalised biaxial stiffness as the relative size of the inclusions becomes very small. In fact, the limiting values of normalised stiffness for these plates in bending with a very large number of inclusions is equal to the values calculated using uniaxial tension. It transpires that, like in the biaxial case, for uniaxial and antisymmetric tension, the normalised stiffness is once again independent of the number of inclusions modelled, for example see Table E.14 which contains the numerical data plotted in Fig. 4.27a. Therefore, knowing that the same results could also be seen in bending if a very large number of inclusions were modelled, all the subsequent FEA is performed on inclusion patterned plates in tension.

4.8.2 Regular patterns

Comparing the stiffness of a regular hexagonal pattern of circular inclusions under uniaxial and antisymmetric tension to biaxial stiffness, Fig. 4.27, we see that the overall stiffness is only minorly impacted. The Finite Plate Theory, Eqn 4.39, is therefore an accurate prediction of the stiffness under any loading condition. For a stiff inclusion, $k = 3$, Fig. 4.27a, the

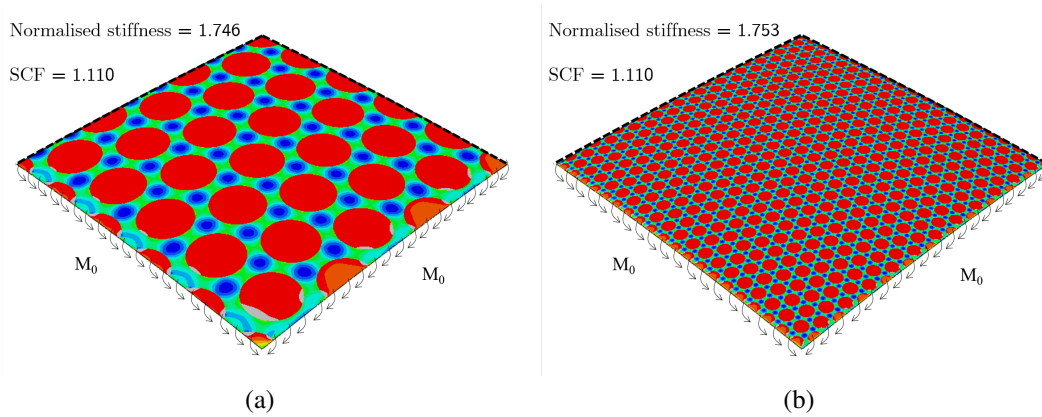


Fig. 4.24 Biaxial bending of hexagonally patterned plates with inclusions of an equal gap-ratio but different absolute size. Due to symmetry only a quarter plate needs to be modelled. Equal moments per unit length load the two outer edges, the edges indicated with a dark dashed line have symmetry boundary conditions applied to them, constraining each edge to remain in its corresponding plane of symmetry, and enforcing a zero rotation perpendicular to the plane of symmetry. The plate has a half-side length L and the inclusions have radius a , $k = 3$, $\nu = 0.3$. The gap-ratio is 0.5 and thus $p = 0.5804$; (a) $L/a = 12.5$ (b) $L/a = 50$. The loading is such that the nominal stress on the top surface is 24MPa. Von Mises stresses are plotted with colour contours [Dark blue, 20MPa] to [Red, 27MPa].

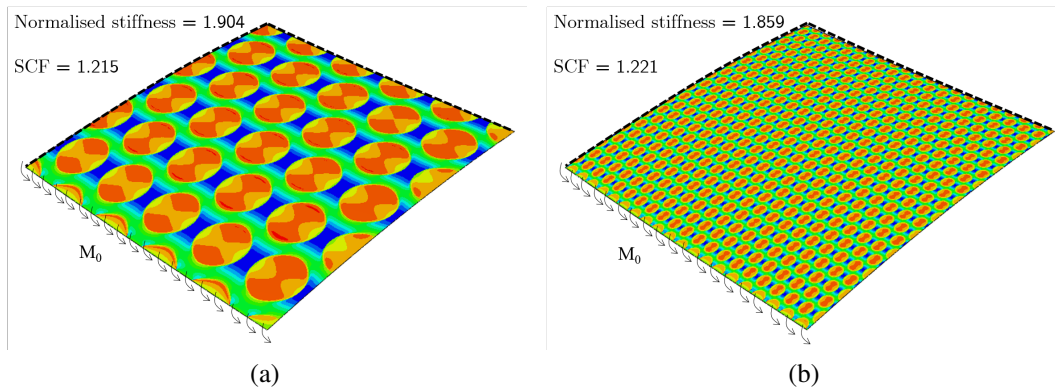


Fig. 4.25 Uniaxial bending of hexagonally patterned plates with inclusions of an equal gap-ratio but different absolute size. Due to symmetry only a quarter plate needs to be modelled. A moments per unit length of M_0 loads one edge, the edges indicated with a dark dashed line have symmetry boundary conditions applied to them, constraining each edge to remain in its corresponding plane of symmetry, and enforcing a zero rotation perpendicular to the plane of symmetry. The plate has a half-side length L and the inclusions have radius a , $k = 3$, $\nu = 0.3$. The gap-ratio is 0.5 and thus $p = 0.5804$; (a) $L/a = 12.5$ (b) $L/a = 50$. The loading is such that the nominal stress on the top surface is 24MPa. Von Mises stresses are plotted with colour contours [Dark blue, 8MPa] to [Red, 35MPa].

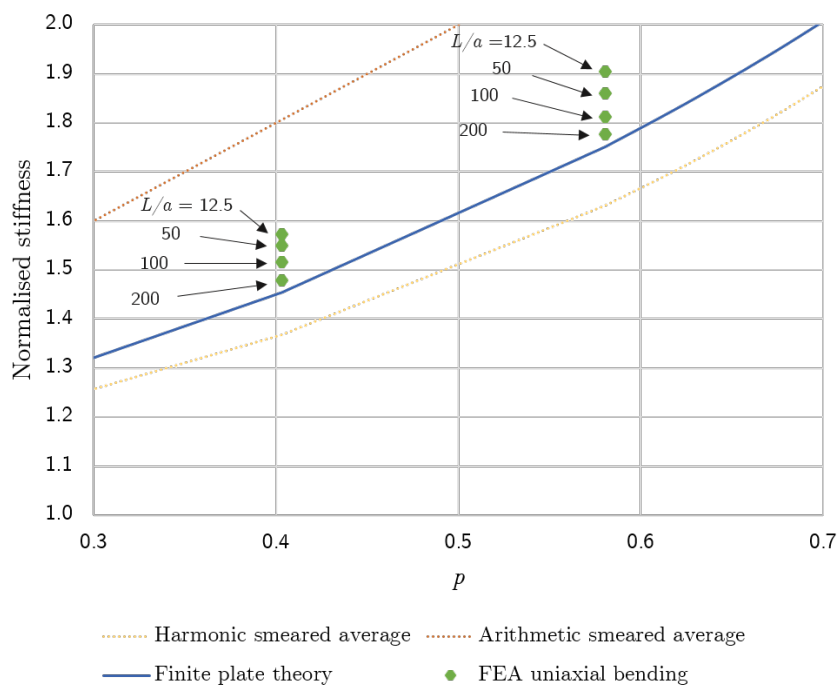


Fig. 4.26 The normalised uniaxial bending stiffness of hexagonally patterned plates. FEA results for plates with $k = 3$, $\nu = 0.3$ and gap-ratio 0.5 or 1 are shown for a variety of L/a , where a is the inclusion radius and L is the half-width of the plate.

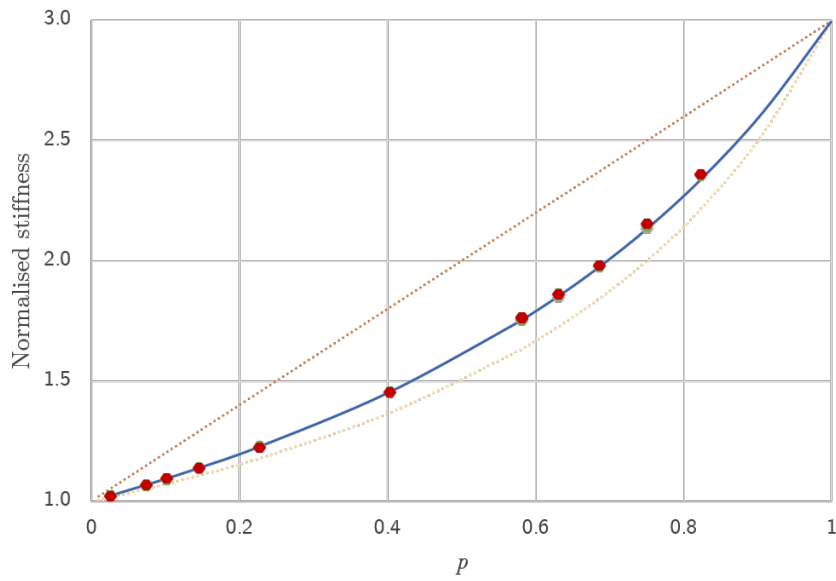
uniaxial, biaxial and antisymmetric stiffnesses are so similar that their points can barely be distinguished on the graph, the antisymmetric stiffness is found to be just 0.25% more stiff on average than the biaxial stiffness. For soft inclusions the plate is found to be slightly less stiff in antisymmetric loading compared with uniaxial loading, which in turn is slightly less stiff than biaxial loading. When $k = 0.2$, Fig. 4.27b, the normalised antisymmetric stiffness is on average 2.4% less stiff than the biaxial stiffness. In each case the uniaxial and antisymmetric display slightly more extreme stiffnesses, less stiff for soft inclusions and more stiff for stiff inclusions. As for the biaxial loading of a hexagonal pattern of inclusions, the uniaxial and antisymmetric behaviour seen was isotropic: the stiffness did not depend on the orientation of the pattern with respect to loading direction.

A regular square pattern of circular inclusions is tested in FEA under uniaxial and antisymmetric tension and the resulting normalised stiffnesses are compared with biaxial normalised stiffness in Fig. 4.28. Unlike the hexagonal patterning, there is a significant change in stiffness for the square patterning under the different types of loading. For both the stiff and soft inclusions, normalised antisymmetric stiffness is significantly higher than normalised biaxial stiffness for larger values of p . For every case the uniaxial stiffness is seen to be between the antisymmetric stiffness and the biaxial stiffness; which is to be expected as the uniaxial case is a superposition of the biaxial and antisymmetric load cases.

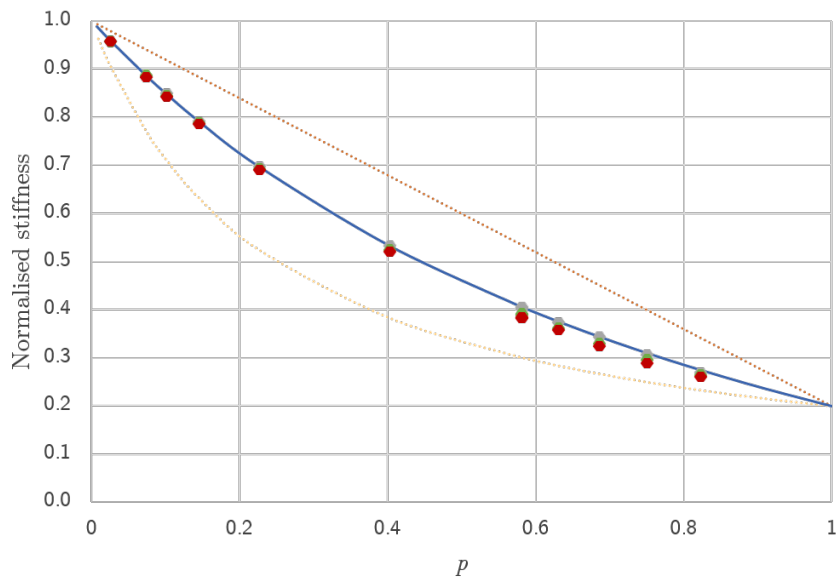
While the hexagonal pattern was seen to be isotropic in uniaxial and antisymmetric loading as well as biaxial loading, the square pattern is not so (Fig. 4.29). Though slightly stiffer than expected when the uniaxial or antisymmetric loading is aligned with the square grid, when the the pattern is loaded at 45° , the stiffness is lower than expected; in fact, it is slightly less stiff than the biaxial loading stiffness. It appears that the slight increase in stiffness seen when the square pattern is loaded parallel to the square grid is almost exactly balanced by the loss of stiffness when it is loaded diagonally at 45° . Taking the average normalised stiffness for the parallel and diagonal orientations under uniaxial loading we find values which agree with the biaxial stiffness to within 0.1% on average. Having the square pattern therefore does not on average increase the normalised stiffness, regardless of loading. While the square pattern is mildly anisotropic, its average stiffness considering various orientations of loading is still reasonably well captured by the Finite Plate Theory.

4.8.3 Irregular patterns

The normalised stiffness under uniaxial loading always seems to fall between the normalised stiffness under biaxial loading and under antisymmetric loading. This should not be too surprising as the uniaxial load state can be seen as a superposition of the biaxial and the antisymmetric loads. Therefore it is sufficient to consider just the antisymmetric loading in

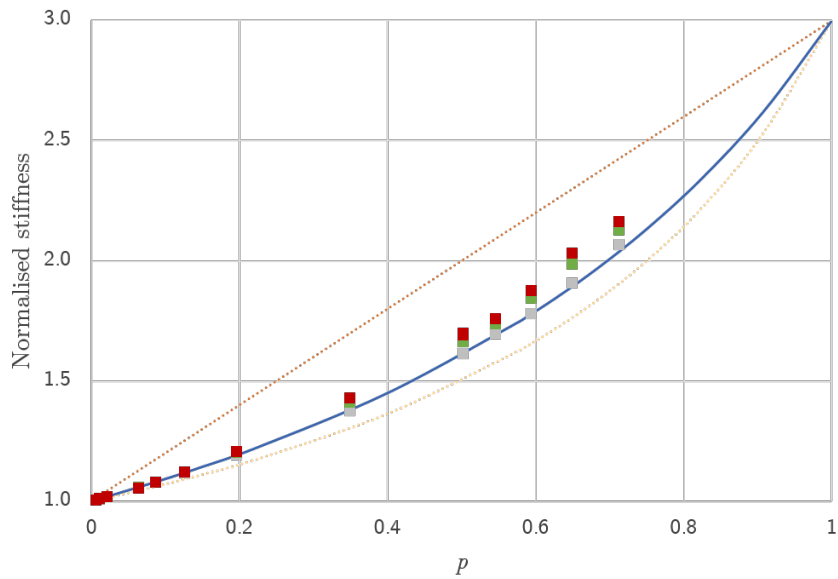


(a)

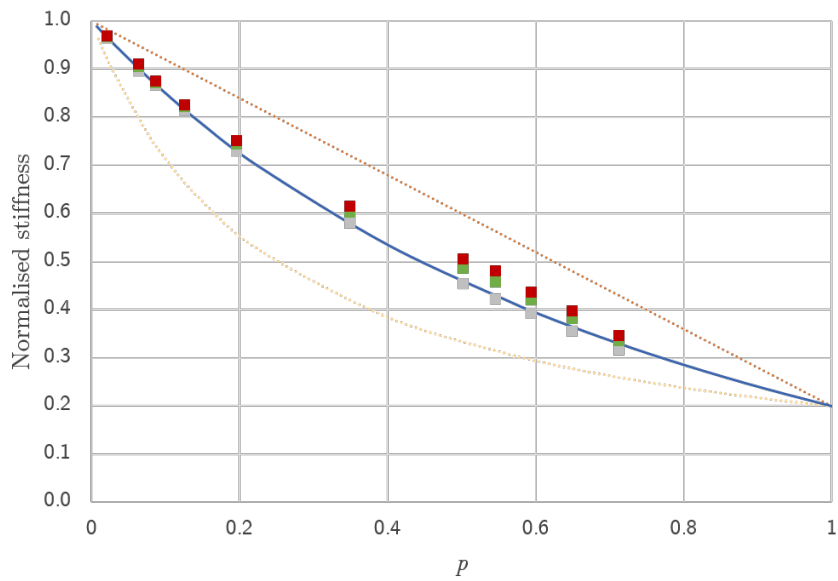


(b)

Fig. 4.27 Biaxial, uniaxial and antisymmetric normalised stiffness for regular hexagonal patterns of circular inclusions: (a) $k = 3$, $\nu = 0.3$; (b) $k = 0.2$, $\nu = 0.3$.



(a)



(b)

..... Harmonic smeared average Arithmetic smeared average
—— Finite plate theory ■ FEA biaxial
■ FEA uniaxial ■ FEA antisymmetric

Fig. 4.28 Biaxial, uniaxial and antisymmetric normalised stiffness for regular square patterns of circular inclusions: (a) $k = 3$, $\nu = 0.3$; (b) $k = 0.2$, $\nu = 0.3$.

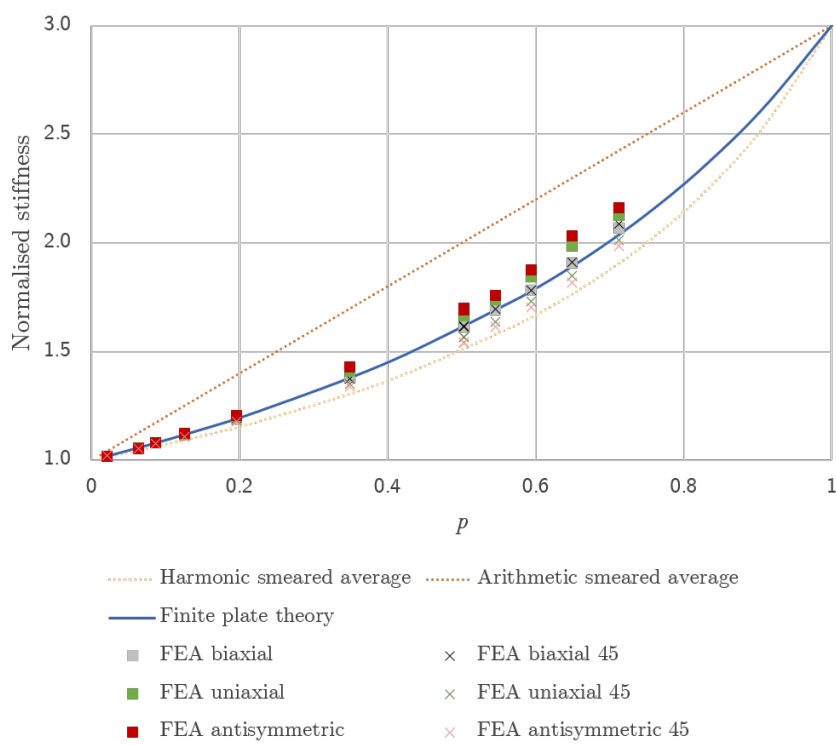


Fig. 4.29 Biaxial, uniaxial and antisymmetric normalised stiffness for regular square patterns of circular inclusions orientated at 45° to the primary loading direction: (a) $k = 3$, $\nu = 0.3$.

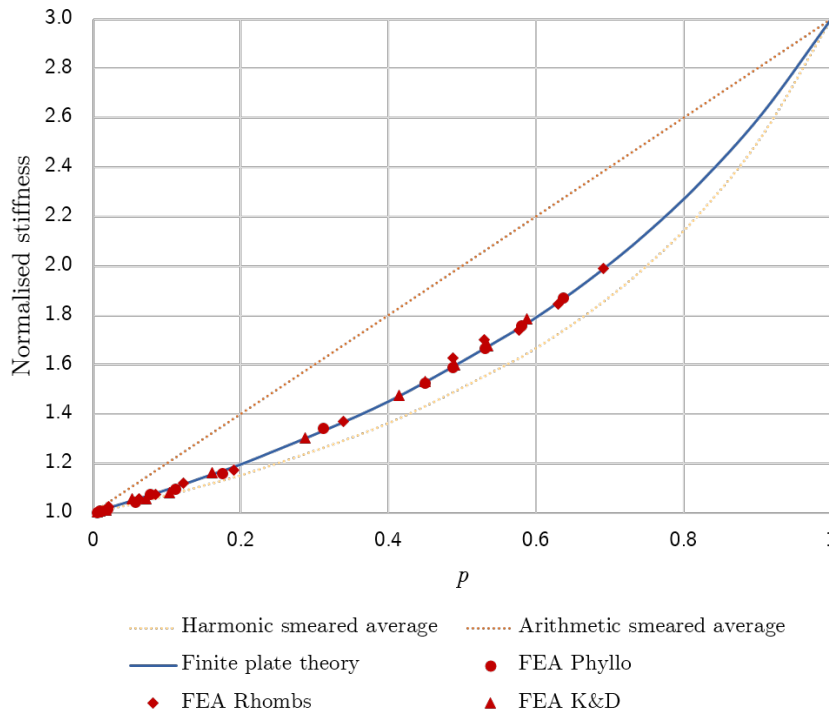


Fig. 4.30 Antisymmetric normalised stiffness for irregular patterns of inclusions: $k = 3$, $\nu = 0.3$.

addition to the biaxial loading in order to get a full sense of the behaviour under general loading. Figure 4.30 compares the normalised stiffness in antisymmetric tension for the three irregular patterns from Section 4.7.3. The antisymmetric normalised stiffness is almost identical to the biaxial normalised stiffness, compare with Fig. 4.18. As before, because the pattern is irregular the normalised stiffness must be taken from the edge displacement and so has a some of scatter due to edge effects. The Finite Plate Theory captures the antisymmetric normalised stiffness very well: it would appear that due to the irregular nature of the patterns the stiffness under different loadings is more consistent than for the regular square patterns.

4.9 Isotropy and homogeneity

An underlying assumption of this chapter has been that the overall behaviour of inclusion patterned plates is isotropic and homogeneous. Isotropy assumes that the stiffness doesn't change depending on the direction in which the plate is loaded: the stiffness is independent of pattern orientation. Homogeneity assumes that it is an acceptable approximation to treat the plate with a constant, (albeit smeared) average, Young's modulus.

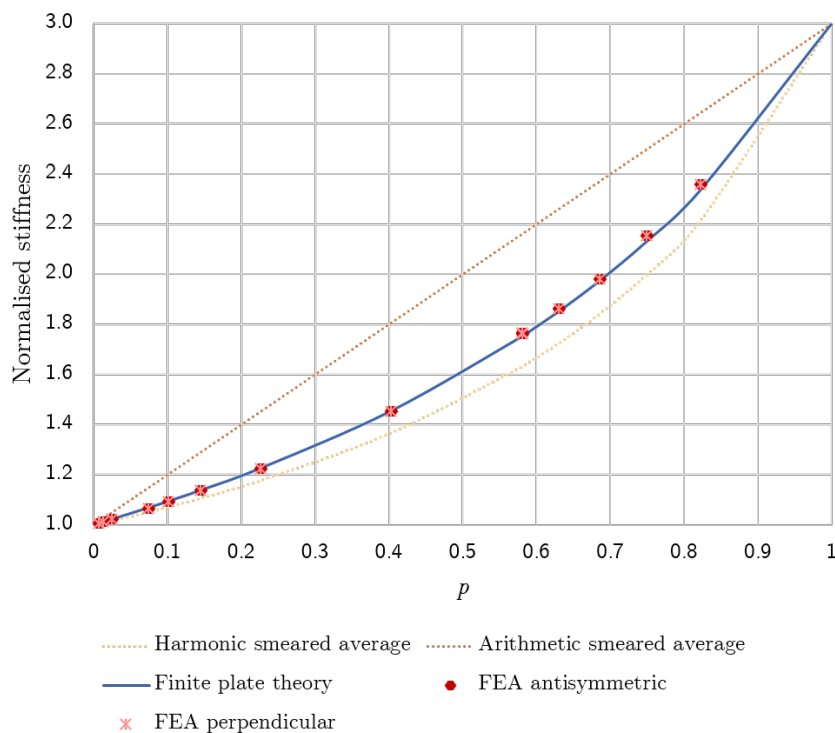


Fig. 4.31 The normalised antisymmetric stiffness of hexagonally patterned plates. Loading in the perpendicular direction is equivalent to rotating the pattern 30° with respect to the primary loading direction, thus the isotropic nature of the plate can be assessed.

4.9.1 Isotropy

Loading the hexagonal pattern in the perpendicular direction is equivalent to rotating the pattern 30° with respect to the primary loading direction. These two different orientations were identified in Section 2.4, where it was suggested that “lines-of-weakness” would make one direction significantly less stiff than the other. However, as Fig. 4.31 shows, there is no difference in stiffness depending on pattern orientation. Only a 0.0013% difference in stiffness between the loading directions is found, well within the bounds of the numerical accuracy, thus confirming the isotropic nature of the hexagonal pattern.

As shown in Fig. 4.29, the square pattern is not totally isotropic: its regular rectangular patterning facilitates the possibility of direction dependent stiffness. Comparing the parallel and diagonal orientations for the square pattern under antisymmetric loading, with $k = 3$, on average a 6% difference is seen, a small but not inconsequential amount of anisotropy. For the square pattern, antisymmetric loading displays the most extreme anisotropic behaviour. Figure 4.32 shows how normalised stiffness varies as the pattern is rotated relative to the principle loading direction. The hexagonal pattern is confirmed to be isotropic, the

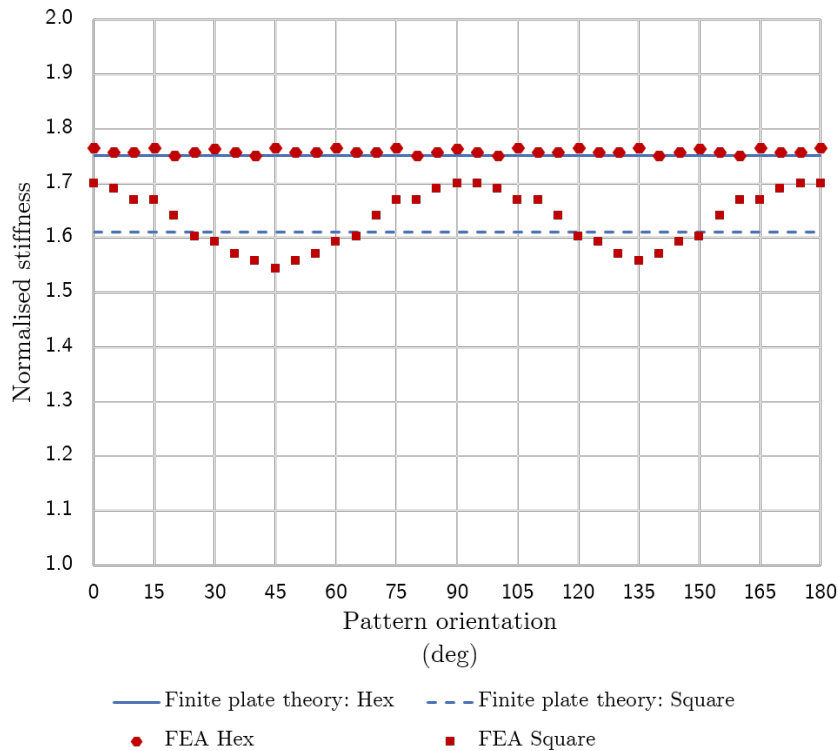


Fig. 4.32 The normalised antisymmetric stiffnesses of the square and hexagonal pattern of circular dimples is shown as a function of rotation angle with respect to the principle loading direction. Each pattern has $k = 3$ and a gap-ratio equal to 0.5, note that this gives the square pattern a slightly lower p .

normalised stiffness is invariant of pattern orientation and is equal to the Finite Plate Theory prediction. A little scatter in the data is seen as stiffnesses have to be calculated using the edge displacements of the plate, which therefore incorporate edge effects. The stiffness of the square pattern is seen to vary in an approximately sinusoidal manner, with maximum and minimum stiffnesses occurring at 0° and 45° respectively. The normalised stiffness averaged over the different pattern orientations is very close to the value predicted by the Finite Plate Theory, with a difference of just 0.8%. Note that the Finite Plate Theory predicts different stiffness for the hexagonal and square patterns in Fig. 4.32 because as the patterns have the same gap-ratio they have different values of p .

Irregular patterns do not seem to be affected by loading orientation, Fig. 4.33 contrasts the normalised antisymmetric stiffnesses when loaded in perpendicular directions, *i.e.* the pattern is rotated 90° to the primary loading direction. As an irregular pattern does not have any clear direction dependence, practically by definition, we would not expect there to be any significant difference in stiffness when changing the loading direction. While, for previously

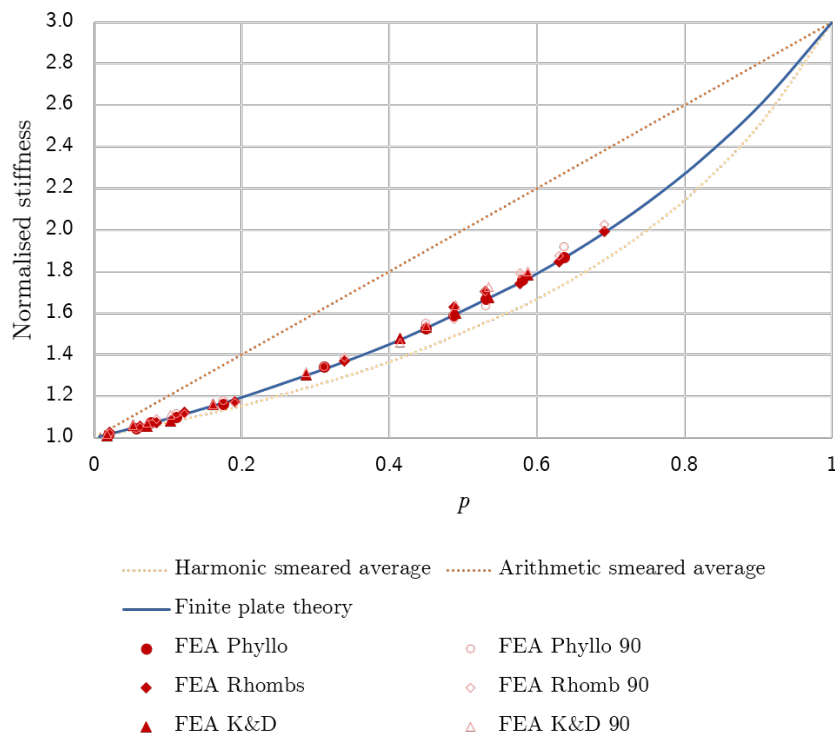


Fig. 4.33 The normalised antisymmetric stiffness of irregularly patterned plates. Loading in the perpendicular direction allows the isotropic nature of the plate to be assessed.

discussed reasons, there is some scatter in the data, Fig. 4.33 confirms the isotropic nature of these irregular patterns. On average the difference in normalised stiffness between the two orientations is 0.5% for the phyllotaxis pattern, 0.3% for the rhombus pattern and 1% for the kite and dart pattern. The measured stiffnesses are scattered closely around the Finite Plate Theory prediction, and the differences between different loading directions are within the range of scatter. When considering the whole set of data it can be seen that there is no significant anisotropy present.

4.9.2 Homogeneity

As discussed in Section 4.4, the validity of the homogeneity assumption clearly has a dependence on the relative size of the inclusions to the size of the overall plate. Defining the half-width of the overall plate to be L and the radius of the inclusions to be a , knowledge of the stress patterns formed around the inclusions can be used to find the corresponding displacement fields and therefore judge how much the true displacement may vary from the smeared homogeneous approximation in terms of a/L . Comparing biaxial bending and tension, the in-plane displacements of the tension case correspond to the rotations of the

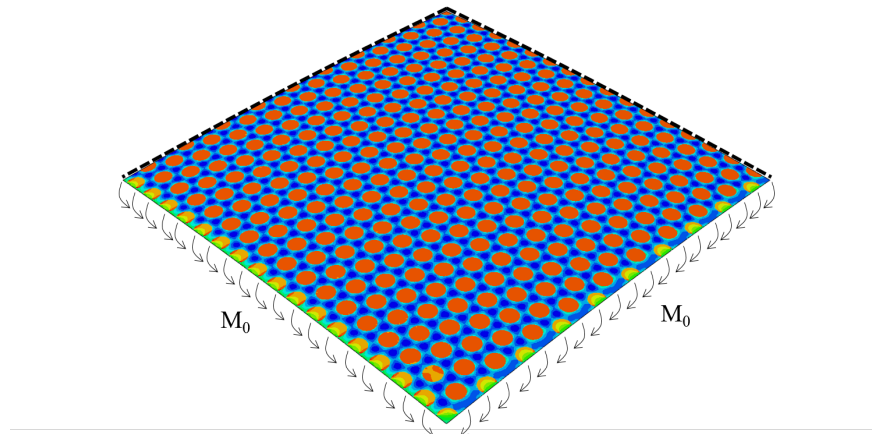
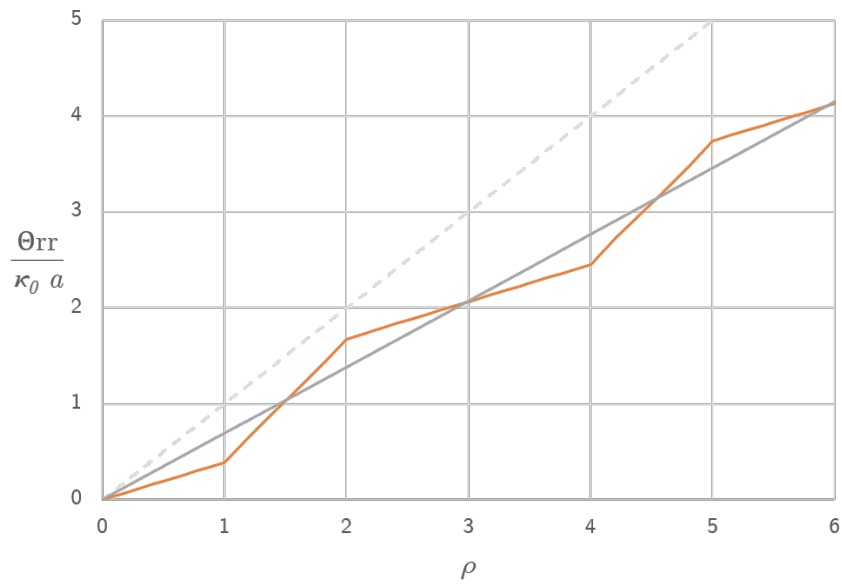


Fig. 4.34 A quarter model of a hexagonally patterned plate is subjected to biaxial bending. Equal moments per unit length load the two outer edges, the edges indicated with a dark dashed line have symmetry boundary conditions applied to them, constraining each edge to remain in its corresponding plane of symmetry, and enforcing a zero rotation perpendicular to the plane of symmetry. Von Mises SCFs (von Mises stress divided by nominal stress) are shown with colour contours ranging from [Dark blue, 0.9] to [Red, 1.3]. $k = 3$, gap-ratio = 1, $p = 0.403$, $a/L = 50$.

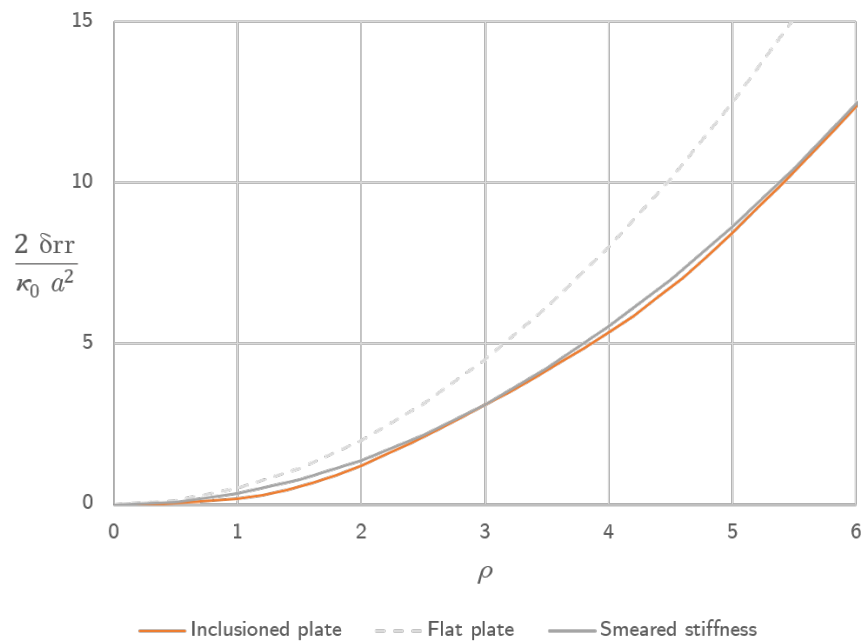
bending case. It is also possible to compare the out-of-plane deflections of a patterned plate in bending to the homogeneous case.

Figure 4.34 shows an inclusion patterned plate in biaxial bending, the rotation and out-of-plane deflection along the dashed line are extracted from the FEA and plotted in Fig. 4.35. The rotations and deflections of a plate which has a homogeneous Young's modulus equal to the homogenised smeared stiffness are also shown for comparison.

Consider the rotation along the centre-line of the plate shown in Fig. 4.34, *i.e.* along the dashed line on the right half of the figure. From Fig. 4.35a we observe that the rotation is approximately a piecewise linear function which fluctuates above and below the homogeneous smeared average rotation. The rotation of a homogeneous plate under pure bending is a simple linear function and by definition the homogenised smeared stiffness is chosen to ensure the slope of this line does exactly bisect the true rotation of the inclusion patterned plate. Note that the rotation in both cases is always less than the plain flat plate which has Young's modulus E_1 . The difference between the rotation of the inclusion patterned plate and smeared homogeneous plate has a constant wavelength; the maximum difference has a constant magnitude and occurs at the edge of each inclusion *e.g.* $\rho = 1, \rho = 2, \rho = 4$. While the absolute magnitude of this difference is constant, the relative size of this difference becomes less as the total rotation of the plate increases. This means that the best way to calculate the magnitude of this difference in rotation is to consider the rotation at the edge of the central



(a)



(b)

Fig. 4.35 An inclusion patterned plate in biaxial bending, Fig. 4.34, is compared to a plain flat plate and to the smeared homogeneous approximation: (a) Rotation, (b) Out-of-plane deflection.

inclusion, *i.e.* the rotation at $\rho = 1$. This can be done reasonably easily by considering the stress distributions assumed using Finite Plate Theory. As seen in Section 4.5.2, the stress in an inclusion is approximately constant and is very well predicted by Eqn 4.41. The rotation at the edge of the inclusion, $r = a$, can therefore be calculated:

$$\Theta_{\text{inclusion}} = \frac{M_0(1-\nu)}{kE_1I_0} a \text{SCF}_{\text{FPT}} = \kappa_0 \frac{a \text{SCF}_{\text{FPT}}}{k} \quad (4.53)$$

and the rotation at $r = a$ for the homogenous smeared plate is:

$$\Theta_{\text{smeared}} = \frac{M_0(1-\nu)}{E_{\text{FPT}}I_0} a = \frac{M_0(1-\nu)}{E_1I_0} \frac{a}{\Psi_{\text{FPT}}} = \kappa_0 \frac{a}{\Psi_{\text{FPT}}} \quad (4.54)$$

where $\kappa_0 = \frac{M_0(1-\nu)}{E_1I_0}$. The magnitude of the difference in rotations is thus:

$$\Theta_{\text{smeared}} - \Theta_{\text{inclusion}} = \kappa_0 \left(\frac{1}{\Psi_{\text{FPT}}} - \frac{\text{SCF}_{\text{FPT}}}{k} \right) \quad (4.55)$$

and the rotation at the edge of the plate, $r = L$ is:

$$\Theta_{\text{plate}} = \kappa_0 \frac{L}{\Psi_{\text{FPT}}} \quad (4.56)$$

Dividing the magnitude of the difference in rotations by the rotation at the edge of the plate we calculate what the maximum relative error we could have by assuming the smeared homogeneous approximation:

$$\frac{\Theta_{\text{smeared}} - \Theta_{\text{inclusion}}}{\Theta_{\text{plate}}} = \frac{a}{L} \left(1 - \frac{\text{SCF}_{\text{FPT}}\Psi_{\text{FPT}}}{k} \right) = \frac{a}{L} \left(1 - \frac{K}{k(1-p\epsilon^*)} \right) \quad (4.57)$$

The bracketed part of the expression is dependent on the packing density p , Poisson's ratios ν , and the inclusion stiffness ratio k , however the value of the function will always be less than or equal to unity. For typical values of k , ν and p , it takes a value of about 0.5, *e.g.* when $k = 3$, $\nu = 0.3$ and $p = 0.5$, the bracketed expression is equal to 0.394. However of more interest is the observation that the relative error in rotation at the edge the plate is proportional to a/L . This allows us to say that the maximum difference between the edge rotation of an inclusion patterned plate and the corresponding homogenised plate is a/L . Thus for the FEA of irregular patterned plates conducted in Section 4.7.3 where the typical inclusion radius to plate half-width was $a/L = 1/50$, the maximum error we expect should be less than 2%. In practice the error which we are likely to encounter will not be the maximum, but could be anywhere between a positive or negative error of this magnitude. On average therefore the average error which is expected should be half of the maximum error

magnitude. Thus we would expect that the stiffnesses of the irregular patterns in Section 4.7.3 would have errors which are around 0.5%. Figure 4.18 shows that the scatter in the data (defined as the average magnitude of the percentage difference between the FEA normalised stiffness and Finite Plate Theory prediction) is 0.36% for the phyllotaxis pattern, 0.43% for the Penrose rhombus pattern and 0.56% for the Penrose kite and dart pattern. This is exactly the amount of scatter we expect, and therefore both confirms the applicability of this analysis of homogeneity, and also further supports the applicability of the Finite Plate Theory prediction for smeared normalised stiffness. This analysis is also equally valid for the stretching of inclusion patterned plates, considering in-plane displacement instead of rotation.

Consider the deflection of the plate in bending: in most applications, the rotation is not the key parameter of concern, but rather the out-of-plane deflection may be more important. Figure 4.35b shows the out-of-plane deflection of the same biaxially bent plate, and again contrasts this against a plain flat plate of Young's modulus E_1 and against the equivalent homogeneous smeared modulus plate. It is apparent that the differences between the inclusion patterned plate and the homogeneous smeared plate are even smaller when considering deflections. For the rotations the largest difference occurred at the edge of each inclusion, however, as deflection is the integral of rotation, for deflections the largest difference occurs halfway between inclusions. The maximum difference in deflection is equal to the area enclosed between the actual rotation curve and the homogenised stiffness rotation curve, calculated between the centre of one inclusion to the midway point between the adjacent inclusion.

Assuming the rotation profile to be piecewise linear, the area between the curves can be calculated straightforwardly as the area of a triangle of width $a(1 + \text{gap-ratio}/2)$ and height equal to the maximum difference in rotations, $\Theta_{\text{smeared}} - \Theta_{\text{inclusion}}$. Thus the magnitude of the maximum difference in deflection between the inclusion patterned plate and the homogeneous smeared stiffness plate is:

$$\begin{aligned} \delta_{\text{smeared}} - \delta_{\text{inclusion}} &= \frac{1}{2}a \left(1 + \frac{\text{gap-ratio}}{2} \right) (\Theta_{\text{smeared}} - \Theta_{\text{inclusion}}) \\ &= \frac{\kappa_0 a^2}{2} \left(1 + \frac{\text{gap-ratio}}{2} \right) \left(1 - \frac{\text{SCF}_{\text{FPT}} \Psi_{\text{FPT}}}{k} \right) \end{aligned} \quad (4.58)$$

The deflection of the plate at the edge of the plate, $r = L$, is:

$$\delta_{\text{plate}} = \frac{\kappa_0 L^2}{2\Psi_{\text{FPT}}} \quad (4.59)$$

Dividing the magnitude of the difference in deflection by the deflection at the edge of the plate we calculate the maximum relative error we could have by assuming the smeared homogeneous approximation:

$$\frac{\delta_{\text{smeared}} - \delta_{\text{inclusion}}}{\delta_{\text{plate}}} = \frac{a^2}{L^2} \left(1 + \frac{\text{gap-ratio}}{2} \right) \left(1 - \frac{\text{SCF}_{\text{FPT}} \Psi_{\text{FPT}}}{k} \right) \quad (4.60)$$

In fact, as shown by Eqn 4.16, equating strains in stretching to curvatures in bending, the increase in rotation by calculating the area above κ_0 , $\int_{\rho=1}^{\infty} (\kappa_{2rr} - \kappa_0)$, is never greater than the decrease in rotation which is the area below κ_0 , $\int_{\rho=0}^1 (\kappa_0 - \kappa_{1rr})$. Therefore the area between the curves in Fig. 4.35a for $1 < \rho < (1 + \text{gap-ratio}/2)$ will always be less than or equal to the area between the curves for $0 < \rho < 1$. Calculating the area between the curves for $0 < \rho < 1$ is straightforward as it is a simple triangular area, doubling it will give a conservative estimation of the maximum difference in out-of-plane deflection:

$$\frac{\delta_{\text{smeared}} - \delta_{\text{inclusion}}}{\delta_{\text{plate}}} = \frac{a^2}{L^2} \cdot 2 \left(1 - \frac{\text{SCF}_{\text{FPT}} \Psi_{\text{FPT}}}{k} \right) \quad (4.61)$$

The main result of this analysis is that the relative error between the out-of-plane deflections of a inclusion patterned plate and a smeared homogenous plate is proportional to $(a/L)^2$, the square of the radius to half-width ratio. As the differences in rotation were proportional to a/L , the differences in deflection will be even smaller. As before, the bracketed expression is has an upper limit of 1 and a typical value of around 0.5. Thus for a typical inclusion radius to plate half-width such as $a/L = 1/50$, the maximum error we might expect in rotation would be less than 2%, however for out-of-plane deflection the maximum error we would expect would be less than 0.08%. In fact, as before if instead we considered the typical difference, we conclude that differences around a quarter of the maximum would be expected. Even for plates with comparatively large inclusions, *e.g.* $a/L = 0.1$, the typical difference in deflections between the edge deflection of an inclusion patterned plate and an equivalent homogenised stiffness plate would be just 0.25%. Consequently, approximating the equivalent value of smeared stiffness by considering the edge deflection of a inclusion patterned plate in bending should give an answer which is accurate to within this same limit.

4.10 Experimental validation

There are obvious practical difficulties in producing specimens of thin plates with many inclusions of a different material inserted into it. These problems are compounded by the desire for the inclusions to be small and numerous. Most notably, attempting to form a good

connection at the inclusion matrix interface would be very difficult: there is only a small contact area due to the thinness of the plate, and trying to ensure the inclusion lay flush to the rest of the plate would also be challenging.

While attempting to drill out material from a plate and fill the voids with a second material as the inclusion might be practically infeasible, there are still some practical examples of inclusions in thin plates. Giving an inclusion a different modulus to the surrounding matrix does not necessarily involve the introduction of a completely new material; it suffices to simply change the material properties of a patch of the plate. For example, a patch of aluminium oxide in an aluminium plate [53], or a spot weld in a steel plate [63].

However, perhaps the most widely occurring inclusion is the case of $k = 0$, where the inclusion is in fact a perforation, *i.e.* a hole. As noted in Section 4.7.2, there are several practical examples of perforated plates having important practical uses, such as nuclear reactor grid plates and tube plates of heat exchangers.

In addition to the FEA validation of the applicability of Finite Plate Theory to perforated plates, Fig. 4.14b, practical experimentation on perforated strips has been carried out. Perforating a thin plate with different patterns of perforations, both regular and irregular, bending and stretching tests were performed.

4.10.1 Experimental method

Specimens of perforated plates were manufactured from a thin sheet of copper beryllium, $t = 0.5\text{mm}$, perforations of diameter 3mm were cut using a water-jet cutter. A total of six different patterns were used: regular hexagonal, phyllotaxis, Penrose rhombus, Penrose kite and dart (see Appendix C), square and the same square pattern but at an orientation of 45° to the loading direction. For each pattern three different choices of gap-ratio were used, $2/3$, $4/3$ and $8/3$, giving a range of nominal p values from $p = 0.110$ to $p = 0.510$ over the total of 18 specimens. The specimens are strips of width 35mm and are 200mm in length, the perforation pattern is centered on the strip and any perforations which would not be wholly within the boundary of the strip are neglected. As only the central 140mm portion is loaded during test, only the central 160mm of the strip is perforated and perforations whose centers would be beyond this limit are neglected. Due to neglecting some perforations due to the finite width of the strip, the nominal p value, considering p of an infinite section of patterning, and the realised p value, considering to the actual amount of material removed, are slightly different in value. The differences between nominal p and realised p are small, typically less than 1%. Copper beryllium has a Poisson's ratio of $\nu = 0.3$.

The specimens are tested in both uniaxial tension and uniaxial bending. The uniaxial tensile test is performed in an INSTRON testing machine, with S16 wedge action grips used

to grip the top and bottom of the strip, leaving the central 140mm to be loaded, Fig. 4.36. A slow quasi-static displacement is imposed as the top grip moves upward, the force response of the sample is recorded, and this allows the stiffness to be calculated by finding the slope of the initial linear force/displacement response. Plain strips of the same geometry and material are also tested in this way, and by comparing the stiffness of the perforated strips to that of the plain strips a normalised stiffness can be calculated. The strips were designed for use with wedge grips with a 35mm face, however these were unavailable at the time of testing, and unfortunately the new grips had only a 25mm face. Because of this, it was not possible to align the centres of the specimens with the line of action. The lack of alignment therefore caused an induced bending in the the specimens, in the plane of the strip. This causes the strip to not to be loaded in pure tension, but rather a linearly varying in-plane tension across the width of the strip which induces bending.

The perforated strips are also tested in a uniaxial 4-point bend test, Fig. 4.37. Each end of the strip is gripped between a pair of aluminium blocks and it is supported at either end on knife-edge supports 200mm apart and two further knife-edges press down the inner edge of the blocks to impart a uniform moment to the central 140mm span. The top half of the rig, with the two inner knife-edges, is displaced downwards quasi-statically and the force response is measured. The aluminium blocks are effectively rigid, and so the edge rotation can be calculated from the displacement of the two central knife-edges, and the applied moment calculated by multiplying the force response by the lever arm. The rotational stiffness of the perforated strip is then found by calculating the initial gradient of the moment/rotation response. Plain strips of the same geometry and material are also tested in this way, and by comparing the stiffness of the perforated strips to that of the plain strips a normalised stiffness can be calculated. Care was taken to ensure that the specimens remained within their elastic limits during both the stretching and the bending tests.

4.10.2 Experimental results

Figure 4.38 compares the results of the 4-point bending and uniaxial tensile stretching test with Eqn 4.40, the Finite Plate Theory prediction, with $\nu = 0.3$. The arithmetic smeared average is also shown for comparison, but note that the harmonic smeared average is undefined when $k = 0$, and so is not shown. The experimental data is plotted against the realised p value of each strip, accounting for the actual amount of material removed.

The results of the tensile stretching test, Fig. 4.38a, show a reasonably good agreement with the theoretical prediction. There is a reasonable amount of scatter in the data, which is assumed to be experimental error. The main cause of experimental error is hypothesised to be the off-centre loading of the samples caused by the narrow grips which had to be



Fig. 4.36 The experimental set-up of the uniaxial tensile loading of a perforated strip. An INSTRON grips the ends of the specimen and imparts a quasi-static displacement, measuring the force response as it does so.



Fig. 4.37 The experimental set-up of the uniaxial bending of a perforated strip. Each edge of the strip is clamped between a pair of aluminium blocks, these blocks are loaded using two pairs of knife-edge supports to develop a central constant moment region.

used, leading to the samples not being in pure uniaxial tension. This is hypothesised to have contributed to the experimental scatter because a non-uniform tensile loading is likely to make the stiffness a little sensitive to the exact patterning. Another potential source of error arises from the pre-loading effect of the wedge action grips. The specimens were placed into position and then the lower grip was tightened, followed by the upper grip. It was noticed that when the upper grip was tightened such that it gripped the specimen, that a pre-load was seen to be imparted. Tightening the grips further increased the level of unwanted pre-load imparted onto the specimen. While some level of pre-load had to be tolerated so that the sample could be securely gripped, the experimental data showed that the specimens which seemed to have a higher stiffness than the theory predicted were also the specimens which had a higher pre-load. As found through FEA analysis, the square pattern exhibited an anisotropic behaviour. The square pattern of perforations which is aligned to the loading direction was more stiff than the other patterns. Additionally a drop in stiffness was observed between the square pattern and the square pattern rotated by 45° .

The bending test results, Fig. 4.38b, show an even better agreement to the Finite Plate Theory prediction. There is less experimental scatter in the bending results, which is pleasing, and adds confidence to the results. Experimental error is seen to be much lower in the bending case, however as the loads applied were much less than in tension, the precision of

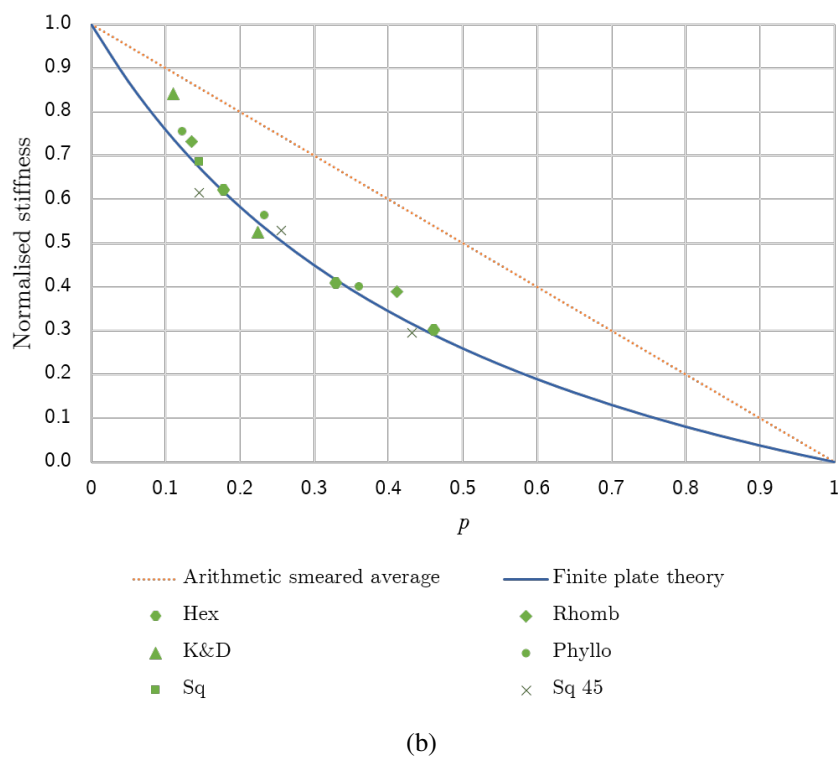
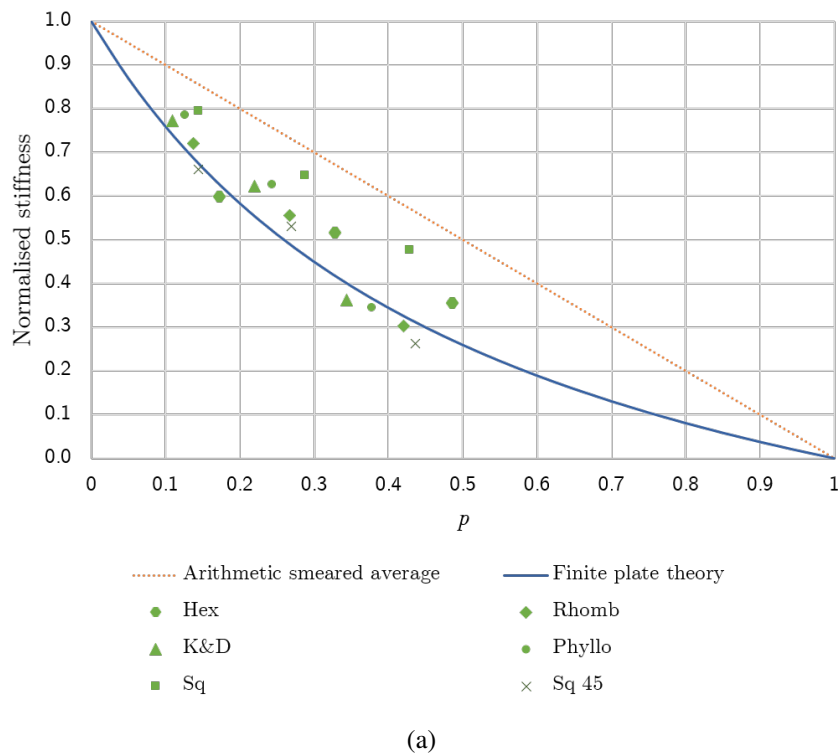


Fig. 4.38 The normalised uniaxial stiffness of perforated plates with regular and irregular patterns of perforations; (a) stretching, (b) bending. Finite plate theoretical prediction is plotted with $\nu = 0.3$.

the INSTRON machine started to become a relevant consideration, and as such the noise present in the data explains at least some of the scatter seen. The experimental data for the perforated sheet experiments is tabulated in Appendix F.

4.11 Rule-of-mixtures comparison

Calculating a smeared homogeneous material property value for a composite of two or more materials is a problem which is found in a variety of contexts, from metal alloys [47], traditional fibre reinforced composites [49], magnetic permeability of dielectrics [48] and even foamed concrete [52].

As a result, a number of different methods of estimating the smeared homogeneous properties have been developed and such methods are termed “rules-of-mixtures”. In general the packing fraction (volume fraction) and material properties of the two phases alone are not sufficient to completely define the overall smeared properties, as (for example) the shape of the inclusions can make a difference [50]. Many early studies give upper and lower bounds as predictions: the bounds of Hashin and Shtrikman (HS-bounds) are perhaps the the best known [48]. The arithmetic and harmonic smeared averages are also very widely known upper and lower bounds, but as seen in Section 4.7, they are not very tight bounds and thus do not provide much help in accurately predicting the smeared material properties.

HS-bounds are derived using a variational approach to magnetic permeability of a two phase material. Tighter bounds are established by Ravichandran [49], who considered a cube of material with a central cubic inclusion, under uniaxial tension, as a combination of little spring elements. Combining these little spring elements in various series and parallel arrangements, an upper and lower bound were calculated depending on if the springs were combined first in series and then parallel or *vice versa*. More recently Zhang *et al.* [64], extended the method of Ravichandran by progressively reducing the size of the springs. They found that in the infinitesimal limit, the upper and lower bounds converged to a single equation, *i.e.* irrespective of the order in which springs were combined in series and parallel, the stiffness prediction was equal.

A further model, known as the “Generalised Self-Consistent model” (GSC) [65, 66], considers a spherical inclusion, contained within a sphere of the matrix material, which itself is included within a large homogeneous medium which has material properties equal to the effective smeared properties of the matrix and inclusion. Using Love’s [67] general elasticity solutions, an energy equality argument is used to match the average strains and stress fields of the considered three phase model and a homogeneous model with the smeared properties. The “Mori-Tanaka” method [68] has a simpler derivation, and can be understood to act as

though each individual inclusion sees the nominal far field strain [69], however reaches exactly the same equation for smeared bulk modulus as the generalised self-consistent model.

The ‘‘Differential method’’ [70] starts with the assumptions of the ‘‘Dilute method’’ [71], taking a very low concentration of inclusions which are assumed not to interact. As the dilute method is suitable only for very low concentrations of inclusions, the differential method views the case as a series of dilute mixtures. First a small number of inclusions are added to the matrix and then this is viewed as a homogeneous material into which the next batch of inclusions are added. The process continues incrementally until the full packing density, p , has been met. The method yields an unwieldy set of simultaneous differential equations; only in very special cases can a simple closed form expression be reached.

While most authors deal with the case of a three dimensional block of material with spherical inclusions, there is some previous literature which explicitly seeks to deal with a two dimensional geometry. Zhang *et al.* perform the same infinitesimalising of series and parallel springs approach to analyse a square inclusion in a square plate [64]. Shevlyakov and Skoblin use an approximation of an average field stress is to estimate the smeared stiffness of a perforated plate [72].

Many authors calculate a smeared bulk modulus, B , and sometimes also a smeared shear modulus G . Rewriting the bulk modulus in terms of the Young’s modulus and the Poisson’s ratio, $B = E/(3(1 - 2\nu))$, we deduce that when the Poisson’s ratio of the inclusion and the matrix are the same, then the ratio of the bulk moduli is equal to the ratio of Young’s moduli, and thus we can directly compare these various rules-of-mixtures. Using consistent notation where p is the proportion of inclusions and k is the ratio of inclusion modulus to matrix modulus, the various rules-of-mixtures presented above can be written:

$$\Psi_{\text{Zhang3D}} = \frac{3k - 2(1 - p)(k - 1)}{3 + (1 - p)(k - 1)} \quad [64] \quad (4.62)$$

$$\Psi_{\text{Zhang2D}} = \frac{2k - (1 - p)(k - 1)}{2 + (1 - p)(k - 1)} \quad [64] \quad (4.63)$$

$$\Psi_{\text{GSC}} = 1 + \frac{p(k - 1)}{1 + \frac{(1 - p)(k - 1)}{1 + \frac{4G_1}{3B_1}}} = \frac{k \left(1 + \frac{4G_1}{3B_1}\right) - \frac{4G_1}{3B_1}(1 - p)(k - 1)}{1 + \frac{4G_1}{3B_1} + (1 - p)(k - 1)} \quad [66] \quad (4.64)$$

$$\Psi_{\text{Mori-Tanaka}} = 1 + \frac{p(k - 1)}{1 + \frac{(1 - p)(k - 1)}{1 + \frac{4G_1}{3B_1}}} = \frac{k \left(1 + \frac{4G_1}{3B_1}\right) - \frac{4G_1}{3B_1}(1 - p)(k - 1)}{1 + \frac{4G_1}{3B_1} + (1 - p)(k - 1)} \quad [68] \quad (4.65)$$

$$\Psi_{\text{FPT}} = \frac{2k - (1 - p)(k - 1)(1 - \nu)}{2 + (1 - p)(k - 1)(1 + \nu)} \quad (4.66)$$

where G_1 is the shear modulus of the matrix and B_1 is the bulk modulus of the matrix. The normalised stiffness calculated from the Finite Plate Theory presented in Section 4.5.2 is also shown for completeness and ease of comparison.

For the special case of $k = 0$, when the inclusions have zero stiffness *i.e.* perforations, holes or voids, then these rules of mixtures can be written in a simpler form. The equations for the differential model and the equation of Shevlyakov are also given:

$$\Psi_{\text{Zhang3D}} = \frac{2(1-p)}{2+p} \quad [64] \quad (4.67)$$

$$\Psi_{\text{Zhang2D}} = \frac{(1-p)}{1+p} \quad [64] \quad (4.68)$$

$$\Psi_{\text{GSC}} = \Psi_{\text{Mori-Tanaka}} = \frac{\frac{4G_1}{3B_1}(1-p)}{\frac{4G_1}{3B_1} + p} \quad [66, 68] \quad (4.69)$$

$$\Psi_{\text{Differential}} = (1-p)^2 \quad [70] \quad (4.70)$$

$$\Psi_{\text{Shevlyakov}} = \frac{(1-p)}{1+2p} \quad [72] \quad (4.71)$$

$$\Psi_{\text{FPT}} = \frac{(1-p)(1-\nu)}{2 - (1-p)(1+\nu)} \quad (4.72)$$

A helpful comparison study [52] compares the differential method (Eqn 4.70), dilute method, Mori-Tanaka model (Eqn 4.69) and generalised self-consistent model (Eqn 4.69) to experimental data of porous concrete [51]. The comparative study uses a Poisson's ratio of $\nu = 0.2$, but wrongly further simplifies Eqn 4.69 to $(1-p)/(1+p)$. In fact, this simplification actually occurs when $\nu = 1/3$, noting that for this value of Poisson's ratio $4G_1/3B_1 = 1$. Noting this simplification, and comparing Eqns 4.64 and 4.65 with Eqn 4.63, we see that when $\nu = 1/3$ and thus $4G_1/3B_1 = 1$, that all these three different methods produce identical expressions. Interestingly, when $\nu = 1/3$ and $k = 0$, the Finite Plate Theory formula, Eqn 4.72, simplifies to the same expression as Shevlyakov, Eqn 4.71.

4.11.1 Comparison of voids and empty inclusions

Each rule-of-mixtures considered here has the expected predictions of unity and zero at $p = 0$ and $p = 1$ respectively. As might be expected from the similar form of the equations, with the exception of the differential method, each curve has a similar shape and do not intersect each other. As noted before, the generalised self-consistent model expression is equal to the Mori-Tanaka expression and both are actually generalised forms of the Zhang expressions, where the term $4G_1/3B_1$ changes the factors multiplying the various bracketed expressions.

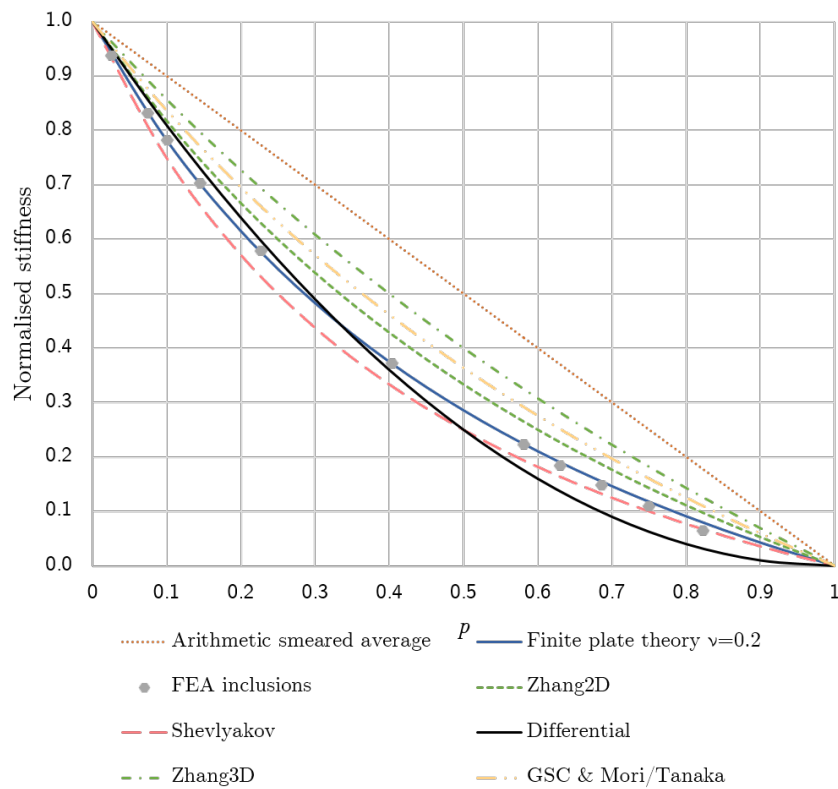


Fig. 4.39 FEA results for inclusion patterned plates, $k = 0$, $\nu = 0.2$, are compared with the various theoretical predictions from Eqns 4.67-4.72.

When $\nu = 1/3$, then the GSC expression is equal to the Zhang2D expression, but when $\nu = 0$ it becomes equal to the Zhang3D expression. For an intermediate value such as $\nu = 0.2$, the GSC expression therefore lies between the two Zhang expressions, which in this case leaves the Zhang2D expression as the most accurate prediction out of the three. As the Finite Plate Theory has the same form as the Zhang2D expression, but includes the Poisson's ratio terms, it perhaps should not be so surprising that the Finite Plate Theory captures the hexagonally patterned inclusion plate FEA results better still. As noted the Shevlyakov expression happens to correspond to the finite plate expression for $\nu = 0.5$. However, as the value of Poisson's ratio being considered in this case is $\nu = 0.2$, this necessitates that the Shevlyakov will predict a lower value than the Finite Plate Theory, and this prediction is indeed seen to fall below the experimental and FEA data. The differential method expression has the most unique form, not having any equivalence to the other expression under any conditions. It has an unusual behaviour at the higher values of p , becoming the lowest estimate by a considerable margin. Overall the Finite Plate Theory is seen to be the best rule-of-mixture for predicting homogeneous stiffness.

4.11.2 Comparison of stiff inclusions

When comparing rules-of-mixtures which allow for inclusions or arbitrary rigidity, similar trends are seen. Again the Zhang3D expression appears to overestimate the normalised stiffness quite significantly. While, for $\nu = 0.3$, the Zhang2D, GSC and Mori-Tanaka expressions are almost identical to each other, each slightly over-predict the values of stiffness seen from the FEA of inclusion patterned plates. As previously noted, the Finite Plate Theory expression reduces to the Zhang2D expression when $\nu = 0$, however as seen in Fig. 4.15, the Finite Plate Theory is excellent at capturing the behaviour with changes in Poisson's ratio. It is of interest to note that while simplifying using the standard expressions for bulk and shear modulus the term $4G_1/3B_1$ can be expressed $4G_1/3B_1 = 2(1-\nu)/(1+\nu)$, if instead the expression $(1-\nu)/(1+\nu)$ is inserted into the GSC expression, then the Finite Plate Theory expression is recovered.

Overall, the Finite Plate Theory is seen to be the best rule-of-mixtures out of all those considered for estimating the overall stiffness of inclusion patterned plates. Despite being formulated from the consideration of elastic circular inclusions in a two dimensional plate, comparison with other rules-of-mixtures and indicate that it may be also be useful in a much wider range of contexts as a powerful tool to predict the elastic modulus of composites, alloys, perforated plates or foamed materials.

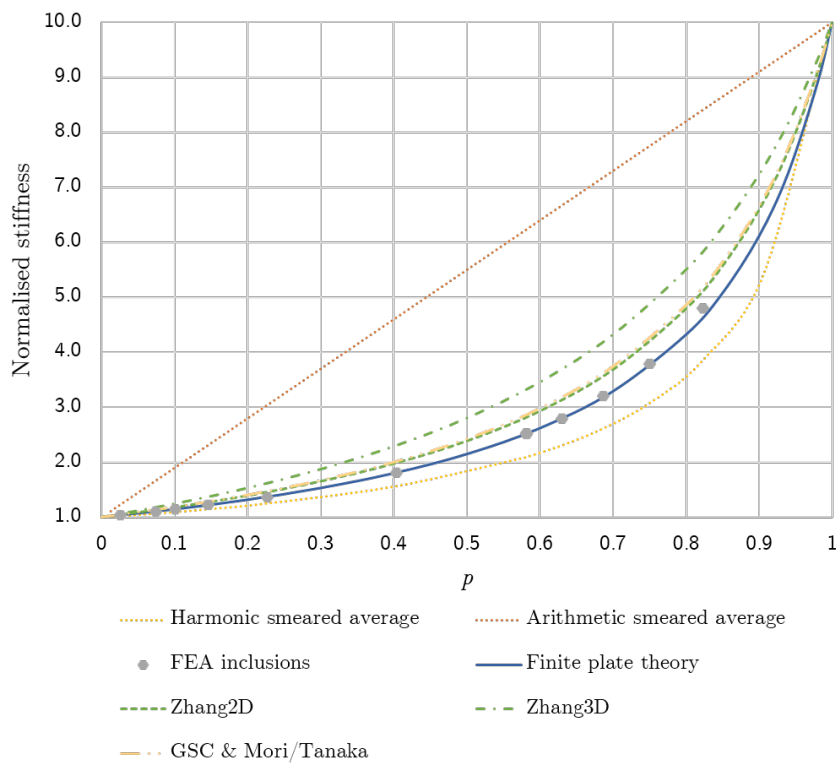


Fig. 4.40 FEA results for inclusion patterned plates, $k = 10$ $\nu = 0.3$, are compared with the various theoretical predictions from Eqns 4.62-4.66.

4.12 Conclusions

Predicting the overall initial elastic stiffness of a plate patterned with many elastic inclusions is a problem well suited to a homogenisation approach which seeks to characterise the plate with a smeared representative material properties. A novel theoretical derivation of an overall smeared stiffness for an inclusion patterned plate is derived from consideration of a single elastic inclusion of arbitrary stiffness within a circular plate of finite size, under an axisymmetric (biaxial) loading. By selecting the radius of the finite plate appropriately, this Finite Plate Theory is able to capture the homogenised stiffness of a plate patterned with many circular inclusions. The result allows for an arbitrary ratio of inclusion Young's modulus to plate Young's modulus and for differing values of Poisson's ratio. The resulting equation can be neatly expressed in terms of the proportion of the sheet which is made of inclusions, p , and this allows the result to be applied to irregular as well as regular patterns of inclusions. When the plate and the inclusion have the same value of Poisson's ratio the analytical result for smeared modulus simplifies further to a very compact form.

FEA shows that for a given pattern of inclusions, of an arbitrary stiffness, a single value of smeared Young's modulus is representative of the overall behaviour of the sheet in both bending and stretching, as well as under biaxial, uniaxial and antisymmetric loading. Inclusion patterned plates are observed to be strongly isotropic for all patterns when under biaxial loading. For Uniaxial loading irregular patterns and a regular hexagonal pattern are still isotropic, however the square pattern had a small degree of anisotropy. The homogeneity of an inclusion patterned plate was seen to be proportional to ratio of inclusion radius to overall plate side length.

Excellent agreement is seen between FEA results for plates patterned with many inclusions and the Finite Plate Theory formula. Agreement is seen to be excellent for regular and irregular patterns of inclusions, stiff and soft inclusions and over a wide range of Poisson's ratios. Excellent agreement is seen over a wide range of p , even for very high values of p where there is very close packing of inclusions and stress distributions around neighbouring inclusions strongly interact. The agreement remains excellent for uniaxial as well as anti-symmetric loading, and for bending as well as stretching. The theoretical prediction is also seen to be very good when the inclusions are square in shape, however it is noted that plates with inclusions of concave shape or different aspect ratios have slightly different normalised stiffnesses. Experimental data of perforated strips further confirms the applicability of the Finite Plate Theory. Comparison against existing "rules-of-mixtures" shows that the Finite Plate Theory is superior at predicting the smeared homogenised stiffness of an inclusion patterned plate. In particular, compared to existing homogenisation formulae, the dependence on Poisson's ratio is a noteworthy improvement.

Chapter 5

Patterned dimpled sheets

5.1 Summary

Combining the results of the preceding chapters, an analytical model of the initial elastic stiffness of a dimpled sheet can be formulated. Having established the equivalence of a single dimple within an infinite plate and an inclusion in an infinite plate, and subsequently predicted the overall smeared stiffness of an inclusion patterned plate, these results can be combined to predict the overall stiffness of a dimpled sheet.

Comparison against FEA of dimpled sheets shows that simply replacing each dimple with an elastic inclusion of the effective stiffness calculated for a single dimple in an infinite sheet gives an over-prediction of the overall stiffness of the sheet. Moreover, the decrease in realised stiffness compared to the prediction is more severe for higher packing densities. This apparent decrease in effective stiffness with increasing pattern density is here termed *k*-degradation. Drawing from the Finite Plate Theory analysis of inclusion patterned plates, which treated each inclusion in a patterned plate as a single inclusion within a circular plate of finite size, the effective stiffness of a dimple can be calculated considering the dimple within a finite plate of the appropriate radius. Such an analysis shows that the reduced horizontal restraint of a finite ring of material surrounding a dimple, compared to an infinite plate, is the cause of *k*-degradation. Considering the correspondingly modified effective stiffness of a dimple, the Finite Plate Theory prediction can be used to predict the overall stiffness of a dimpled sheet. Noting that the effective stiffness of the dimples will vary with the packing density of dimples. This combined theory is seen to provide excellent predictions of the initial biaxial bending stiffness of a dimpled sheet and also provide excellent predictions of the initial biaxial stretching stiffness. This is verified against FEA of dimpled sheets for a variety of dimple shapes and a range of packing densities.

Where adjacent dimples are in differing up and down directions respectively, the effective horizontal restraint of the surrounding plate is greater. Where a dimple is entirely surrounded by dimples in the opposing direction the horizontal restraint experienced by that dimple is

effectively the same as the restraint provided by an infinite sheet. Therefore it is seen that having up and down patterns of dimples can negate some of the impact of k -degradation. This provides rational to the slight increases in bending stiffness observed in the initial experimental results of dimpled sheets and additionally this behaviour is confirmed by FEA results.

Experimental testing of circular dimpled sheets is undertaken, utilising two concentric circular knife-edges to create a region of pure biaxial bending. The test set-up is considered analytically for the case of a flat plate. Results from experimental testing confirm that dimpled sheets have a higher biaxial bending stiffness than a flat plate, however the increase in initial stiffness is difficult to quantify due to highly non-linear force-displacement response of this set-up.

Unlike inclusion patterned plates, the normalised bending stiffness of a dimpled sheet is not independent of the type of loading. FEA shows that the normalised bending stiffness of a dimpled sheet under uniaxial bending is greater than the normalised stiffness of the same sheet under biaxial bending. While this increased stiffness cannot be captured by increasing the effective stiffness of the dimples, a good approximation can be made by scaling the increase in stiffness seen for the biaxial case by an empirically derived constant.

5.2 Introduction

In order to understand the structural behaviour of a dimpled sheet the work of the previous chapters is combined in order to derive an analytical equation for the initial elastic stiffness in bending and in stretching for a dimpled sheet.

Recall from Chapter 2 that a thin plate or sheet can have its bending stiffness increased by dimpling (the act of indenting the surface in order to produce a plastic deformation out of plane). Indeed, the increased stiffness is a geometric effect alone, and a sheet which is formed directly into such a geometry, *e.g.* by 3D printing, also has the same bending stiffness benefits.

Chapter 3 analysed the structural performance of a single dimple, in both bending and stretching. It was shown that a single dimple in an infinite plate may be considered to be an inclusion of the same radius, provided that the inclusion stiffness was chosen correctly. Formulae for the effective modular ratios of such inclusions were theoretically calculated for the case of biaxial stretching and biaxial bending, as functions of the dimple geometry. These theoretical predictions were validated against FEA. Additional FEA on single inclusions and dimples in an infinite plate subjected to uniaxial and antisymmetric load cases showed that

the effective inclusion stiffness was about 15% higher than the theoretical prediction in these cases, and gave a good equivalence for displacements and curvatures.

Chapter 4 then considered how patterns of inclusions in a plate behave and found that it was possible to take a homogenised smeared Young's modulus based on the modular ratio of the inclusions, k , and the proportion of the area which is inclusions p . An excellent agreement was seen with FEA of inclusion patterned plates, and FEA also confirmed that the overall stiffness of such plates was independent of both pattern and the type of loading.

Combining these results should therefore provide a good method of predicting the performance of a dimpled sheet, giving an overall homogeneous effective Young's modulus for bending and for stretching. First transforming each individual dimple into its equivalent inclusion, then smearing out the properties of these effective inclusions in order to arrive at the overall properties of the dimpled sheet.

Even without going into the details of this method, some initial conclusions can be instantly drawn. For example, this approach tells us why, in stark contrast to the Euler-Bernoulli structural depth analysis of Section 2.4, not much advantage is gained, if any, from having half of the dimples going up and the other half going down. Regardless of dimple direction, the dimple geometry is still the same and thus it will still be transformed into the same effective inclusion. Therefore, given the same effective inclusion stiffness, the overall plate stiffness will be the same.

5.3 Initial findings

Combining the theory of the previous two chapters, it is straightforward to make a prediction for the overall behaviour of a sheet patterned with dimples. For example, a spherical cap dimple with the geometry $a/t = 6$ and $d/a = 1/6$, has its value of k_{bend} theoretically calculated to be 1.920, or alternatively using an axisymmetric FEA a more accurate value can be calculated $k_{\text{bend}} = 1.798$; see Fig. 3.9. Utilising the Finite Plate Theory from Chapter 3, this value of k_{bend} , along with the proportion of the sheet which is dimpled, p , can be used to predict the overall bending stiffness of the sheet. Figure 5.1 compares the FEA results for normalised biaxial bending stiffness for sheets dimpled with hexagonal or square patterns of such spherical cap dimples.

For both the square and the hexagonal pattern, the Finite Plate Theory curve accurately predicts the overall stiffness for low values of p . However, as p increases, the achieved stiffness of the dimpled sheets falls distinctly below the predicted value, though it is interesting to note that both patterns do so in an identical fashion. In fact, the decrease in bending performance compared to prediction at high p is so pronounced that it even falls below the

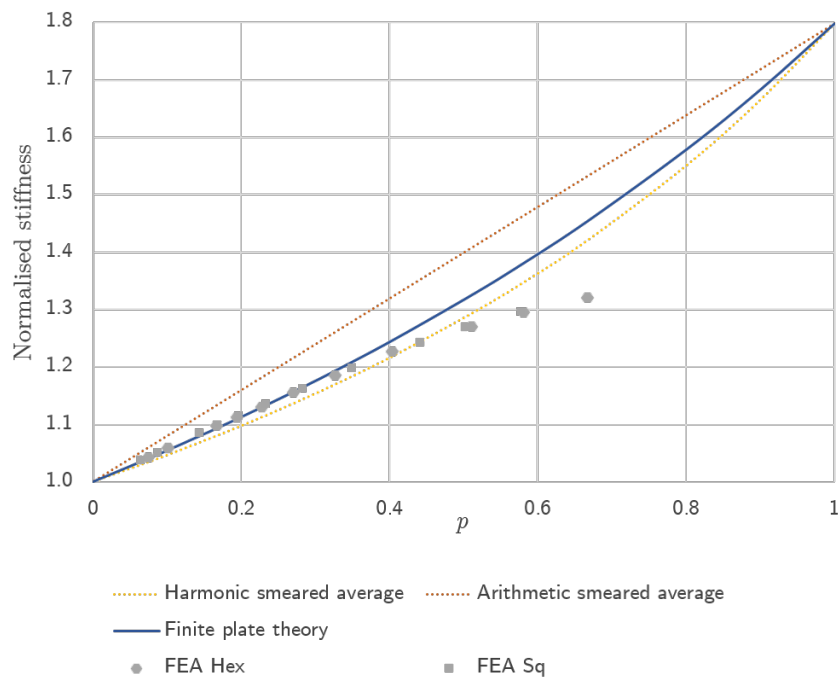


Fig. 5.1 FEA results of normalised biaxial stiffness for a dimpled sheet with spherical cap dimples with geometry $a/t = 6$ and $d/a = 1/6$. Hexagonal and square patterns of dimples are modelled and the sheet has $\nu = 0.3$. From Fig 3.9 the effective stiffness in bending for such a dimple is $k_{\text{bend}} = 1.798$, harmonic, arithmetic and Finite Plate Theory predictions are plotted for this value of k .

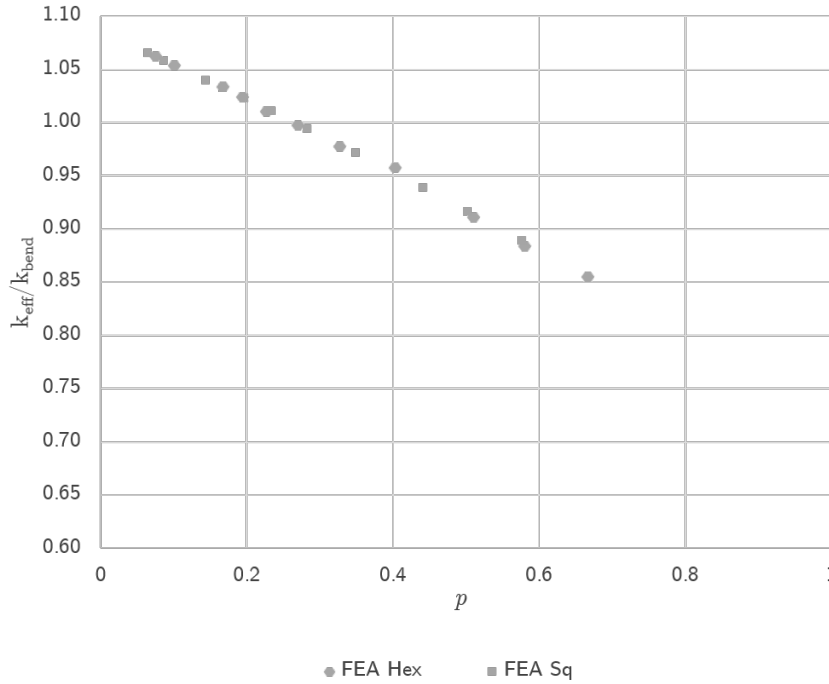


Fig. 5.2 The normalised stiffnesses of dimpled sheets in Fig. 5.1 are used to calculate effective inclusion stiffnesses using Eqn 5.1. These values of k_{eff} are divided by the nominal k_{bend} values from the axisymmetric FEA, to find a normalised measure of the dimple performance compared to expectation.

harmonic smeared average, a strange occurrence as the harmonic smeared average is known to be an absolute lower bound on rules-of-mixtures.

As the Finite Plate Theory was seen to be very good at estimating the performance of inclusion patterned plates, it is possible to use it to back calculate the effective value of inclusion stiffness, k_{eff} , for the dimples in each case given the overall stiffness of the dimpled sheet. Starting with the Finite Plate Theory expression from Eqn 4.40:

$$\Psi_{\text{FPT}} = \frac{2k - (1-p)(k-1)(1-\nu)}{2 + (1-p)(k-1)(1+\nu)} \rightarrow k_{\text{eff}} = \frac{2\Psi - (1-p)[(1+\nu)\Psi + (1-\nu)]}{2 - (1-p)[(1+\nu)\Psi + (1-\nu)]} \quad (5.1)$$

There are two interesting phenomena to note from Fig. 5.2. The first and most important is that there is a degradation in the realised values of k when the dimples get packed close together and p increases. This “ k -degradation” is almost linear and is identical for both the square and hexagonal patterning. Secondly, the effective k for small values of p is slightly greater than the predicted value of k_{bend} . Careful inspection of Fig. 5.1, confirms that indeed,

the normalised stiffness seen in FEA is slightly higher than the predicted Finite Plate Theory value for the lowest values of p .

The presence of both of these phenomena is unexpected, however, both will be explained in the following sections. Section 5.4 outlines the FEA methodology for modelling dimpled sheets and then section 5.5 builds upon the theoretical analysis presented in previous chapters to more fully capture the initial structural behaviour of dimpled sheets.

5.4 FEA methodology

The finite element analysis conducted on dimpled sheets is based on the FEA of inclusion patterned plates from section 4.6, and as such shares much in common. Again, linear elastic models were tested in both bending and stretching using ABAQUS [37].

Dimpled sheets are modelled as per the inclusion case, but with dimples of a given geometry instead of inclusions of a given modular ratio, see Fig. 5.3. The dimples are of either spherical cap or quartic shape and are modelled for a variety of a/t and d/a ratios. In-plane forces and applied moments per unit length apply loading to the edges. Using appropriate mirror symmetry conditions, only a quarter of the overall plate needs to be analysed, for computational efficiency; the mesh distribution itself is fine and non-uniform to mitigate mesh sensitivity effects. A sufficiently large number of dimples are modelled so that edge effects are confined in very narrow bands, much smaller than the plate width. The geometry is tricky to construct using the ABAQUS graphical interface, and therefore the geometry is made in Rhino [73], and imported into ABAQUS as a STEP geometry file format. As before, quadratic shell elements (SR8) are used as a full 3D modelling would require a much larger number of elements to accurately model the geometry, and the computational cost required to run such simulations would be prohibitive. Selected geometries were modelled using quadratic full 3D stress elements (C3D10), and these simulations confirmed the validity of using the shell elements. The geometry of the mid-surface of the dimpled sheet profile is defined as a shell, and then the shell thickness is defined by the section properties. The mesh shown in Fig. 5.4a contains 54802 shell elements in the quarter sheet model, leading to 325848 degrees of freedom on the model and the corresponding model in Fig. 5.4b has 137124 solid elements leading to 824352 degrees of freedom. Production FEA analyses for the dimpled sheet data presented in this chapter utilise a finer mesh to increase the accuracy of the results, a typical analysis has 225000 quadratic shell elements and 4000000 degrees of freedom, equating to each dimple being modelled with approximately 600 shell elements.

When the dimples intersect the edge of the modelled plate, the boundary edge is no longer a straight line, but undulates up and down slightly. Applying a bending moment to

such a boundary is not problematic, despite the extra length of edge to which the moment per unit length is applied. When a moment per unit length is applied to a edge with a gradient the moment per unit length applied perpendicular to the plate thickness is just equal to the projected horizontal length of the line; the other component of the bending moment acts as a small twisting force, but by the nature of the dimple's shape, this will be cancelled out by an equal and opposite twist from the other side of the dimple. By Saint-Venant's principle the effect of these twisting moments will only be seen locally as an edge effect as overall they cancel out. Thus overall, the total moment applied to the edge will be equal to the nominal moment $2LM_0$.

When an in-plane force is applied to the edge of the plate, more care needs to be taken. In applying a force per unit edge directly to the edge of the plate, the total force applied will be greater than the nominal force assumed because the undulating edge which cuts through some dimple cross-sections has a slightly greater length. However, even more problematically, because the dimples undulate vertically from the mid-plane of the plate, the overall force is not acting in same plane as the mid-plane of the plate, and this force acting at a small lever arm causes a moment. In order to alleviate these problems, when dimpled sheets are tested in biaxial in-plane tension the edge loading is applied only to the boundary regions of flat plate, and not where the boundary intersects a dimple. The total length of flat boundary edge which is being loaded is calculated and the applied loading per unit length is scaled up accordingly such that the correct total load is applied. While this method will cause differences in stresses locally, via Saint-Venant's principle, the middle of the sheet will still have the correct behaviour. Normalised stiffnesses will therefore be extracted by considering the deformation of a central unit cell, rather than the displacement at the very edge of the sheet.

The quadratic shell elements, by the nature of their formulation, assume a plane stress condition and therefore zero stress in the through-thickness direction. While the shell elements do neglect through-thickness stress, this is not a bad assumption, as the dimpled sheets are very thin and thus through-thickness stresses are negligible. However, due to their implementation they model a slightly different geometry to that of the assumed constant vertical thickness dimple profile. The shell model assumes a constant through-thickness, rather than vertical thickness; while this was exactly equivalent in the inclusion case, as the geometry was completely flat, this is not so for dimples. The undulating surface of a dimple necessitates that the mid-surface has a greater surface area than the nominal area in plan view, πa^2 . The shell elements model therefore models a slightly larger total volume of material, *i.e.* slightly larger than the nominal volume of $4L^2t$, for a plate with side length $2L$ and thickness t . Figure 5.4 shows a comparison between a shell element mesh and a solid element mesh

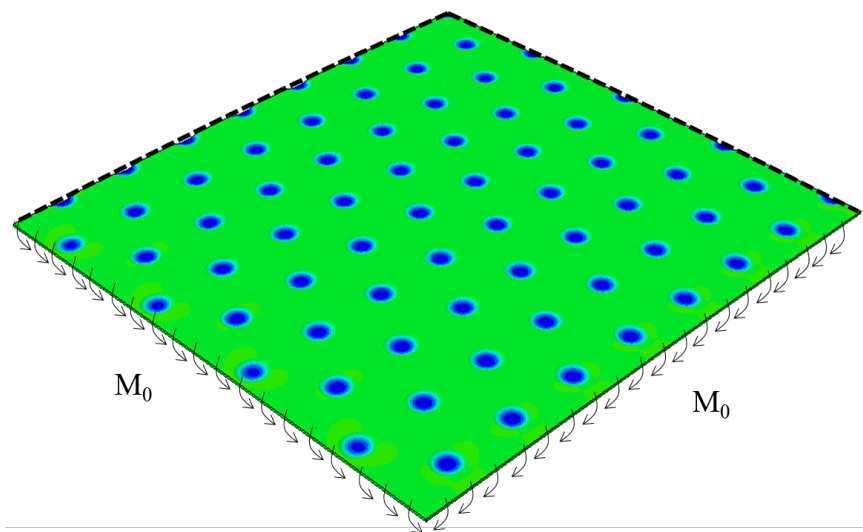
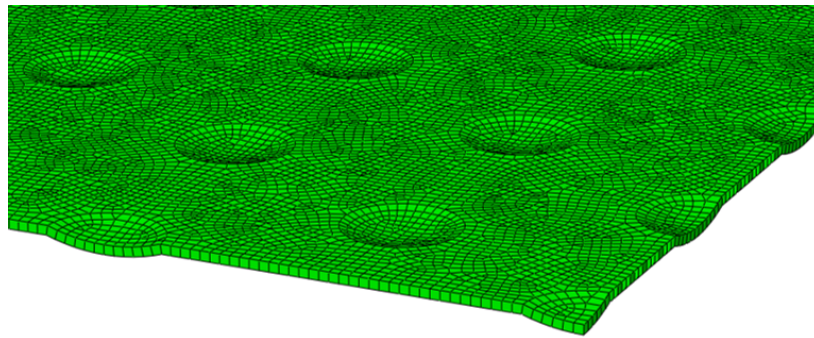
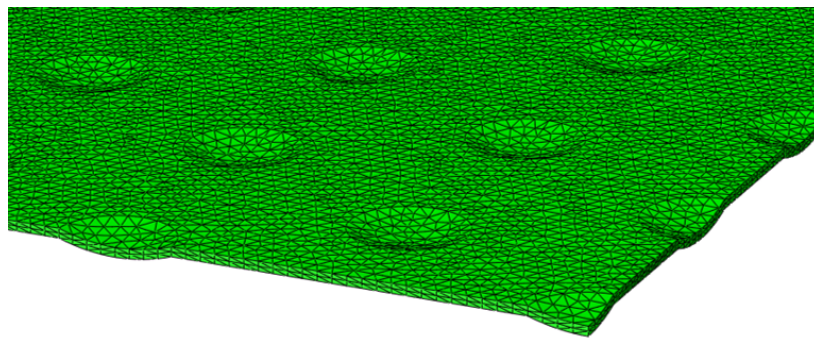


Fig. 5.3 A quarter model of a square plate with a hexagonal pattern of dimples, modelled in ABAQUS [37]. Equal moments per unit length load the two outer edges with M_0 equal to unity, the edges indicated with a dark dashed line have symmetry boundary conditions applied to them, constraining each edge to remain in its corresponding plane of symmetry, and enforcing a zero rotation perpendicular to the plane of symmetry. Colour contours show SCFs with a range from [Dark blue, 0] to [Red, 2]. Here spherical cap dimples are modelled with: $a/t = 6$, $d/a = 1/6$, $\nu = 0.3$, gap-ratio = $8/3$; thus $p = 0.1666$. Dimples of this shape are close up in Fig. 5.4. The radius of the dimples compared to the half-length of the sheet is $a/L = 3/100$.



(a)



(b)

Fig. 5.4 A comparison of the mesh of a dimpled sheet modelled in FEA: (a) shell elements (SR8), (b) solid elements (C3D10).

for the same dimpled sheet. Because of the extra material modelled in each dimple, the k_{bend} value for the same dimple geometry is slightly larger when using shell elements than when using solid elements. The stiffness parameters extracted from axisymmetric FEA analysis of a dimple ($a/t = 6$, $d/a = 1/6$) when modelled with shell elements and solid elements respectively are shown in Table 5.1. As expected we see that the shell elements, due to modelling slightly more material, give slightly stiffer results. Note that while this is of the order of 10% for bending, the stretching stiffness in each case is almost identical.

5.5 Analytical model of dimpled sheets

The differences between the FEA results for dimpled sheets presented in Fig. 5.1, and theoretical prediction which simply combined the theory from Chapters 3 and 4, indicates the need for a slight development of the theoretical analysis for sheets with patterns of dimples.

Table 5.1 Comparison of stiffness parameters of a dimple modelled with shell and solid elements; $a/t = 6$, $d/a = 1/6$, $\nu = 0.3$.

	α_1	α_2	α_3	α_4	k_{bend}	k_{stretch}
FEA shell	0.2847	0.8932	0.8932	1.2687	1.9523	0.3388
FEA solid	0.2810	0.9381	0.9381	1.1657	1.7982	0.3382

5.5.1 Over-prediction of k_{bend}

For a dimple with a given nominal geometry, a small difference in the bending stiffness is realised in the FEA model depending on whether shell or solid elements are used to model it, which sheds light on the second of the phenomena noted from Fig. 5.2. Using a shell element representation of a dimple geometry gives a slight over-prediction of the bending stiffness. When predicting the performance of a dimpled sheet as modelled with shell elements, *e.g.* Fig. 5.4a, the corresponding value of bending stiffness should be that of the dimple modelled by shell.

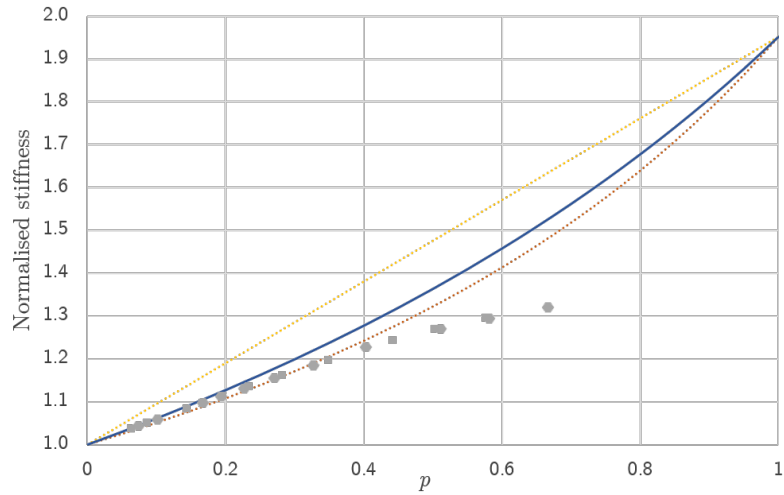
Therefore, for the dimpled sheets in Fig. 5.1, a value of $k_{\text{bend}} = 1.952$ should be used rather than 1.782. Normalised stiffnesses from FEA of dimpled sheets are compared with the Finite Plate Theory prediction using $k_{\text{bend}} = 1.952$ in Fig. 5.5a. The corresponding k -degradation, Fig. 5.5b, confirms that this is the correct value to use, as the effective stiffness of the dimples approaches this value of k_{bend} as the packing density approaches zero; *i.e.* $k_{\text{eff}}/k_{\text{bend}} \rightarrow 1$ as $p \rightarrow 0$.

While not strictly a change in the theoretical analysis, this does highlight an important feature of any FEA simulations of dimpled sheets. When predicting the behaviour of a sheet modelled by solid elements or a physical dimpled sheet, a value of k_{bend} from the solid element axisymmetric analysis should be used to give the most accurate prediction.

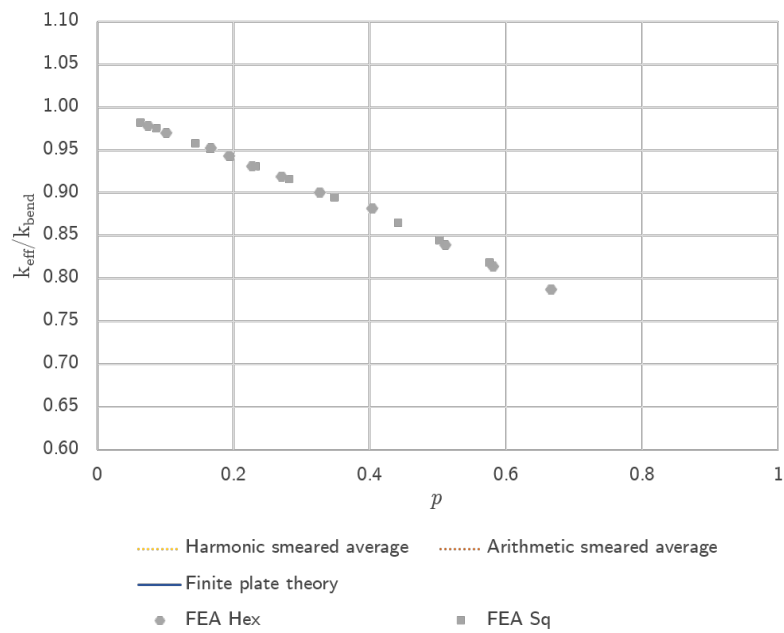
5.5.2 k -degradation

Of greater importance and consequence to the analytical model is the first phenomenon noted from Fig. 5.2, namely k -degradation, the tendency for the effective stiffness of a dimple to decrease as packing proportion, p , increases. The effective k values for dimples can be back calculated from the FEA results for normalised stiffness using Eqn 5.1.

Consider the behaviour of a dimple under bending, Fig. 5.6. When it is bent, it also naturally wants to undergo a horizontal displacement at its edge. This coupling of stretching and bending gives rise to the α_3 term, see Eqn 3.23. A dimple completely restrained from



(a)



(b)

Fig. 5.5 (a) Normalised biaxial stiffness of dimples sheet from Fig. 5.1 is compared against homogenisation theory predictions using the FEA shell element value of $k_{\text{bend}} = 1.952$. (b) The k -degradation when accounting for this slightly increased value of k_{bend} .

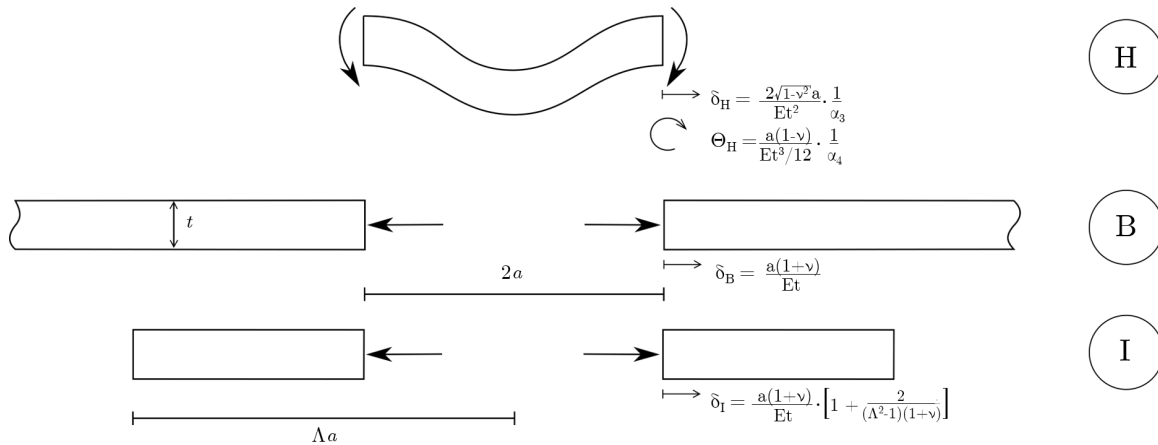


Fig. 5.6 A general dimple in bending has both a resulting edge rotation and horizontal edge displacement (H). The horizontal restraint provided by an infinite plate around a hole (B) is greater than that of a finite hoop of material (I). Compare to Fig. 3.7.

horizontal expansion would therefore have an increase in its bending stiffness. For a given applied moment, a horizontal in-plane force which prevents the horizontal displacement is provided by the restraint, and this force, via α_2 , acts to oppose the rotation of the dimple. When a dimple is part of an infinite plate, it does experience some, but not total, horizontal restraint due to the surrounding material. This is why the value of k_{bend} , the bending stiffness of a dimple included in a plate, is greater than α_4 , the bending stiffness of a dimple on its own. As we are considering a linear elastic response, it is clear that the surrounding plate restrains horizontal expansion and contraction equally. Thus for a single dimple in an infinite plate, neither the sense of the dimple and the sense of the loading affect the initial stiffness.

The superposition analysis of Section 3.4.3 considered a dimple and an inclusion which were at the centre of an infinite plate. The horizontal restraint provided by a finite hoop of material is obviously going to be slightly less than the restraint offered by an infinite plate. Calculating the stiffness of a finite hoop of material to an internal loading (see Appendix D), the displacement of the internal edge for a unit load is given as δ_I , Fig. 5.6. Comparing to δ_B , the displacement of the internal edge of a hole in an infinite plate due to a unit load, confirms that the finite plate is less stiff (it displaces more under the same load), and that as $\Lambda \rightarrow \infty$, that $\delta_I \rightarrow \delta_B$.

As deduced in Section 4.5.2, for a pattern of inclusions in a large plate, it is permissible to treat each inclusion as a single inclusion in a finite circular plate which has an equal area to the average tile area of that pattern, *i.e.* treat each inclusion to be at the centre of a finite plate with radius $\Lambda = \sqrt{1/p}$. Therefore instead of analysing the equivalence of a dimple and an inclusion in an infinite plate, when considering the effective stiffness of a dimple which is in a

patterned sheet the superposition analysis should consider how a dimple and inclusion behave when part of a finite plate of radius $\Lambda = \sqrt{1/p}$. Conducting the superposition analysis of Section 3.4.3, but using the finite plate (superposition state I) rather than the infinite plate (superposition state B), we find that similarly to before:

$$k_{\text{bend}}^* = \frac{\alpha_4}{1 - \gamma^*} \quad (5.2)$$

where the expression for γ is now slightly adjusted to include the p term:

$$\gamma^* = \frac{\Theta_G \delta_H}{\Theta_H (\delta_I + \delta_G)} = \frac{(1 + \nu) \alpha_4}{\left(1 + \nu + \frac{2p}{1-p} + \frac{1-\nu}{\alpha_1}\right) \alpha_2 \alpha_3} \quad (5.3)$$

Increasing the value of p , decreases the value of γ^* and a lower value of γ^* thus decreases the value of k_{bend}^* . A higher value of p consequently has a smaller finite plate, which provides less horizontal restraint, therefore it has a smaller ability to increase the bending stiffness of the dimple. This equation shows how putting dimples closer together decreases their effective stiffness, providing an analytical basis for k -degradation. When $p = 0$ then the original expression for γ is recovered. Similarly for the effective stiffness of a dimple in stretching:

$$k_{\text{stretch}}^* = \frac{\alpha_1}{1 - \zeta^*} \quad (5.4)$$

with the adjusted expression for ζ :

$$\zeta^* = \frac{(1 + \nu) \alpha_1}{\left(1 + \nu + \frac{2p}{1-p} + \frac{1-\nu}{\alpha_4}\right) \alpha_2 \alpha_3} \quad (5.5)$$

As the value of ζ was already very small for a typical dimple, the reduction due to p is almost negligible when considering the value of k_{stretch}^* . As before, the stretching stiffness of a dimple in a plate is approximately equal to the stiffness of that dimple by itself, $k_{\text{stretch}}^* \approx \alpha_1$.

The superposition analysis indicates that there will be a state of in-plane stress around a dimple in bending, even if a pure biaxial bending is applied globally. An inclusion has no coupling between stretching and bending, and therefore an inclusion subjected to a pure global bending moment will have no in-plane stresses, only the bending stresses. However, as in-plane forces do not affect the initial bending performance of a flat plate, a dimple and an inclusion of the equivalent stiffness can be treated as interchangeable. Correspondingly, a dimple under a global biaxial stretching, because of its bending–stretching coupling will impart a small bending moment on the surrounding plate. However, not only does this

bending moment decay with the inverse square of normalised radius, but any resulting curvatures due to the moments do not affect the initial in-plane performance of the sheet.

5.5.3 Up–down dimples

While the direction of a single dimple in an infinite plate has no effect on the bending performance, changing the orientation of the dimple does affect the sense of the surrounding in-plane stresses, although the magnitude remains unchanged. For a dimple which is orientated with respect to the loading direction as per Fig. 5.6, the bending induces an outward horizontal displacement, which leads to a tensile in-plane hoop stress. However for a dimple which is the other way up, the bending would induce an inward horizontal contraction, which leads to a compressive in-plane hoop stress. For dimples which are in the same direction as each other, the in-plane stresses during bending are all of the same sense, and so each dimple behaves as though in a finite plate of radius $\Lambda = \sqrt{1/p}$. However, if a dimple is surrounded by dimples which are in the opposite direction, then the surrounding in-plane stress fields are of an opposite sense and the restraint to horizontal displacement which the surrounding plate provides is equal to the infinite plate case. Therefore for up-down patterns of dimples the effective value of k_{bend} can be up to the maximum value calculated for the infinite plate case. While having alternating upwards and downwards facing dimples does not provide the significant amount of performance enhancement that was predicted from the flawed second moment of area calculations of Chapter 2, it does have the ability to negate the effects of k -degradation.

Ideally an up-down pattern would fully surround each dimple with dimples of the opposite direction. However, a quick consideration shows that this ideal can never be achieved in practice. For example, taking a hexagonal pattern and surrounding a single up dimple with six down dimples, instantly we find that each down dimple is adjacent to two other down dimples: thus it is impossible to have every dimple surrounded by only dimples of the opposite direction.

Two alternative up-down patterns of dimples based on the regular hexagonal patterning are shown in Fig. 5.7. Each dimple in Fig. 5.7a has an identical set of surrounding dimples, however the pattern is globally anisotropic. In the Hex up-down B pattern, Fig. 5.7b, there is global isotropy as it exhibits six-fold rotational symmetry. However, not each dimple is alike in its surroundings: of the six surrounding dimples some dimples have four opposite direction dimples, other dimples are surrounded entirely by opposite direction dimples, whereas some are adjacent to just three opposite direction dimples. In both cases however, on average four out of six of the surrounding dimples are in the opposite direction.

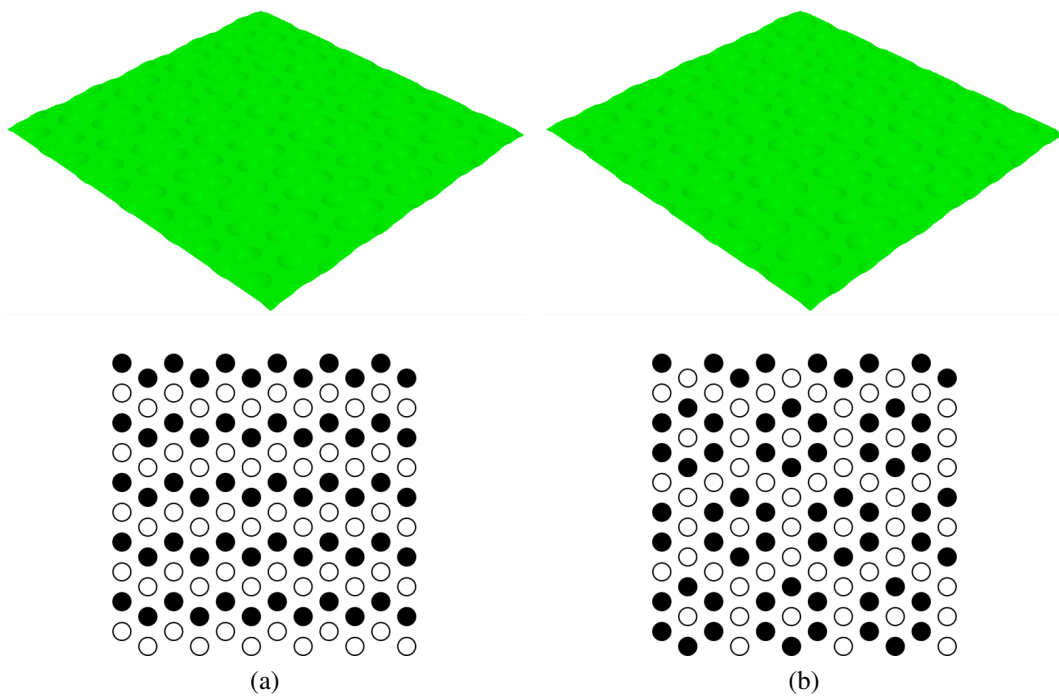


Fig. 5.7 For the hexagonal patterning, two alternative up-down dimple patterns are presented. In both cases exactly 50% of dimples are in each direction. (a) Hex up-down A, (b) Hex up-down B.

FEA results for biaxial bending of a sheet dimpled in the Hex up-down A pattern, $p = 0.6663$, using spherical cap dimples with $a/t = 6$ and $d/a = 1/6$, show a 31% difference in bending stiffness between the two orthogonal directions, with $\Psi = 1.7206$ and $\Psi = 1.3111$ respectively. The same dimpled sheet but using the Hex up-down B pattern has a measured normalised biaxial bending stiffness of $\Psi = 1.4791$ and $\Psi = 1.4816$, less than a 0.2% difference.

While as previously discussed the k -degradation would be entirely negated if each dimple was entirely surrounded by opposite direction dimples, in realisable up-down patterns where this is not quite the case we expect the k -degradation to be only partly negated. For the hexagonal up-down patterns in Fig. 5.7 four out of six surrounding dimples were in the opposite direction, and thus it seems reasonable to assume that two thirds of the k -degradation will be negated.

5.5.4 Stress concentration factors

The ability to predict the maximum stress concentration factor in a dimpled sheet allows for the prediction of the maximum stress in the sheet under an applied loading, which allows for a prediction of when first yield will occur and thus the effective yield strength of the dimpled sheet. The influence which large residual stresses generated by an indentation process have on the yielding of a dimpled sheet is not considered here. However, dimpled sheet manufactured by 3D printing or indented dimpled sheets subjected to subsequent annealing to remove the residual stresses will have first yielding dependent on the maximum SCFs calculated in this section. The stress distributions around a dimple and around an inclusion in a plate in biaxial bending are identical for an inclusion with the correct effective stiffness. However, the stress distribution within the dimple itself and within the inclusion are quite different: see Fig. 3.15 which shows the case of a single dimple and a single inclusion within an large plate. An inclusion has a high, practically constant radial and circumferential stress; however, in a dimple the stresses decay away quickly, oscillating around zero. The maximum stress concentration factor for an inclusion sheet is in the inclusion itself, however the maximum stress in the plate also needs to be calculated to account for a potential difference in yield stress between the plate material and inclusion material, see Section 4.5.2. For a dimpled sheet, the dimple and the plate are made of the same material and thus the yield strength should be constant, therefore only the location of maximum stress needs to be considered, which for the dimpled case is at the edge of the dimple. The stresses are equal to those at the inclusion/plate interface and are given by:

$$\frac{\sigma_{1rr}}{\sigma_0} = \frac{K^*}{1 + (K^* - 1)p} \quad \frac{\sigma_{1\theta\theta}}{\sigma_0} = \frac{2 - K^*}{1 + (K^* - 1)p} \quad \frac{\sigma_{1tt}}{\sigma_0} = 0 \quad (5.6)$$

where $K^* = 2k^*/[(1 - \nu) + (1 + \nu)k^*]$ and k^* is the relevant effective dimple stiffness accounting for the packing density p of the pattern. Thus the maximum normalised radial stress can be written:

$$\frac{\sigma_{1rr}}{\sigma_0} = \frac{2k^*}{(1 - \nu) + (1 + \nu)k^* + (k^* - 1)(1 - \nu)p} \quad (5.7)$$

The maximum von Mises stress can be calculated using the expression

$\sigma_{\text{vonMises}} = \sqrt{0.5[(\sigma_{rr} - \sigma_{\theta\theta})^2 + (\sigma_{rr} - \sigma_{tt})^2 + (\sigma_{\theta\theta} - \sigma_{tt})^2]}$, which gives a maximum von Mises stress around a dimple as:

$$\frac{\sigma_{\text{vonMises}}}{\sigma_0} = \frac{\sqrt{3K^{*2} - 6K^* + 4}}{1 + (K^* - 1)p} \quad (5.8)$$

Using a Tresca criterion, first yield will occur when the maximum difference between any pair of principle stresses is equal to σ_{Y1} . For a dimple in bending $\sigma_{1\theta\theta} > 0$ so $\sigma_{Y1} = \sigma_{1rr} - \sigma_{1tt}$ but for a dimple in stretching $\sigma_{1\theta\theta} < 0$ thus $\sigma_{Y1} = \sigma_{1rr} - \sigma_{1\theta\theta}$. The overall yield stress of the dimpled sheet is:

$$\text{Bending} \quad \sigma_{Y\text{Dimpled}} = \sigma_{Y1} \frac{1 + (K^* - 1)p}{K^*} \quad (5.9)$$

$$\text{Stretching} \quad \sigma_{Y\text{Dimpled}} = \sigma_{Y1} \frac{1 + (K^* - 1)p}{2 - K^*} \quad (5.10)$$

Alternatively, using von Mises criterion, the effective yield stress of the overall plate is governed when the maximum von Mises stress reaches σ_{Y1} , and is thus:

$$\sigma_{Y\text{Dimpled}} = \sigma_{Y1} \frac{1 + (K^* - 1)p}{\sqrt{3K^{*2} - 6K^* + 4}} \quad (5.11)$$

However, although the overall stiffness of patterns of inclusions and dimples is very well predicted using Finite Plate Theory, the stresses are not quite so accurately captured. A conservative estimate of the maximum SCF in a dimpled sheet can be calculated assuming a single dimple in an infinite plate, $\sigma/\sigma_0 = K$. This infinite plate theory prediction would thus predict a lower bound on the first yield stress of the dimpled sheet:

$$\sigma_{Y\text{Dimpled}} = \sigma_{Y1} \frac{(1 - \nu) + (1 + \nu)k}{2k} \quad (5.12)$$

5.6 Biaxial behaviour of dimpled sheets

Using the analysis of shells of revolution (or axisymmetric FEA) to calculate the stiffness parameters $\alpha_1 - \alpha_4$, and then using the adjusted superposition theory described in Section 5.5, an accurate value of effective stiffness can be calculated for any given dimple geometry. Using these values of k_{bend} and k_{stretch} , the Finite Plate Theory can accurately predict the overall stiffness in bending and stretching for a sheet patterned with dimples. As seen in Chapter 4, the exact patterning should not affect the overall stiffness, rather just the packing density of the pattern p is required. Therefore for any well distributed pattern a very accurate prediction of overall stiffness should be able to be made.

If a dimpled sheet has dimples in both the up and the down direction, the effective values of stiffness can be calculated by using the proportion of the adjacent dimples which are of the opposite sense to negate some of the k -degradation effect.

5.6.1 FEA results: Biaxial bending

Normalised stiffness

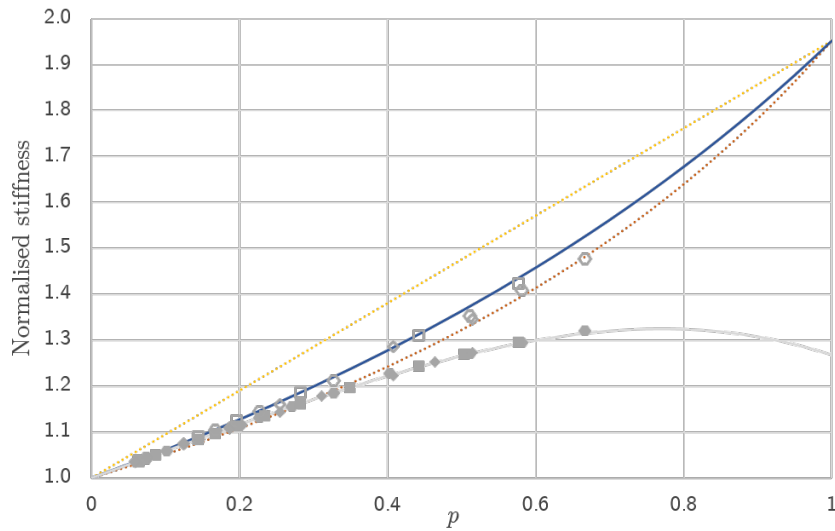
Using the FEA methodology laid out in Section 5.4, the bending stiffness of dimpled sheets under biaxial bending was found for a variety of patterns and dimple profiles. The normalised bending stiffnesses were then compared against the theoretical predictions. In particular the use of the graph of k -degradation is especially helpful in comparing the accuracy of the theory.

To plot the FEA data for k -degradation, as before, use the Finite Plate Theory to back calculate the effective dimple stiffness, Eqn 5.1, then divide by the nominal dimple stiffness which is calculated assuming it is in an infinite plate. To calculate the theoretical curve for k -degradation we take the dimple stiffness accounting for the finite plate, Eqn 5.2, and divide by the nominal value of k_{bend} to find:

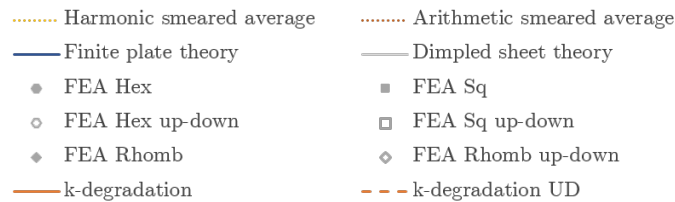
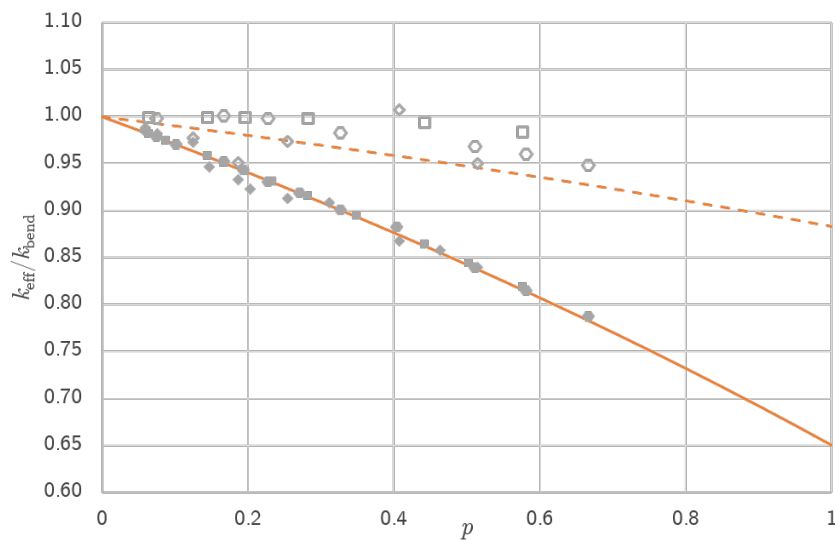
$$k\text{-degradation} = \frac{1 - \gamma}{1 - \gamma^*} = \frac{1 - \frac{(1+\nu)\alpha_4}{\left(1+\nu+\frac{1-\nu}{\alpha_1}\right)\alpha_2\alpha_3}}{1 - \frac{(1+\nu)\alpha_4}{\left(1+\nu+\frac{2p}{1-p}+\frac{1-\nu}{\alpha_1}\right)\alpha_2\alpha_3}} \quad (5.13)$$

Assuming that the hexagonal up-down pattern negates two thirds of the k -degradation, we can calculate:

$$k\text{-degradation UD} = 1 - \frac{\gamma - \gamma^*}{3(1 - \gamma^*)} \quad (5.14)$$



(a)



(b)

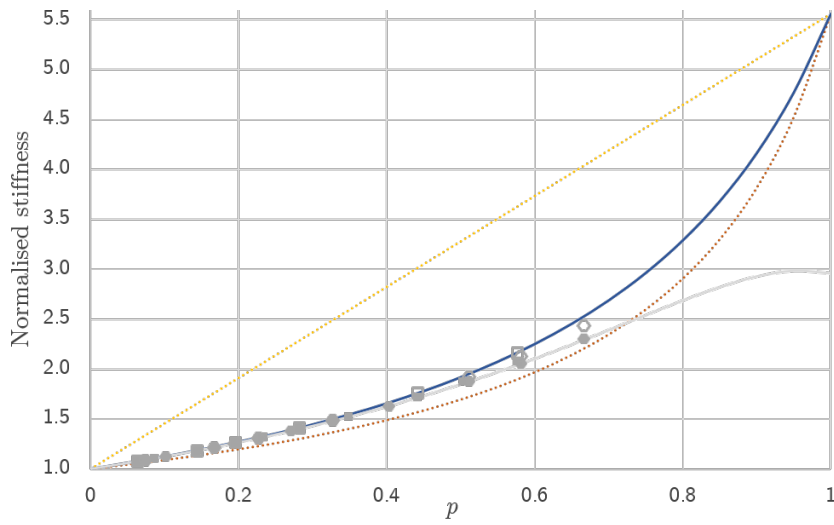
Fig. 5.8 FEA results of dimpled sheets with various patterns of dimples are compared to theoretical predictions. Spherical cap dimples are used with $a/t = 6$, $d/a = 1/6$ and $\nu = 0.3$. (a) Normalised biaxial stiffness is compared to the Finite Plate Theory with a constant value of $k_{\text{bend}} = 1.952$ and against the complete dimpled sheet theory, Eqn 5.18, which accounts for k -degradation with increasing p . (b) Back-calculated effective dimple stiffnesses are calculated from FEA and the corresponding k -degradation is compared against theoretical k -degradation.

Figure 5.8a shows normalised biaxial stiffnesses of dimpled sheets extracted from FEA models for a variety of patterns. The same hexagonal, square and Penrose Rhombus patterns are the same as for the inclusion patterned plates in Section 4.7. The dimples have a spherical cap geometry with $a/t = 6$ and $d/a = 6$, the dimple radius to half-width of the sheet is $a/L = 3/50$ and the Poisson's ratio is $\nu = 0.3$. The up-down patterning for the hexagonal pattern is Hex up-down B, Fig. 5.7b. The square up-down patterning has alternating up and down dimples such that the four adjacent dimples are all of the opposite direction, in a similar fashion to Fig. 4.1b. The up-down pattern for the Penrose Rhombus pattern is as described in Appendix C.

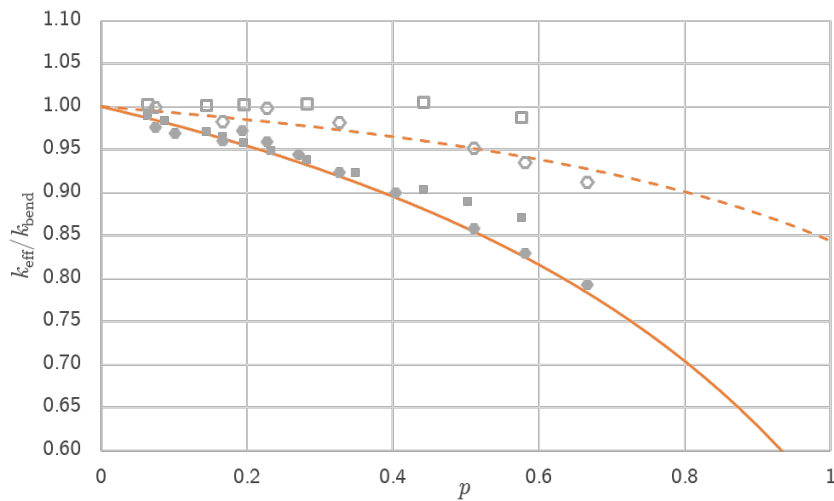
When all the dimples are in the same direction, the pattern has almost no influence on normalised stiffness. As found from the FEA results of inclusion patterned plates, the overall stiffness is essentially independent of pattern. Comparing the k -degradation, Fig. 5.8b, confirms the independence of pattern. Furthermore, an excellent agreement is seen between the measured k -degradation from FEA and the predicted k -degradation from Eqn 5.13.

As noted before, the up-down patterns of dimples have a slightly superior performance in bending, almost attaining standard Finite Plate Theory prediction. There is not much influence on bending performance depending on the pattern, as for the single dimple direction case. However, there is a slight variation: for example for a given p , the square up-down pattern seems to have a slightly higher stiffness. This is understandable, as for a square pattern all four of the nearest dimples are in the opposite direction, whereas in the hexagonal pattern only four out of the adjacent six dimples were in the opposite direction. Therefore we would expect that the square up-down pattern would negate the k -degradation effects even more than the hexagonal up-down pattern. We do not expect a total negation for the square up-down pattern, because the next nearest surrounding dimples, the four dimples which are diagonally adjacent, are in the same direction. The theoretical prediction that the up-down patterning negates two thirds of the k -degradation compares reasonably well with FEA – in fact, it even seems to be marginally conservative prediction.

For the comparatively thick dimple in Fig. 5.8, k_{bend} had a reasonably low value. The trends and compatibility of theory to FEA seen for this low stiffness dimple also hold true for dimpled sheets with a spherical cap dimple with $a/t = 30$, $d/a = 1/6$, $\nu = 0.3$ and hence $k_{\text{bend}} = 5.562$, see Fig. 5.9. For stiffer dimples a key observation is that k -degradation does not influence the overall normalised stiffness as much. The normalised biaxial stiffness of the dimpled sheets is pretty close to the standard Finite Plate Theory, even when the dimples are all in the same direction. However, considering Fig. 5.9b, the k -degradation itself is more severe for this dimple. The theoretical predictions of k -degradation once again compare very



(a)



(b)

Fig. 5.9 FEA results of dimpled sheets with various patterns of dimples are compared to theoretical predictions. Spherical cap dimples are used with $a/t = 30$, $d/a = 1/6$ and $\nu = 0.3$. (a) Normalised biaxial stiffness is compared to the Finite Plate Theory with a constant value of $k_{bend} = 5.562$ and against dimpled sheet theory, Eqn 5.18. (b) k -degradation.

accurately with FEA. For this stiffer dimple, the difference in k -degradation between the square up-down pattern and hexagonal up-down pattern is more pronounced.

It is important to also check that the theoretical predictions are not just valid for the spherical cap dimple profiles. FEA results of normalised stiffness for dimpled sheets with quartic dimples are shown in Fig. 5.10a. The quartic dimples chosen have the geometric parameters $a/t = 30$ and $d/a = 1/3$, and with a Poisson's ratio of $\nu = 0.3$, this gives $k_{\text{bend}} = 3.762$. Again the normalised stiffnesses are seemingly independent of pattern, and the k -degradation, Fig. 5.10b, is accurately predicted by the theory.

In general the k -degradation is more severe for dimples with a higher value of γ , *i.e.* the reduction in the ratio of effective dimple stiffness to nominal dimple stiffness decreases more when there is more bending–stretching coupling. The quartic dimple, Fig. 5.10, has $\gamma = 0.242$ and it has less k -degradation than either of the spherical cap dimple cases, Figs 5.8–5.9 which have values of $\gamma = 0.351$ and $\gamma = 0.467$ respectively.

Stress concentration factors

The maximum stress concentration factors seen from FEA are plotted against the predictions of maximum SCF from Eqns 5.7–5.8 and Eqn 5.15, Fig. 5.11.

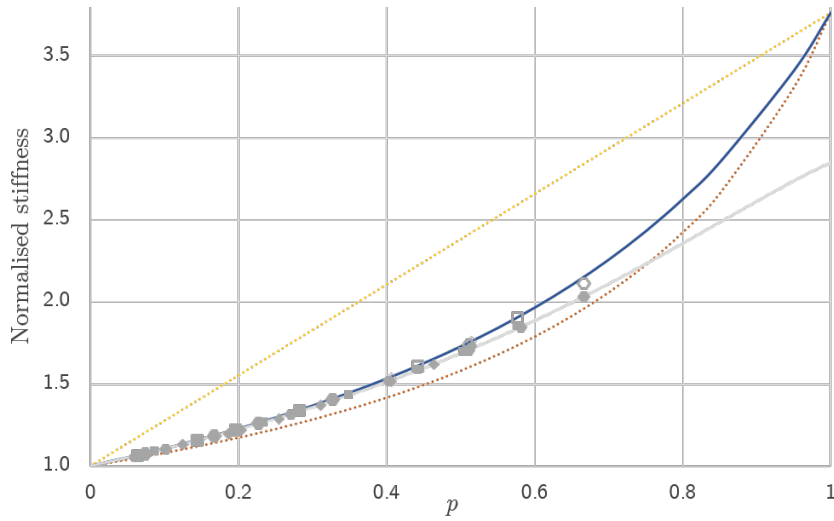
Unlike the inclusion patterned plates, where the maximum SCF was seen inside the inclusion, for dimpled sheets the maximum SCF occurs just outside the dimple. Rather than the whole circular inclusion being subjected to this maximum stress, only a thin ring of material around the dimple is highly stressed. The maximum stresses observed in the FEA dimpled sheets approximately fall between the predictions of maximum stress from Eqn 5.7 and Eqn 5.8. Additionally, the FEA results show that the up-down dimpled sheets tend to have higher SCFs than when all the dimples are in the same direction. The SCFs seen are quite varied, and the square and rhombus patterns develop higher stresses than the hexagonal pattern. Considering the variation between the different patterns, the best idea is to assume that the infinite plate theory approximation for SCF provides an upper bound. *I.e.* the maximum SCF developed in a dimpled sheet is:

$$\frac{\sigma_{\text{Dimpled}}}{\sigma_0} = K = \frac{2k}{(1-\nu) + (1+\nu)k} \quad (5.15)$$

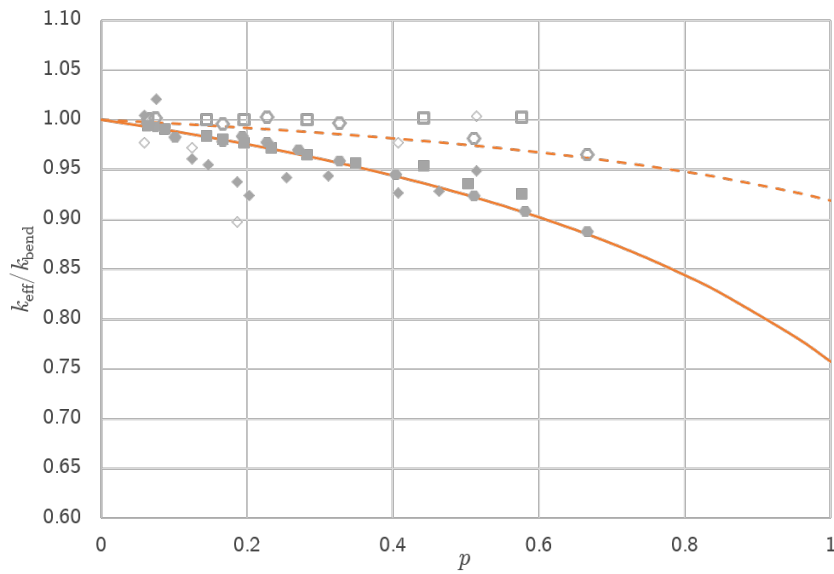
Therefore a good, yet conservative, prediction of the overall first yield stress of a dimpled sheet is:

$$\sigma_{Y_{\text{Dimpled}}} = \sigma_{Y1} \frac{(1-\nu) + (1+\nu)k}{2k} \quad (5.16)$$

where k is the stiffness of a dimple in an infinite plate.



(a)



(b)

Fig. 5.10 FEA results of dimpled sheets with various patterns of dimples are compared to theoretical predictions. Quartic dimples are used with $a/t = 30$, $d/a = 1/3$ and $\nu = 0.3$. (a) Normalised biaxial stiffness is compared to the Finite Plate Theory with a constant value of $k_{\text{bend}} = 3.762$ and against dimpled sheet theory, Eqn 5.18. (b) k -degradation.

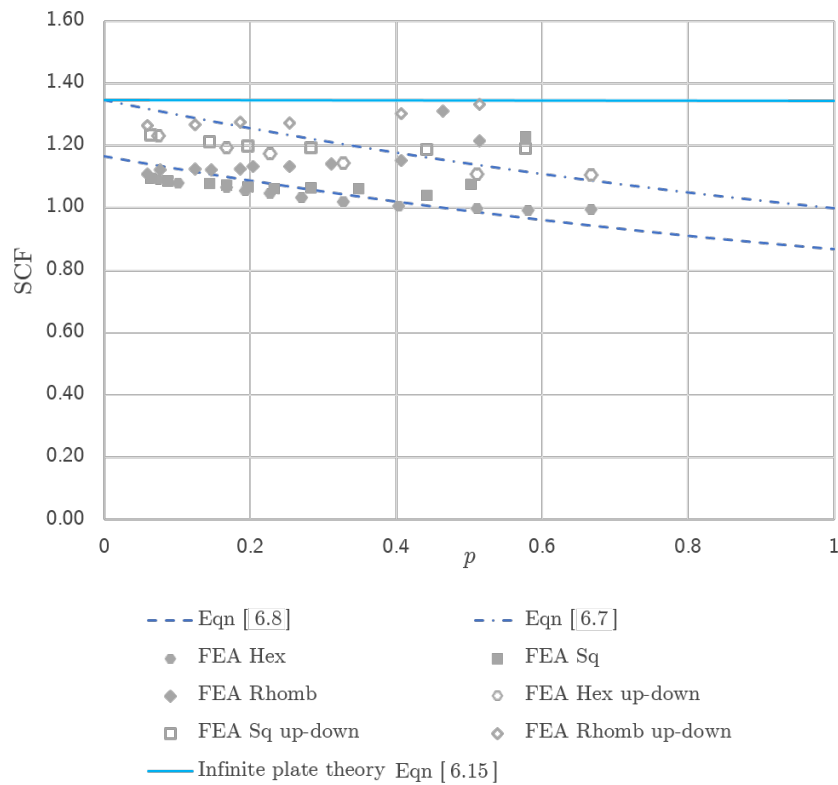


Fig. 5.11 SCFs from FEA of dimpled sheets with various patterns of dimples are compared to theoretical predictions. Quartic dimples are used with $a/t = 30$, $d/a = 1/3$ and $\nu = 0.3$.

5.6.2 FEA results: Biaxial stretching

The case of biaxial stretching of a dimpled sheet is quite similar to that of biaxial bending. Using the same FEA methodology, but applying normal edge forces per unit length instead of applied moments per unit length, the normalised stiffnesses in stretching were calculated by extracting the horizontal displacements.

The most obvious difference is that while dimpled sheets are stiffer in bending than a flat sheet, because generally $k_{\text{bend}} > 1$, they are less stiff in stretching due to $k_{\text{stretch}} < 1$. However the theoretical analysis is practically unchanged, calculating k_{stretch} for a dimple in a plate using the superposition method, the normalised stiffness is well predicted by the Finite Plate Theory. Calculating the effective k_{stretch} for the dimple in a finite plate allows for an excellent prediction of how k -degradation is affected by p .

As for the bending case, the normalised stiffness in biaxial stretching, Fig. 5.12a, is slightly less than the standard Finite Plate Theory curve when all the dimples are in the same direction, and is independent of pattern. When the dimples are half up and half down, the normalised stiffness is much closer to the standard Finite Plate Theory prediction, in fact unlike the biaxial bending case, the stiffness is even slightly higher than predicted. Figure 5.12b indicates that the k -degradation seen for the single direction dimples is very well predicted, however the up-down dimples actually have a slight increase in effective k_{stretch} with increasing p . The increase is only minor, and as such, it would be perfectly reasonable, and also conservative, to simply assume that in biaxial stretching there is no k -degradation for up-down dimple patterns.

5.6.3 Homogeneous smeared properties

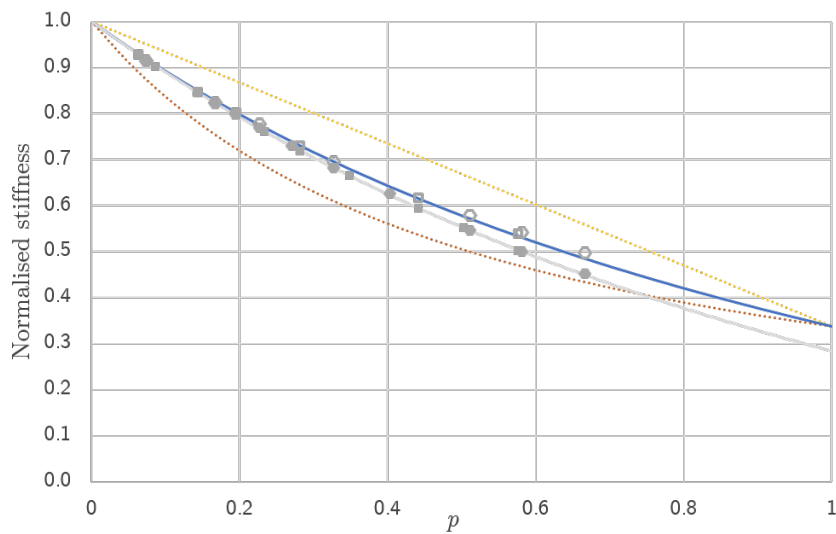
For a dimpled sheet in biaxial bending or stretching, with material properties E_1 and ν , the overall homogeneous Young's modulus is:

$$E_{\text{Dimpled}} = E_1 \Psi_{\text{Dimpled}} \quad (5.17)$$

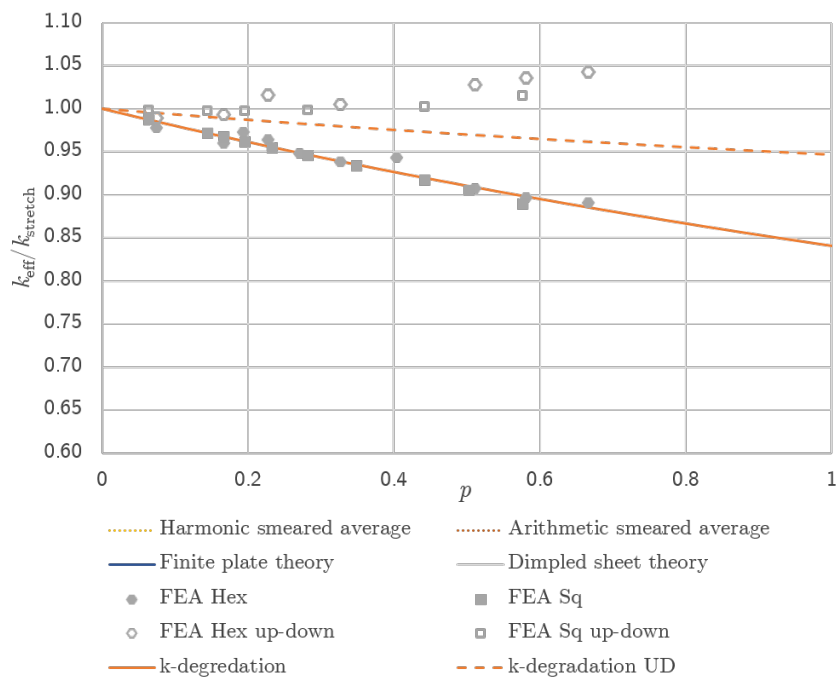
where the normalised stiffness is given by the Finite Plate Theory equation:

$$\Psi_{\text{Dimpled}} = \frac{2k^* - (1-p)(k^* - 1)(1-\nu)}{2 + (1-p)(k^* - 1)(1+\nu)} \quad (5.18)$$

The effective stiffness of a dimple, k^* , is given by consideration of geometry, and differs depending on whether bending or stretching is being considered. The effective stiffness of a dimple also is affected by the dimple packing proportion, p , as seen via k -degradation. For dimples which are all in the same direction:



(a)



(b)

Fig. 5.12 FEA results of dimpled sheets with various patterns of dimples are compared to theoretical predictions. Spherical cap dimples are used with $a/t = 6$, $d/a = 1/6$ and $\nu = 0.3$. (a) Normalised biaxial stretching stiffness is compared to the Finite Plate Theory with a constant value of $k_{\text{stretch}} = 0.3388$ and against dimpled sheet theory, Eqn 5.18. (b) k -degradation.

$$k_{\text{bend}}^* = \frac{\alpha_1}{1 - \gamma^*} \quad \text{where} \quad \gamma^* = \frac{(1 + \nu)\alpha_4}{\left(1 + \nu + \frac{2p}{1-p} + \frac{1-\nu}{\alpha_1}\right)\alpha_2\alpha_3} \quad (5.19)$$

$$k_{\text{stretch}}^* = \frac{\alpha_1}{1 - \zeta^*} \quad \text{where} \quad \zeta^* = \frac{(1 + \nu)\alpha_1}{\left(1 + \nu + \frac{2p}{1-p} + \frac{1-\nu}{\alpha_4}\right)\alpha_2\alpha_3} \quad (5.20)$$

A conservative lower bound on the stress at which first yield will occur in a dimpled sheet, assuming a material yield stress of σ_{Y1} , is:

$$\sigma_{Y_{\text{Dimpled}}} = \sigma_{Y1} \frac{(1 - \nu) + (1 + \nu)k}{2k} \quad (5.21)$$

This prediction assumes that the greatest stress in a dimpled sheet is equal to that which occurs around a single dimple in an infinite sheet, not accounting for any possible reduction due to finite plate effects or a lowering effective dimple stiffness due to an increase in p .

5.7 Experimental validation

5.7.1 Experimental methodology

The analytical predictions of the biaxial stiffness of dimpled sheets match very well with the FEA results. Experimental work would provide a further way to verify the analytically predicted performance of dimpled sheets.

Given that the theory is based on biaxial behaviour, and that the main interest in dimpled sheets is the increase in performance in bending, the experimental set-up should ideally test a sheet in pure uniform biaxial bending. However, this is challenging to achieve practically. Loading a flat square sheet in biaxial bending, each of the edges which are being loaded do not remain straight, but rather begin to curve. This makes it very difficult to apply a moment to each edge but without adding any additional restraint. A common test to impart a uniform uniaxial bending moment is a four-point bend test, where two pairs of knife-edge supports are used at each edge of the sample to induce a constant uniaxial moment region in the central section. However, trying to apply this methodology to each direction of a square sheet becomes problematic: each edge of a plate in pure biaxial loading has transverse curvature, however the knife-edge supports do not.

One way to overcome this problem is to exploit the circular symmetry of biaxial bending. Using two concentric circular knife-edge supports, each diametric cross-section is effectively a four-point bend test, Fig. 5.13. However, because the deflected shape of a biaxially bent

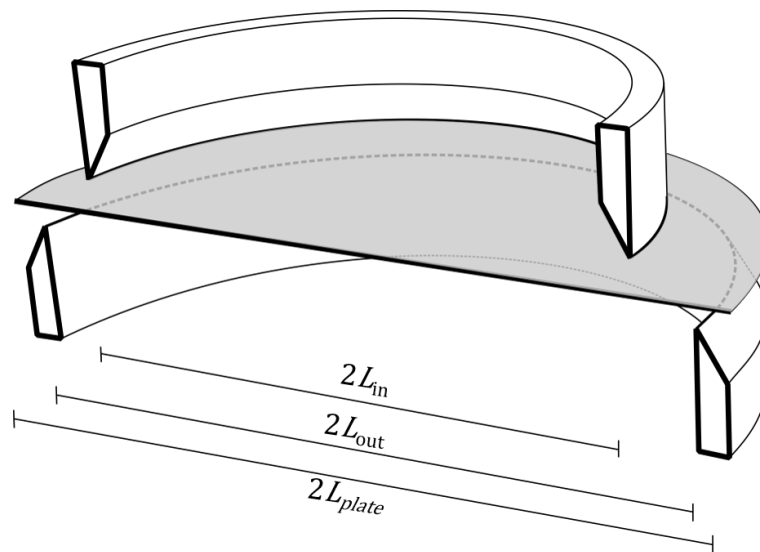


Fig. 5.13 A diametric cut-through of the biaxial bending test rig set-up. A circular plate is supported between two concentric circular knife-edge supports. The top support is pressed downwards, which induces a constant uniform biaxial bending moment in the central circular region. The radius of the inner support is L_{in} , the radius of the outer support is L_{out} and the radius of the plate is L_{plate} .

plate is axisymmetric, a ring at a given radius in the plate will be planar and thus the plate will remain in contact with both the inner and outer circular knife-edge supports. Pressing the top knife-edge support downwards will induce a constant uniform biaxial bending moment in the central circular region of the plate.

However, this set-up has a few complications and is not as straightforward to analyse as a uniaxial four-point bending test. For example, in a standard four-point bending test, the magnitude of the uniform bending moment per unit width in the central span is simply the applied force per unit length at each knife-edge support multiplied by the lever arm between each pair of supports. In the biaxial bending rig, although the level arm is well defined, $L_{out} - L_{in}$. Applying a total force of F to the upper support, we would calculate a force per unit length of $F/(2\pi L_{in})$. However, from equilibrium we know that the same total reaction force must be applied from the lower support, but here the force per unit length is $F/(2\pi L_{out})$. It is not clear therefore whether the magnitude of the uniform central bending moment is equal to $(L_{out} - L_{in})F/(2\pi L_{out})$ or $(L_{out} - L_{in})F/(2\pi L_{in})$. In reality the answer is neither, but rather it is somewhere inbetween.

Timoshenko presents the case of a circular plate simply supported on its boundary and loaded with a ring load [74], which is equivalent to the biaxial test rig case when $L_{out} = L_{plate}$. In this case the magnitude of the central bending moment is:

$$M = \frac{F(L_{\text{out}} - L_{\text{in}})^2(1 - \nu)}{8\pi L_{\text{out}}^2} - \frac{F \ln \frac{L_{\text{in}}}{L_{\text{out}}}(1 + \nu)}{4\pi} \quad (5.22)$$

and the corresponding deflection at inner support is:

$$\delta|_{L_{\text{in}}} = \frac{F}{8\pi D} \left[(L_{\text{out}}^2 - L_{\text{in}}^2) \left(1 + \frac{1 - \nu}{2(1 + \nu)} \frac{L_{\text{out}}^2 - L_{\text{in}}^2}{L_{\text{out}}^2} \right) + 2L_{\text{in}}^2 \ln \frac{L_{\text{in}}^2}{L_{\text{out}}^2} \right] \quad (5.23)$$

where D is the flexural rigidity of the plate, $D = \frac{Eh^3}{12(1-\nu^2)}$. Therefore from a practical test in an INSTRON machine, where the deflection of the upper support, $\delta|_{L_{\text{in}}}$, and the total force applied, F , are measured outputs of the test, Eqn 5.23, can calculate a value of D for the plate. If the plate was patterned with dimples over the whole plate, then we would assume that the value of D would simply be scaled up uniformly across the plate, and thus simply taking the ratio of the F/δ stiffnesses of a flat plate to the different samples would allow for calculation of normalised stiffness. However, in order to get a distributed continuous contact with the circular edge supports, only the centre section of the plate can be dimpled.

However unfortunately, unlike a uniaxial four-point bend test, the biaxial bending test is not quite so straightforward. If the middle section of the plate is more stiff than the rest of the plate, then the moment distribution changes. A similar analysis assuming that the central dimpled region of the plate has an effective stiffness of k , has to be performed in order to find an equation that relates the force-displacement characteristic of the ring to the effective stiffness of the middle section. Additionally, a practical consideration is that the circular plate being tested must have a slightly larger radius than that of the outer support, or else it would be prone to slipping and falling inside the outer support. Unlike the uniaxial four-point bend test, the presence of an overhang outside the outer support affects the moment distribution and the measured stiffness of the circular plate. While in the uniaxial case the material which overhangs the outer support is completely unloaded, in the biaxial case this is not so. It is not immediately obvious why this is so, however consider the plate without any overhang: there is a radial rotation at the support, therefore a ring of plate which overhangs must also have a compatible rotation at the support. While in the uniaxial case the overhanging material had no restraint and could freely adopt this outer support rotation, the circular overhanging ring must have an applied internal moment to adopt this shape, because forming from a flat ring into a conic slice is opposed by circumferential hoop stresses. This has the effect of modifying Eqn 5.23, where an additional term represents the additional stiffness of such a plate due to an overhang. Appendix D.2 derives the modified equations which describe

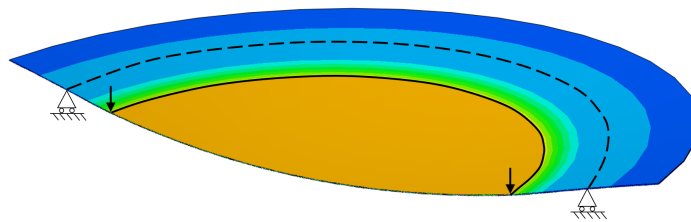


Fig. 5.14 A biaxial bending test rig set-up is analysed using FEA. An axisymmetric analysis is used, so just one two dimensional slice is modelled. The figure here shows a visualisation of the results swept around 180° . Von Mises stresses are shown and colour contours range from [Dark blue, 0 MPa] to [Red, 0.15 MPa]. The plate is simply supported against vertical movement at L_{out} , indicated as a dashed black line. The force response is recorded as a downwards displacement is imposed at L_{in} , solid black line. For this particular case shown: $L_{in} = 50\text{mm}$, $L_{out} = 60\text{mm}$, $L_{plate} = 80\text{mm}$, $t = 0.5\text{mm}$, $k = 3$, $E = 120000\text{ MPa}$ and $\nu = 0.3$.

the combined case, a circular plate which has a stiff central section and also an arbitrary overhang. The displacement at L_{in} is calculated in terms of the applied force F in Eqn D.15.

Axisymmetric FEA is conducted on the biaxial bending rig set-up, the plate is simply supported against vertical movement at L_{out} , and the force response is recorded as a downwards displacement is imposed at L_{in} . Comparison of the plate stiffness from FEA confirms the theoretical stiffness calculated in Appendix D.2. For the geometry shown in Fig. 5.14, the initial stiffness from FEA is $F/\delta = 20.5897\text{N/mm}$. The theoretical stiffness from Eqn D.15 is $F/\delta = 20.5901\text{N/mm}$, a difference of less than 0.002%.

The theoretical calculation matches the FEA results very well, and therefore using Eqn D.15 it is possible to back-calculate an effective stiffness of the central region of the sheet from the force-displacement characteristic measured from a practical test.

Practical experimentation was undertaken using the custom made testing rig shown in Fig. 5.15. Circular plate samples were manufactured with $L_{plate} = 65\text{mm}$. Choosing a relatively small overhanging width reduces the dependence of stiffness on the overhang. Dimple patterned sheets were produced using the same four patterns as the dimpled sheets in Section 2.5, however just the central circular region was dimpled, Fig. 5.16. In addition the hexagonal pattern forming plate was also used to produce a sparse hexagonal pattern. In addition to the dimple forming techniques used in Section 2.5, the dimpling process was found to have a non-negligible influence on the global curvature of the dimpled sheets. The self-stress caused by the dimple forming process induced a global curvature on the plates, of the order of a several plate thickness. The self-stress itself will not have any influence on the initial bending stiffness of the dimpled sheet, however the resulting change in global curvature will. In order to combat this, a heat treatment was used. Keeping the dimpled sheets clamped in the forming plates in order to retain their flat global shape, an oven applied

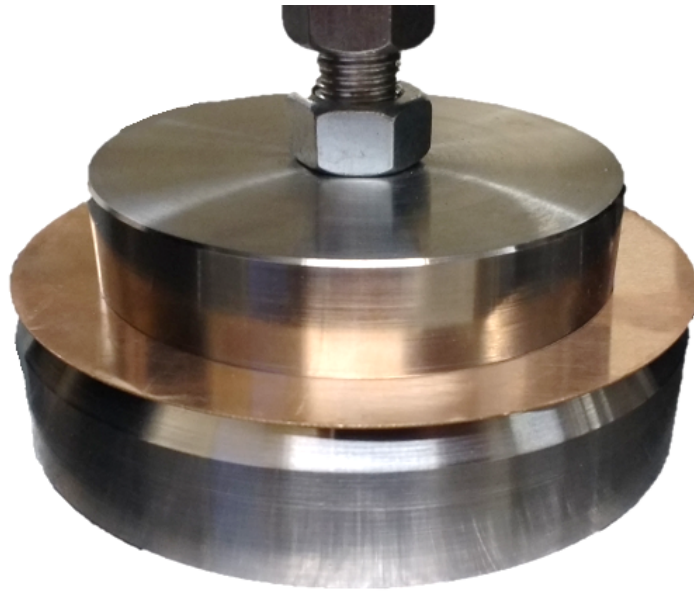


Fig. 5.15 The experimental biaxial bending test rig set-up used for the INSTRON testing. The steel top and bottom loading rings have knife-edges, as per Fig. 5.13, as well as solid plates which connect them to the INSTRON machine. The test rig is made with $L_{in} = 50\text{mm}$ and $L_{out} = 60\text{mm}$.

a heat treatment of 400°C for 6 hours. By applying this high temperature heat treatment the stress relaxation is practically total [75], and thus the self-stresses caused by dimpling are completely relaxed, therefore the dimpled sheets no longer adopt the induced curved shape but rather are globally flat, Fig. 5.17. An additional feature of this heat treatment process is the change in yield stress. Copper beryllium alloys are prized for their high increase in yield strength due to heat treatment. However, while the yield stress can be affected significantly by a heat treatment, the Young's modulus is not, and thus initial stiffness should remain unchanged. Additionally, the colour of the copper beryllium changes during the heat treatment, tarnishing and dulling the bright shiny copper colour of the non heat-treated plate.

5.7.2 Experimental results

The dimpled sheets are tested in the biaxial bending rig in an INSTRON machine and the force-displacement characteristics are extracted. A flat circular plate of the same material, thickness, and radius is tested in the biaxial bending rig in order to be able to calculate an effective value of shell stiffness, D . However, the force-displacement characteristic found from the experimental data is not as straightforward as desired. The initial stiffness of the plate is found by extracting the initial slope of the force-displacement characteristic, which should

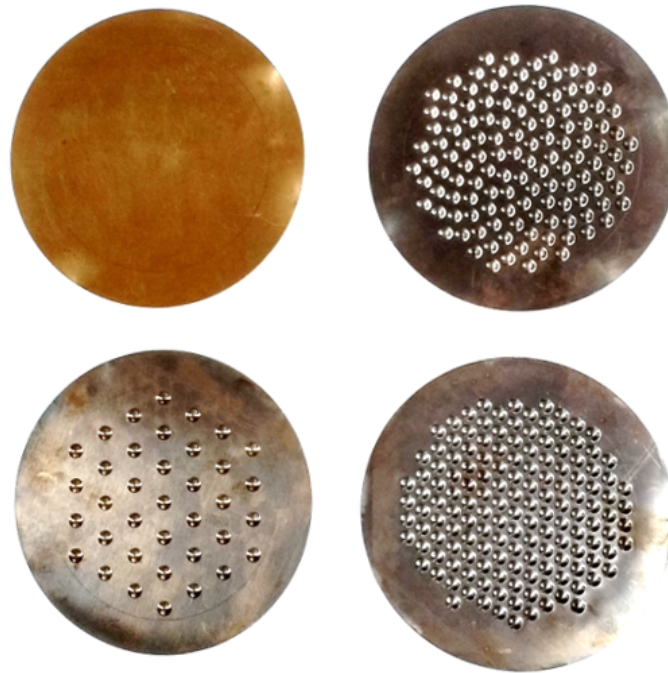


Fig. 5.16 Four circular dimpled sheet samples for the biaxial bending test. The samples have $L_{\text{plate}} = 65\text{mm}$, thickness $t = 0.5\text{mm}$ and are dimpled within the central section which has a radius $L_{\text{in}} = 50\text{mm}$. Upper left: flat plate. Upper right: phyllotaxis. Lower left: sparse hexagonal. Lower right: dense hexagonal.



Fig. 5.17 A circular dimpled sheet with a phyllotaxis dimple pattern is shown before and after a heat treatment of 400°C for 6 hours. (a) Before the heat treatment, the self-stress induce a global curvature. (b) After the heat treatment complete stress relaxation is observed and sheet is globally flat.

ideally be a straight linear section at the start of the response. However, neither the flat circular plate nor the circular dimpled sheet have a clear flat initial region in the force-displacement characteristic (Fig. 5.18), making it hard to determine an accurate initial gradient in order to calculate the initial stiffness. The raw data is offset in the x and y direction in order to align the origin. For example, the data shown for the hexagonally patterned dimpled sheet is offset by about 2.5mm, as the loading doesn't increase until this point because of the top support not being exactly in contact with the dimpled sheet when the test began. Having offset the data to the origin, it is clear that the bending stiffness of the dimpled sheet is significantly greater than that of the flat plate; however, trying to quantitatively measure this improved stiffness is difficult due to the lack of initial linear region. There are two distinct effects which make the initial gradient of the force-displacement characteristic difficult to determine. The first is that there is a force uptake effect which occurs as the loading ring makes contact with the dimpled sheet, if the ring support does not make contact with the sheet in a clean defined manner, then there will not be a clear defined start to the force response, but rather a gentle ramp. One issue that gives rise to this effect is if the top loading ring is not entirely parallel to the bottom support. If this is the case then contact will not occur simultaneously around the concentric circles. Attempting to get these plates parallel to within a tolerable margin is surprisingly difficult. Assuming an error of no more than half the plate thickness is allowed, then over the 100mm diameter of the loading ring, a discrepancy of 0.25mm indicates a need for the leveling accuracy to be within 0.057° . Therefore, small errors in the leveling of the top and bottom loading rings, or equally tiny distortions in the flatness of the sheet, can cause take-up issues to obscure the initial stiffness.

In many practical experimental tests, these take-up issues also prevent an accurate reading of the initial stiffness region. However, many of these tests, such as a four-point bending test, have a reasonably large linear (or very nearly linear) regime, and as such the gradient can be taken from this subsequent linear region and this value used as the initial gradient. This circumvents issues associated with slack and take-up errors which might be present in the experimental data. However, unfortunately it transpires that this biaxial bending set-up has a strongly non-linear response. Performing the axisymmetric FEA simulation on the biaxial test set-up, but allowing for large displacement non-linear behaviour confirms the non-linear behaviour seen experimentally in Fig. 5.18. Within a deflection which is of just a single plate thickness, the stiffness is seen to increase, by more than a factor of 6. Large deflections in this biaxial bending test would make the thin plate adopt a globally doubly curved cap shape, and any further deflection would be resisted due to circumferential hoop stresses. It is well known that in a thin shell, the in-plane "membrane" forces quickly dominate the bending behaviour of doubly curved surfaces. Equivalently, the rapid increase in stiffness

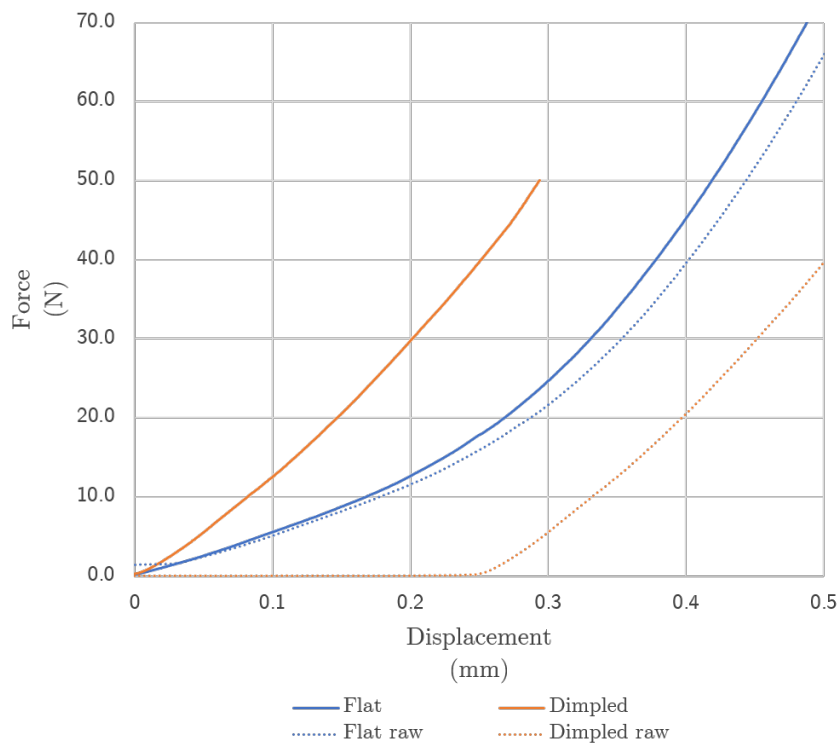


Fig. 5.18 The experimental force-displacement characteristics of circular sheets under biaxial bending. The results are given for a flat circular plate and for the dense hexagonal patterned dimpled sheet shown in Fig. 5.16. In each case $L_{in} = 50\text{mm}$, $L_{out} = 60\text{mm}$, $L_{plate} = 65\text{mm}$ and $t = 0.5\text{mm}$. The raw results are given, as well as the same data offset in the x and y directions to align the origin.

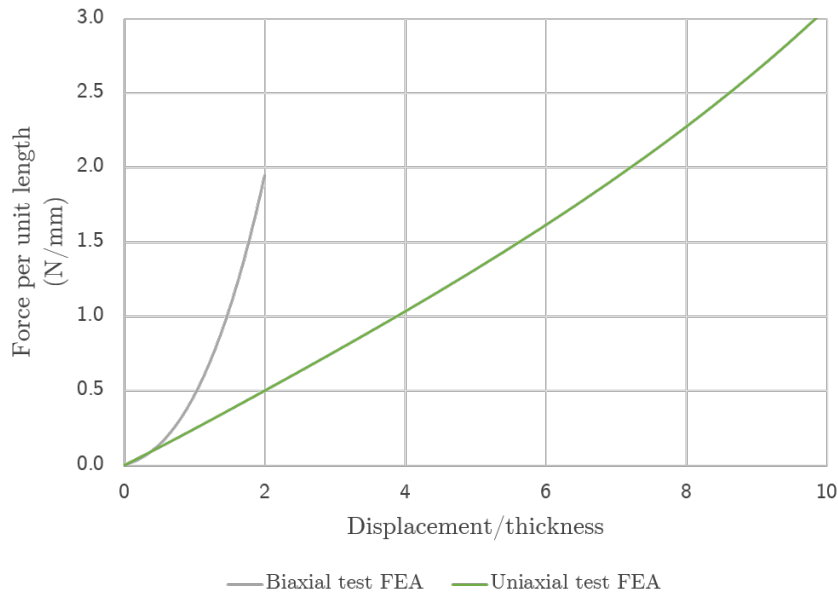


Fig. 5.19 FEA force-displacement response of a flat circular plate in the biaxial bending test set-up and a uniaxial four-point bending of a flat rectangular plate are compared. Large non-linear displacements are modelled in both cases. The biaxial set-up is as shown in Fig. 5.13. The uniaxial bending set-up is chosen to have the same profile as the biaxial cross-section geometry, with $L_{in} = 50\text{mm}$, $L_{out} = 60\text{mm}$, $L_{plate} = 65\text{mm}$ and $t = 0.5\text{mm}$.

observed can be explained by reasoning that the change of shape from flat disc to doubly curved cap necessitates a change in Gaussian curvature, which in turn requires a relatively large amount of in-plane stretching. As the in-plane stiffness of a thin plate is much greater than the out-of-plane stiffness, this in-plane stretching causes the sharp non-linear increase in stiffness.

Considering a four-point bend test, which has a profile equal to the diametric cross-section of the biaxial testing rig, allows for an interesting comparison between biaxial and uniaxial bending. While both tests have a central span of $2L_{in}$ and a lever arm of $L_{out} - L_{in}$, the biaxial test has additional restraints added by the axisymmetric nature of the set-up. The force per unit length applied in the biaxial case is calculated as $F/(2\pi L_{out})$, and the displacement at L_{out} is normalised by dividing by the plate thickness. Figure. 5.19 compares the force-displacement characteristics of each case from FEA. Notice how both the biaxial and uniaxial four-point bending tests start off with approximately the same initial stiffness, however the biaxial case quickly increases in stiffness with increasing deflection. In stark contrast, the uniaxial bending test is much more linear over a much larger range. The uniaxial stiffness does increase slightly with large displacements, the shallow arch shape which is being formed is capable of carrying some load, however this only starts to be a significant

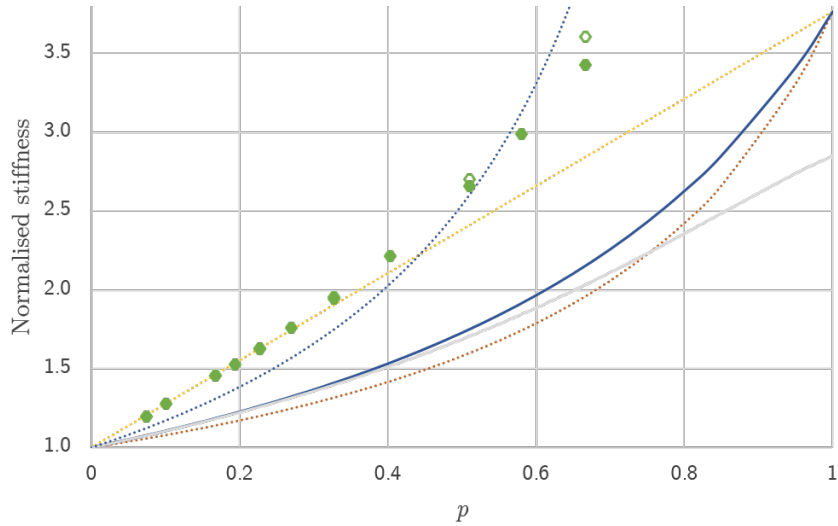
contribution for comparatively large deflections, of the order of half a dozen plate thicknesses or more. The gradient of the force-displacement response in this uniaxial four-point bending test changes less than 20% within the first five plate thickness of deflection. In comparison, the biaxial test shows an increase in gradient of over 500% within a deflection equal to a single plate thickness.

5.8 Uniaxial behaviour of dimpled sheets

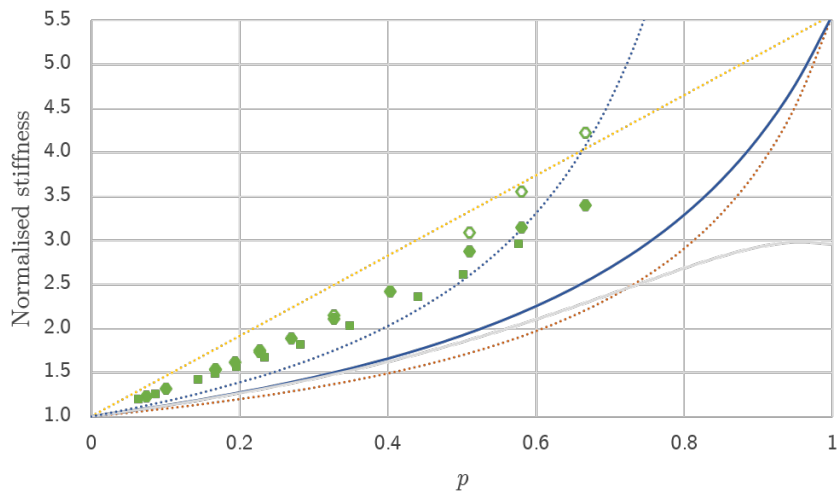
The uniaxial behaviour of a dimpled sheet is expected to vary slightly from the biaxial behaviour. While in Section 4.8 it was seen that the behaviour of an inclusion patterned plate practically independent of the type of loading, in Section 3.5.3 the equivalence of a dimple and an inclusion was seen to be different when under biaxial or antisymmetric loading. In the biaxial case the stress distributions and curvature distributions around a dimple and around an inclusion of the correct stiffness are equal. However, for antisymmetric and uniaxial loading, while the curvature and hence rotation distributions are very similar for a modified value of inclusion stiffness, the stress distributions are significantly different, see Fig. 3.18.

FEA simulations of dimpled sheets are conducted as per Section 5.4, but with a bending moment per unit length applied to just one edge. The rotation along the centre line is extracted in order to find a normalised stiffness. Normalised uniaxial bending stiffnesses for regular patterns of dimples, for two different dimple geometries are compared to the theoretical biaxial stiffness predictions, Fig. 5.20. Unlike the inclusion patterned plates, the normalised stiffness of dimpled sheets is seen to vary substantially when comparing biaxial to uniaxial bending. In uniaxial bending the dimpled sheets are significantly stiffer. Furthermore, Fig. 5.20a shows that adopting a different rule-of-mixtures is not going to capture the normalised uniaxial bending stiffness. It is more stiff than even the arithmetic smeared average, which is a strict upper limit of a rule-of-mixtures. It is tempting to consider whether the behaviour can be captured by adjusting the value of effective inclusion assumed, as, when comparing a single dimple to a single inclusion this approach found a reasonable correlation. However, this idea too is flawed: plotting the Finite Plate Theory curve for rigid inclusions, $k = \infty$, shows that for medium values of p , a dimpled sheet in uniaxial bending is stiffer even than an inclusion patterned plate with rigid inclusions.

While the uniaxial bending stiffnesses for dimpled sheets are significantly more stiff than for the biaxial case, the overall trend of the stiffnesses with p does seem to be similar in form. Considering the biaxial case, Finite Plate Theory predicts an increase in normalised stiffness, above unity. For the uniaxial case this increase in stiffness seems to occur by a greater



(a)



- Harmonic smeared average
- Arithmetic smeared average
- Finite plate theory
- Dimpled sheet theory
- FEA Hex
- ◇ FEA Hex up-down
- FEA Sq
- FPT $k=\infty$

(b)

Fig. 5.20 Normalised uniaxial bending stiffness of dimpled sheets from FEA. Hexagonal and square patterns of dimples are modelled as well as the isotropic up-down hexagonal pattern. (a) Quartic profile dimples, $a/t = 1/30$, $d/a = 1/3$, $\nu = 0.3$. (b) Spherical cap profile dimples, $a/t = 1/30$, $d/a = 1/6$, $\nu = 0.3$.

amount. It is therefore proposed that the uniaxial stiffness can be estimated by applying an additional scaling on the improvement given by the biaxial normalised stiffness:

$$\Psi_{\text{uniaxial}} = 1 + (\Psi_{\text{Dimpled}} - 1) \cdot c_{\text{uniaxial}} \quad (5.24)$$

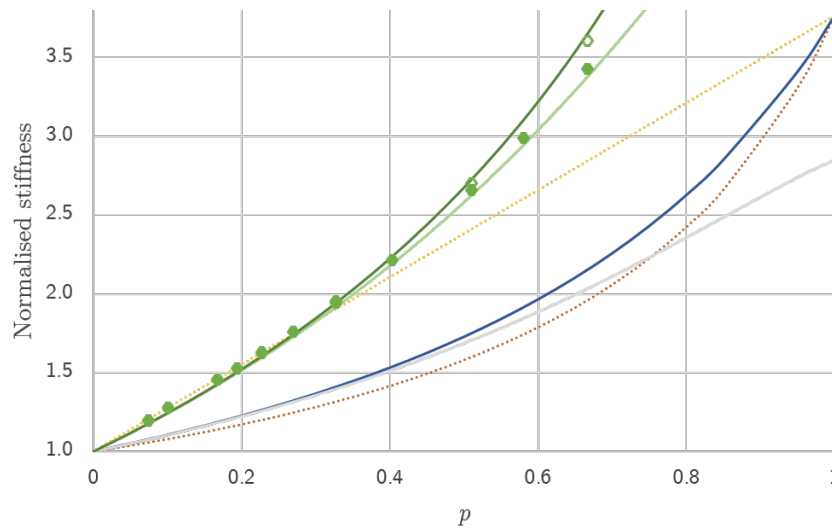
Using the Finite Plate Theory expression for normalised biaxial stiffness, a theoretical prediction for the uniaxial stiffness of a dimpled sheet can be calculated, this should predict the stiffness of up-down patterns of dimples as well. When accounting for the effective stiffness of a dimple given k -degradation, k^* , the stiffness of a dimpled sheet with a single direction of dimples should be well predicted. The constant c_{uniaxial} , is determined by examining the best fit to the FEA data. Figure 5.21 shows Eqn 5.24 for the empirically derived value of $c_{\text{uniaxial}} = 2.3$. A good agreement is seen, for both the spherical cap and the quartic dimples, for this value of c_{uniaxial} . The least good agreement is seen for the highest value of p for the spherical cap dimples. For these dimpled sheets the greatest amount of k -degradation is seen, and since we therefore know that for these sheets the greatest interaction between adjacent dimples is taking place, this may explain why the greatest discrepancy occurs for these sheets. The square pattern of dimples, Fig. 5.21b, are slightly less stiff than the hexagonally patterned dimpled sheets for a given p . It is suspected that this is due to the square pattern not being isotropic, as for the patterns of inclusions the square patterns in uniaxial loading had a slightly different stiffness to that expected.

5.9 Antisymmetric behaviour of dimpled sheets

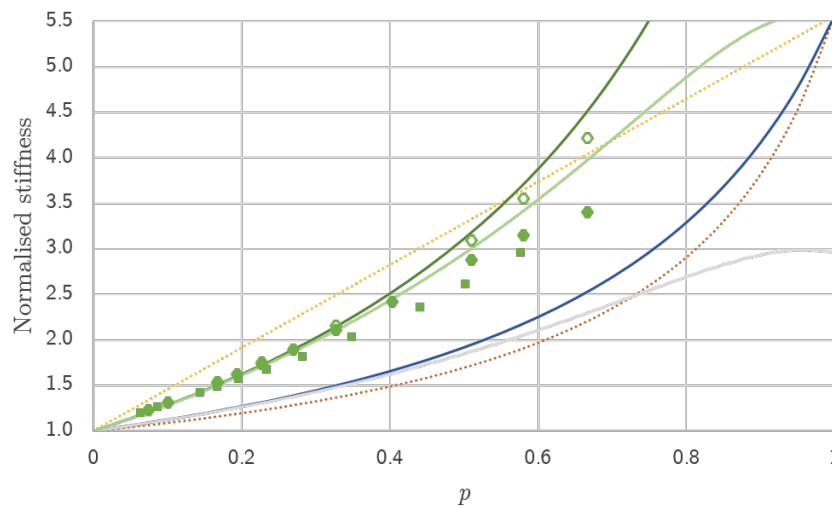
For dimpled sheets under antisymmetric bending, FEA is performed and the normalised stiffnesses are compared in Fig. 5.22. Similarly to the uniaxial case, the normalised stiffness in antisymmetric bending is seen to be significantly greater than that in the biaxial bending case. It is proposed that the normalised antisymmetric stiffness of a dimpled sheet can be estimated by scaling the improvement seen for the biaxial case by a constant factor:

$$\Psi_{\text{antisymmetric}} = 1 + (\Psi_{\text{Dimpled}} - 1) \cdot c_{\text{antisymmetric}} \quad (5.25)$$

Figure 5.22 compares the FEA results for two different dimple profiles to the empirical prediction Eqn 5.25. When accounting for the effective stiffness of a dimple given k -degradation, k^* , the stiffness of a dimpled sheet with a single direction of dimples should be well predicted. When a constant value of k_{bend} is used the normalised stiffness of up-down dimpled sheets should be well predicted. When the value of $c_{\text{antisymmetric}} = 3.6$ is used, a



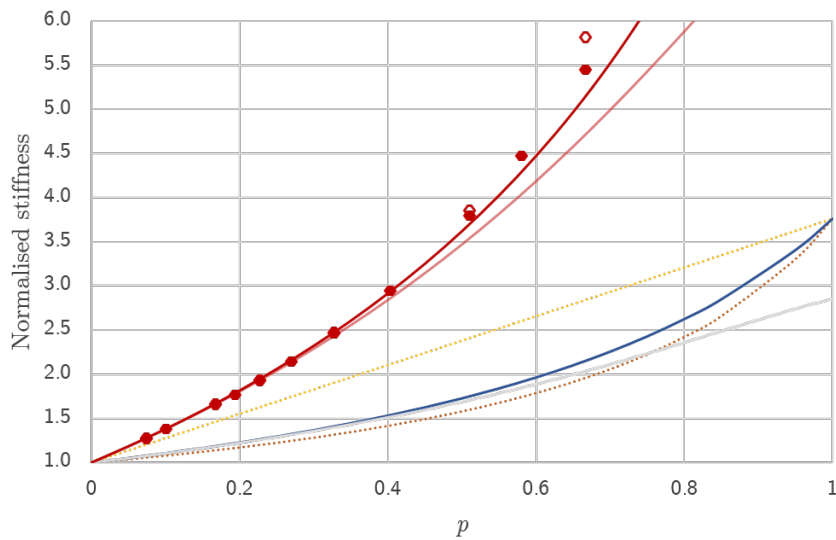
(a)



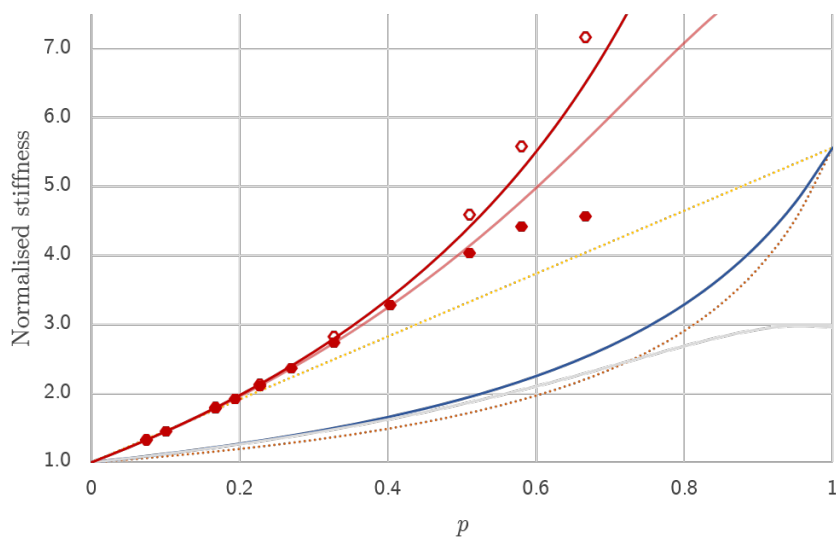
..... Harmonic smeared average Arithmetic smeared average
 — Finite plate theory — Dimpled sheet theory
 — Uniaxial theory — Uniaxial theory k^*
 ● FEA Hex ◇ FEA Hex up-down
 ■ FEA Sq

(b)

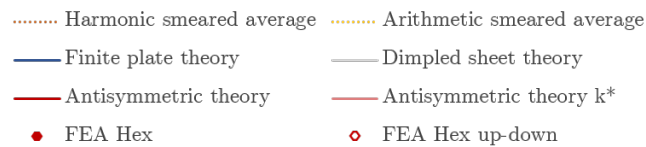
Fig. 5.21 Normalised uniaxial bending stiffness of dimpled sheets from FEA are compared with the modified dimpled sheet theory for uniaxial bending, Eqn 5.24 with an empirically fitted value of $c_{uniaxial} = 2.3$. (a) Quartic profile dimples, $a/t = 1/30$, $d/a = 1/3$, $\nu = 0.3$. (b) Spherical cap profile dimples, $a/t = 1/30$, $d/a = 1/6$, $\nu = 0.3$.



(a)



(b)



(b)

Fig. 5.22 Normalised antisymmetric bending stiffness of dimpled sheets from FEA are compared with the modified dimpled sheet theory for antisymmetric bending, Eqn 5.25 with an empirically fitted value of $c_{\text{antisymmetric}} = 3.6$. (a) Quartic profile dimples, $a/t = 1/30$, $d/a = 1/3$, $\nu = 0.3$. (b) Spherical cap profile dimples, $a/t = 1/30$, $d/a = 1/6$, $\nu = 0.3$.

reasonably good agreement is seen for both types of dimple profile as well as for both single direction and up-down dimpled sheets.

For antisymmetric loading, as for both the biaxial and uniaxial cases, when p is small there is effectively no difference in stiffness between dimpled sheets which have dimples going in a single direction compared to those sheets with up-down dimples. However, as is also seen before, for high p values, dimpled sheets with dimples in just a single direction are slightly less stiff than those with dimples in both directions. This is seen to be the case particularly for spherical cap dimples, as shown in Fig. 5.22b, where even scaling the dimpled sheet theory curve which accounts for k -degradation does not fully capture the reduction in stiffness compared to the prediction. The shape of the dimpled sheet theory curve does however give a good indication of the form of k -degradation which is seen in the antisymmetric case. The quartic dimple profile is seen to be affected much less by k -degradation, the smooth transition between the quartic profile and the flat plate is presumed to be the reason for this.

5.10 Discussion

The normalised biaxial stiffness of a dimpled sheet is predicted excellently by the dimpled sheet theory equation, Eqn 5.18, for both bending and stretching. The adjusted value of equivalent inclusion stiffness, to account for the k -degradation, is accurately captured by the assumption of each dimple behaving as if it were isolated in its own circular finite sheet. As in the case of inclusion patterned plates, the exact patterning of dimples was seen to not have any great effect on the overall stiffness. For regular and irregular patterns alike, the overall stiffness was just a function of the total proportion of plate which was dimpled.

Dimpled sheets which had dimples going in both up and down directions were seen to be marginally stiffer than the corresponding patterns which had dimples only in one direction. When sparsely spaced, the equivalent inclusion stiffness of a dimple was independent of dimple direction, as expected. However, when closely packed, the up-down dimples were less impacted by k -degradation, and as such made the sheets slightly stiffer overall. This validates the experimental findings seen in Section 2.5.2, with up-down patterns being only marginally stiffer.

A uniaxial load case can be seen as a combination of a biaxial and antisymmetric load case. Superposing a biaxial loading with a magnitude of half of unity to an antisymmetric load case with a magnitude of half of unity gives an overall uniaxial load with a magnitude of unity. It is therefore perhaps unsurprising that the normalised stiffness in uniaxial bending is very accurately predicted by taking an average of the biaxial and antisymmetric normalised

stiffnesses, Fig. 5.23. It can additionally be shown that the assumption of uniaxial and antisymmetric normalised stiffnesses being given by multiplying the improvement in the biaxial case by a constant factor, is consistent with uniaxial behaviour being an average of the biaxial and antisymmetric cases.

$$\frac{\Psi_{\text{biaxial}} + \Psi_{\text{antisymmetric}}}{2} = \Psi_{\text{uniaxial}} \quad (5.26)$$

$$1 + (\Psi_{\text{biaxial}} - 1) \cdot c_{\text{uniaxial}} = \Psi_{\text{uniaxial}} \quad (5.27)$$

$$1 + (\Psi_{\text{biaxial}} - 1) \cdot c_{\text{antisymmetric}} = \Psi_{\text{antisymmetric}} \quad (5.28)$$

Equation 5.26 states that the normalised uniaxial stiffness is equal to the average normalised stiffness of the biaxial and antisymmetric cases. Equations 5.27 and 5.28 are the proposed predictions of uniaxial and antisymmetric stiffness for a dimpled sheet, multiplying the improvement of the biaxial case by the constant factors c_{uniaxial} and $c_{\text{antisymmetric}}$ respectively. Substituting Eqns 5.27 and 5.28 into Eqn 5.26 yields:

$$\frac{(\Psi_{\text{biaxial}} - 1) + (\Psi_{\text{biaxial}} - 1)c_{\text{antisymmetric}}}{2} = (\Psi_{\text{biaxial}} - 1)c_{\text{uniaxial}} \quad (5.29)$$

and hence:

$$\frac{1 + c_{\text{antisymmetric}}}{2} = c_{\text{uniaxial}} \rightarrow c_{\text{antisymmetric}} = 2c_{\text{uniaxial}} - 1 \quad (5.30)$$

It can be verified that the empirically chosen values of $c_{\text{uniaxial}} = 2.3$ and $c_{\text{antisymmetric}} = 3.6$, which showed the best fit with the FEA results, are consistent with Eqn 5.30.

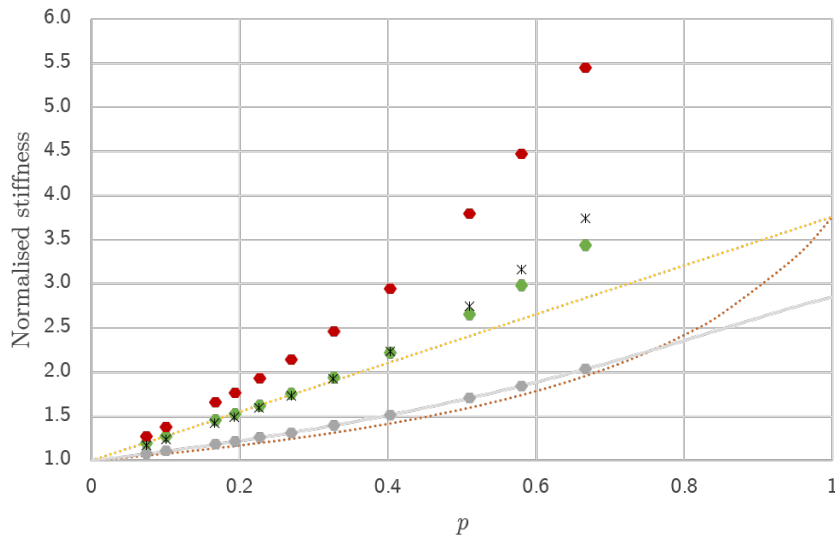
It is therefore possible to predict the normalised stiffness of a dimpled sheet which is loaded under a general loading, with generalised loading parameter F . Knowing that the normalised stiffness in biaxial loading (when $F = 1$) is very well predicted by Eqn 5.18, and assuming the antisymmetric stiffness can be approximately given by Eqn 5.25 (when $F = -1$), the following expression for normalised stiffness can be derived:

$$\Psi_{\text{general}} = 1 + (\Psi_{\text{Dimpled}} - 1) \left[1 + \frac{(c_{\text{antisymmetric}} - 1)(1 - F)}{2} \right] \quad (5.31)$$

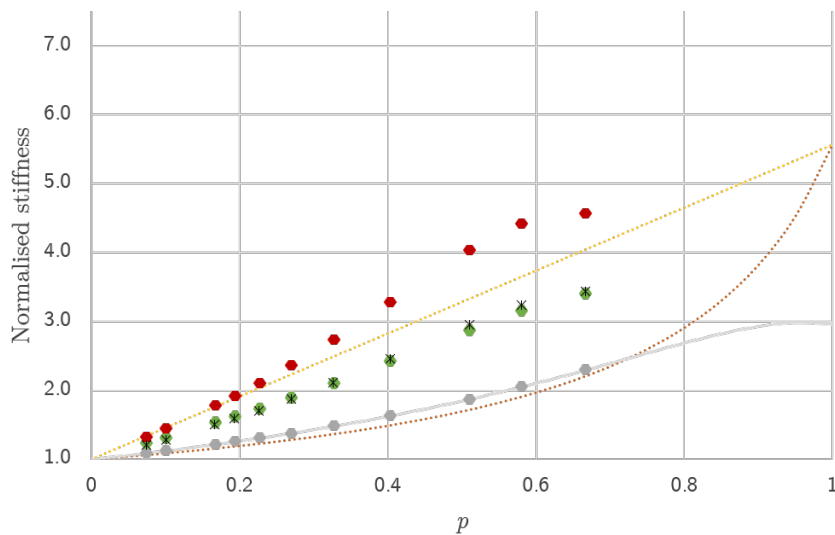
where:

$$\Psi_{\text{Dimpled}} = \frac{2k^* - (1 - p)(k^* - 1)(1 - \nu)}{2 + (1 - p)(k^* - 1)(1 + \nu)} \quad (5.32)$$

and where $c_{\text{antisymmetric}}$ is an empirically derived constant.



(a)



..... Harmonic smeared average Arithmetic smeared average
 — Dimpled sheet theory ● FEA biaxial
 ● FEA uniaxial ● FEA antisymmetric
 × FEA average

(b)

Fig. 5.23 Normalised bending stiffness of dimpled sheets from FEA are compared for biaxial, uniaxial and antisymmetric loadings. An average of the normalised antisymmetric stiffness and normalised biaxial stiffness is calculated, and plotted also for comparison against the normalised uniaxial stiffness. The dimpled sheets compared have hexagonal patterns of single direction dimples: (a) Quartic profile dimples, $a/t = 1/30$, $d/a = 1/3$, $\nu = 0.3$. (b) Spherical cap profile dimples, $a/t = 1/30$, $d/a = 1/6$, $\nu = 0.3$.

Note that when $F = 1$, the expression simplifies to Ψ_{Dimpled} and when $F = -1$, the expression for antisymmetric normalised stiffness, Eqn 5.25, is recovered. When $F = 0$, the term in the square brackets is equal to the expression for c_{uniaxial} from Eqn 5.30.

5.11 Conclusions

Combining the theoretical understanding of inclusion patterned plates, with the equivalence of an inclusion and a dimple, allows for a good understanding of the behaviour of dimpled sheets. Having multiple dimples within a close proximity of each other however has the additional effect of reducing the effective stiffness of each dimple. This effect is examined and theoretically analysed, Section 5.5.2, and when combined with the Finite Plate Theory for patterns of inclusions allows for an analytically rigorous prediction of the biaxial stiffness of a dimpled sheet. The theoretical prediction of normalised stiffness under biaxial loading is compared to FEA and the agreement is found to be excellent, Section 5.6.

Unlike inclusion patterned plates however, the normalised stiffness of dimpled sheets in uniaxial and antisymmetric loading is significantly different to the normalised biaxial stiffness. FEA simulations show that the normalised uniaxial stiffness of a dimpled sheet is significantly greater than the normalised biaxial stiffness, Section 5.8, and the normalised antisymmetric stiffness is greater still, Section 5.9. However empirical equations, based on the analytically biaxial stiffness expression, are produced which are able to capture the normalised stiffnesses of the uniaxial and antisymmetric case to within a good degree of accuracy. While these equations require an empirically found constant, the value of this constant is seen to be fixed for a variety of dimple profiles. Furthermore, these equations can be generalised to give an expression which predicts the normalised stiffness of a dimpled sheet under a general loading, Eqn 5.31.

This new insight into the structural performance of dimpled sheets allows for a much better understanding which aids both the analysis and design of dimpled sheets. For example, both the patterning of the dimples and the dimple profiles themselves can be optimised. Unlike the simplistic second moment of area theory, the performance enhancement of up-down patterns compared with single direction dimples can be understood. The profile of a dimple too can be optimised: the effective bending stiffness of a dimple does not simply increase with increasing dimple depth, there is actually an optimum depth to radius ratio which maximises the value of k_{bend} . Equally the bending stiffness of a dimple is seen to increase with the square root of the radius to thickness ratio, which informs the choice of dimple size. Comparing regular and irregular patterns shows that there is only a minimal influence of pattern on overall stiffness. Unlike the conclusions of some previous authors

[12], dimpled sheets do not suffer from “lines of weakness”, but rather are generally isotropic in behaviour. While a square pattern was seen to introduce some anisotropy, both the regular hexagonal and the irregular patterns showed strongly isotropic behaviour. Having found the independence of pattern on overall stiffness for the inclusion patterned plates, one seeks to maximise the stiffness by maximising the packing density p . For this reason a hexagonal packing will be optimum, as it allows for the highest possible values of p . However, if an irregular pattern can also obtain the desired value of p , then this pattern too could be used too.

Chapter 6

Conclusions

The experimental, theoretical and computational work presented here confirms that an increase in bending stiffness is obtained by the presence of dimples, compared to a flat sheet. While this was already known qualitatively to be the case, previous assumptions as to the mechanism by which the dimples increase stiffness [12] based on structural depth approaches, were shown to be flawed. A detailed quantitative analysis considering a structural depth approach was performed Section 2.4, and the results of this methodology were seen to give predictions of stiffness an order of magnitude higher than the experimental results obtained, Section 2.5.

In this work, a new method of analysing the performance of dimpled sheets was derived. Focusing first on the behaviour of a single dimple as an axisymmetric shell of revolution, Section 3.4, and then incorporating this single dimple into a infinite flat plate, Section 3.4.3. The behaviour of an isolated single dimple in axisymmetric loading is a known problem [34], and the literature provides good analytical predictions for the stiffness parameters for conic and spherical cap dimple geometries with constant through-thickness. Comparison to FEA shows that the stiffness of such dimple profiles is changed only slightly if a constant vertical thickness rather than through-thickness is assumed, Section 3.5.1. This helpful discovery is justified analytically, and is useful for the subject of dimpling, where a constant vertical thickness, which is compatible with the conservation of volume, is a better assumption of a practical dimple profile than a constant through-thickness. A new analytical method for predicting the axisymmetric bending stiffness of an arbitrary dimple profile is developed, Section 3.4.2, and excellent agreement is found between this prediction and FEA, Section 3.5.2. Understanding the axisymmetric behaviour of a dimple which is included in the centre of an infinite flat plate allows for an equivalence between a dimple and an elastic inclusion to be seen, Section 3.4.3. Analytical theory is developed to prove this equivalence and predict the stiffness value of such an equivalent inclusion in terms of the stiffness parameters of an arbitrary dimple profile. The theory is equally able to predict the increase in bending stiffness $k_{\text{bend}} > 1$, as well as the decrease in stretching stiffness $k_{\text{stretch}} < 1$. FEA simulations

verify the equivalence of dimple and inclusion and show that the analytical predictions for equivalent dimple stiffnesses are extremely accurate for both stretching and bending.

Having established the equivalence of a single dimple to a single inclusion, Chapter 4 investigates the effects of elastic inclusions in flat plates. The influence of a single elastic inclusion within an infinite elastic plate is a problem which has previously been studied, both for plates in stretching [44], as well as plates in bending [45]. A comparison between the stress fields developed around an inclusion in bending and the same inclusion in the same infinite sheet in stretching is made in Section 4.5.1. While in general these are different, for biaxial loading, both bending and stretching have identical stress distributions, which additionally can be expressed in a reasonably simple analytical form. The behaviour of patterns of multiple inclusions is then considered, Section 4.5.2, and various analytical models are proposed to capture the overall behaviour of a plate patterned with elastic inclusions. Finite element analysis of inclusion patterned plates is carried out for a wide variety of inclusion patterns and inclusion stiffnesses, Section 4.7, and the results are compared to the analytical predictions. It is seen that the Finite Plate Theory method, Eqn 4.39, is by far the best predictor of overall stiffness of inclusion patterned plates, and additionally predicts the stress concentration factors present. Investigation of the overall homogeneity and isotropy of inclusion pattern plates, Section 4.9, shows the validity of representing an inclusion patterned plate with an smeared overall material stiffness. FEA analysis confirms the validity of using this value of smeared stiffness, which is calculated based on an axisymmetric analysis, to all loading cases, including uniaxial and antisymmetric loading, Section 4.8. One of the most striking findings is the independence of the overall stiffness on the exact patterning of the inclusions, Section 4.7.3. Even for irregular patterns, the overall stiffness was seen to be isotropic and dependant only on the inclusion proportion of the plate p . New rules-of-mixture formulae, based on the analysis of a single inclusion within a circular plate of finite size, are given for the overall smeared stiffness and for the yield strength of inclusion patterned plates, Eqns 4.42 and 4.48. The incorporation of the Poisson's ratio terms in the Finite Plate Theory expression for normalised stiffness sets it apart from other existing rules-of-mixtures found in the literature and makes it both more accurate and more versatile.

Combining the theoretical understanding of inclusion patterned plates, with the equivalence of an inclusion and a dimple, allows for a good understanding of the behaviour of dimpled sheets. Having multiple dimples within a close proximity of each other however has the additional effect of reducing the effective stiffness of each dimple. This effect is examined and theoretically analysed, Section 5.5.2, and when combined with the Finite Plate Theory for patterns of inclusions allows for an analytically rigorous prediction of the biaxial

stiffness of a dimpled sheet. The theoretical prediction of normalised stiffness under biaxial loading is compared to FEA and the agreement is found to be excellent, Section 5.6.

Unlike inclusion patterned plates however, the normalised stiffness of dimpled sheets in uniaxial and antisymmetric loading is significantly different to the normalised biaxial stiffness. FEA simulations show that the normalised uniaxial stiffness of a dimpled sheet is significantly greater than the normalised biaxial stiffness, Section 5.8, and the normalised antisymmetric stiffness is greater still, Section 5.9. However empirical equations, based on the analytically biaxial stiffness expression, are produced which are able to capture the normalised stiffnesses of the uniaxial and antisymmetric case to within a good degree of accuracy. While these equations require an empirically found constant, the value of this constant is seen to be fixed for a variety of dimple profiles. Furthermore, these equations can be generalised to give an expression which predicts the normalised stiffness of a dimpled sheet under a general loading, Eqn 5.31.

This new insight into the structural performance of dimpled sheets allows for a much better understanding which aids both the analysis and design of dimpled sheets. For example, both the patterning of the dimples and the dimple profiles themselves can be optimised. Unlike the simplistic second moment of area theory, the performance enhancement of up-down patterns compared with single direction dimples can be understood. The profile of a dimple too can be optimised: the effective bending stiffness of a dimple does not simply increase with increasing dimple depth, there is actually an optimum depth to radius ratio which maximises the value of k_{bend} . Equally the bending stiffness of a dimple is seen to increase with the square root of the radius to thickness ratio, which informs the choice of dimple size. Comparing regular and irregular patterns shows that there is only a minimal influence of pattern on overall stiffness. Unlike the conclusions of some previous authors [12], dimpled sheets do not suffer from “lines of weakness”, but rather are generally isotropic in behaviour. While a square pattern was seen to introduce some anisotropy, both the regular hexagonal and the irregular patterns showed strongly isotropic behaviour. Having found the independence of pattern on overall stiffness for the inclusion patterned plates, one seeks to maximise the stiffness by maximising the packing density p . For this reason a hexagonal packing will be optimum, as it allows for the highest possible values of p . However, if an irregular pattern can also obtain the desired value of p , then this pattern may be used too.

Application of this work to the design of dimpled sheets should allow for increased use of dimpled sheets in practical contexts. Many current applications use dimpled sheets as cladding, and therefore require a separate structural skeleton. A greater understanding of structural properties of dimpled sheets, such as bending and stretching stiffness, should enable dimpled sheets themselves to be used structurally, in addition to their other useful

properties such as increased heat transfer. Therefore, more efficient structures can be designed which remove or reduce the use of an additional underlying structural skeleton. For example, rather than adding dimpled jackets around pressure vessels, pressure vessels could be manufactured directly out of dimpled sheets. This should reduce complexity as well as cost, without compromising on the structural and thermal properties required of the pressure vessel. In applications such as elevated walkways, where dimpled sheets are already used, understanding their structural behaviour should allow for more efficient design. The increased bending stiffness of a dimpled sheet compared to a flat plate enables further application opportunities, particularly in designs where weight is a principle concern, for example in aerospace or high-end automotive applications. In such contexts where a flat plate is currently used, a thinner dimpled sheet may be able to carry the same loading but requiring less material. The analysis in this thesis enables bending stiffness to be maximised by selecting optimum packing patterns and optimum depth to radius ratios for dimples. Future work on this subject could explore optimising designs of dimpled sheets for a combination of properties such as heat transfer and structural behaviour. Understanding the differences in initial stiffness of dimpled sheets under uniaxial and biaxial loading, and investigating the non-linear regime of dimpled sheets under load, would also be questions worthy of future research.

References

- [1] B. Cantor, P. Grant, and C. Johnston. *Automotive Engineering: Lightweight, Functional, and Novel Materials*. CRC Press, Cambridge, 2008.
- [2] R. Barry. *The Construction of Buildings: Volume 3, Single Story Frames, Shells and Lightweight Coverings*. Blackwell Scientific Publications, Oxford, 1993.
- [3] P. LeFort. Bending of perforated plates with square penetration patterns. *Nuclear Engineering and Design*, 12:341–345, 1970.
- [4] I. D. Rowland and T. N. Howe. *Vitruvius: Ten Books on Architecture*. Cambridge University Press, Cambridge, 2001.
- [5] M. Altin. The structural analysis of domes: from the Pantheon until Reichstag. *Historical Constructions*, 1:197–208, 2001.
- [6] K. A. Seffen. Bi-stable concepts for reconfigurable structures. *45th AIAA/ASME/ASCE/AHS/ASC Structures, Structural Dynamics and Materials Conference*, 2004.
- [7] F. Javid, E. Smith-Roberge, M. C. Innes, A. Shanian, J. C. Weaver, and K. Bertoldi. Dimpled elastic sheets: A new class of non-porous negative poisson’s ratio materials. *Scientific Reports*, 5:18373, 2015.
- [8] G. D. Farmer and W. B. Spangler. Technical report 1727-TR, Investigation of calottan sheet stiffening process. *US Army Engineer Research and Development Laboratories*, 8S93:31–001–08, 1962.
- [9] M. D. Heaton. A calculation of the elastic constants of a unidirectional fibre-reinforced composite. *Journal of Physics D: Applications of Physics*, 1:1039–1048, 1968.
- [10] D. Briassoulis. Equivalent orthotropic properties of corrugated sheets. *Computers and Structures*, 23:129–138, 1986.
- [11] C. R. Calladine. *Theory of Shell Structures*. Cambridge University Press, Cambridge, 1983.
- [12] M. R. Golabchi and S. D. Guest. Morphing multistable textured shells. *Proceedings of the International Association for Shells and Spatial Structures Symposium. Evolution and Trends in Design, Analysis and Construction of Shell and Spatial Structures*, 2009.
- [13] V. B. Nguyen, C. J. Wang, D. J. Mynors, M. A. English, and M. A. Castellucci. Dimpling process in cold roll metal forming by element modelling and experimental validation. *Journal of Manufacturing Processes*, 16:363–372, 2014.

- [14] A.D. Norman, M.R. Golbchi, K. A. Seffen, and S. D. Guest. Multistable textures shell structures. *Advances in Science and Technology*, 54:168–173, 2008.
- [15] G. W. Brodland and H. Cohen. Deflection and snapping of spherical caps. *International Journal of Solids and Structures*, 29(10):1341–1356, 1987.
- [16] Y. Wang, B. Guan, and Y. Zang L. Mu. Equivalent tensile properties analysis of the dimpled sheet. *Journal of Failure Analysis and Prevention*, 18:791–798, 2018.
- [17] I. P. Nascimento and E. C. Garcia. Heat transfer performance enhancement in compact heat exchangers by using shallow square dimples in flat tubes. *Applied Thermal Engineering*, 96:659–670, 2016.
- [18] R. Jackson. Metallic panels would insulate at 2700 f. *NASA Tech Briefs*, 6(1):100–101, 1981.
- [19] Highland Equipment Incorporated. The benefits of dimple jackets for pressure vessels, Accessed 4th August 2020. [online] www.highlandequip.com/blog/benefits-dimple-jackets-pressure-vessels/.
- [20] Thomas P. Pastor and Jay Vattappilly. *Section VIII–Division I: Rules for Construction of Pressure Vessels. Online Companion Guide to the ASME Boiler and Pressure Vessel Codes: Criteria and Commentary on Select Aspects of the Boiler & Pressure Vessel Codes*. ASME Press, 2020.
- [21] Metal Sheets Ltd. Embossed stainless sheet, Accessed 4th August 2020. [online] www.metalsheets.co.uk/embossed-stainless-sheet/.
- [22] Hengda. Dimple perforated sheet steel grating, Accessed 4th August 2020. [online] www.perforated-metal.net/perforatedmetal/perforated-dimple-sheet-metal-plank-grating.html.
- [23] L. Gao, H. Sun, F. Jin, and H. Fan. Load-carrying capacity of high-strength steel box-sections I: Stub columns. *Journal of Constructional Steel Research*, 65:918–924, 2008.
- [24] B. Uy. Local and postlocal buckling of fabricated steel and composite cross sections. *Journal of Structural Engineering*, 127(6):666–677, 2001.
- [25] T. Yokozeki, S. I. Takeda, T. Ogasawara, and T. Ishikawa. Mechanical properties of corrugated composites for candidate materials of flexible wing structures. *Composites Part A: Applied Science and Manufacturing*, 37(10):1578–1586, 2006.
- [26] A. Samanta and M. Mukhopadhyay. Finite element static and dynamic analyses of folded plates. *Engineering Structures*, 23:277–287, 1999.
- [27] K.M. Liew, L. X. Peng, and S. Kitipornchai. Nonlinear analysis of corrugated plates using a fsdt and a meshfree method. *Computer Methods in Applied Mechanics and Engineering*, 196(21):2358–2376, 2007.
- [28] Y. Xia, Friswell M, I, and E. I. Saavedra Flores. Equivalent models of corrugated panels. *International Journal of Solids and Structures*, 49:1453–1462, 2012.

- [29] Mathworks. *MATLAB 2016a*. The Mathworks, Inc, Natick, Massachusetts, 2014.
- [30] N. Sanderson and S. R. Reid. Photoelastic approach to the determination of the flexural rigidity of rectangular beams with abrupt changes in cross section. *International Journal of Mechanical sciences*, 18:431–346, 1976.
- [31] Plastics – determination of flexural properties. Standard, International Organization for Standardization, Geneva, CH, 2019.
- [32] H. Reissner. Spannungen in Kugelschalen. *Festschrift Müller-Breslau*, 181:623, 1912.
- [33] E. R. Meissner. Über Elastizität und Festigkeit dünner Schalen. *Vierteljahrschrift der Naturforschenden Gesellschaft in Zürich*, 60, 1915.
- [34] J. W. Geckler. Über die festigkeit aahsensymmetrischer schalen. *Forschungsarb Ingews*, 276:1–52, 1926.
- [35] M. Heteényi. Spherical shells subjected to axial symmetric bending. *International Association for Bridge and Structural Engineering*, 5:173–205, 1938.
- [36] A. Zingoni. *Shell Structures in Civil and Mechanical Engineering: Theory and Closed-Form Analytical Solutions*. Thomas Telford Ltd, London, 1997.
- [37] Hibbit, Karlsson, and Sorensen. *ABAQUS Version 6.14-5*. Hibbit, Karlsson & Sorensen, Inc. Pawtucket, 1998.
- [38] P. M. Sobota and K. A. Seffen. Effects of boundary conditions on bistable behaviour in axisymmetrical shallow shells. *Proceedings of the Royal Society A: Mathematical, Physical and Engineering Sciences*, 473(2203):20170230, 2017.
- [39] J. E. Goldberg and K. N. Jabbour. Stresses and displacements in perforated plates. *Nuclear Structural Engineering*, 2(4):360–381, 1965.
- [40] Y. Benveniste, G. J. Dvorak, and T. Chen. Stress fields in composites with coated inclusions. *Mechanics of Materials*, 7(4):305–317, 1989.
- [41] C. T. Sun and R. S. Vaidya. Prediction of composite properties from a representative volume element. *Composites Science and Technology*, 56(2):171–179, 1996.
- [42] A. N. Norris. A differential scheme for the effective moduli of composites. *Mechanics of Materials*, 4(1):1–16, 1985.
- [43] E. G. Kirsch. Die Theorie der Elastizität und die Bedürfnisse der Festigkeitslehre. *Zeitschrift des Vereines Deutscher Ingenieure*, 42:797–807, 1889.
- [44] H. J. Hardiman. Elliptical elastic inclusions in an infinite elastic plate. *The Quarterly Journal of Mechanics and Applied Mathematics*, 7:226–230, 1955.
- [45] C. W. Bert. Generalized bending of a plate with a circular inclusion of arbitrary rigidity. *The Journal of Strain Analysis for Engineering Design*, 36(3):341–345, 2001.
- [46] C. C. Lo and A.W. Leissa. Bending of plates with circular holes. *Acta Mechanica*, 3(1):64–78, 1967.

- [47] B. Paul. Prediction of elastic constants of multiphase material. *Transactions of The Metallurgical Society of AIME*, 218:36–41, 1960.
- [48] Z. Hashin and S. Shtrikman. A variational approach to the theory of the effective magnetic permeability of multiphase materials. *Journal of Applied Physics*, 33(10):3125–3131, 1962.
- [49] K. S. Ravichandran. Elastic properties of two-phase composites. *Journal of the American Ceramic Society*, 77(5):3125–3131, 1994.
- [50] T.T. Wu. The effect of inclusion shape on the elastic moduli of a two-phase material. *International Journal of Solids and Structures*, 2(1):1–8, 1966.
- [51] K. Miled. *Effet de taille dans le béton léger de polystyrène expansé*. PhD thesis, École des ponts ParisTech, 2005.
- [52] K. Miled, K. Sab, and R. Le Roy. Effective elastic properties of porous materials: Homogenization schemes vs experimental data. *Mechanics Research Communications*, 38(2):131–135, 2011.
- [53] Y. Y. Deryugin, G. V. Lasko, and S. Schmauder. Field of stresses in an isotropic plane with circular inclusions under tensile stress. *Engineering*, 4(9):583–589, 2012.
- [54] J. N. Goodier. Concentration of stress around spherical and cylindrical inclusions and flaws. *Transactions of ASME*, 55:39, 1933.
- [55] H. G. Hanson. Voronoi cell properties from simulated and real random spheres and points. *Journal of Statistical Physics*, 30(3):591–605, 1983.
- [56] H. Gercek. Poisson’s ratio values for rocks. *International Journal of Rock Mechanics and Mining Sciences*, 44(1):1–13, 2007.
- [57] J. F. Sadoc, J. Charvolin, and N. Rivier. Phyllotaxis on surfaces of constant gaussian curvature. *Journal of Physics A: Mathematical and Theoretical*, 46(29):295202, 2013.
- [58] J. F. Sadoc, J. Charvolin, and N. Rivier. Phyllotaxis: a non-conventional crystalline solution to packing efficiency in situations with radial symmetry. *Acta Crystallographica Section A Foundations of Crystallography*, 68:470–483, 2012.
- [59] M. Gardener. *Penrose Tiles to Trapdoor Ciphers: And the Return of Dr Matrix*. Cambridge University Press, 1997.
- [60] M. Gardener. Extraordinary nonperiodic tiling that enriches the theory of tiles. *Scientific American*, 236:110–119, 1977.
- [61] L. Effinger-Dean. The empire problem in penrose tilings. Master’s thesis, Williams College, Massachusetts, 2006.
- [62] G. P. Tandon and G. J. Weng. The effect of aspect ratio of inclusions on the elastic properties of unidirectionally aligned composites. *Polymer Composites*, 5(4):327–333, 1984.

- [63] P. C. Lin, S. H. Lin, and J. Pan. Modeling of failure near spot welds in lap-shear specimens based on a plane stress rigid inclusion analysis. *Engineering Fracture Mechanics*, 73(15):2229–2249, 2006.
- [64] Z. J. Zhang, Y. K. Zhu, P. Zhang, Y. Y. Zhang, W. Pantleon, and Z. F. Zhang. Analytical approximations for the elastic moduli of two-phase materials. *Physical Review B*, 4(13):134107, 2017.
- [65] R. M. Christensen. A critical evaluation for a class of micro-mechanics models. *Journal of the Mechanics and Physics of Solids*, 38(3):379–404, 1990.
- [66] R. M. Christensen and K. H. Lo. Solutions for effective shear properties in three phase sphere and cylinder models. *Journal of the Mechanics and Physics of Solids*, 27(4):315–330, 1979.
- [67] A. E. H. Love. *A Treatise on the Mathematical Theory of Elasticity*. Cambridge University Press, 1927.
- [68] T. Mori and K. Tanaka. Average stress in matrix and average elastic energy of materials with misfitting inclusions. *Acta Metallurgica*, 21(5):571–574, 1973.
- [69] Y. Benveniste. A new approach to the application of Mori-Tanaka’s theory in composite materials. *Mechanics of Materials*, 66(2):147–157, 1987.
- [70] V. D. Bruggeman. Berechnung verschiedener physikalischer Konstanten von heterogenen Substanzen. II. Dielektrizitätskonstanten und Leitfähigkeiten von Vielkristallen der nichtregulären Systeme. *Annalen der Physik*, 416(7):636–664, 1935.
- [71] J. D. Eshelby. The determination of the elastic field of an ellipsoidal inclusion, and related problems. *Proceedings of the Royal Society of London. Series A. Mathematical and Physical Sciences*, 241(1226):376–396, 1957.
- [72] Y. A. Shevlyakov and A. A. Skoblin. Relative stiffness of irregularly perforated plates. *Journal of Soviet Mathematics*, 65(1):1389–1395, 1994.
- [73] R. McNeel. *Rhinoceros, Verison 5*. Robert McNeel & Associates, 2018.
- [74] S. P. Timoshenko and S. Woinowsky-Krieger. *Theory of plate and shells*. McGraw-hill, 1959.
- [75] J. C. Harkness, W. S. Loewenthal, and C. S. Lorenz. *Atlas of Stress Relaxation Curves for Beryllium Copper and Selected Copper Alloy Spring Materials*. Brush Wellman, 1993.
- [76] J. J. G. Savard. Quadibloc: Penrose tilings, 2000. [online] <http://www.quadibloc.com/math/pen01.htm>.

Appendix A

Cross-sections of dimpled sheets

A.1 Calculating the second moment of area of a single dimple cross-section

A.1.1 Hemispherical and semi-ellipsoidal dimples

When a dimple has a semicircular profile along its radius, the revolved geometry of the dimple is hemispherical. Every cross-section of the dimple is a semicircle, albeit of a varying size depending on the location of the cut. The second moment of area for a semicircular cross-section is calculated as follows.

For a semicircular profile the equation of the mid-surface is given by:

$$z = \sqrt{a^2 - x^2} \quad (\text{A.1})$$

The area of the cross-section is:

$$A = 2at \quad (\text{A.2})$$

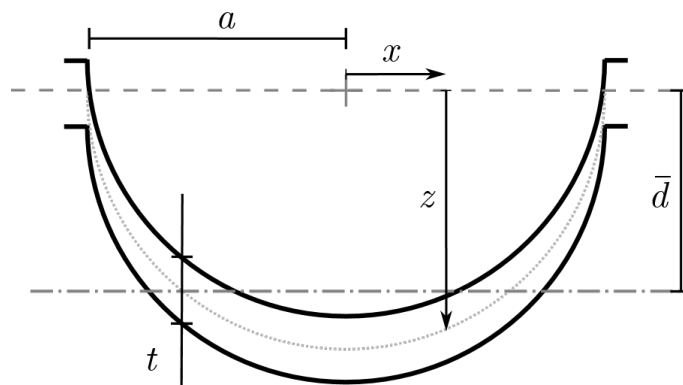


Fig. A.1 A semicircular dimple profile is shown. The dimple has a constant vertical thickness.

Calculating the depth of the neutral axis of the section:

$$\bar{d} = \frac{\int_{-a}^a t \cdot z \cdot dx}{A} = \frac{1}{2a} \int_{-a}^a \sqrt{a^2 - x^2} dx = \frac{\pi a}{4} \quad (\text{A.3})$$

The second moment of area can then be calculated about the reference plane:

$$I_{\text{datum}} = \int_{-a}^a t \cdot z^2 \cdot dx = \int_{-a}^a t(a^2 - x^2) dx = \frac{4a^3 t}{3} \quad (\text{A.4})$$

Thus using the parallel axis theorem the second moment of area about the neutral axis is thus:

$$I_{\text{centroid}} = I_{\text{datum}} - A\bar{d}^2 = \frac{4a^3 t}{3} - 2at \left(\frac{\pi a}{4} \right)^2 = a^3 t \left(\frac{4}{3} - \frac{\pi^2}{8} \right) \quad (\text{A.5})$$

For dimples with an elliptical profile the revolved dimple geometry is a semi-ellipsoid. Being geometrically equivalent to a hemisphere under a vertical scaling, this provides a convenient way to generalise to a dimple of arbitrary depth. For a dimple of depth d , the second moment of area is:

$$I_{\text{centroid}} = ad^2 t \left(\frac{4}{3} - \frac{\pi^2}{8} \right) \quad (\text{A.6})$$

A.1.2 Spherical cap dimple

When a dimple has a circular arc as its radial profile, the revolved geometry of the dimple is a spherical cap. At every cross-section of the dimple the cross-section is a circular arc, but the radius of curvature and subtended angle of the arc depend on the location of the cut. The second moment of area for a circular arc cross-section is calculated as follows.

For a circular arc profile it is convenient to first calculate the section properties about the centre of curvature and then use the parallel axis theorem to refer the properties to the neutral axis.

It is convenient to work in terms of R and ϕ_0 , the radius of curvature and subtended half-angle. The relationship to the depth d and radius a are:

$$a = R \sin(\phi_0) \quad d = R(1 - \cos(\phi_0)) \quad (\text{A.7})$$

The area of the cross-section is:

$$A = 2at = 2Rt \sin(\phi_0) \quad (\text{A.8})$$

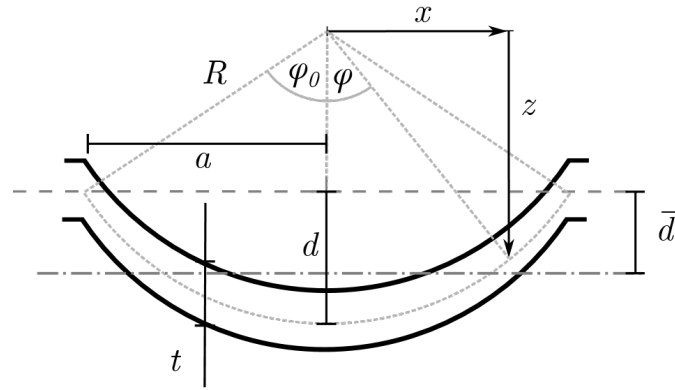


Fig. A.2 A circular arc dimple profile is shown. The dimple has a constant vertical thickness.

The distance from the centre of curvature to the neutral axis of the section is:

$$\frac{\int_{-a}^a t \cdot z \cdot dx}{A} = \frac{1}{2R \sin(\phi_0)} \int_{-\phi_0}^{\phi_0} R \cos(\phi) \cdot R \cos(\phi) d\phi = \frac{R}{2} \left(\frac{\phi_0}{\sin(\phi_0)} + \cos(\phi_0) \right) \quad (\text{A.9})$$

Thus the depth of the neutral axis below the datum plane is:

$$\bar{d} = \frac{R}{2} \left(\frac{\phi_0}{\sin(\phi_0)} + \cos(\phi_0) \right) - R \cos(\phi_0) = \frac{R}{2} \left(\frac{\phi_0}{\sin(\phi_0)} - \cos(\phi_0) \right) \quad (\text{A.10})$$

The second moment of area about the centre of curvature is:

$$I_{\text{CoC}} = \int_{-a}^a t \cdot z^2 \cdot dx = \int_{-\phi_0}^{\phi_0} t R^2 \cos^2(\phi) \cdot R \cos(\phi) d\phi = \frac{R^3 t}{6} (9 \sin(\phi_0) + \sin(3\phi_0)) \quad (\text{A.11})$$

The second moment of area can be referred to the neutral axis using the parallel axis theorem:

$$I_{\text{centroid}} = I_{\text{CoC}} - A(\bar{d} + R \cos(\phi_0))^2 = \frac{R^3 t}{6} \left(\frac{33 \sin(\phi_0)}{4} + \frac{\sin(3\phi_0)}{4} - \frac{3\phi_0^2}{\sin(\phi_0)} - 6\phi_0 \cos(\phi_0) \right) \quad (\text{A.12})$$

A.2 Calculating the second moment of area of an arbitrary cross-section

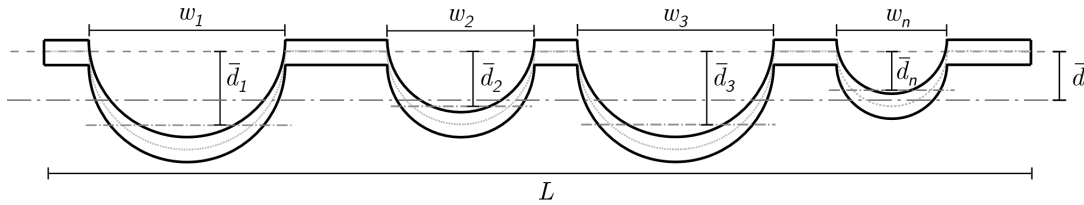


Fig. A.3 The general cross-section of a dimpled sheet. There are a number of intersections with dimples and the width of each intersection will depend on how far from the dimple centre the cut is made.

For a general cross-section through a dimpled sheet, there will be a mixture of dimple profiles and flat sections between dimples. The total second moment of area can then be calculated by summing all the contributions of the dimples around their centroids, the sum of the products of the dimple areas by the square of their centroids distance to the neutral axis, the product of the square of the distance between the neutral axis and the flat sections and the area of the flat sections, and the contribution of the thickness to the second moment of area.

$$I_{xx} = \sum_{i=1}^n I_{\text{dimple}_i} + \left(L - \sum_{i=1}^n w_i \right) \cdot \bar{d}^2 + \frac{Lt^3}{12} \quad (\text{A.13})$$

where:

$$I_{\text{dimple}_i} = I_{\text{centroid}_i} + w_i(\bar{d} - \bar{d}_i)^2 t, \quad \bar{d} = \sum_{i=1}^n \frac{w_i \bar{d}_i}{L} \quad (\text{A.14})$$

The relevant width of the dimple intersection, w_i can be calculated from the distance of the dimple centre to cross-section plane V , using the formula:

$$w_i = 2\sqrt{a^2 - V^2} \quad (\text{A.15})$$

For a given dimple profile knowing the width of the intersection, the relevant values of I_{centroid} can be calculated.

Listing A.1 Matlab script calculating second moments of area across a dimpled sheet

```
1 filename = 'Hex_POINTS.csv';
2 M = csvread(filename,1,0);
3 x = M(:,1);
4 y = M(:,2);
5 %%if x=M(:,1) y=M(:,2) then the script scans along the x direction
6 %%if y=M(:,1) and x=M(:,2) then script scans along the y direction
7
8 nMax = length(x); % number of points to be plotted
9 a = 3; %Dimple radius
10 b = 1.8; %max dimple depth
11 t = 1; %Thickness of sheet
12
13 dx=0.1; % coarseness of samplng in the y direction
14 Xmax=50; %ranges of limiting rectangle
15 Ymax=50;
16 Xmin=-50;
17 Ymin=-50;
18
19 % selecting only points within the rectangle defined by Xmax, Xmin,
    Ymax and Ymin
20 end;
21 for i = 1:nMax
22     if x(i)> (Xmax-0.5*a)
23         x(i)=NaN;
24         y(i)=NaN;
25     end
26     if x(i)< (Xmin+0.5*a)
27         x(i)=NaN;
28         y(i)=NaN;
29     end
30     if y(i)> (Ymax-0.5*a)
31         x(i)=NaN;
32         y(i)=NaN;
33     end
34     if y(i)< (Ymin+0.5*a)
```

```

35         x(i)=NaN;
36         y(i)=NaN;
37     end
38
39     Ixx=zeros(1,((Xmax-Xmin)/dx));
40
41     for j= 1:((Xmax-Xmin)/dx);    %%((Xmax-Xmin)/dx);
42
43         Xd=Xmin+(j-1)*dx; %Xd is dummy variable x
44
45         w=zeros(1,nMax); %width of intersections
46         V=NaN(1,nMax); %distance of intesection plane from dimple centre
47         r=zeros(1,nMax); %radius of curvature of cross-section
48         phi=zeros(1,nMax); %subtanded angle of cross-section
49         depth=zeros(1,nMax); %depth of dimple centroid
50         Idimples=zeros(1,nMax); %incl  $A*(d-dBar)^2$  contibution of dimples
51         Icentroid=zeros(1,nMax);
52         d=zeros(1,nMax);
53
54     for i= 1:nMax;
55         if abs(x(i)-Xd)<=a;
56             w(i)=2*sqrt(a^2-(x(i)-Xd)^2);
57             %If intersection occurs, write width of intersection to w
58             V(i)=abs(x(i)-Xd);
59             %write distance of this intersection plane from dimple
              centre
60             depth(i)=sqrt(((a^2+b^2)/(2*b))^2-V(i)^2)-((a^2-b^2)/(2*b))
              ;
61             r(i)=((w(i)/2)^2+depth(i)^2)/(2*depth(i));
62             phi(i)=2*atan(depth(i)/(w(i)/2));
63             Icentroid(i)=((t*r(i)^3)/6)*((33/4)*sin(phi(i))+sin(3*phi(i)
              ))/4 -(3*phi(i)^2)/sin(phi(i)) - 6*phi(i)*cos(phi(i));
64             d(i)=(r(i)/2)*((phi(i)/sin(phi(i)))-cos(phi(i))); %depth of
              centroids for each dimple
65         end
66     end

```

```
67
68     dBar=(sum(d.*w))/(Xmax-Xmin); %dBar is overall cenroid depth
69     % d.*Intersect is controibution of each dimple to overall centroid
70     flatplate(j)=(Xmax-Xmin)-sum(w); %amount of flat plate left
71     Iflat= t*flatplate(j)*dBar^2; %contibution of flat plate to Ixx
72     Ithick= (Xmax-Xmin)*(t^3)/12; %contibution of plate thickness
73     Idimples= Icentroid + t*w.*(d-dBar).^2;
74     Ixx(j)= sum(Idimples)+ + Ithick + Iflat;
75 end
```


Appendix B

Inclusion stresses

B.1 Scaled superposition of stresses around adjacent inclusions

The scaled superposition of two finite plate stress distributions from adjacent inclusions can be used to accurately predict the true stress distribution found between two adjacent inclusions which are part of a regular hexagonal pattern of inclusions in a large plate.

Defining the normalised centre to centre distance between the inclusions to be $d = \text{gap-ratio} + 2$, the stress distributions around a finite plate of normalised radius d will be superposed together. The scaling will be based on the correlation of stresses seen for a finite plate which has radius $d/2$, as highlighted by red circles in Fig. 4.7, namely the radial stress at $\rho = 0$ and the circumferential stress at $\rho = 1^+$.

The stresses for a finite plate with normalised radius, d , are:

$$\frac{\sigma_{rr}}{\sigma_0} = \begin{cases} 1 + \frac{(K-1)(1-d^{-2})}{1+(K-1)d^{-2}} & \rightarrow 0 < \rho < 1 \\ 1 + \frac{(K-1)(\rho^{-2}-d^{-2})}{1+(K-1)d^{-2}} & \rightarrow 1 < \rho < d \end{cases} \quad (\text{B.1})$$

$$\frac{\sigma_{\theta\theta}}{\sigma_0} = \begin{cases} 1 + \frac{(K-1)(1-d^{-2})}{1+(K-1)d^{-2}} & \rightarrow 0 < \rho < 1 \\ 1 - \frac{(K-1)(\rho^{-2}+d^{-2})}{1+(K-1)d^{-2}} & \rightarrow 0 < \rho < d \end{cases} \quad (\text{B.2})$$

Where K is the inclusion stress for the infinite plate case as defined in Eqn. 4.15. The stresses of a finite plate of the same radius, but with its centre at $\rho = d$:

$$\frac{\sigma_{rr}}{\sigma_0} = \begin{cases} 1 + \frac{(K-1)(1-d^{-2})}{1+(K-1)d^{-2}} & \rightarrow d > \rho > d-1 \\ 1 + \frac{(K-1)((d-\rho)^{-2} - d^{-2})}{1+(K-1)d^{-2}} & \rightarrow d-1 > \rho > 0 \end{cases} \quad (\text{B.3})$$

$$\frac{\sigma_{\theta\theta}}{\sigma_0} = \begin{cases} 1 + \frac{(K-1)(1-d^{-2})}{1+(K-1)d^{-2}} & \rightarrow d > \rho > d-1 \\ 1 - \frac{(K-1)((d-\rho)^{-2} + d^{-2})}{1+(K-1)d^{-2}} & \rightarrow d-1 > \rho > 0 \end{cases} \quad (\text{B.4})$$

These two stress distributions can be superposed together. Superposing only the difference in stresses from unity for these two distributions, as per Eqn 4.38:

$$\frac{\sigma_{rr}}{\sigma_0} = \begin{cases} 1 + \frac{(K-1)(1+(d-\rho)^{-2} - 2d^{-2})}{1+(K-1)d^{-2}} & \rightarrow 0 < \rho < 1 \\ 1 + \frac{(K-1)(\rho^{-2} + (d-\rho)^{-2} - 2d^{-2})}{1+(K-1)d^{-2}} & \rightarrow 1 < \rho < \frac{d}{2} \end{cases} \quad (\text{B.5})$$

$$\frac{\sigma_{\theta\theta}}{\sigma_0} = \begin{cases} 1 + \frac{(K-1)(1-(d-\rho)^{-2} - 2d^{-2})}{1+(K-1)d^{-2}} & \rightarrow 0 < \rho < 1 \\ 1 - \frac{(K-1)(\rho^{-2} + (d-\rho)^{-2} + 2d^{-2})}{1+(K-1)d^{-2}} & \rightarrow 1 < \rho < \frac{d}{2} \end{cases} \quad (\text{B.6})$$

Note that as the distribution is symmetric, the function is only shown up to $d/2$.

The superposed stresses are now scaled appropriately. For the radial stresses, the superposed stress is scaled by a constant factor, c_{rr} , which is defined to match the stress at the centre of the inclusion to that found from a inscribed finite plate which has radius $d/2$.

$$\sigma_{rr_{\text{scaled}}} = c_{rr} \cdot \sigma_{rr_{\text{superposed}}} \quad (\text{B.7})$$

$$c_{rr} = \frac{\sigma_{rr} \Big|_{\substack{\rho=0 \\ \Lambda=d/2}}}{\sigma_{rr_{\text{superposed}}} \Big|_{\rho=0}} = \frac{1+(K-1)d^{-2}}{1+(K-1)(d/2)^{-2}} \quad (\text{B.8})$$

For the circumferential stresses the scaling is applied to only the difference between the stress and unity, Eqn B.9. The scaling factor, $c_{\theta\theta}$, is defined such that the stress just outside the inclusion will become equal to that of the inscribed finite sheet at this location.

$$\sigma_{\theta\theta_{\text{scaled}}} = \sigma_0 + c_{\theta\theta} \cdot (\sigma_{\theta\theta_{\text{superposed}}} - \sigma_0) \quad (\text{B.9})$$

$$c_{\theta\theta} = \frac{\sigma_{\theta\theta} \Big|_{\substack{\rho=1+ \\ \Lambda=d/2}} - \sigma_0}{\sigma_{\theta\theta_{\text{superposed}}} \Big|_{\rho=1+} - \sigma_0} = \frac{1 + (K-1)d^{-2}}{1 + (K-1)(d/2)^{-2}} \frac{1 + (d/2)^{-2}}{1 + (d-1)^{-2} + 2d^{-2}} \quad (\text{B.10})$$

Calculating the radial strain in the plate as $\varepsilon_{rr} = (\sigma_{rr} - \nu\sigma_{\theta\theta})/EI$, gives the strain after superposition and scaling as:

$$\varepsilon_{rr} = \begin{cases} \frac{1}{kEI} \left[(c_{rr} - \nu) + \frac{(K-1)([c_{rr} - \nu c_{\theta\theta}][1 - 2d^{-2}] + [c_{rr} + \nu c_{\theta\theta}][d - \rho]^{-2})}{1 + (K-1)d^{-2}} \right] & \rightarrow 0 < \rho < 1 \\ \frac{1}{EI} \left[(c_{rr} - \nu) + \frac{(K-1)([c_{rr} + \nu c_{\theta\theta}][\rho^{-2} + (d - \rho)^{-2}] - [c_{rr} - \nu c_{\theta\theta}]2d^{-2})}{1 + (K-1)d^{-2}} \right] & \rightarrow 1 < \rho < \frac{d}{2} \end{cases} \quad (\text{B.11})$$

Integrating the strain between $\rho = 0$ and $\rho = d/2$ calculates the displacement at the midpoint between two adjacent inclusions. Dividing by $(d/2) \cdot \sigma_0(1 - \nu)/EI$, the displacement of a homogeneous sheet at this point, and inverting allows us to calculate the normalised stiffness of a plate which has stresses defined by the superposition and scaling method. When we allow the Poisson's ratios of the inclusion and the plate to be equal, $\nu_1 = \nu_2 = \nu$, then $K = 2k/[(1 - \nu) + (1 + \nu)k]$, and the normalised stiffness becomes:

$$\Psi_{ss} = 1 \div \left[1 - \frac{2(k-1)}{kd} + \frac{2(k-1)}{c_a d^3 (d-1)} \left([d^3 - 4.5d^2 + 7.5d + 5] + \frac{1}{k} [d^3 - d^2 - 6d + 5] + \nu c_b [d^3 - d^2 - 3d + 2] \frac{k-1}{k} \right) \right] \quad (\text{B.12})$$

where $c_a = k(1 + \nu) + (1 - \nu) + (k-1)(1 - \nu)(d/2)^{-2}$ and $c_b = \frac{c_{\theta\theta}}{c_{rr}} = \frac{1 + (d/2)^{-2}}{1 + (d-1)^{-2} + 2d^{-2}}$.

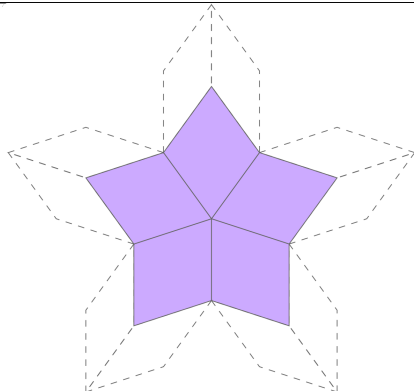
Appendix C

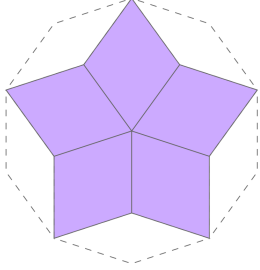
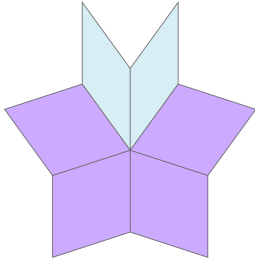
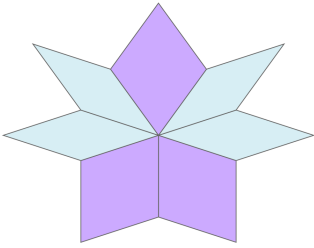
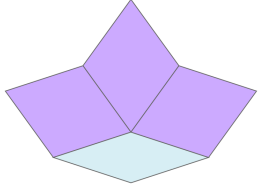
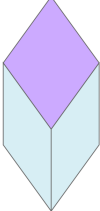
Aperiodic patterns

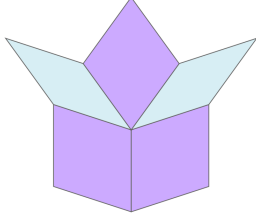
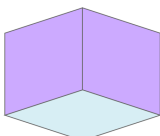
C.1 Penrose tilings

In Penrose rhombus and Penrose kite and dart tiling, while there are only two distinct prototiles, there are a number of ways that these prototiles can join to form a vertex. The tiles around a tiling vertex are known as the “vertex neighbourhood”: due to matching rules enforced on the tiles, defining a vertex may also force the placement of some surrounding tiles. These additional forced tiles are known as the vertex “empire”. This appendix shows the different vertex neighbourhoods of Penrose tiling [76] and the relative occurrences of each of these vertices is also given. The relative abundances are conveniently given in terms of the golden ratio, $\tau = \frac{1+\sqrt{5}}{2}$.

Table C.1 The eight vertex neighbourhoods that occur in the Penrose rhombus tiling

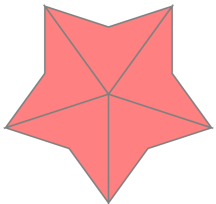
Vertex neighbourhood	Name	Relative occurrence
	S	$\frac{\tau^4}{\tau^4-1}$

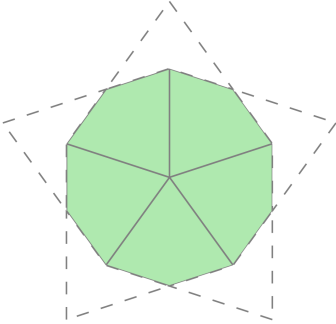
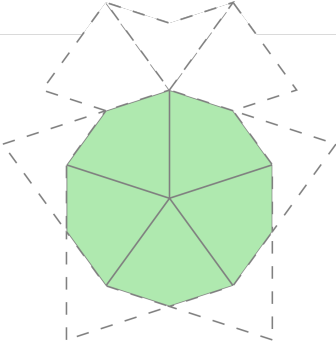
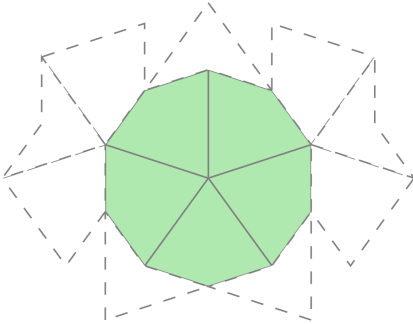
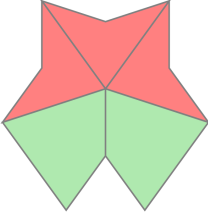
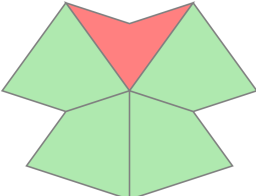
Vertex neighbourhood	Name	Relative occurrence
	S5	$\frac{\tau^2}{\tau^4-1}$
	S4	1
	S3	τ
	K	τ^2
	Q	τ^3

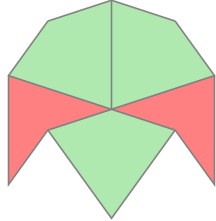
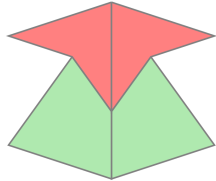
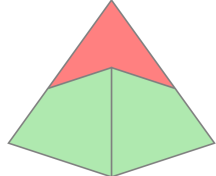
Vertex neighbourhood	Name	Relative occurrence
	J	τ^4
	D	τ^5

The abundances are scaled such that the relative occurrence of the ‘S4’ vertex is unity. Note that the relative occurrence of thin rhombi is τ^5 as every thin rhombi is part of exactly one ‘D’ vertex, the relative occurrence of fat rhombi is τ^6 . The sum of the relative occurrences for ‘S’ and ‘S5’ is equal to τ . The dashed white tiles shown around the ‘S’ and ‘S5’ vertices are not technically part of the vertex neighbourhood, as they don’t have a vertex at the centre of the neighbourhood, however they are forced tiles that are part of the empire and allow the two vertex neighbourhoods to be easily differentiated.

Table C.2 The nine vertex neighbourhoods that occur in the Penrose kite and dart tiling

Vertex neighbourhood	Name	Relative occurrence
	Star	$\frac{\tau^4}{\tau^4 - 1}$

Vertex neighbourhood	Name	Relative occurrence
	Sun 5	$\frac{\tau^2}{\tau^4-1}$
	Sun 4	1
	Sun 3	τ
	King	τ^2
	Queen	τ^3

Vertex neighbourhood	Name	Relative occurrence
	Jack	τ^4
	Deuce	τ^5
	Ace	τ^6

The dashed white tiles shown around the ‘Sun 5’, ‘Sun 4’ and ‘Sun 3’ vertices are not technically part of the vertex neighbourhood, as they don’t have a vertex at the centre of the neighbourhood, however they are forced tiles that are part of the empire and allow the vertices to be differentiated (note that the suffix of the name in each case indicates the number of darts surrounding the central five kites). As the vertex neighbourhood names suggest, note the correlation between the vertex neighbourhoods in the rhombus tiling and the kite and dart tiling. The relative occurrence of kite is τ^5 and the relative occurrence of dart is τ^6 .

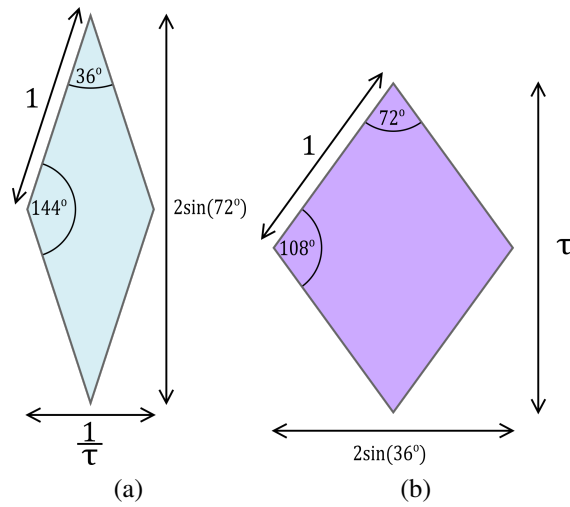


Fig. C.1 (a) A 'thin' rhomb prototile (b) A 'thick' rhomb prototile.

C.2 Penrose rhombus patterns

The Penrose rhombus pattern shown in Fig. 4.17 is created by locating an inclusion on each vertex of the underlying Penrose rhombus tiling, except for the 'K' and 'Q' vertices.

The proportion of area which can be inclusions, p , is calculated for Penrose rhombus patterns. By using some of the fundamental relationships between occurrences of different vertex neighbourhoods and calculating geometric properties of the two prototiles the maximum packing density p , can be calculated.

Figure C.1 shows the two rhombus prototiles, often referred to as 'rhombs'; Fig. C.1a 'thin' and Fig. C.1b 'thick'. Both prototiles have the same side length, which is prescribed to be unity, the area of the thin rhomb is thus:

$$A_{\text{thin}} = \frac{1}{\tau} \sin 72^\circ = \sqrt{\frac{5 - \sqrt{5}}{8}} \quad (\text{C.1})$$

the area of the thick rhomb is:

$$A_{\text{thick}} = \tau \sin 36^\circ = \sqrt{\frac{5 + \sqrt{5}}{8}} \quad (\text{C.2})$$

The ratio of thick to thin rhombs is $\tau : 1$, therefore the average tile size is:

$$\frac{A_{\text{thick}} \tau + A_{\text{thin}}}{\tau + 1} = \sqrt{\frac{5(5 - 2\sqrt{5})}{4}} \quad (\text{C.3})$$

For a patterning with one inclusion of radius a per tile, the value of p is:

$$p = \frac{\pi a^2}{\sqrt{\frac{5(5-2\sqrt{5})}{4}}} \quad (\text{C.4})$$

If instead the pattern has an inclusion centred on each vertex, we first need to calculate the vertices density in the pattern. First calculate the average number of tiles at a vertex by calculating the number of tiles that meet at each vertex neighbourhood, and then multiply each by the relative abundance of that neighbourhood. Dividing throughout by the total relative abundance give the average number of tiles at a vertex:

$$\frac{5 \cdot \tau + 6 \cdot 1 + 7 \cdot \tau + 4 \cdot \tau^2 + 3 \cdot \tau^3 + 5 \cdot \tau^4 + 3 \cdot \tau^5}{\tau + 1 + \tau + \tau^2 + \tau^3 + \tau^4 + \tau^5} = 4 \quad (\text{C.5})$$

as each tile has four vertices that must mean that there an identical number of vertices as tiles, and thus again the p value is given by Eqn C.4.

When locating an inclusion at the each tiling vertex, the limiting size of inclusion occurs due to the thin rhombs, Fig. C.1a. The maximum radius in this case is half the width of the thin rhomb, $a = 0.5/\tau \approx 0.309$, therefore the maximum packing for this pattern is:

$$p = \frac{\pi(\frac{1}{2\tau})^2}{\sqrt{\frac{5(5-2\sqrt{5})}{4}}} = \frac{\pi}{\sqrt{10(5+\sqrt{2})}} \approx 0.369 \quad (\text{C.6})$$

Modifying the pattern by removing inclusions from certain vertices allows the maximum inclusion radius to increase. We wish to eliminate the inclusions which are currently limiting the maximum inclusion radius, therefore we need to get rid of one of the inclusions from each thin rhomb. Considering the vertex neighbourhoods, Table C.1, we note that each pair of thin rhombs occurs at a 'Q' vertex and each single thin rhomb has one side which is part of a 'K' vertex. Locating an inclusion on all vertices apart from on the 'K' or 'Q' vertex neighbourhoods thus increases the maximum allowable inclusion size to $a = 1/2$; however this pattern now has a few less inclusions per unit area. Calculating the proportion of vertices being used compared to the total number of vertices:

$$\frac{1 \cdot \tau + 1 \cdot 1 + 1 \cdot \tau + 0 \cdot \tau^2 + 0 \cdot \tau^3 + 1 \cdot \tau^4 + 1 \cdot \tau^5}{\tau + 1 + \tau + \tau^2 + \tau^3 + \tau^4 + \tau^5} = 3 - \sqrt{5} \approx 0.764 \quad (\text{C.7})$$

Therefore the overall pattern density is:

$$p = \frac{\pi(\frac{1}{2})^2}{\sqrt{\frac{5(5-2\sqrt{5})}{4}}} \cdot (3 - \sqrt{5}) = \frac{\pi}{5} \frac{5 - \sqrt{5}}{2} \approx 0.739 \quad (\text{C.8})$$

To divide this pattern into two sets so that it can be used as a pattern where dimples are pushed through in both directions, we need to define a way of systematically selecting two groups. A good system here is to define all the ‘D’ vertices as one set, and the other vertices, namely ‘S’, ‘S3’, ‘S4’, ‘S5’ and ‘J’, as the other set. Noting that the ‘K’ and ‘Q’ vertex neighbourhoods are not being used at all the percentage of ‘D’ vertex neighborhoods is:

$$\frac{\tau^5}{\tau + 1 + \tau + \tau^2 + \tau^3 + \tau^4 + \tau^5} = 0.5 = 50\% \quad (\text{C.9})$$

Therefore this splits the pattern into two exactly equal sets.

The packing density can be increased slightly more however. Choosing to remove the inclusion not on the ‘K’ vertex side of a single thin rhomb but from the opposite side we find that the ‘S5’ vertex neighbourhood is often quite sparsely patterned. Each of the five thin rhombs surrounding a ‘S5’ can be either a single thin rhomb or a thin rhomb pair, *i.e.* a ‘K’ vertex or a ‘Q’ vertex. If surrounded by five single thin rhombs, then the ‘S5’ vertex has just a single inclusion surrounded by a regular decagon of inclusions, and there is a noticeable excess of space, Fig. C.2a. The space inside the decagon is large enough to fit not just the single inclusion which is present, but up to three inclusions. Choosing to centre an equilateral triangle with a side length equal to unity on the centre of the ‘S5’ vertex, the central inclusion can be replaced by three inclusions placed at each corner of the triangle. When the ‘S5’ vertex is surrounded by three single thin rhombs and two pairs of thin rhombs, Fig. C.2b, there is enough space for two inclusions. The original ‘S5’ inclusion is replaced by two inclusions located on two corners of the centered equilateral triangle. When four pairs of thin rhombs surround the ‘S5’ vertex, Fig. C.2c, there is not enough space for any additional inclusions. The maximum inclusion radius is unchanged, however a few more inclusions have been packed in, two additional inclusions for each ‘S5’ vertex with five surrounding single rhombs and one additional inclusion for each ‘S5’ vertex with three surrounding single rhombs. The corresponding packing density is thus:

$$p = \frac{\pi(\frac{1}{2})^2}{\frac{5}{22}\sqrt{25-2\sqrt{5}}} \approx 0.763 \quad (\text{C.10})$$

See Fig. 4.17a for a sample of this pattern.

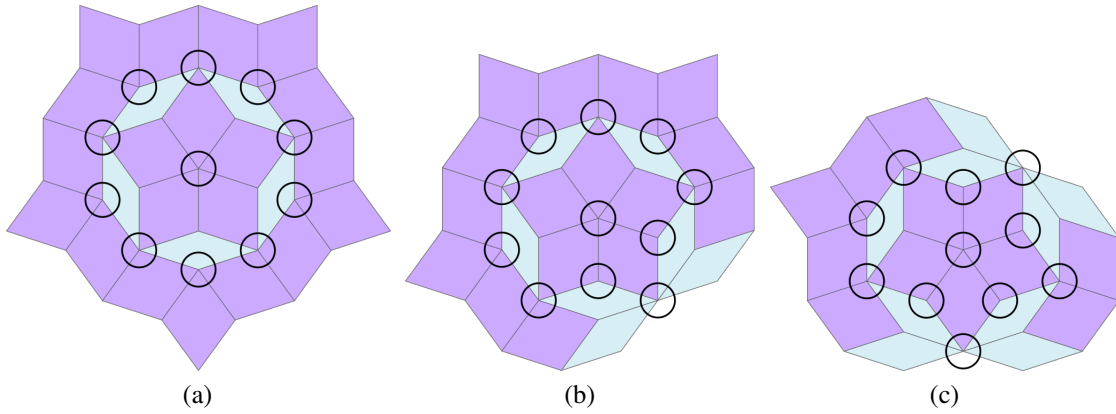


Fig. C.2 (a) A ‘S5’ vertex surrounded by five single thin rhomb ‘K’ vertices. (b) A ‘S5’ vertex surrounded by three single thin rhombs and two pairs of thin rhombs, three ‘K’ and two ‘Q’ vertices. (c) A ‘S5’ vertex surrounded by one single thin rhomb and four pairs of thin rhombs, one ‘K’ and four ‘Q’ vertices.

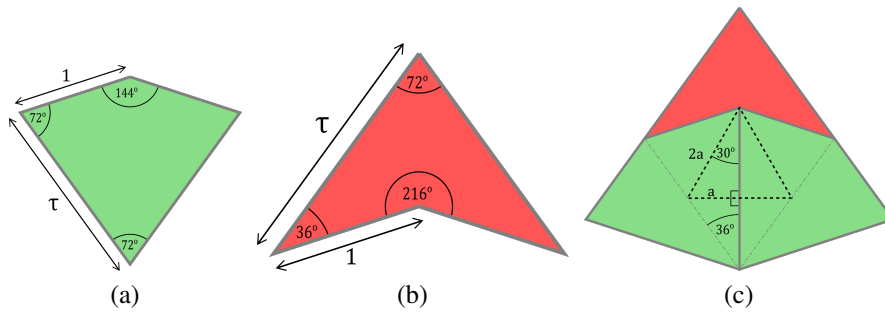


Fig. C.3 (a) A kite prototile (b) A dart prototile. (c) An ‘Ace’ vertex neighborhood.

C.3 Penrose kite and dart patterns

The Penrose kite and dart pattern shown in Fig. 4.17 is created by locating one inclusion per prototile of the underlying Penrose kite and dart tiling. The inclusions are located at concave vertex of the dart prototile and on the centre line of each kite prototile, as defined by Fig. C.3c.

Figure C.3 shows the kite and dart prototiles. The short side length of both prototiles is equal to unity and the long side length is equal to τ . The area of the respective prototiles is:

$$A_{\text{kite}} = \sqrt{\frac{5 + 2\sqrt{5}}{4}} \tag{C.11}$$

$$A_{\text{dart}} = \sqrt{\frac{5 + \sqrt{5}}{8}} \tag{C.12}$$

The ratio of kites to darts is $\tau : 1$, therefore the average tile size is:

$$\frac{A_{\text{kite}}\tau + A_{\text{dart}}}{\tau + 1} = \sqrt{\frac{5(5 - \sqrt{5})}{8}} \quad (\text{C.13})$$

For a pattern with one inclusion per tile, and an inclusion radius of a , the pattern packing p is:

$$p = \frac{\pi a^2}{\sqrt{\frac{5(5 - \sqrt{5})}{8}}} \quad (\text{C.14})$$

The kite and dart prototiles have less well defined centers than the rhombus prototiles. The single line of symmetry of both kite and dart suggests that selecting the centre-line for an inclusions placement would be sensible however. Considering the ‘Ace’ vertex neighbourhood, Fig. C.3c, we could define the concave vertex as a pattern location, and define the pattern location of the kite as to form an equilateral triangle. Solving the geometry of this problem gives a maximum radius of:

$$a = \frac{1}{4} \sqrt{85 + 37\sqrt{5} - \sqrt{30(445 + 199\sqrt{5})}} \approx 0.521 \quad (\text{C.15})$$

The maximum packing for this pattern is hence:

$$p = \frac{\pi a^2}{\sqrt{\frac{5(5 - \sqrt{5})}{8}}} = \pi \left(\frac{17}{16} \sqrt{10 + 2\sqrt{5}} - \sqrt{15} + \frac{37}{8} \sqrt{\frac{5 + \sqrt{5}}{10}} - \frac{9\sqrt{3}}{4} \right) \approx 0.648 \quad (\text{C.16})$$

See Fig. 4.17b for a sample of this pattern

Defining the kite prototiles which are around a ‘King’ vertex or a ‘Jack’ vertex and the dart tile of a ‘Queen’ vertex neighbourhood to be one set, the percentage of the total that they make up is:

$$\frac{3 \cdot \tau^2 + 1 \cdot \tau^3 + 2 \cdot \tau^4}{5 \cdot \frac{\tau^4}{\tau^4 - 1} + 5 \cdot \frac{\tau^2}{\tau^4 - 1} + 5 \cdot 1 + 5 \cdot \tau + 3 \cdot \tau^2 + 1 \cdot \tau^3 + 2 \cdot \tau^4} = 3 - \sqrt{5} \approx 0.507 = 50.7\% \quad (\text{C.17})$$

Note that as there is only one inclusion per prototile, but each prototile belongs to multiple vertex neighborhoods, a tile is here defined to belong to a vertex if the point of the dart is at the vertex or the tail of the kite is at the vertex. Therefore the ‘Jack’ vertex neighborhood is defined to have two tiles which belong to it, the two kites who’s tails meet at the vertex.

A 'Deuce' or 'Ace' vertex by this definition have no associated tiles, so do not appear in Eqn C.17. This choice splits the pattern into two almost equal sets, and so can be used to define the direction of dimple in this pattern as up or down.

Appendix D

Stiffnesses of circular plates

D.1 Stiffness of a finite plate with a central hole with internal loading

This appendix uses an Airy's stress function, Φ , to calculate the displacement of the inner edge of a finite plate with an internal loading, this is superposition case I in Fig. 5.6. Using an axisymmetric Airy's stress function:

$$\Phi = c_0 + c_1 r^2 + c_2 r^2 \ln r + c_3 \ln r \quad (\text{D.1})$$

then:

$$\sigma_{rr} = \frac{1}{r} \frac{\partial \Phi}{\partial r} + \frac{1}{r^2} \frac{\partial^2 \Phi}{\partial \theta^2} = 2c_1 + c_2(1 + 2 \ln r) + \frac{c_3}{r^2} \quad (\text{D.2})$$

$$\sigma_{\theta\theta} = \frac{\partial^2 \Phi}{\partial r^2} = 2c_1 + c_2(3 + 2 \ln r) - \frac{c_3}{r^2} \quad (\text{D.3})$$

where c_0, c_1, c_2 and c_3 are arbitrary constants. Using the boundary conditions that there is a unit stress on the internal boundary and zero radial stress at the outer boundary:

$$\left. \frac{\sigma_{rr}}{\sigma_0} \right|_{r=a} = -1 \quad \left. \frac{\sigma_{rr}}{\sigma_0} \right|_{r=\Lambda a} = 0 \quad (\text{D.4})$$

thus:

$$c_1 = \frac{-1}{2(1 - \Lambda^2)} \quad c_2 = 0 \quad c_3 = \frac{-(\Lambda a)^2}{(1 - \Lambda^2)} \quad (\text{D.5})$$

the stress distributions are therefore:

$$\frac{\sigma_{rr}}{\sigma_0} = \frac{-(1 - (\Lambda a/r)^2)}{1 - \Lambda^2} \quad \frac{\sigma_{\theta\theta}}{\sigma_0} = \frac{-(1 + (\Lambda a/r)^2)}{1 - \Lambda^2} \quad (\text{D.6})$$

The circumferential strain is given by $\varepsilon_{\theta\theta} = (\sigma_{\theta\theta} - \nu\sigma_{rr})/E$:

$$\frac{\varepsilon_{\theta\theta}}{\sigma_0} = \frac{-((1 - \nu) + (1 + \nu)(\Lambda a/r)^2)}{E(1 - \Lambda^2)} \quad (\text{D.7})$$

The radial displacement can be calculated using $\delta_{rr} = \varepsilon_{\theta\theta}r$, and thus, the displacement at the internal boundary, $r = a$, for a unit force per unit load is:

$$\delta|_{r=a} = \frac{-a(1 - \nu) + (1 + \nu)\Lambda^2}{Et(1 - \Lambda^2)} = \frac{a(1 + \nu)}{Et} \left(1 + \frac{2}{(\Lambda^2 - 1)(1 + \nu)} \right) \quad (\text{D.8})$$

D.2 Stiffness of a circular plate with stiff central section and an overhang under a transverse ring loading

The biaxial bending rig described in Section 5.7 is analysed here for the case of an arbitrary overhang and also a central section which has a rigidity k compared with the rest of the plate. Figure D.1 shows a cross-section through the set-up and also shows an exploded view of the plate, labeling the internal shear forces and moments which act on each free body section.

The effect of having a stiff central section is to act as a stress concentrator, and as such the moment which is carried by the central section, increases by the dimensionless constant c , which accounts for the relative size and stiffness of this central section. Considering a circular plate with zero overhang and equating the rotations at L_{in} for the inner plate and the ring of plate between the supports, but accounting for the increased flexural rigidity of the central region, allows the magnitude of the uniform biaxial moment to be calculated as:

$$M = \frac{2}{1 + \frac{1}{k} + (1 - \frac{1}{k}) \left(\frac{L_{out}^2}{L_{in}^2} + \nu \left(1 - \frac{L_{in}^2}{L_{out}^2} \right) \right)} \left[\frac{T(L_{out} - L_{in})^2(1 - \nu)}{8\pi L_{out}^2} - \frac{T \ln \frac{L_{in}}{L_{out}}(1 + \nu)}{4\pi} \right] \quad (\text{D.9})$$

Noting that the expression inside the square bracket is equal to the moment carried by the central region of a uniform plate, see Eqn 5.22, and denoting this as M_1 , we can write the moment carried by the stiff section of plate as:

$$M = (1 + c)M_1 \quad (\text{D.10})$$

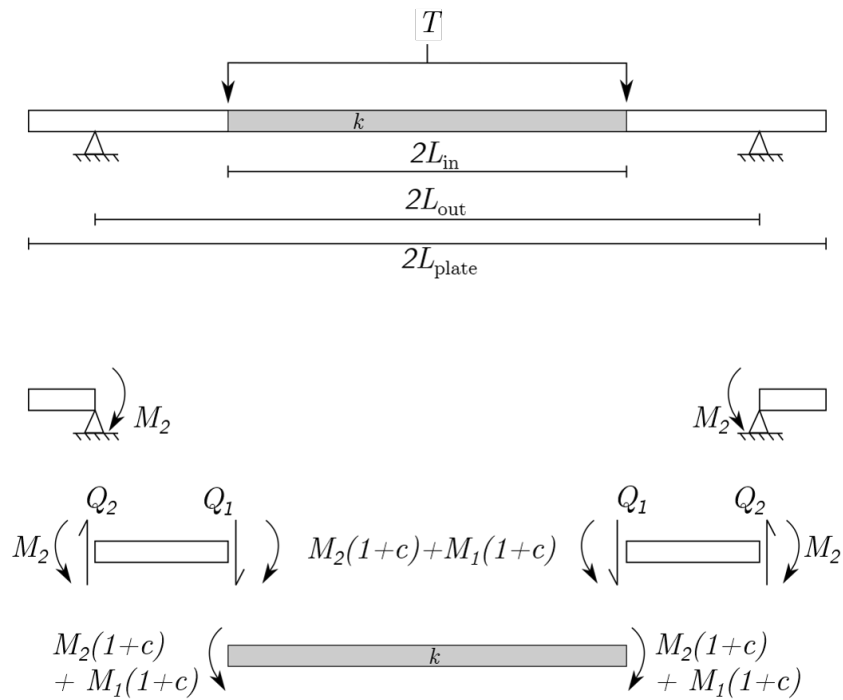


Fig. D.1 A cross-section through the biaxial bending test rig set-up. A total force T is applied to the top support which applies a ring load at a radius L_{in} . The moment which is applied to the overhanging ring in order to ensure a compatible rotation at L_{out} has a magnitude M . The magnitude of the uniform biaxial bending moment in the central section is $M(1+c)$, where c is a constant which depends on the relative size and stiffness of the central section. The shear forces acting on the plate are $Q_1 = T/(2\pi L_{\text{in}})$ and $Q_2 = T/(2\pi L_{\text{out}})$.

And thus deduce an expression for c :

$$1 + c = \frac{2}{1 + \frac{1}{k} + \left(1 - \frac{1}{k}\right) \left(\frac{L_{\text{out}}^2}{L_{\text{in}}^2} + \nu \left(1 - \frac{L_{\text{in}}^2}{L_{\text{out}}^2}\right)\right)} \quad (\text{D.11})$$

When combined with an overhang, there is an additional moment per unit length applied to the plate at L_{out} , which we denote M_2 . As before, the stiff central section has a stress amplification effect, and thus the total moment carried by the central section is $M_1(1 + c) + M_2(1 + c)$. The value of M_2 can be calculated by equating the rotations of the overhanging plate and the plate between the two supports. The overhanging plate, when loaded by M_2 has a radial rotation at L_{out} of:

$$\Theta|_{L_{\text{out}}} = \frac{M_2 L_{\text{out}}^3}{D(L_{\text{plate}}^2 - L_{\text{out}}^2)(1 + \nu)} \left(1 + \frac{L_{\text{plate}}^2(1 + \nu)}{L_{\text{out}}^2(1 - \nu)}\right) \quad (\text{D.12})$$

The plate between the supports, when loaded by the moment M_2 and the ring load T , has a rotation at L_{out} of:

$$\begin{aligned} \Theta|_{L_{\text{out}}} = & \frac{-T(L_{\text{out}}^2 - L_{\text{in}}^2)}{4\pi D(1 + \nu)L_{\text{out}}} \\ & + c \left[\frac{T(L_{\text{out}}^2 - L_{\text{in}}^2)(1 - \nu)}{8\pi L_{\text{out}}^2} - \frac{T \ln \frac{L_{\text{in}}}{L_{\text{out}}}(1 + \nu)}{4\pi} \right] \frac{2L_{\text{out}}L_{\text{in}}^2}{D(L_{\text{out}}^2 - L_{\text{in}}^2)(1 + \nu)(1 - \nu)} \\ & + \frac{M_2 L_{\text{out}}}{D(1 + \nu)} - \frac{2M_2 c L_{\text{out}} L_{\text{out}}^2}{D(L_{\text{out}}^2 - L_{\text{in}}^2)(1 + \nu)(1 - \nu)} \end{aligned} \quad (\text{D.13})$$

equating Eqn D.13 and Eqn D.12 gives M_2 as a function of T :

$$M_2 = \frac{T(1 - \nu)}{8\pi} \frac{\frac{L_{\text{out}}^2 - L_{\text{in}}^2}{L_{\text{out}}^2} - c \left(-\ln \frac{L_{\text{in}}}{L_{\text{out}}}(1 + \nu)\right)}{\frac{L_{\text{plate}}^2}{L_{\text{plate}}^2 - L_{\text{out}}^2} - \frac{c L_{\text{in}}^2}{L_{\text{out}}^2 - L_{\text{in}}^2}} \frac{2L_{\text{in}}^2}{(L_{\text{out}}^2 - L_{\text{in}}^2)(1 - \nu)} \quad (\text{D.14})$$

Finally the vertical deflection at L_{in} can be calculated:

$$\begin{aligned}
 \delta|_{L_{in}} = & \frac{T}{8\pi D} \left[(L_{out}^2 - L_{in}^2) \left(1 + \frac{1-\nu}{2(1+\nu)} \frac{L_{out}^2 - L_{in}^2}{L_{out}^2} \right) + 2L_{in}^2 \ln \frac{L_{in}^2}{L_{out}^2} \right] \\
 & + \frac{cT}{8\pi D} \left[\frac{(L_{out}^2 - L_{in}^2)(1-\nu)}{L_{out}^2} - 2 \ln \frac{L_{in}}{L_{out}} (1+\nu) \right] \left(\frac{-L_{in}^2}{2(1+\nu)} + \frac{L_{out}^2 L_{in}^2 \ln \frac{L_{in}}{L_{out}}}{(1-\nu)(L_{out}^2 - L_{in}^2)} \right) \\
 & - \frac{M_2}{D} \left[\frac{L_{out}^2 - (1+c)L_{in}^2}{2(1+\nu)} + \frac{cL_{out}^2 L_{in}^2 \ln \frac{L_{in}}{L_{out}}}{(1-\nu)(L_{out}^2 - L_{in}^2)} \right] \quad (D.15)
 \end{aligned}$$

And thus, using the expression for M_2 , this allows a complete equation which relates the force applied by the ring load to the deflection at the point of application. This therefore allows an experimental result of force displacement characteristic to calculate the effective stiffness of the middle section, as required.

Appendix E

FEA normalised stiffness data

E.1 Normalised stiffness of inclusion patterned plates

Table E.1 Normalised biaxial stiffnesses and SCF of inclusion patterned sheets, regular hexagonal pattern, $k = 3$ and $\nu = 0.3$

Gap ratio	p	L/a	Normalised stiffness	SFC
0.1	0.8226	12.5	2.3551	1.0478
0.2	0.7495	12.5	2.1348	0.10656
0.3	0.6857	12.5	1.9762	1.0785
0.4	0.6298	12.5	1.8473	1.0955
0.5	0.5804	12.5	1.7558	1.1108
0.5	0.5804	25	1.7537	1.1097
0.5	0.5804	50	1.7512	1.1087
1	0.4031	50	1.4514	1.1615
2	0.2267	50	1.2257	1.2198
3	0.1451	50	1.1378	1.2494
4	0.1008	50	1.0926	1.2662
5	0.0740	50	1.0669	1.2747
10	0.0252	50	1.0230	1.2950

Table E.2 Normalised biaxial stiffnesses and SCF of inclusion patterned sheets, regular hexagonal pattern, $k = 0.2$ and $\nu = 0.3$

Gap ratio	p	L/a	Normalised stiffness	SFC
0.1	0.8226	12.5	0.2693	0.8173
0.2	0.7495	12.5	0.3092	0.7471
0.3	0.6857	12.5	0.3390	0.7033
0.4	0.6298	12.5	0.3761	0.6603
0.5	0.5804	12.5	0.4130	0.6266
0.5	0.5804	25	0.4064	0.6305
0.5	0.5804	50	0.4051	0.6314
1	0.4031	50	0.5296	0.5459
2	0.2267	50	0.6948	0.4804
3	0.1451	50	0.7914	0.4550
4	0.1008	50	0.8499	0.4422
5	0.0740	50	0.8830	0.4365
10	0.0252	50	0.9621	0.4226

Table E.3 Normalised biaxial stiffnesses and SCF of inclusion patterned sheets, regular square pattern, $k = 3$ and $\nu = 0.3$

Gap ratio	p	L/a	Normalised stiffness	SFC
0.1	0.7124	12.5	2.0678	1.0905
0.2	0.6491	12.5	1.9024	1.1056
0.3	0.5939	12.5	1.7940	1.1096
0.4	0.5454	12.5	1.7019	1.1185
0.5	0.5027	12.5	1.6155	1.1354
0.5	0.5027	50	1.6145	1.1353
1	0.3491	50	1.3764	1.1821
2	0.1963	50	1.1921	1.2310
3	0.1257	50	1.1180	1.2560
4	0.0873	50	1.0807	1.2696
5	0.0641	50	1.0593	1.2776
10	0.0218	50	1.0201	1.2947

Table E.4 Normalised biaxial stiffnesses and SCF of inclusion patterned sheets, Penrose Rhombus pattern, $k = 3$ and $\nu = 0.3$

Gap ratio	p	L/a	Normalised stiffness	SFC
0.1	0.6918	25	1.9967	1.0804
0.2	0.6304	25	1.8549	1.1145
0.3	0.5767	25	1.7502	1.1253
0.4	0.5297	25	1.6758	1.1351
0.5	0.4881	25	1.5890	1.1392
0.5	0.4881	50	1.5899	1.1420
1	0.3390	50	1.3709	1.1867
2	0.1907	50	1.1818	1.2342
3	0.1220	50	1.1178	1.2576
4	0.0847	50	1.0813	1.2710
5	0.0623	50	1.0537	1.2809
10	0.0212	50	1.0285	1.2924

Table E.5 Normalised biaxial stiffnesses and SCF of inclusion patterned sheets, Penrose Kite and Dart pattern, $k = 3$ and $\nu = 0.3$

Gap ratio	p	L/a	Normalised stiffness	SFC
0.1	0.5874	25	1.8010	1.1511
0.2	0.5352	25	1.6961	1.1484
0.3	0.4897	25	1.6003	1.1531
0.4	0.4497	25	1.5257	1.1527
0.5	0.4144	25	1.4615	1.1623
0.5	0.4144	50	1.4730	1.1701
1	0.2878	50	1.3015	1.2012
2	0.1619	50	1.1586	1.2416
3	0.1036	50	1.0970	1.2644
4	0.0720	50	1.0677	1.2775
5	0.0529	50	1.0517	1.2836
10	0.0180	50	0.0158	1.2969

Table E.6 Normalised biaxial stiffnesses and SCF of inclusion patterned sheets, phyllotaxis pattern, $k = 3$ and $\nu = 0.3$

Gap ratio	p	L/a	Normalised stiffness	SFC
0.1	0.6372	25	1.8699	1.1358
0.2	0.5806	25	1.7338	1.1272
0.3	0.5312	25	1.6597	1.1388
0.4	0.4878	25	1.5934	1.1368
0.5	0.4496	25	1.5327	1.1400
0.5	0.4496	50	1.5349	1.1276
1	0.3122	50	1.3332	1.1785
2	0.1756	50	1.1700	1.2286
3	0.1124	50	1.1074	1.2597
4	0.0781	50	1.0679	1.2805
5	0.0573	50	1.0474	1.2849
10	0.0195	50	1.0169	1.2962

Table E.7 Normalised biaxial stiffnesses of inclusion patterned sheets, regular hexagonal pattern, $k = 10$ and $\nu = 0.3$

Gap ratio	p	L/a	Normalised stiffness
0.1	0.8226	12.5	4.8171
0.2	0.7495	12.5	3.7981
0.3	0.6857	12.5	3.2169
0.4	0.6298	12.5	2.8100
0.5	0.5804	12.5	2.5134
0.5	0.5804	25	2.5065
0.5	0.5804	50	2.4963
1	0.4031	50	1.8029
2	0.2267	50	1.3667
3	0.1451	50	1.2148
4	0.1008	50	1.1427
5	0.0740	50	1.1050
10	0.0252	50	1.0314

Table E.8 Normalised biaxial stiffnesses of inclusion patterned sheets, regular hexagonal pattern, $k = 0$ and $\nu = 0.3$

Gap ratio	p	L/a	Normalised stiffness
0.1	0.8226	12.5	0.0619
0.2	0.7495	12.5	0.0994
0.3	0.6857	12.5	0.1312
0.4	0.6298	12.5	0.1704
0.5	0.5804	12.5	0.2097
0.5	0.5804	25	0.2009
0.5	0.5804	50	0.2001
1	0.4031	50	0.3377
2	0.2267	50	0.5413
3	0.1451	50	0.6739
4	0.1008	50	0.7596
5	0.0740	50	0.8089
10	0.0252	50	0.9364

Table E.9 Normalised biaxial stiffnesses of inclusion patterned sheets, regular hexagonal pattern, $k = 3$ and $\nu = 0.1$

Gap ratio	p	L/a	Normalised stiffness
0.1	0.8226	12.5	2.3854
0.2	0.7495	12.5	2.1775
0.3	0.6857	12.5	2.0299
0.4	0.6298	12.5	1.8986
0.5	0.5804	12.5	1.7878
0.5	0.5804	50	1.7964
1	0.4031	50	1.4895
2	0.2267	50	1.2457
3	0.1451	50	1.1488
4	0.1008	50	1.1002
5	0.0740	50	1.0718
10	0.0252	50	1.0226

Table E.10 Normalised biaxial stiffnesses of inclusion patterned sheets, regular hexagonal pattern, $k = 3$ and $\nu = 0.5$

Gap ratio	p	L/a	Normalised stiffness
0.1	0.8226	12.5	2.3049
0.2	0.7495	12.5	2.0921
0.3	0.6857	12.5	1.9406
0.4	0.6298	12.5	1.8144
0.5	0.5804	12.5	1.7073
0.5	0.5804	50	1.7144
1	0.4031	50	1.4282
2	0.2267	50	1.2103
3	0.1451	50	1.1264
4	0.1008	50	1.0853
5	0.0740	50	1.0631
10	0.0252	50	1.0197

Table E.11 Normalised biaxial stiffnesses of inclusion patterned sheets, regular square pattern of square inclusions, $k = 3$ and $\nu = 0.3$

Gap ratio	p	L/a	Normalised stiffness
0.1	0.9070	12.5	2.6188
0.2	0.8264	12.5	2.3464
0.3	0.7561	12.5	2.1584
0.4	0.6944	12.5	2.0022
0.5	0.6400	12.5	1.8772
0.5	0.6400	25	1.8766
0.5	0.6400	50	1.8765
1	0.4444	50	1.5187
2	0.2500	50	1.2575
3	0.1600	50	1.1564
4	0.1111	50	1.1063
5	0.0816	50	1.0777

Table E.12 Normalised biaxial stiffnesses of inclusion patterned sheets, regular square pattern of concave star inclusions, $k = 3$ and $\nu = 0.3$

Gap ratio	p	L/a	Normalised stiffness
0.2	0.5270	25	1.6760
0.3	0.4822	25	1.6032
0.4	0.4428	25	1.5403
0.5	0.4081	25	1.4839
0.5	0.4081	50	1.4840
1	0.2834	50	1.3068
3	0.1020	50	1.0991
4	0.0709	50	1.0682
5	0.0521	50	1.0502

Table E.13 Normalised uniaxial bending stiffnesses of inclusion patterned sheets, regular hexagonal pattern, $k = 3$ and $\nu = 0.3$

Gap ratio	p	L/a	Normalised stiffness
0.5	0.5804	12.5	1.9045
0.5	0.5804	50	1.8594
0.5	0.5804	100	1.8128
0.5	0.5804	200	1.7762
1	0.4031	12.5	1.5720
1	0.4031	50	1.5496
1	0.4031	100	1.5158
1	0.4031	200	1.4792

Table E.14 Normalised uniaxial and antisymmetric stiffnesses of inclusion patterned sheets, regular hexagonal pattern, $k = 3$ and $\nu = 0.3$

Gap ratio	p	L/a	Normalised stiffness	
			uniaxial	antisymmetric
0.1	0.8226	12.5	2.3580	2.3596
0.2	0.7495	12.5	2.1478	2.1552
0.3	0.6857	12.5	1.9782	1.9802
0.4	0.6298	12.5	1.8586	1.8619
0.5	0.5804	12.5	1.7602	1.7646
0.5	0.5804	25	1.7576	1.7620
0.5	0.5804	50	1.7596	1.7640
1	0.4031	50	1.4539	1.4545
2	0.2267	50	1.2250	1.2244
3	0.1451	50	1.1369	1.1366
4	0.1008	50	1.0931	1.0936
5	0.0740	50	1.0660	1.0651
10	0.0252	50	1.0223	1.0222

Table E.15 Normalised uniaxial and antisymmetric stiffnesses of inclusion patterned sheets, regular hexagonal pattern, $k = 0.2$ and $\nu = 0.3$

Gap ratio	p	L/a	Normalised stiffness uniaxial	Normalised stiffness antisymmetric
0.1	0.8226	12.5	0.2641	0.2607
0.2	0.7495	12.5	0.2954	0.2887
0.3	0.6857	12.5	0.3292	0.3241
0.4	0.6298	12.5	0.3603	0.3584
0.5	0.5804	12.5	0.3895	0.3825
0.5	0.5804	25	0.3896	0.3825
0.5	0.5804	50	0.3912	0.3843
1	0.4031	50	0.5239	0.5203
2	0.2267	50	0.6925	0.6901
3	0.1451	50	0.7871	0.7851
4	0.1008	50	0.8444	0.8421
5	0.0740	50	0.8866	0.8872
10	0.0252	50	0.9578	0.9576

Table E.16 Normalised uniaxial and antisymmetric stiffnesses of inclusion patterned sheets, regular square pattern, $k = 3$ and $\nu = 0.3$

Gap ratio	p	L/a	Normalised stiffness uniaxial	Normalised stiffness antisymmetric
0.1	0.7124	12.5	2.1284	2.1627
0.2	0.6491	12.5	1.9846	2.0318
0.3	0.5939	12.5	1.8456	1.8756
0.4	0.5454	12.5	1.7383	1.7597
0.5	0.5027	12.5	1.6653	1.6936
0.5	0.5027	25	1.6671	1.6968
0.5	0.5027	50	1.6692	1.7004
1	0.3491	50	1.4112	1.4305
2	0.1963	50	1.2015	1.2066
3	0.1257	50	1.1207	1.1223
4	0.0873	50	1.0804	1.0803
5	0.0641	50	1.0566	1.0553
10	0.0218	50	1.0182	1.0172

Table E.17 Normalised uniaxial and antisymmetric stiffnesses of inclusion patterned sheets, regular square pattern, $k = 0.2$ and $\nu = 0.3$

Gap ratio	p	L/a	Normalised stiffness uniaxial	Normalised stiffness antisymmetric
0.1	0.7124	25	0.3352	0.3464
0.2	0.6491	25	0.3819	0.3977
0.3	0.5939	25	0.4197	0.4361
0.4	0.5454	25	0.4581	0.4806
0.5	0.5027	25	0.4865	0.5056
1	0.3491	50	0.6021	0.6152
2	0.1963	50	0.7439	0.7514
3	0.1257	50	0.8219	0.8254
4	0.0873	50	0.8721	0.8756
5	0.0641	50	0.9055	0.9104
10	0.0218	50	0.9667	0.9686

Table E.18 Normalised uniaxial and antisymmetric stiffnesses of inclusion patterned sheets, regular square pattern aligned at 45° to the direction of primary loading, $k = 3$ and $\nu = 0.3$

Gap ratio	p	L/a	Normalised stiffness uniaxial	Normalised stiffness antisymmetric
0.1	0.7124	12.5	2.0138	1.9847
0.2	0.6491	12.5	1.8489	1.8182
0.3	0.5939	12.5	1.7313	1.7040
0.4	0.5454	12.5	1.6391	1.6123
0.5	0.5027	25	1.5655	1.5410
0.5	0.5027	50	1.5678	1.5444
1	0.3491	50	1.3525	1.3392
2	0.1963	50	1.1835	1.1796
3	0.1257	50	1.1123	1.1092
4	0.0873	50	1.0787	1.0787
5	0.0641	50	1.0557	1.0543
10	0.0218	50	1.0197	1.0203

Table E.19 Normalised antisymmetric stiffnesses of inclusion patterned sheets loaded in perpendicular directions, regular hexagonal pattern, $k = 3$ and $\nu = 0.3$

Gap ratio	p	L/a	Normalised stiffness	Normalised stiffness perpendicular
0.1	0.8226	12.5	2.3596	2.3654
0.2	0.7495	12.5	2.1552	2.1553
0.3	0.6857	12.5	1.9802	1.9756
0.4	0.6298	12.5	1.8619	1.8602
0.5	0.5804	12.5	1.7646	1.7697
0.5	0.5804	25	1.7620	1.7628
0.5	0.5804	50	1.7640	1.7629
1	0.4031	50	1.4545	1.4520
2	0.2267	50	1.2244	1.2238
3	0.1451	50	1.1366	1.1368
4	0.1008	50	1.0936	1.0936
5	0.0740	50	1.0651	1.0645
10	0.0252	50	1.0222	1.0230

Table E.20 Normalised antisymmetric stiffnesses of inclusion patterned sheets loaded in perpendicular directions, Penrose Rhombus pattern, $k = 3$ and $\nu = 0.3$

Gap ratio	p	L/a	Normalised stiffness	Normalised stiffness perpendicular
0.1	0.6918	25	1.9915	2.0281
0.2	0.6304	25	1.8450	1.8742
0.3	0.5767	25	1.7415	1.7935
0.4	0.5297	25	1.7031	1.7053
0.5	0.4881	25	1.6294	1.5698
1	0.3390	50	1.3702	1.3872
2	0.1907	50	1.1728	1.1686
3	0.1220	50	1.1219	1.1161
4	0.0847	50	1.0735	1.0900
5	0.0623	50	1.0572	1.0515
10	0.0212	50	1.0275	1.0246

Table E.21 Normalised antisymmetric stiffnesses of inclusion patterned sheets loaded in perpendicular directions, Penrose Kite and Dart pattern, $k = 3$ and $\nu = 0.3$

Gap ratio	p	L/a	Normalised stiffness	Normalised stiffness perpendicular
0.1	0.5874	25	1.7856	1.7995
0.2	0.5352	25	1.6770	1.7274
0.3	0.4897	25	1.5992	1.6392
0.4	0.4497	25	1.5322	1.5383
0.5	0.4144	25	1.4771	1.4568
1	0.2878	50	1.3030	1.3156
2	0.1619	50	1.1615	1.1603
3	0.1036	50	1.0822	1.1116
4	0.0720	50	1.0585	1.0756
5	0.0529	50	1.0590	1.0624
10	0.0180	50	1.0128	1.0175

Table E.22 Normalised antisymmetric stiffnesses of inclusion patterned sheets loaded in perpendicular directions, phyllotaxis pattern, $k = 3$ and $\nu = 0.3$

Gap ratio	p	L/a	Normalised stiffness	Normalised stiffness perpendicular
0.1	0.6372	25	1.8690	1.9199
0.2	0.5806	25	1.7574	1.7766
0.3	0.5312	25	1.6677	1.6357
0.4	0.4878	25	1.5878	1.5935
0.5	0.4496	25	1.5243	1.5507
1	0.3122	50	1.3421	1.3398
2	0.1756	50	1.1595	1.1780
3	0.1124	50	1.0979	1.1159
4	0.0781	50	1.0736	1.0639
5	0.0573	50	1.0449	1.0437
10	0.0195	50	1.0163	1.0143

Table E.23 Normalised antisymmetric stiffnesses of a regular hexagonal pattern of inclusions as the pattern is oriented at different angles to the direction of primary loading, $k = 3$ and $\nu = 0.3$

Gap ratio	p	L/a	Orientation	Normalised stiffness
0.5	0.5804	50	0°	1.7640
0.5	0.5804	50	5°	1.7562
0.5	0.5804	50	10°	1.7566
0.5	0.5804	50	15°	1.7640
0.5	0.5804	50	20°	1.7498
0.5	0.5804	50	25°	1.7559
0.5	0.5804	50	30°	1.7629
0.5	0.5804	50	35°	1.7559
0.5	0.5804	50	40°	1.7498
0.5	0.5804	50	45°	1.7640
0.5	0.5804	50	50°	1.7566
0.5	0.5804	50	55°	1.7562
0.5	0.5804	50	60°	1.7640
0.5	0.5804	50	65°	1.7562
0.5	0.5804	50	70°	1.7566
0.5	0.5804	50	75°	1.7640
0.5	0.5804	50	80°	1.7498
0.5	0.5804	50	85°	1.7559
0.5	0.5804	50	90°	1.7629

Table E.24 Normalised antisymmetric stiffnesses of a regular square pattern of inclusions as the pattern is oriented at different angles to the direction of primary loading, $k = 3$ and $\nu = 0.3$

Gap ratio	p	L/a	Orientation	Normalised stiffness
0.5	0.5027	50	0°	1.7004
0.5	0.5027	50	5°	1.6905
0.5	0.5027	50	10°	1.6693
0.5	0.5027	50	15°	1.6699
0.5	0.5027	50	20°	1.6403
0.5	0.5027	50	25°	1.6027
0.5	0.5027	50	30°	1.5934
0.5	0.5027	50	35°	1.5707
0.5	0.5027	50	40°	1.5579
0.5	0.5027	50	45°	1.5444
0.5	0.5027	50	50°	1.5579
0.5	0.5027	50	55°	1.5707
0.5	0.5027	50	60°	1.5934
0.5	0.5027	50	65°	1.6027
0.5	0.5027	50	70°	1.6403
0.5	0.5027	50	75°	1.6699
0.5	0.5027	50	80°	1.6693
0.5	0.5027	50	85°	1.6905
0.5	0.5027	50	90°	1.7004

E.2 Normalised stiffness of dimpled sheets

Table E.25 Normalised biaxial bending stiffnesses and SCF of dimpled sheets, regular hexagonal pattern, quartic dimple profile, $d/a = 1/3$, $a/t = 30$, $\nu = 0.3$ and $L/a = 100/3$

Gap ratio	p	Normalised stiffness	Normalised stiffness up-down	SCF	SCF up-down
0.333	0.6663	2.0339	2.1164	0.9957	1.1065
0.5	0.5804	1.8454		0.9937	
0.667	0.5101	1.7060	1.7396	0.9992	1.109
1	0.4031	1.5171		1.0062	
1.333	0.3265	1.3976	1.4075	1.0193	1.1445
1.667	0.2698	1.3166		1.0348	
2	0.2267	1.2588	1.2627	1.0463	1.1768
2.333	0.1932	1.2160		1.0552	
2.667	0.1666	1.1821	1.1839	1.0658	1.1938
4	0.1008	1.1055		1.0812	
5	0.0740	1.0765	1.0769	1.0920	1.0769

Table E.26 Normalised biaxial bending stiffnesses and SCF of dimpled sheets, regular square pattern, quartic dimple profile, $d/a = 1/3$, $a/t = 30$, $\nu = 0.3$ and $L/a = 100/3$

Gap ratio	p	Normalised stiffness	Normalised stiffness up-down	SCF	SCF up-down
0.333	0.5770	1.8516	1.9076	1.2758	1.1900
0.5	0.5027	1.6985		1.0757	
0.667	0.4418	1.5897	1.6104	1.0403	1.1868
1	0.3491	1.4321		1.0623	
1.333	0.2827	1.3342	1.3415	1.0642	1.1923
1.667	0.2337	1.2672		1.0623	
2	0.1963	1.2191	1.2221	1.0670	1.1995
2.333	0.1673	1.1833		1.0723	
2.667	0.1443	1.1557	1.1571	1.0788	1.2133
4	0.0873	1.0909		1.0872	
5	0.0641	1.0659	1.0661	1.0960	1.2353

Table E.27 Normalised biaxial bending stiffnesses and SCF of dimpled sheets, Penrose Rhombus pattern, quartic dimple profile, $d/a = 1/3$, $a/t = 30$, $\nu = 0.3$ and $L/a = 100/3$

Gap ratio	p	Normalised stiffness	Normalised stiffness up-down	SCF	SCF up-down
0.333	0.5146	1.7303	1.7861	1.2165	1.3338
0.5	0.4637	1.6185		1.3115	
0.667	0.4072	1.5168	1.5365	1.1523	1.3013
1	0.3110	1.3703		1.1420	
1.333	0.2545	1.2899		1.1337	
1.667	0.2036	1.2210		1.1323	
2	0.1866	1.2019	1.1966	1.1238	1.2763
2.333	0.1470	1.1564		1.1223	
2.667	0.1244	1.1307	1.1316	1.1258	1.12658
4	0.0763	1.0802		1.1232	
5	0.0594	1.0611	1.0603	1.1088	1.2643

Table E.28 Normalised biaxial bending stiffnesses of dimpled sheets, regular hexagonal pattern, spherical cap dimple profile, $d/a = 1/6$, $a/t = 6$, $\nu = 0.3$ and $L/a = 100/3$

Gap ratio	p	Normalised stiffness	Normalised stiffness up-down
0.333	0.6663	1.3203	1.4791
0.5	0.5804	1.2948	1.4102
0.667	0.5101	1.2705	1.3543
1	0.4031	1.2274	
1.333	0.3265	1.1859	1.2139
1.667	0.2698	1.1556	
2	0.2267	1.1313	1.1457
2.333	0.1932	1.1127	
2.667	0.1666	1.0976	1.1048
4	0.1008	1.0592	
5	0.0740	1.0436	1.0447

Table E.29 Normalised biaxial bending stiffnesses of dimpled sheets, regular square pattern, spherical cap dimple profile, $d/a = 1/6$, $a/t = 6$, $\nu = 0.3$ and $L/a = 100/3$

Gap ratio	p	Normalised stiffness	Normalised stiffness up-down
0.333	0.5770	1.2964	1.4235
0.5	0.5027	1.2692	
0.667	0.4418	1.2431	1.3097
1	0.3491	1.1980	
1.333	0.2827	1.1628	1.1860
1.667	0.2337	1.1357	
2	0.1963	1.1146	1.1247
2.333	0.1673	1.0979	
2.667	0.1443	1.0846	1.0897
4	0.0873	1.0513	
5	0.0641	1.0377	1.0386

Table E.30 Normalised biaxial bending stiffnesses of dimpled sheets, Penrose Rhombus pattern, spherical cap dimple profile, $d/a = 1/6$, $a/t = 6$, $\nu = 0.3$ and $L/a = 100/3$

Gap ratio	p	Normalised stiffness	Normalised stiffness up-down
0.333	0.5146	1.2734	1.3466
0.5	0.4637	1.2530	
0.667	0.4072	1.2230	1.2867
1	0.3110	1.1785	
1.333	0.2545	1.1444	1.1595
1.667	0.2036	1.1154	
2	0.1866	1.1068	1.1100
2.333	0.1470	1.0848	
2.667	0.1244	1.0740	1.0745
4	0.0763	1.0451	
5	0.0594	1.0352	1.0350

Table E.31 Normalised biaxial bending stiffnesses of dimpled sheets, regular hexagonal pattern, spherical cap dimple profile, $d/a = 1/6$, $a/t = 30$, $\nu = 0.3$ and $L/a = 100/3$

Gap ratio	p	Normalised stiffness	Normalised stiffness up-down
0.333	0.6663	2.3063	2.4410
0.5	0.5804	2.5063	2.1367
0.667	0.5101	1.8742	1.9255
1	0.4031	1.6321	
1.333	0.3265	1.4806	1.4932
1.667	0.2698	1.3802	
2	0.2267	1.3092	1.3140
2.333	0.1932	1.2571	
2.667	0.1666	1.2157	1.2176
4	0.1008	1.1241	
5	0.0740	1.0894	1.0902

Table E.32 Normalised biaxial bending stiffnesses of dimpled sheets, regular square pattern, spherical cap dimple profile, $d/a = 1/6$, $a/t = 30$, $\nu = 0.3$ and $L/a = 100/3$

Gap ratio	p	Normalised stiffness	Normalised stiffness up-down
0.333	0.5770	2.0780	2.1598
0.5	0.5027	1.8716	
0.667	0.4418	1.7225	1.7609
1	0.3491	1.5249	
1.333	0.2827	1.4020	1.4130
1.667	0.2337	1.3193	
2	0.1963	1.2606	1.2650
2.333	0.1673	1.2172	
2.667	0.1443	1.1841	1.1861
4	0.0873	1.1068	
5	0.0641	1.0772	1.0775

Table E.33 Normalised biaxial stretching stiffnesses of dimpled sheets, regular hexagonal pattern, spherical cap dimple profile, $d/a = 1/6$, $a/t = 6$, $\nu = 0.3$ and $L/a = 100/3$

Gap ratio	p	Normalised stiffness	Normalised stiffness up-down
0.333	0.6663	0.4519	0.4989
0.5	0.5804	0.5012	0.5423
0.667	0.5101	0.5468	0.5805
1	0.4031	0.6273	
1.333	0.3265	0.6824	0.6975
1.667	0.2698	0.7298	
2	0.2267	0.7692	0.7783
2.333	0.1932	0.8003	
2.667	0.1666	0.8228	0.8275
5	0.0740	0.9171	0.9180

Table E.34 Normalised biaxial stretching stiffnesses of dimpled sheets, regular square pattern, spherical cap dimple profile, $d/a = 1/6$, $a/t = 6$, $\nu = 0.3$ and $L/a = 100/3$

Gap ratio	p	Normalised stiffness	Normalised stiffness up-down
0.333	0.5770	0.5010	0.5381
0.5	0.5027	0.5507	
0.667	0.4418	0.5938	0.6163
1	0.3491	0.6643	
1.333	0.2827	0.7188	0.7293
1.667	0.2337	0.7616	
2	0.1963	0.7957	0.8013
2.333	0.1673	0.8232	
2.667	0.1443	0.8456	0.8488
4	0.0873	0.9036	
5	0.0641	0.9283	0.9290

Table E.35 Normalised uniaxial bending stiffnesses of dimpled sheets, regular hexagonal pattern, quadratic dimple profile, $d/a = 1/3$, $a/t = 30$, $\nu = 0.3$ and $L/a = 100/3$

Gap ratio	p	Normalised stiffness	Normalised stiffness up-down
0.333	0.6663	3.4332	3.6105
0.5	0.5804	2.9863	
0.667	0.5101	2.6557	2.7025
1	0.4031	2.2160	
1.333	0.3265	1.9431	1.9525
1.667	0.2698	1.7581	
2	0.2267	1.6253	1.6284
2.333	0.1932	1.5255	
2.667	0.1666	1.4540	1.4550
4	0.1008	1.2765	
5	0.0740	1.1981	1.1983

Table E.36 Normalised uniaxial bending stiffnesses of dimpled sheets, regular hexagonal pattern, spherical cap dimple profile, $d/a = 1/6$, $a/t = 30$, $\nu = 0.3$ and $L/a = 100/3$

Gap ratio	p	Normalised stiffness	Normalised stiffness up-down
0.333	0.6663	3.4000	4.2199
0.5	0.5804	3.1532	3.5531
0.667	0.5101	2.8776	3.0920
1	0.4031	2.4228	
1.333	0.3265	2.1097	2.1535
1.667	0.2698	1.8929	
2	0.2267	1.7362	1.7512
2.333	0.1932	1.6186	
2.667	0.1666	1.5323	1.5392
4	0.1008	1.3171	
5	0.0740	1.2323	1.2333

Table E.37 Normalised uniaxial bending stiffnesses of dimpled sheets, regular square pattern, spherical cap dimple profile, $d/a = 1/6$, $a/t = 30$, $\nu = 0.3$ and $L/a = 100/3$

Gap ratio	p	Normalised stiffness
0.333	0.5770	2.9600
0.5	0.5027	2.66070
0.667	0.4418	2.3579
1	0.3491	2.0282
1.333	0.2827	1.8188
1.667	0.2337	1.6933
2	0.1963	1.5662
2.333	0.1673	1.4842
2.667	0.1443	1.4196
4	0.0873	1.2591
5	0.0641	1.1928

Table E.38 Normalised antisymmetric bending stiffnesses of dimpled sheets, regular hexagonal pattern, quadratic dimple profile, $d/a = 1/3$, $a/t = 30$, $\nu = 0.3$ and $L/a = 100/3$

Gap ratio	p	Normalised stiffness	Normalised stiffness up-down
0.333	0.6663	5.4537	5.8245
0.5	0.5804	4.4729	
0.667	0.5101	3.7921	3.8499
1	0.4031	2.9464	
1.333	0.3265	2.4601	2.4668
1.667	0.2698	2.1456	
2	0.2267	1.9270	1.9293
2.333	0.1932	1.7673	
2.667	0.1666	1.6596	1.6597
4	0.1008	1.3813	
5	0.0740	1.2757	1.2757

Table E.39 Normalised antisymmetric bending stiffnesses of dimpled sheets, regular hexagonal pattern, spherical cap dimple profile, $d/a = 1/6$, $a/t = 30$, $\nu = 0.3$ and $L/a = 100/3$

Gap ratio	p	Normalised stiffness	Normalised stiffness up-down
0.333	0.6663	4.5661	7.1725
0.5	0.5804	4.4243	5.5877
0.667	0.5101	4.0431	4.5932
1	0.4031	3.2764	
1.333	0.3265	2.7351	2.8215
1.667	0.2698	2.3658	
2	0.2267	2.1061	2.1323
2.333	0.1932	1.9151	
2.667	0.1666	1.7822	1.7932
4	0.1008	1.4514	
5	0.0740	1.3257	1.3269

Appendix F

Perforated strips experimental data

F.1 Uniaxial stretching stiffness of perforated strips

The experimentally found stiffnesses of the perforated strips of copper beryllium under uniaxial tension, described in Section 4.10, are given here. The p value of each strip is given in two ways, the first calculating the theoretical p of the pattern for a infinite plane, and the second based on number of perforations actually realised in the finite width strip. The average of these two values is also calculated. The stiffness is the initial linear gradient of the loading curve of applied load (N) against displacement (mm). The average stiffness of the three plain specimens is used to calculate the normalised stiffness of the perforated strips.

Table F.1 Uniaxial stretching stiffnesses of perforated strips

Pattern	Gap ratio	p theory	p actual	p average	Stiffness (N/mm)	Normalised stiffness
Plain	n/a	0	0	0	5.333	0.9975
Plain	n/a	0	0	0	5.267	0.9850
Plain	n/a	0	0	0	5.440	1.0175
Hexagonal	0.6667	0.5101	0.4607	0.4854	1.900	0.3554
Hexagonal	1.3333	0.3265	0.3282	0.3273	2.760	0.5162
Hexagonal	2.6667	0.1666	0.1780	0.1723	3.200	0.5985
Square	0.6667	0.4418	0.4145	0.4282	2.550	0.4769
Square	1.3333	0.2827	0.2916	0.2872	3.467	0.6484
Square	2.6667	0.1443	0.1452	0.1447	4.250	0.7949
Square 45°	0.6667	0.4418	0.4317	0.4367	1.400	0.2618
Square 45°	1.3333	0.2827	0.2562	0.2695	2.833	0.5299
Square 45°	2.6667	0.1443	0.1452	0.1447	3.533	0.6608
Rhombus	0.6667	0.4290	0.4115	0.4203	1.620	0.3030
Rhombus	1.3333	0.2746	0.2600	0.2673	2.967	0.5549
Rhombus	2.6667	0.1401	0.1351	0.1376	3.850	0.7201
Kite and Dart	0.6667	0.3361	0.3522	0.3441	1.933	0.3616
Kite and Dart	1.3333	0.2151	0.2247	0.2199	3.333	0.6234
Kite and Dart	2.6667	0.1098	0.1098	0.1098	4.133	0.7731
Phyllotaxis	0.6667	0.3951	0.3610	0.3781	1.840	0.3441
Phyllotaxis	1.3333	0.2529	0.2335	0.2432	3.350	0.6266
Phyllotaxis	2.6667	0.1290	0.1224	0.1257	4.200	0.7860

F.2 Uniaxial bending stiffness of perforated strips

The experimentally found stiffnesses of the perforated strips of copper beryllium under uniaxial four point bending, described in Section 4.10, are given here. The rotational stiffness of the strip is found from the initial linear gradient of the curve of applied moment (Nmm) against rotation (rad). The applied moment is calculated from the applied force at each knife-edge, which is half the total force seen at the load cell and the lever arm, which is 30mm. The rotation is calculated as the displacement of the upper knife-edge divided by the lever arm. The rotational stiffness can thus be calculated as half of the gradient of the force-displacement curve multiplied by the lever arm squared. Some of the specimens gave unusable results due to slippage occurring between the knife-edges and the notches in the clamping plates, the corresponding rows of the results table have been omitted correspondingly.

Table F.2 Uniaxial bending stiffnesses of perforated strips

Pattern	Gap ratio	p theory	p actual	p average	Stiffness (Nmm/rad)	Normalised stiffness
Plain	n/a	0	0	0	0.7425	1.0683
Plain	n/a	0	0	0	0.6825	0.9820
Plain	n/a	0	0	0	0.6600	0.9496
Hexagonal	0.6667	0.5101	0.4607	0.4854	0.2093	0.3011
Hexagonal	1.3333	0.3265	0.3282	0.3273	0.2844	0.4092
Hexagonal	2.6667	0.1666	0.1780	0.1723	0.4320	0.6216
Square	0.6667	0.4418	0.4145	0.4282	-	-
Square	1.3333	0.2827	0.2916	0.2872	-	-
Square	2.6667	0.1443	0.1452	0.1447	0.4770	0.6863
Square 45°	0.6667	0.4418	0.4317	0.4367	0.2053	0.2954
Square 45°	1.3333	0.2827	0.2562	0.2695	0.3682	0.5298
Square 45°	2.6667	0.1443	0.1452	0.1447	0.4275	0.6151
Rhombus	0.6667	0.4290	0.4115	0.4203	0.2700	0.3885
Rhombus	1.3333	0.2746	0.2600	0.2673	-	-
Rhombus	2.6667	0.1401	0.1351	0.1376	0.5085	0.7317
Kite and Dart	0.6667	0.3361	0.3522	0.3441	0.4725	0.6799
Kite and Dart	1.3333	0.2151	0.2247	0.2199	0.3656	0.5261
Kite and Dart	2.6667	0.1098	0.1098	0.1098	-	-
Phyllotaxis	0.6667	0.3951	0.3610	0.3781	0.2789	0.4013
Phyllotaxis	1.3333	0.2529	0.2335	0.2432	0.3915	0.5633
Phyllotaxis	2.6667	0.1290	0.1224	0.1257	0.5250	0.7554

Appendix G

Patterns for experimental testing of dimpled sheets

Four distinct patterns of dimples were chosen for experimental testing. In each case the pattern covers an area which is a square with 100mm sides. The dimples are chosen to have a radius of 3mm, and are spaced such that there is a minimum of 1mm spacing between the edges of the dimples. The four patterns chosen are a regular hexagonal packing, a phyllotaxis pattern, a pattern based on the Penrose Rhombus tiling and a pattern based on the Penrose Kite and Dart tiling. These patterns are displayed graphically in Fig. G.1.

The Penrose tiling based patterns are original to this thesis and their construction and relationship to the underlying Penrose tiling's is given in Appendix C.1.

Each pattern is also given as a pattern split into two subsets, to facilitate dimpling with dimples in opposing directions. Exactly 50% of the pattern is in each subset for the hexagonal, phyllotaxis and Penrose Rhombus patterns. The Penrose Kite and Dart pattern is split into subsets which make up 50.7% and 49.3% respectively. The choice of how to divide the hexagonal pattern is indicated in Fig. G.1a. The phyllotaxis pattern, defined by Eqn 4.52, is split by assigning odd and even values of n to each subset. For the Penrose tiling based patterns, the method of choosing the two subsets is detailed in Appendix C.1. In all four cases, the percentage split is calculated based on the infinite pattern, and a finite patch of this pattern is not guaranteed to have exactly the split by subsection as calculated for the overall pattern. The split of the patterns into these two subsets is shown graphically in Fig. G.2.

The x and y coordinates of the centers of the dimples for each of the four patterns are given in tables in Section G.2. In each case the coordinates for each subset of the pattern, as per Fig. G.2, are given separately.

G.1 Figures of patterns used for experimental testing

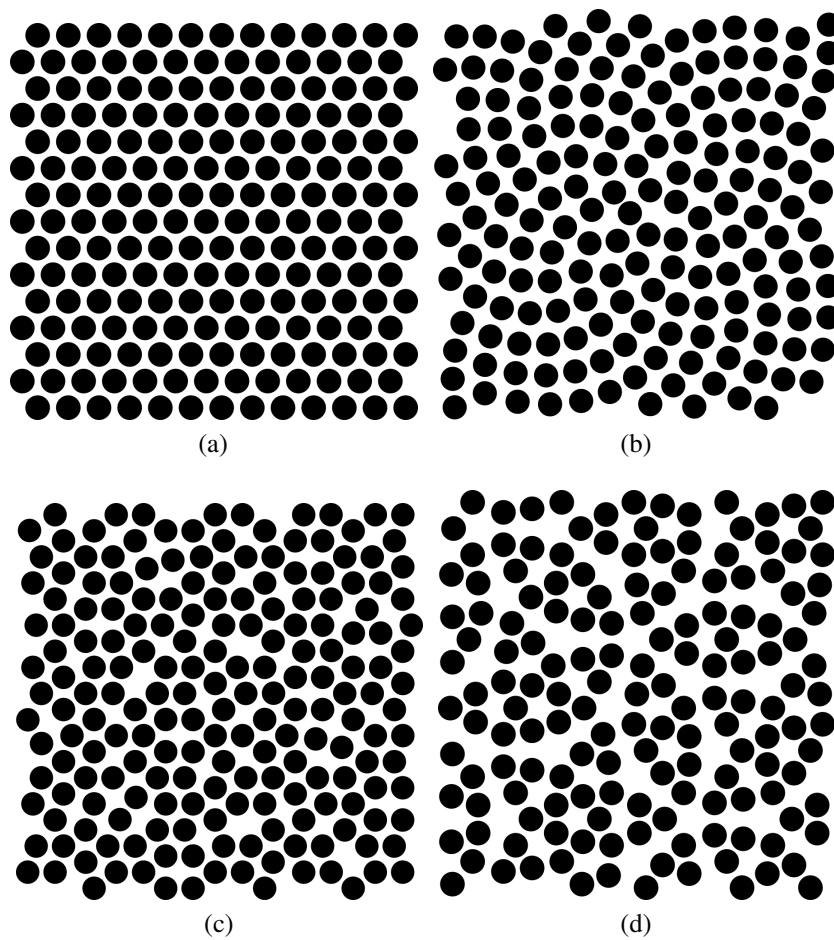


Fig. G.1 (a) A regular hexagonal packing of circles (b) A phyllotaxis spiral pattern. (c) A pattern based on Penrose Rhombus tiling. (d) A pattern based on Penrose Kite and Dart tiling. These patterns are used as dimpling locations for square dimpled sheets. Note that these patterns are scaled down to fit onto the page.

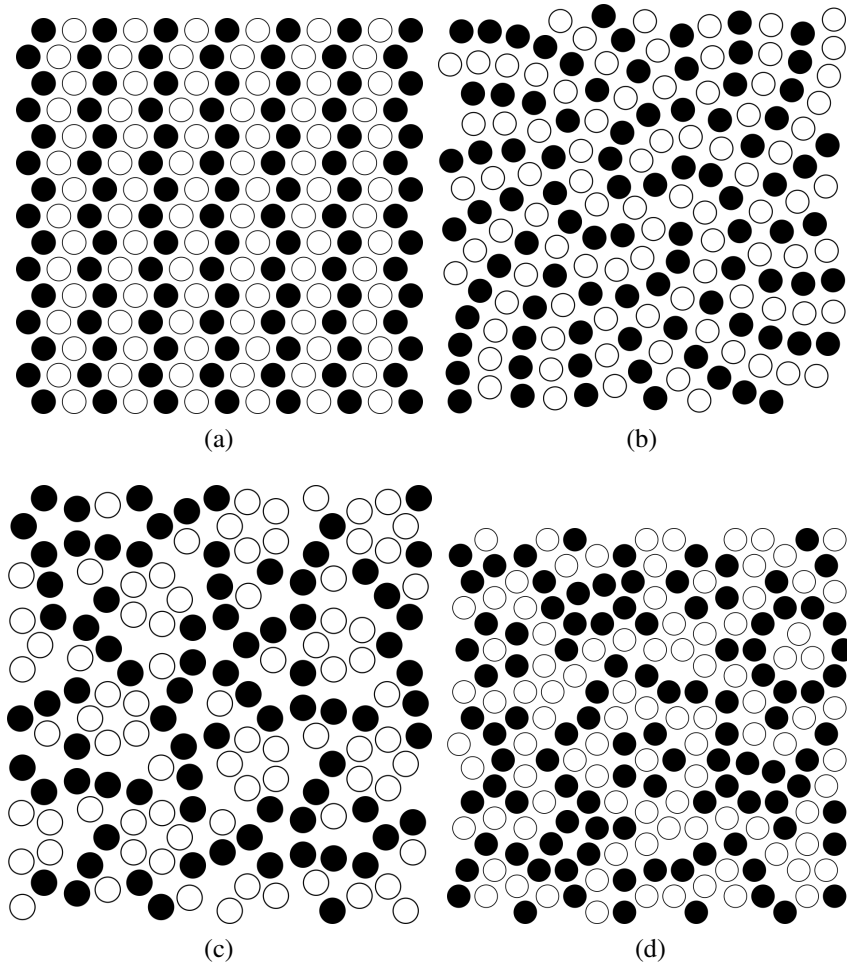


Fig. G.2 (a) A regular hexagonal packing of circles (b) A phyllotaxis spiral pattern. (c) A pattern based on Penrose Rhombus tiling. (d) A pattern based on Penrose Kite and Dart tiling. These patterns are used as dimpling locations for square dimpled sheets, the two subsets given in white and black fill indicate the sets of opposing direction dimples. Note that these patterns are scaled down to fit onto the page.

G.2 Tables of coordinates for patterns used for experimental testing

These tables give the coordinates of the dimple centers (in mm) from the centre of the square plate.

Table G.1 The x and y coordinates of the hexagonal pattern given in Fig. G.2a

Black		White	
x	y	x	y
-46.549	-38.7	-39.101	-38.7
-46.549	-25.8	-39.101	-25.8
-46.549	-12.9	-39.101	-12.9
-46.549	0	-39.101	0
-46.549	12.9	-39.101	12.9
-46.549	25.8	-39.101	25.8
-46.549	38.7	-39.101	38.7
-42.825	-45.15	-35.377	-45.15
-42.825	-32.25	-35.377	-32.25
-42.825	-19.35	-35.377	-19.35
-42.825	-6.45	-35.377	-6.45
-42.825	6.45	-35.377	6.45
-42.825	19.35	-35.377	19.35
-42.825	32.25	-35.377	32.25
-42.825	45.15	-35.377	45.15
-31.653	-38.7	-24.205	-38.7
-31.653	-25.8	-24.205	-25.8
-31.653	-12.9	-24.205	-12.9
-31.653	0	-24.205	0
-31.653	12.9	-24.205	12.9
-31.653	25.8	-24.205	25.8
-31.653	38.7	-24.205	38.7
-27.929	-45.15	-20.481	-45.15
-27.929	-32.25	-20.481	-32.25
-27.929	-19.35	-20.481	-19.35
-27.929	-6.45	-20.481	-6.45
-27.929	6.45	-20.481	6.45

Black		White	
x	y	x	y
-27.929	19.35	-20.481	19.35
-27.929	32.25	-20.481	32.25
-27.929	45.15	-20.481	45.15
-16.758	-38.7	-9.31	-38.7
-16.758	-25.8	-9.31	-25.8
-16.758	-12.9	-9.31	-12.9
-16.758	0	-9.31	0
-16.758	12.9	-9.31	12.9
-16.758	25.8	-9.31	25.8
-16.758	38.7	-9.31	38.7
-13.034	-45.15	-5.586	-45.15
-13.034	-32.25	-5.586	-32.25
-13.034	-19.35	-5.586	-19.35
-13.034	-6.45	-5.586	-6.45
-13.034	6.45	-5.586	6.45
-13.034	19.35	-5.586	19.35
-13.034	32.25	-5.586	32.25
-13.034	45.15	-5.586	45.15
-1.862	-38.7	5.586	-38.7
-1.862	-25.8	5.586	-25.8
-1.862	-12.9	5.586	-12.9
-1.862	0	5.586	0
-1.862	12.9	5.586	12.9
-1.862	25.8	5.586	25.8
-1.862	38.7	5.586	38.7
1.862	-45.15	9.31	-45.15
1.862	-32.25	9.31	-32.25
1.862	-19.35	9.31	-19.35
1.862	-6.45	9.31	-6.45
1.862	6.45	9.31	6.45
1.862	19.35	9.31	19.35
1.862	32.25	9.31	32.25
1.862	45.15	9.31	45.15
13.034	-38.7	20.481	-38.7

Black		White	
x	y	x	y
13.034	-25.8	20.481	-25.8
13.034	-12.9	20.481	-12.9
13.034	0	20.481	0
13.034	12.9	20.481	12.9
13.034	25.8	20.481	25.8
13.034	38.7	20.481	38.7
16.758	-45.15	24.205	-45.15
16.758	-32.25	24.205	-32.25
16.758	-19.35	24.205	-19.35
16.758	-6.45	24.205	-6.45
16.758	6.45	24.205	6.45
16.758	19.35	24.205	19.35
16.758	32.25	24.205	32.25
16.758	45.15	24.205	45.15
27.929	-38.7	35.377	-38.7
27.929	-25.8	35.377	-25.8
27.929	-12.9	35.377	-12.9
27.929	0	35.377	0
27.929	12.9	35.377	12.9
27.929	25.8	35.377	25.8
27.929	38.7	35.377	38.7
31.653	-45.15	39.101	-45.15
31.653	-32.25	39.101	-32.25
31.653	-19.35	39.101	-19.35
31.653	-6.45	39.101	-6.45
31.653	6.45	39.101	6.45
31.653	19.35	39.101	19.35
31.653	32.25	39.101	32.25
31.653	45.15	39.101	45.15
42.825	-38.7		
42.825	-25.8		
42.825	-12.9		
42.825	0		
42.825	12.9		

Black		White	
x	y	x	y
42.825	25.8		
42.825	38.7		
46.549	-45.15		
46.549	-32.25		
46.549	-19.35		
46.549	-6.45		
46.549	6.45		
46.549	19.35		
46.549	32.25		
46.549	45.15		

Table G.2 The x and y coordinates of the phyllotaxis pattern given in Fig. G.2b

Black		White	
x	y	x	y
3.38	-49.608	46.328	47.228
32.69	-49.518	-1.245	46.624
-30.216	-49.325	-22.743	45.96
-14.229	-49.088	30.764	45.853
25.976	-47.454	15.293	45.62
19.613	-44.135	-16.602	41.951
-46.574	-43.711	46.548	40.201
-0.634	-43.335	2.224	39.703
-31.002	-42.318	30.908	38.725
-16.026	-41.967	16.388	38.111
13.728	-39.37	-11.009	36.336
-46.239	-36.711	-43.234	34.853
-3.481	-35.667	-36.129	34.417
-30.453	-35.078	45.638	33.255
39.695	-34.802	-28.938	32.532
46.737	-34.591	29.601	31.378
-16.327	-34.021	4.342	31.118
32.542	-33.672	15.763	29.64
8.463	-32.754	-21.671	28.845
25.317	-30.948	-6.112	28.462

Black		White	
x	y	x	y
-44.732	-29.845	43.504	26.496
-28.301	-27.619	26.477	23.784
17.976	-26.106	-14.168	22.514
-4.702	-25.847	39.991	20.032
-14.566	-24.855	-36.901	19.856
-41.934	-23.22	12.485	19.417
3.974	-23.121	-44.44	19.368
-24.006	-19.835	4.352	19.344
40.753	-19.803	-28.581	18.575
32.859	-19.473	-2.046	15.785
47.974	-18.589	20.66	15.68
10.075	-17.581	-18.84	14.591
23.976	-17.031	34.804	13.971
-37.635	-16.945	-4.912	9.457
-8.833	-12.564	27.239	8.398
-31.398	-11.121	-31.157	7.169
-15.91	-11.07	-19.711	6.288
12.584	-10.605	-39.789	5.749
-2.545	-9.467	45.963	5.273
-48.774	-7.649	7.482	4.759
25.97	-7.117	14.434	3.173
35.702	-6.675	-46.926	2.859
-21.953	-5.787	39.304	1.241
43.512	-4.461	-16.965	-0.702
10.753	-3.927	-1.5	-1.5
-42.82	-3.127	30.818	-1.576
-35.343	0.345	18.757	-2.524
-7.701	1.362	-29.476	-3.674
24.111	1.998	-11.265	-4.65
-25.488	2.362	4.021	-5.245
0.448	5.1	-37.607	-7.884
33.874	5.652	19.753	-10.382
-12.264	7.107	46.428	-11.161
19.162	8.853	-24.244	-12.442

Black		White	
x	y	x	y
-49.808	9.816	38.996	-12.861
40.824	10.336	30.421	-12.906
5.461	11.669	4.054	-12.924
-25.479	12.075	-43.612	-12.981
-42.832	12.189	-0.83	-17.96
12.395	12.334	-16.673	-18.023
-34.882	13.126	16.967	-18.704
-11.826	14.172	-48.089	-18.761
46.022	15.796	-31.038	-19.321
28.053	15.894	-8.307	-19.85
-7.419	20.626	25.647	-23.959
-21.46	21.777	10.513	-25.826
33.402	22.76	-35.258	-26.221
19.443	22.843	48.089	-26.484
0.121	24.905	33.527	-26.492
-29.651	25.489	40.984	-27.208
9.583	25.85	-21.316	-27.248
-44.58	27.011	1.104	-30.267
-37.3	27.048	-10.033	-30.926
36.677	29.707	16.748	-33.032
-13.603	29.824	-37.706	-33.212
22.537	31.4	-23.234	-35.371
-2.708	34.742	23.246	-37.753
9.899	35.442	4.62	-38.601
-19.962	35.639	-9.305	-39.555
38.377	36.728	-38.717	-40.247
23.487	39.196	29.994	-40.744
-26.593	39.44	36.913	-42.322
-33.438	41.697	43.912	-42.657
-6.794	41.979	-23.35	-42.892
-47.411	42.392	9.195	-44.954
-40.409	42.637	-7.005	-46.863
8.323	43.346	-38.474	-47.251
38.744	43.758	14.579	-49.869

Black		White	
x	y	x	y
22.861	46.469	-22.05	-49.928
-11.798	47.574	-31.157	7.169
-45.817	-50.741	-50.196	34.034

Table G.3 The x and y coordinates of the Penrose Rhombus pattern given in Fig. G.2c

Black		White	
x	y	x	y
-19.527	46.954	-13.865	-48.424
39.779	46.954	39.778	-44.309
-48.717	42.934	-26.527	-44.308
11.463	42.839	-42.18	-44.308
-6.864	42.839	-1.201	-44.308
-32.19	42.839	21.452	-44.308
19.289	40.296	5.8	-44.308
44.656	40.296	-34.313	-41.766
-40.017	40.295	13.626	-41.765
6.626	36.182	-13.864	-40.194
31.952	36.181	37.615	-37.651
-4.7	36.181	44.616	-37.651
-27.353	36.181	-40.017	-37.651
-45.68	36.181	19.289	-37.651
-12.033	35.341	31.953	-33.537
-18.691	33.178	-9.027	-33.536
19.289	32.067	39.778	-30.994
-6.864	29.524	-1.2	-30.994
34.115	29.524	4.463	-26.88
-25.19	29.524	11.463	-26.879
41.157	29.524	-32.191	-26.879
11.463	29.524	-47.843	-26.879
-19.527	25.409	27.116	-26.879
-12.526	25.409	19.289	-24.336
28.452	25.409	-39.946	-24.208
-1.201	25.409	-1.2	-22.765
-42.18	25.409	39.82	-22.765
46.779	25.409	-27.354	-20.222
-34.354	22.866	6.626	-20.222
-47.017	18.752	-9.027	-20.221
-21.69	18.752	44.656	-16.107
48.982	18.752	-13.863	-13.564
19.289	18.752	11.463	-13.564

Black		White	
x	y	x	y
26.289	18.751	-32.19	-13.563
-9.027	14.637	-45.64	-11.47
-34.354	14.637	46.819	-9.45
28.563	12.295	-1.201	-9.449
-42.181	12.095	-19.527	-9.449
46.779	12.094	-49.14	-5.408
-1.201	12.094	-32.191	-5.336
4.463	7.98	34.115	-5.335
41.156	7.98	-13.864	-5.335
11.463	7.98	11.463	-5.334
34.116	7.98	26.289	-2.793
-13.864	7.98	38.993	1.322
19.289	5.437	-27.354	1.323
-16.027	1.322	6.626	1.323
-34.354	1.322	-9.027	1.323
31.952	1.322	13.733	1.388
-45.68	1.322	46.82	3.865
-21.69	-2.793	-1.2	3.866
0.962	-2.793	-40.018	5.436
44.656	-2.793	26.29	5.438
-40.017	-2.793	-47.844	7.979
19.288	-2.793	-25.191	7.98
-6.863	-5.335	-32.19	7.98
17.126	-9.45	-6.863	7.981
-37.853	-9.45	-19.527	12.095
5.8	-9.45	21.453	12.095
-26.527	-9.45	-27.354	14.637
39.779	-9.45	13.626	14.637
24.54	-10.291	41.156	16.732
31.197	-12.454	34.156	16.732
-6.864	-13.564	-40.018	18.752
0.962	-16.108	7.963	18.752
37.657	-16.108	0.963	18.752
-40.017	-16.108	-14.69	18.752

Black		White	
<i>x</i>	<i>y</i>	<i>x</i>	<i>y</i>
19.289	-16.108	-6.863	21.295
-21.691	-16.108	37.656	22.793
-45.68	-20.221	13.626	22.867
24.953	-20.222	-27.354	22.867
-16.027	-20.222	5.8	25.409
13.626	-20.223	21.493	25.41
-34.355	-20.223	-32.19	29.524
31.953	-20.223	-47.843	29.524
46.78	-22.766	26.289	32.066
-21.458	-25.236	-40.017	32.067
34.115	-26.88	0.963	32.067
-6.864	-26.88	46.819	33.638
-13.864	-26.88	38.993	36.181
-25.572	-30.899	13.625	36.181
21.453	-30.994	-34.353	36.181
-42.18	-30.994	0.963	40.296
46.779	-30.995	-21.69	40.296
-16.027	-33.537	26.289	40.296
13.626	-33.538	-13.864	42.839
-34.354	-33.538	34.115	42.839
7.963	-37.651	-26.528	46.953
-28.69	-37.651	-42.18	46.953
26.289	-37.652	28.452	46.953
-21.69	-37.652	5.799	46.953
0.963	-37.652	-1.201	46.953
-47.017	-37.652	46.819	46.954
-6.864	-40.194	21.452	46.954
-49.18	-44.309		
-19.528	-44.309		
28.494	-44.309		
46.779	-44.309		
11.463	-48.424		
-32.191	-48.424		
34.116	-48.424		

Black		White	
x	y	x	y
-6.864	-48.424		

Table G.4 The x and y coordinates of the Penrose Kite and Dart pattern given in Fig. G.2d

Black		White	
x	y	x	y
21.446	47.994	-1.127	47.995
5.848	47.139	-40.333	47.995
37.801	47.139	44.776	47.995
-25.87	46.418	-18.66	47.995
31.319	45.033	-32.845	45.562
12.33	45.033	-7.887	45.032
41.806	41.626	25.173	41.626
1.843	41.625	-44.96	41.625
12.33	38.218	-14.033	41.624
31.319	38.218	-32.845	37.689
-7.886	38.217	-25.87	36.833
37.801	36.112	44.776	35.256
5.849	36.112	21.445	35.256
-29.876	31.319	-1.127	35.256
-45.473	30.464	-40.333	35.256
-13.52	30.463	-18.66	35.255
25.452	29.742	10.988	31.32
-20.002	28.357	32.661	31.319
44.049	27.912	18.476	28.886
6.082	25.806	-38.992	28.358
-9.515	24.95	-0.399	27.912
-20.001	21.543	37.567	25.806
-45.238	20.158	-26.147	24.95
25.451	20.158	42.707	21.014
-13.52	19.437	-38.263	21.014
31.933	18.052	0.942	21.014
-41.232	14.644	18.476	21.013
21.445	14.644	-30.776	18.581
-32.117	11.682	-6.545	18.58
31.933	11.238	11.716	18.051
11.716	11.236	38.08	14.644
-13.521	9.852	5.57	14.644
25.451	9.13	-25.635	13.789

Black		White	
x	y	x	y
-45.239	9.13	-6.546	10.708
37.567	3.483	42.707	8.275
-25.87	3.482	-20.73	8.275
-0.399	1.376	18.476	8.275
-19.389	1.376	0.942	8.275
-29.876	-2.032	-9.515	4.338
-19.389	-5.439	-32.845	4.338
-39.605	-5.439	6.061	3.665
21.446	-5.969	44.048	1.377
5.848	-6.824	-39.605	1.376
37.801	-6.824	18.476	0.401
-25.87	-7.545	25.468	-0.458
12.33	-8.93	-13.242	-2.031
31.32	-8.93	32.661	-2.031
41.807	-12.337	10.988	-2.032
1.843	-12.338	-45.751	-2.032
-13.755	-13.193	44.776	-5.968
12.33	-15.744	-1.126	-5.968
31.32	-15.745	-32.845	-8.4
5.849	-17.85	-8.615	-8.401
37.801	-17.851	25.173	-12.337
-29.876	-22.644	-45.239	-13.194
-13.521	-23.499	-7.273	-15.299
-45.473	-23.499	-32.845	-16.274
25.452	-24.22	-25.87	-17.13
0.215	-25.604	21.446	-18.706
-20.002	-25.604	-18.66	-18.707
-38.992	-25.606	-40.333	-18.707
-9.515	-29.012	32.661	-22.642
-20.002	-32.42	10.989	-22.643
43.435	-32.42	-6.545	-22.643
-38.991	-32.42	18.476	-25.076
-13.521	-34.525	43.434	-25.604
-45.473	-34.526	-26.148	-29.012

Black		White	
<i>x</i>	<i>y</i>	<i>x</i>	<i>y</i>
21.446	-39.318	6.361	-29.012
37.801	-40.174	37.288	-29.012
5.849	-40.174	0.215	-32.419
-25.87	-40.895	18.476	-32.948
31.319	-42.28	25.452	-33.805
12.33	-42.28	10.988	-35.381
-7.273	-42.726	32.66	-35.382
-45.239	-44.832	-6.545	-35.382
41.807	-45.687	-29.876	-35.382
1.842	-45.688	-40.334	-39.318
		-18.661	-39.318
		-32.845	-41.751
		-13.755	-44.832
		25.173	-45.687
